TECHNISCHE
UNIVERSITÄT
WIEN
Vienna | Austria

INSTITUT FÜR
MECHANIK UND
MECHATRONIK
Mechanics & Mechatronics

DISSERTATION

Advanced modeling, control and observation concepts for thermal energy systems

ausgeführt zum Zwecke der Erlangung des akademischen Grades
eines Doktors der technischen Wissenschaften
unter der Leitung von

Priv. Doz. Dipl.-Ing. Dr.techn. Alexander Schirrer

am Institut für Mechanik und Mechatronik
Forschungsbereich für Regelungstechnik und Prozessautomatisierung

eingereicht an der Technischen Universität Wien,
Fakultät für Maschinenwesen und Betriebswissenschaften

von

Dipl.-Ing. Dominik Pernsteiner
Fred-Zinnenmann-Platz 4/6/15
1030 Wien

Geboren am 19.02.1991
Matr.Nr.: 01026269

Wien, am 14. Oktober 2021

Meiner Familie,
insbesondere meiner Liebe Lisa,
und meinen Eltern Eva und Roland

Danksagung

Leider lässt sich eine wahrhafte Dankbarkeit mit Worten nicht ausdrücken.

Johann Wolfgang von Goethe (1749-1832)

Eidesstattliche Erklärung

Ich erkläre eidesstattlich, dass ich die Arbeit selbständig angefertigt, keine anderen als die angegebenen Hilfsmittel benutzt und alle aus ungedruckten Quellen, gedruckter Literatur oder aus dem Internet im Wortlaut oder im wesentlichen Inhalt übernommenen Formulierungen und Konzepte gemäß den Richtlinien wissenschaftlicher Arbeiten zitiert, durch Fußnoten gekennzeichnet bzw. mit genauer Quellenangabe kenntlich gemacht habe.

Wien, am 14. Oktober 2021 Dominik Pernsteiner

Kurzfassung

Die vorliegende Arbeit liefert neuartige Methoden im Bereich der modellbasierten Optimierung von thermischen Energiesystemen mit besonderem Fokus auf einen hybriden Energiespeicher. Die Beiträge der Arbeit lassen sich gliedern in: 1.) Modellierung, 2.) Modellreduktion und 3.) Zustandsschätzung für einen hybriden Energiespeicher und schließlich 4.) Betriebsoptimierung eines gesamten thermischen Energiesystems.

Zunächst wird das hybride Energiespeichersystem genauer untersucht. Dazu wird eine Co-Simulationsmethodik eingeführt, die effizient Teilmodelle unterschiedlicher Komplexität unter garantierter Energieerhaltung miteinenader koppelt. Die erforderliche Anzahl von Teilmodellen zur genauen Darstellung des hybriden Speichersystems wird durch ein Optimierungskriterium bestimmt.

Eines der Teilmodelle, das ein Phasenwechselmaterial (PCM) beschreibt, ist rechenintensiv und nicht echtzeitfähig. Es wird ein datenbasierter Modellreduktionsansatz entwickelt, der die aufwändige Lösung der Navier-Stokes-Gleichungen im Phasenwechselproblem ersetzt, ohne die Modellgenauigkeit zu beeinträchtigen.

Das erhaltene echtzeitfähige PCM-Zellenmodell dient als Basis für einen Beobachter, ist aber immer noch von hoher Ordnung. In dem Beobachter werden zwei Modelle unterschiedlicher Ordnung verwendet, um den verteilten Zustand im PCM zu schätzen. Das echtzeitfähige PCM-Zellenmodell hoher Ordnung sagt die zukünftigen Systemausgänge voraus. Der Beobachter verwendet die vorhergesagten Systemausgänge, Messungen und ein Modell, das nur dominante Zustände abbildet, um das PCM-Zellenmodell hoher Ordnung zu korrigieren. Dadurch können die Zustände innerhalb des PCM genau geschätzt werden, während die Rechenlast reduziert und die Beobachtbarkeit sichergestellt wird.

Schließlich wird eine umfassendere Perspektive eingenommen und die Regelung eines gesamten thermischen Energiesystems untersucht. Der dabei betrachtete industrielle Anwendungsfall besteht aus Komponenten mit unterschiedlicher Komplexität und stochastischen Störungen. Das vorgeschlagene hierarchische Betriebsoptimierungskonzept beinhaltet ein neuartiges Kooperationskonzept zwischen den Optimierungsebenen und führt zu optimalen erwarteten Anlagenbetriebskosten.

Alle entwickelten Methoden lassen sich einfach anpassen und auf andere Komponenten oder Konfigurationen übertragen. Sie ermöglichen eine fortschrittliche Modellierung, Steuerung und Beobachtung komplexer Systeme und steigern deren Betriebseffizienz.

Abstract

The present thesis provides novel methods in the area of model-based optimization of thermal energy systems with special focus on a hybrid energy storage. The contributions of the thesis can be structured into: 1.) modeling, 2.) model reduction and 3.) state estimation for a hybrid energy storage and finally 4.) operation optimization of an entire thermal energy system.

First, the hybrid energy storage system is investigated in more detail. Therefore, a co-simulation methodology is introduced, which efficiently couples sub-models of different complexity with guaranteed energy conservation. The required number of sub-models to accurately represent the hybrid storage system is determined by an optimization criterion.

One of the sub-models describing a phase change material (PCM) is computational expensive and not real-time capable. A data-based model reduction approach is developed to replace the laborious solution of the Navier-Stokes equations in the phase change problem without compromising model accuracy.

The obtained real-time capable PCM cell model serves as basis in a state observer, but is still of high order. In the observer, two models of different order are employed to estimate the distributed system state in the PCM. The real-time capable but high-order PCM cell model predicts future system outputs. The observer uses the predicted outputs, measurements and a dominant-states only model to correct the high-order PCM cell model. As a result the states inside the PCM can be estimated accurately while reducing the computational load and ensuring observability.

Finally, a broader perspective is taken and the control of an entire thermal energy system is examined. The investigated industrial use case is comprised of components with different complexities and stochastic disturbances. The proposed hierarchical operation optimization framework incorporates a novel cooperation concept between the optimization layers and leads to optimal expected plant operating costs.

All developed tools can be easily adapted and transferred to other components or plant setups. They enable advanced modeling, control and observation of complex systems and thus result in improved operation efficiency.

Acknowledgment

The author want to acknowledge the support provided by the doctoral school Smart Industrial Concept [SIC!] (`https://sic.tuwien.ac.at`). The Climate and Energy Fund KLIEN/FFG funded a research project started in 2018: HyStEPs grant number 868842.

Contents

Chapter 1

Overview

The operation of thermal energy systems is becoming increasingly complex due to the integration of renewable energies and the reliability required for highly sophisticated industrial processes. Therefore, optimal management of thermal energy systems is necessary to meet energy supply and demand at any given time. In this work, a special focus is given to energy storage and plant operation. On the one hand, optimal storage management is enabled by developing a model-based observer of an advanced storage system with a distributed system state. On the other hand, a generic multi-layer operation optimization framework for thermal energy system control is presented, in which a novel cooperation concept between the optimization layers is implemented.

In Chapter 1, the concept and motivation of this work are introduced. Then, the context to the state of the art is provided and the problem statement is defined. Finally, the methodology of the research approach is presented and a conclusion is drawn. Chapter 2 contains the core element of this thesis, the selected journal publications, and indicates the author's contribution to each publication.

1.1 Motivation and introduction

Each year, the International Energy Agency (IEA) publishes the *World Energy Outlook* to provide insight into the medium- to long-term development of the energy sector [1]. The purpose of this outlook is to shape energy policy and research priorities in order to sustainably meet future energy requirements while ensuring security of supply. The two most relevant scenarios in the *World Energy Outlook 2020* are those that aim either to meet the Paris climate targets [2] or to achieve a more ambitious zero net emissions target by 2050. Both scenarios rely on renewable (sustainable) energy sources, greater flexibility on the supply and demand side of energy systems, and higher efficiency. The present work focuses on the latter two requirements.

The thesis developed here assumes the following typical plant configuration of a thermal

energy system in the energy-intensive industry and presents advanced methods to optimize plant operation, see Figure 1.1. In the investigated plant configuration, thermal energy is generated and applied in further processes. Therefore, a furnace “FN” burns fuel and supplies heat to a drum boiler “DB”. Water evaporates in the drum boiler “DB” and is further heated in the superheater “SH”. Steam from the superheater “SH” can be stored in a thermal energy storage “TES” for later use, or can find immediate application, such as in electricity generation through a steam turbine “ST”, in district heating systems or in the manufacture of goods. In this thesis, the foundation for efficient integration of a complex component into a sophisticated thermal energy system is set by investigating advanced methods of model building (Publication A), model reduction (Publication B), and state estimation (Publication C) using a hybrid thermal energy storage as an example. Then a broader perspective is taken and approaches to control the entire thermal energy system are examined. Therefore, a novel cooperation concept in multi-layer operation optimization is developed, which operates the entire plant at optimal expected costs (Publication* D).

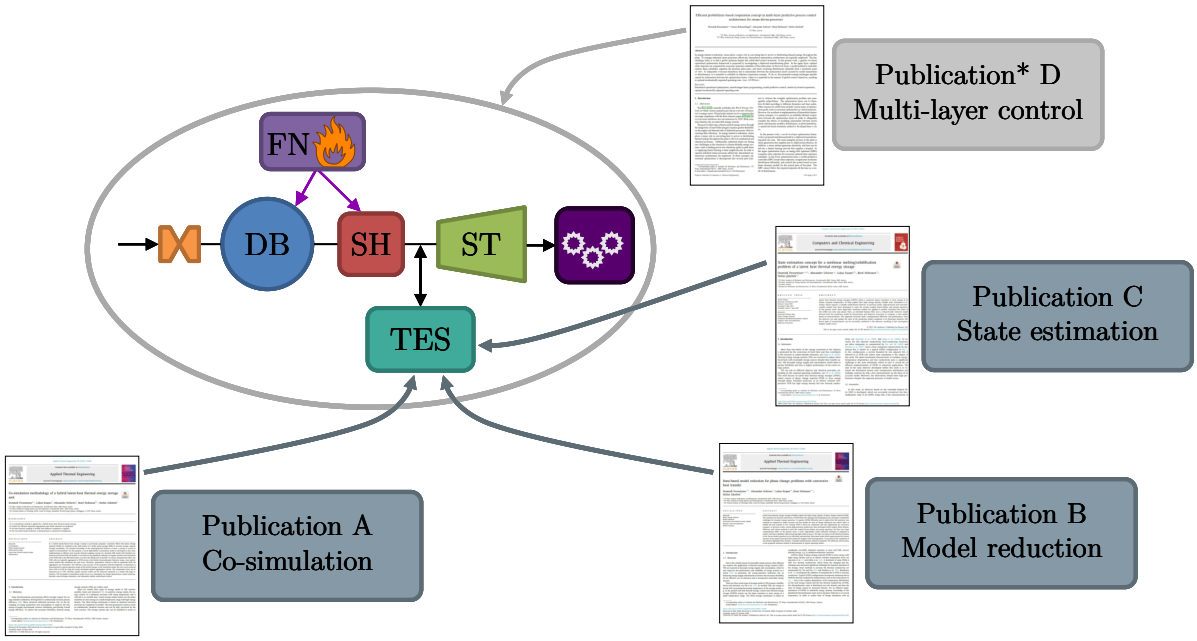

Figure 1.1: A typical plant configuration of a thermal energy system in the energy-intensive industry may include of a furnace (FN), a drum boiler (DB), a super heater (SH), a thermal energy storage (TES), a steam turbine (ST) or manufacturing processes. The scope of the publications is highlighted.

A closer look at thermal energy storages (TES) and optimal plant operation reveals the

*in submission

following main tasks to be addressed in this work.

1.1.1 Thermal energy storages

Thermal energy storages (TES) are often implemented to decouple energy supply and demand in industrial processes and thus increase the flexibility of thermal energy systems. TES can be classified into three main categories according to their underlying storage media: sensible, latent, and chemical storage systems [3]. A sensible heat storage changes its temperature with the stored energy content. A latent heat thermal energy storage (LHTES) accumulates most of the energy utilizing the phase change enthalpy. In a chemical heat storage, thermal energy is stored using a reversible chemical reaction.

When deploying a storage system, the following question arises: How much energy can be stored/released at any given time?

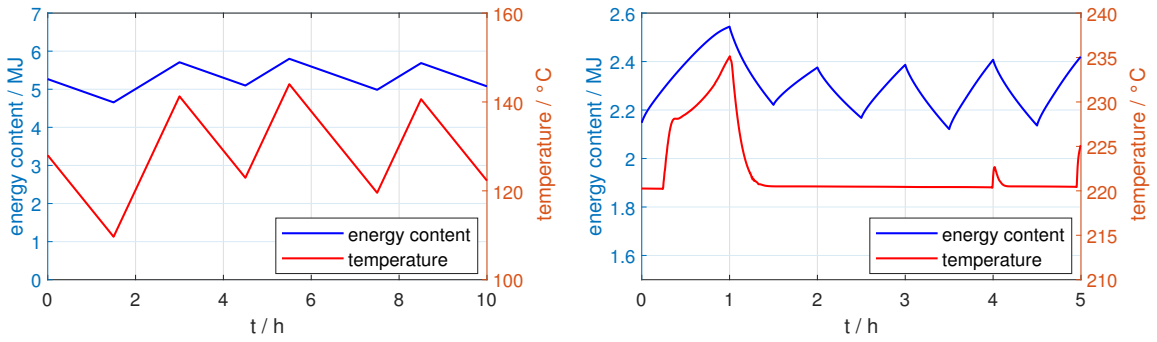

Figure 1.2: A direct relation between energy content and a temperature measurement exists for a sensible storage (a), but not for a latent heat thermal energy storage (b).

In the case of a sensible heat storage unit, such as a Ruths steam storage (RSS), the system's state of charge can be determined by a direct relationship to a temperature and mass measurement. However, in the case of an LHTES, most of the energy is stored during the phase transition at almost constant temperature, thus no direct relationship exists between the temperature and the stored energy content inside, see Figure 1.2. Therefore, a model-based observer/estimator (used synonymously in this thesis) is required to estimate the distributed system state of an LHTES and obtain the state of charge.

In the present thesis, a novel hybrid storage concept combining a sensible RSS with

an LHTES is investigated and a suitable observer concept is developed to estimate the LHTES' distributed system state. First, a high-fidelity co-simulation model of the hybrid storage is built (Publication A). Then, a novel model reduction method is developed to obtain a real-time capable LHTES model suitable for online state estimation tasks (Publication B). Finally, an observer based on the extended Kalman filter is adapted to accurately estimate the distributed system state of the LHTES and obtain its state of charge (Publication C).

1.1.2 Optimal plant operation

Heat treatments are classic tasks of thermal energy systems in the energy-intensive industry. During heat treatments, thermal energy is used to alter physical or chemical properties of a product. In the course of the energy transition, thermal energy systems are facing new tasks, e.g. feeding electricity into the power grids at peak times or supplying the neighborhood with district heating. For an efficient operation of a thermal energy system, especially to cope with these new demanding tasks, hierarchical optimization methods can be applied [4]. Hierarchical optimization methods divide the plant operation into several layers to better abstract the complex optimization problem into manageable subproblems. The different layers can be subdivided according to different time scales (dynamics) or optimization objectives and thus operate at different levels of detail. These different levels of detail in the optimization, such as different underlying models or occuring disturbances, can lead to conflicts between the optimization layers resulting in infeasibility or poor performance.

Hence, the question arises how these conflicts between the optimization layers can be resolved in order to operate the entire plant efficiently?

In this thesis, a generic two-layer operation optimization framework with an sensitivity-based cooperation concept between the optimization layers is presented to do so. The novel cooperation concept evaluates the importance of the setpoints given by the higher economic optimization layer and passes them on to the lower control layer in order to operate the plant at optimal expected costs (Publication* D).

1.2 Investigated system configurations

The underlying characteristics of the systems studied (the hybrid storage geometry and the plant topology of the thermal energy system) are described in this section.

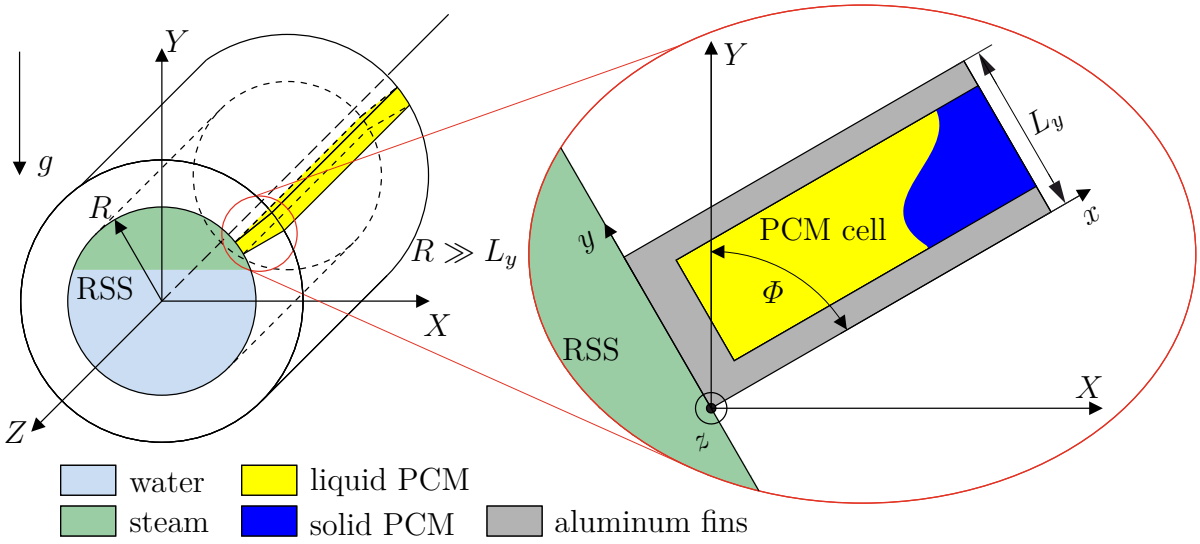

Figure 1.3: In the hybrid storage system, the RSS is surrounded by PCM cells (LHTES).

1.2.1 Investigated hybrid storage setup

The investigated hybrid storage system consists of two different storage types: an RSS and an LHTES, see Figure 1.3 (left). The RSS comprises a pressure vessel filled with a two-phase fluid (here, water and steam). It possesses a high thermal conductivity and thus reaction time, but only a low energy density. When the sensible RSS is loaded or unloaded, the pressure or temperature of the fluid inside is high or low, respectively. The other storage type, the LHTES, surrounds the RSS. In contrast to the RSS, the LHTES has a low thermal conductivity but a high energy density. It exploits the phase transition of PCM to store the main energy content at almost constant temperature. To enhance heat transfer within the PCM, heat-conducting structures, such as aluminum fins, are often employed, see Figure 1.3 (right). The PCM enclosed by two aluminum fins is referred to as PCM cell. The RSS and the PCM cell are subject to model building (Publication A). The PCM cell model is made real-time capable by model reduction (Publication B) and an observer is designed to estimate the PCM cell's distributed system state (Publication C).

1.2.2 Investigated plant setup

The multi-layer control concept is developed by investigating a chipboard manufacturing plant, such as the setup in Figure 1.1. In the plant, the main energetic process is steam generation. Therefore, fuel combusts in a furnace and transfers heat to a drum boiler. The evaporating water from the drum boiler is further heated in superheaters. The

resulting steam is used either for drying wood, hardening adhesives in a heated press, or generating electricity in a steam turbine. In addition, the neighborhood is supplied with district heating.

As a result of stochastic fluctuations in the combustion process, the steam demand cannot always be covered perfectly. To ensure sufficient steam supply at any given time, additional steam must be generated and thus more fuel consumed than necessary. The trade-off between fuel costs and demand violation costs is the basis for a cooperation concept in an operation optimization framework (Publication* D).

1.3 Context (state of the art)

In this section, the state of the art is highlighted and set into context. The focus is first on methods to efficiently integrate the hybrid storage into a thermal energy system, i.e., model building, model reduction, and state estimation techniques. Then a broader perspective is taken and approaches to control an entire thermal energy system are discussed.

1.3.1 Modeling of a hybrid storage system

A co-simulation model for a hybrid storage system consisting of an RSS and an LHTES is developed (Publication A). The models for the RSS and the LHTES are created separately and, finally, merged into a co-simulation model of the entire hybrid storage. The developed model can serve as a basis for system analysis as well as state estimation and control methods.

To model an RSS, a thermodynamic equilibrium is commonly assumed in the literature [5, 6]. Thereby, the two phases inside the storage vessel, namely water and steam, are considered in saturated state with the same temperature for both phases. A non-equilibrium model is proposed in [7] to account for pressure transients as a function of evaporation and condensation rates. These fast transients are neglected for the co-simulation presented here, since the very low thermal conductivity of the PCM in the LHTES is the limiting factor in terms of dynamics of the overall hybrid storage system. The implemented RSS model is adapted from the validated equilibrium model in [8, 9].

Reviews on the mathematical modeling of phase change systems have been presented in [10, 11]. In general, the predominant effects in an LHTES are the phase transition, and the heat transfer mechanisms conduction as well as natural convection. The effects of natural convection are often neglected due to their complexity [12]. Nevertheless, the legitimacy of such a simplification depends on the geometry of the PCM encapsulation and the PCM's material properties. Vogel et al. [13] and Kasper et al. [14] found a

substantial improvement of heat transfer enhancement for the phase change material sodium nitrate and potassium nitrate (KNO2-NaNO3), which is also employed in this work. Therefore, the effects of natural convection need to be included in the LHTES model. When modeling LHTES with heat transfer in two or more directions, typically numerical methods, such as the enthalpy method [15] or the apparent heat capacity method [16], are applied. Finite element methods are capable of discretizing partial differential equations and solving complex thermomechanical problems accurately [17]. Kasper [18] applied finite element methods, the effective heat capacity method, and an adaptation of the finite difference code published in [19] to model conduction, phase change, and the two-dimensional Navier-Stokes equations for natural convection, respectively. This coupled finite element/finite difference model was experimentally validated and is adapted for the co-simulation model (Publication A).

The RSS and the LHTES model are combined in a co-simulation. Only a few models for a combination of RSS and PCM storage systems have been presented in literature, such as in [20, 21, 8, 9]. All of them are subject to various model simplifications and thus do not fully capture the main behavior of the hybrid storage system investigated in this work. The co-simulation model presented here (Publication A) efficiently combines two high-precision sub-models, the RSS model and the LHTES model. The models are computed on different time scales to account for their different complexity. The LHTES model is represented by selected sections referred to as PCM cell models, see Figure 1.3.

1.3.2 Model reduction

The co-simulation model (Publication A) is of high accuracy, but not real-time capable for online estimation and control tasks. A first analysis shows that the PCM cell model requires approximately 99 % of the computation time. In the PCM cell model, the Navier-Stokes equations are responsible for 80 % of the calculation effort. Therefore, a model reduction method for the Navier-Stokes equations is required to achieve real-time capability and enable model-based state estimation.

In recent decades, model reduction methods have been an important research area and were covered in many reviews, such as in [22] for linear systems and in [23] for coupled systems. Two broad categories of model reduction methods are [24]: (1) moment matching methods, and (2) SVD-based methods. The former group is numerically more efficient but has no global error bounds, see for example [25] for applications in linear systems and their nonlinear enhancement. The latter group of SVD-based methods can maintain stability and provide error bounds, but is numerically more expensive. Linear applications of this group are the balanced truncation [26], the Hankel-norm approximation [27], and the singular pertubation [28]. For nonlinear systems, such as the problem considered here, the proper orthogonal decomposition (POD) can be an appropriate choice.

The main idea of POD is to decompose the behavior of a complex system into orthonormal basis vectors. For this purpose, data representative for a relevant operating range are empirically investigated [29]. The basis vectors describing the most characteristic system behavior are collected in a set and the system's governing equations are projected onto this set (Galerkin projection). The resulting low-dimensional system representation can be solved instead of the real system.

Other methods for reducing nonlinear systems are dynamic mode decomposition (DMD) [30] and proper general decomposition (PGD) [31]. DMD does not attempt to best describe the data set as in POD, but to best approximate the dynamics of a time series [32]. Unlike POD and DMD, PGD is not data driven and the reduced modes are not necessarily orthogonal among themselves. The "a priori" PGD iteratively adds modes to the approximation of the solution until a stop criterion is reached.

In fluid mechanics, systems are often described by coupled partial differential equations. The solution of these complex problems poses a significant challenge to the available computational resources and thus numerous model reduction approaches were adapted for this research domain, as reviewed in [33, 34]. The previously described methods for nonlinear models have been applied for the shallow water equation (DMD and POD) [35], the Navier-Stokes equations for a lid-driven cavity (PGD) [36] and the flow around an oscillating cylinder (POD) [37]. Other methods with high potential in fluid dynamics are based on deep learning algorithms [38]. Deep learning successfully uses artificial neural networks instead of the physically interpretable modes in DMD, POD, or PGD. Unsolved issues in deep-learning are the unspecified number of required nodes, layers, and amount of training data as well as the physically uninterpretable operating principle.

The model reduction approaches for nonlinear coupled systems described above are challenging and complex to adapt, resulting in a lack of easy-to-implement methods. The reduction approach presented here (Publication B) provides a convenient method for dominant flow patterns. Instead of projecting the dominant modes onto the governing equations as in POD, an ARX model is estimated using an intuition-based regressor (expert knowledge) to describe the dynamic behavior of the dominant modes.

1.3.3 State estimation in distributed-parameter phase change problems

An LHTES is mainly comprised of phase change material (PCM), which posses a high energy density but low thermal conductivity. Most energy is stored at almost constant temperature during phase change. These characteristics constitute a particular challenge to state estimation since, on the one hand, a distributed system state arises and, on the other hand, the state of charge does not simply result from a measurement of the temperature and mass.

The state of the art to estimate the PCM's state of charge is summarized in [39]. Basically, there are two different types of measurements: (1) a local measurement that determines a quantity at a specific point, and (2) a global measurement that uses an integral quantity describing the state of the entire system. In the first case, an approriate number of sensors is needed to determine the distributed system state. For example, multiple temperature sensors in the PCM can resolve the distributed temperature field to derive the state of charge. In the second case, a direct relationship exists between an integral measured quantity and a global system measure in at least one particular operating region. For example, a pressure or volume measurement can determine the fraction of molten PCM within a domain if the PCM changes its density significantly during the phase transition. Limitations are that a pressure or volume change must be distinguished into one influenced by sensible effects and one influenced by latent effects. In addition, the encapsulation must be absolutely sealed and the pressure must be distributed homogeneously over the entire domain, even in the case of complex storage geometries. Other measurements include electrical resistance or image sensors. Zsembinszki et al. [39] suggested that a combination of two or more different measurement methods could compensate for their limitations resulting in an accurate state of charge estimation.

Not only the state of charge but also the distributed system state may be of additional interest, as it defines the dynamic behavior of the storage system. In order to appropriately combine several different types of measurements and obtain an estimation of the distributed system state, a model-based observer is necessary.

There exist numerous reviews focusing on observers in a wide variety of applications, such as in [40, 41] for chemical processes. In general, observers can be categorized based on their underlying system dynamics [42]:

- Lumped-parameter systems: The dynamics are defined by ordinary differential equations (linear or nonlinear).
- Distributed-parameter systems: The dynamics are defined by partial differential equations (linear or nonlinear) and depend on two or more variables, such as time and space.

The distributed system state in the PCM is space and time dependent. Two main methods exist to investigate distributed-parameter systems: (1) early-lumping and (2) late-lumping. In early-lumping, the infinite-dimensional characteristics of a system are resolved in one dimension using discretization methods to obtain a finite representation defined by ordinary differential equations, e.g., by applying finite element methods for spatial discretization. In the late-lumping method, the infinite-dimensional characteristics are preserved in the system analysis.

An example for a late-lumping observer can be found in [43], where correction functions are injected into the model's partial differential equations and boundary conditions.

However, the focus of this thesis is on the more common early-lumping approach. In early-lumping, the well-known Luenberger observer [44] and Kalman filter in its discrete [45] and continuous form [46] can be applied. Both were originally designed for linear systems and many observers later developed are modifications of them. To account for nonlinear systems, these observers were extended, see for example [47, 48].

Observers have already been applied to phase change problems in the past. Barz et al. [49] estimated the temperature fields inside an LHTES using 4 temperature sensors, an extended Kalman filter (EKF), and a collocation model to approximate the energy balance equations. In a fish freezing process, Backi et al. [50, 51] used an EKF with a finite difference model to estimate the inner domain temperatures. Akkari et al. [52] presented an EKF combined with a finite volume model for the energy balance equations to determine the state of a microwave defrosting process. All state observers for phase change problems developed so far are based on low-order models and model simplifications (for example, neglecting the effects of natural convection). Therefore, they are not suitable to fully characterize the behavior of a general phase change problem, such as the one considered in this thesis. A state estimation concept is required that can handle high-order models fully describing the dominant behavior of the system.

When applying an EKF to high-order models, two challenges may arise: (1) the problem becomes infeasible in real-time due to its computing complexity, and (2) the system becomes unobservable when the entire state dimension is taken into account. To address these challenges, research has been conducted on various types of reduced-order EKFs, see for example [53, 54, 55]. Model reduction methods in observer design can be used to compute a Kalman gain and a covariance update in a reduced system representation. After back-transformation to the full state dimension, the states of the original high-order system can be updated. A reduction method suitable to preserve the dominant system behavior is balanced truncation [26]. Farrell and Ioannou [56] were able to apply this method to a high-order model for the accurate tracking of storms.

The observer concept presented in this thesis (Publication C) is based on an EKF in which models of different complexity are combined to accurately estimate the distributed state of a phase change problem, while considering all relevant heat transfer effects, such as conduction and natural convection. The main idea is that a high-order model predicts future system states. These predicted states are updated by an EKF based on a successively linearized model reduced by balanced truncation. As a result, the state update is computed based only on the dominant system behavior. To increase the estimation accuracy, two different types of measurements, namely temperature and volume, are combined in the observer concept.

1.3.4 Multi-layer control

Hierarchical operation optimization structures are often applied to efficiently control industrial plants [57]. In hierarchical control architectures, plant operation is divided into layers to abstract the complex optimization into manageable sub-problems. However, the task of finding a global optimum for these divided structures remains difficult.

Typically, plant operation is decomposed according to the different plant dynamics and time scales. In an upper layer, the economic characteristics of a process are exploited based on static models and only slow varying disturbances, such as pricing factors, are considered. The upper layer is usually referred to as real-time optimzation (RTO) and provides setpoints to the lower layer. The lower layer usually consists of advanced control methods, such as model predictive control (MPC). The MPC tries to follow the RTO's setpoints as close as possible while accounting for dynamics and disturbances. In doing so, the following problems may arise. During transient operation, the RTO's steady-state setpoints do not provide any information about economically optimal operation. Furthermore, optimization in the RTO and MPC relies on different models, objectives and disturbances, which may lead to infeasibility or unreachability of setpoints and thus in poor performance. An approach to unify these potentially competing interests of the two optimization layers is strongly recommended [58].

There are several approaches in the literature addressing this issue. One approach adds an additional layer between the RTO and the MPC to compute feasible setpoint updates for the MPC. This steady-state target optimizer incorporates a static model consistent with the MPC and takes informations from the RTO into account, as for example in [59, 60]. However, this approach may be limited in terms of transient operations or fast disturbances.

Another approach includes dynamic instead of static optimization in the upper layer. The dynamic real-time optimization (DRTO) accounts for disturbances as well as transient operations and provides target trajectories to the lower-layer MPC, as for example in [61, 62, 63]. Nevertheless, DRTO-MPC is computational demanding and is not reasonable for complex industrial plants.

Other approaches incorporate the economic optimization problem directly in the MPC, resulting in an economic MPC with high computational complexity [64].

In this thesis (Publication* D), an operation optimization framework is developed, which consists of two layers and a novel cooperation concept in-between. The cooperation concept exploits stochastic information about the disturbances and the sensitivities of the upper layer's economic cost function. As a result, the plant is operated at optimal expected costs (risk costs).

1.4 Problem statement

The research questions are formulated and the main contributions of the developed methods are stated.

1.4.1 Research questions

The overarching key objective of this thesis can be formulated as:

O. How to best exploit system structure for advanced model-based tasks in observation and control applications (multi-stage and purpose-driven approaches accounting for the relevant behavior/modes/information)?

The various aspects of this objective are structured and addressed through the following specific research questions:

Q.1 How to model a complex component, such as the hybrid energy storage system, to make it accessible to dynamic control/observation tasks?

Q.2 How to achieve real-time capability when considering highly detailed models with partial differential equations (e.g., the Navier-Stokes equations)?

Q.3 How to design an observer that estimates the high-order states of a system with distributed parameters while enabling computational efficiency, observability, and accuracy?

Q.4 How to design a hierarchical operation optimization framework for a heterogeneous thermal energy system with special emphasis on the interaction between the optimization layers?

1.4.2 Main contributions

The aforementioned research questions result in the following main contributions of the developed and published methods.

Co-simulation model: A co-simulation model for a hybrid storage system consisting of an LHTES and an RSS is required to provide insight into typical storage behavior and to subsequently apply model-based techniques for operation. In this setting, two sub-models of different complexities are employed: (1) a sub-model describing the RSS, and (2) a sub-model describing a particular section of the LHTES, called PCM cell. An accurate implementation of the co-simulation model is needed, which accounts for the different sub-model complexities, global energy conservation, and an optimal number of sub-models. The main contributions of the co-simulation methodology (Publication A)

are:

- An efficient computation algorithm couples the different sub-model complexities. The one-dimensional RSS model is calculated on a larger time scale than the finite-element PCM cell model, which includes the effects of phase transition, conduction and natural convection. The developed coupling concept of the sub-models ensures energy conservation at all times. [according **Q.1**]
- The behavior of one PCM cell depends on its location at the RSS shell surface. In order to ensure efficient computation, several PCM cells are summarized to one PCM sector and computed as one. A quantitative optimization-based aggregation criterium is presented to do so. [according **Q.1**]
- The typical storage behavior is investigated in simulation studies.

Model reduction: A model reduction approach is necessary to obtain real-time capable models for online state estimation or advanced control methods. In a first analysis, the natural convection effects in the PCM cell model were the most time-consuming computational task. Therefore, a short-cut of the Navier-Stokes equations' laborious solution seems adequate. An easy-to-implement data-based reduction method is required to do so. A particular challenge lies in the solution-dependent flow domain of the Navier-Stokes equations. The main contributions of the data-based model reduction for phase change problems (Publication B) are:

- A novel data-based model reduction method for phase change problems is proposed that accurately characterizes convective heat transfer while accounting for the changing flow domain due to the melting/solidification process. [according **Q.2**]
- The computation efficiency is significantly increased while solution accuracy is maintained, resulting in a real-time capable model. [according **Q.2**]
- The effectiveness of the proposed method is demonstrated in simulation studies by examining typical operating scenarios.
- In contrast to the original system with complete Navier-Stokes modeling, the solution of the reduced model is less dependent on mesh and time step size.

State estimation concept: An observer is required to estimate the distributed system state of an LHTES and thus determine the amount of energy that can be stored/released at any given time. A particular challenge lies in the implementation of the nonlinear as well as high-order PCM cell model into an EKF while ensuring real-time feasibility and system observability. The resulting observer shall possess a robust behavior and be able to implement different types of measurements to increase estimation accuracy. To do so, two different model structures have been implemented: (1) the real-time capable high-order nonlinear PCM cell model predicts future states inside the LHTES, and (2) a low-order linear model obtained from balanced truncation provides the basis for a state

update by the EKF. The main contributions of the state estimation concept (Publication C) are:

- The development of an efficient observer concept to estimate the distributed system state of high-order phase change problems based on already existing modeling and observation methods. [according **Q.3**]
- The observer correction is restricted to the dominant system behavior and accounts for different types of measurements. [according **Q.3**]
- Temperature sensor placement is improved by analyzing the most relevant mode shapes.
- Simulation studies are conducted showing the efficiency and accuracy of the presented method even despite model errors. The melting front inside the LHTES and the state of charge can be estimated correctly.

Multi-layer cooperation concept: A novel cooperation concept between hierarchical optimization layers is required to efficiently control a thermal energy system. The cooperation concept shall lead to optimal expected operating costs of the entire plant despite acting disturbances. A particular challenge in two-layer operation optimization is that each layer has different objectives, operates on different time scales, and applies different models (dynamic/static). The idea of the cooperation concept lies in passing additional sensitivity information from the upper-layer to the lower-layer and exploiting stochastic information about the disturbances. The main contributions of the multi-layer cooperation concept (Publication* D) are:

- A multi-layer operation optimization framework in a hierarchical structure is proposed, which employs a novel cooperation concept between the control layers and results in optimal expected plant operating costs. [according **Q.4**]
- The developed cooperation concept exploits stochastic information of the disturbances and the upper layer's cost function senstivities.
- The control approach is generic and easy-to-adapt.
- The effectiveness of the novel concept is demonstrated on a plant model calibrated with industrial measurement data.

1.5 Methodology

In this section, the methodology of the modeling, model reduction, state estimation, and multi-layer control approach is briefly presented. For further details, the reader is referred to the corresponding publications.

1.5.1 Modeling approach

The main principles of modeling are highlighted and then the features of the co-simulation model are outlined.

Ruths steam storage

The two phases inside the RSS (water and steam) will be always considered in thermodynamic equilibrium (saturated state), such as in [6]. The dynamic RSS model employed is adapted from [8, 9]. The variables pressure and temperature, which are directly related in thermodynamic equilibrium, are not sufficient for a complete description of the system. Therefore, another variable is required to fully characterize the state of the system, for example, the specific enthalpy.

The energy and mass balances are expressed as combinations of the two phases (one-dimensional), treating the two phases together as a single fluid mixture. The corresponding governing equations are

$$m_{\mathrm{RSS}}\frac{dh_{\mathrm{RSS}}}{dt} = \dot{m}_{\mathrm{RSS,in}}(h_{\mathrm{RSS,in}} - h_{\mathrm{RSS}}) + \dot{m}_{\mathrm{RSS,out}}(h_{\mathrm{RSS,out}} - h_{\mathrm{RSS}}) + \dot{Q}_{\mathrm{RSS}} + V_{\mathrm{RSS}}\frac{dp_{\mathrm{RSS}}}{dt} \text{ and} \tag{1.1}$$

$$V_{\mathrm{RSS}}\frac{d\rho_{\mathrm{RSS}}}{dt} = \dot{m}_{\mathrm{RSS,in}} + \dot{m}_{\mathrm{RSS,out}} \ . \tag{1.2}$$

The steam mass fraction and the mixing law are defined as

$$x_{\mathrm{RSS}} = \frac{m_{\mathrm{RSS,s}}}{m_{\mathrm{RSS,s}} + m_{\mathrm{RSS,w}}} \text{ and} \tag{1.3}$$

$$h_{\mathrm{RSS}} = x_{\mathrm{RSS}}h_{\mathrm{RSS,s}} + (1 - x_{\mathrm{RSS}})h_{\mathrm{RSS,w}} \ . \tag{1.4}$$

Therein, m_{RSS}, $\dot{m}_{\mathrm{RSS}}$, h_{RSS} and ρ_{RSS} denote the mass, mass flow, specific enthalpy, and density of an equivalent water-steam mixture, respectively. In the assumed saturated state, the pressure p_{RSS} is the same for both phases. The indices w and s stands for the water and steam inside (liquid and vapour phase). The RSS model is considered as an aggregate domain where the balance equations are not further subdivided. The overall volume V_{RSS} is subject to the heat flow $\dot{Q}_{\mathrm{RSS}}$,

$$\dot{Q}_{\mathrm{RSS}} = \dot{Q}_{\mathrm{RSS2PCM}} + \dot{Q}_{\mathrm{RSS,loss}} \ , \tag{1.5}$$

which includes heat losses to the environment $\dot{Q}_{\mathrm{RSS,loss}}$ and the heat flow to the attached PCM cells $\dot{Q}_{\mathrm{RSS2PCM}}$. The RSS is loaded/unloaded with steam and additionally water

can be extracted to control the filling level. The incoming and outgoing quantities are indicated by the indices "in" and "out".

The equations above describe the RSS under the following simplifying assumptions:

- The potential and kinetic energies are not considered.
- The thermal conduction in the circumferential direction of the RSS vessel is neglected.
- The heat capacity of the RSS steel shell is neglected.

Latent heat thermal energy storage

The representation of the LHTES is subdivided into several PCM cell models. A PCM cell model consists of the PCM itself and two adjacent halves of aluminum fins, see Figure 1.3 (right). In order to fully characterize the thermodynamic behavior of the PCM cell, a detailed multiphase model for phase transition, heat conduction, and natural convection in two dimensions is considered, developed and fully documented in [18]. The model is built on the conservation laws of mass, energy, and momentum, which leads to the following energy (1.6), Navier-Stokes (1.7), and continuity equations (1.8):

$$\rho_{\mathrm{PCM}} c_{\mathrm{PCM}} \frac{\partial T_{\mathrm{PCM}}}{\partial t} = \lambda_{\mathrm{PCM}} \nabla \cdot (\nabla T_{\mathrm{PCM}}) - \rho_{\mathrm{PCM}} c_{\mathrm{PCM}} (\boldsymbol{v}_{\mathrm{PCM}} \cdot \nabla) T_{\mathrm{PCM}} \ , \tag{1.6}$$

$$\rho_{\mathrm{PCM}} \frac{\partial \boldsymbol{v}_{\mathrm{PCM}}}{\partial t} + \rho_{\mathrm{PCM}} (\boldsymbol{v}_{\mathrm{PCM}} \cdot \nabla) \boldsymbol{v}_{\mathrm{PCM}} - \mu_{\mathrm{PCM}} \nabla \cdot (\nabla \boldsymbol{v}_{\mathrm{PCM}}) = \boldsymbol{f}_{\mathrm{PCM}}(T_{\mathrm{PCM}}) - \nabla p_{\mathrm{PCM}} \ , \tag{1.7}$$

$$\text{and } \nabla \cdot \boldsymbol{v}_{\mathrm{PCM}} = 0 \ . \tag{1.8}$$

Therein, the temperature field $T_{\mathrm{PCM}} = T_{\mathrm{PCM}}(x, y, t)$ of (1.6), and the velocity field $\boldsymbol{v}_{\mathrm{PCM}} = [v_{\mathrm{PCM},x}, v_{\mathrm{PCM},y}]^T$ of (1.7)-(1.8) are space and time dependent. The symbols ρ_{PCM}, λ_{PCM}, μ_{PCM}, and p_{PCM} denote the density, thermal conductivity, dynamic viscosity, and the pressure in the PCM, respectively.

The phase transition takes place in a small temperature range referred to as "*mushy region*" and is modeled via a temperature dependent heat capacity, the apparent heat capacity $c_{\mathrm{PCM}}(T)$ [16]. The force density $\boldsymbol{f}_{\mathrm{PCM}}$ describes the buoyancy force due to volumetric thermal expansion using the Boussinesq approximation [65].

The PCM model [18] is discretized via a finite element scheme (Galerkin approach) for the energy equation (1.6) and a finite difference scheme for the incompressible Navier-Stokes equations (1.7)-(1.8) [19]. The velocity field obtained from the solution of the Navier-Stokes equations (1.7)-(1.8) is substituted into the energy equation (1.6) at the next time step.

The following main assumptions are made to reduce the modeling to the significantly occurring phenomena described above:

- The material properties are kept constant within a phase, but can take different values for the liquid and solid phases.
- Isothermal phase change, although inherently not representable by the apparent heat capacity method, can be approximated using a small "*mushy region*".
- The temperature field alone determines the phase ratio in the PCM cell model (no effects due to hysteresis, dynamics, subcooling).
- Surface effects are neglected.
- The only body force results from the buoyancy term (Boussinessq approximation).

The PCM cell's upper and lower domain boundaries are modeled as adiabatic, so that no heat flow occurs there. Heat transfer boundary conditions are applied to the left and right wall (Newton's law of cooling),

$$\boldsymbol{q}_{\mathrm{PCM,in}} = \alpha_{\mathrm{PCM,in}}(T_{\mathrm{PCM}}(x,y,t) - T_{\mathrm{PCM,in}}) \text{ and} \tag{1.9}$$

$$\boldsymbol{q}_{\mathrm{PCM,out}} = \alpha_{\mathrm{PCM,out}}(T_{\mathrm{PCM}}(x,y,t) - T_{\mathrm{PCM,out}}) \ , \tag{1.10}$$

where $\alpha_{\mathrm{PCM,in}}, \alpha_{\mathrm{PCM,out}}$ are heat transfer coefficients at the boundary, $\boldsymbol{q}_{\mathrm{PCM,in}}, \boldsymbol{q}_{\mathrm{PCM,out}}$ are the specific heat fluxes across the boundary, and $T_{\mathrm{PCM,in}}, T_{\mathrm{PCM,out}}$ represent boundary temperatures at the left and right wall surfaces, respectively.

With regard to the Navier-Stokes equations (1.7)-(1.8), no-slip conditions are assumed for the velocity field $\boldsymbol{v}_{\mathrm{PCM}}$ at the domain boundaries. In addition, the velocity field of the PCM can take non-zero values only in fully liquefied regions.

Co-simulation model

The sub-models (RSS model and PCM cell model) have different complexities and need to be computed at different time step levels. The co-simulation model couples the RSS model and the surrounding PCM cell models via the heat flow $\dot{Q}_{\mathrm{RSS2PCM}}$ (1.5). The coupling heat flow $\dot{Q}_{\mathrm{RSS2PCM}}$ is computed at the minor time step level via the PCM cell models, then is integrated and passed to the RSS model at the major time step level. While the heat flow is computed at minor time step, the properties of the RSS model are assumed to be constant due to its much larger heat capacity. The energy conservation of the coupling mechanism is always ensured.

The thermodynamic behavior of the PCM cells attached to the RSS shell is essentially influenced by two effects:

- The natural convection inside a PCM cell depends on its orientation Φ with respect to the gravitional force and the location of the induced heat flow.

- The heat transfer properties between the fluid inside the RSS and the PCM cell depend on whether water or steam is in contact with the wall at the PCM cell's attachment location.

Therefore, every PCM cell has its individual thermodynamic behavior. However, it is not possible to compute the state of each of the numerous PCM cells individually. To save computational effort, multiple PCM cells are combined into a logically aggregated PCM sector and computed as one representative PCM cell having the same thermodynamic behavior. An optimization-based PCM sector aggregation criterium is formulated as follows.

Given the heat flow exchanged between the RSS model and all PCM cells n_{cell} is

$$\dot{Q}_{\text{RSS2PCM}}(t) = -\sum_{i=1}^{n_{\text{cell}}} \dot{Q}_{\text{RSS2PCM},i}(t) \ , \tag{1.11}$$

and the estimated heat flow exchanged between the RSS model and the n_{sect} PCM sectors is

$$\hat{\dot{Q}}_{\text{RSS2PCM}}(t) = -\sum_{j=1}^{n_{\text{sect}}} \dot{Q}_{\text{RSS2PCM},j}(t) \ , \tag{1.12}$$

an optimal aggregation criterium is obtained by minimizing the error between the heat flow of the complete model $\dot{Q}_{\text{RSS2PCM}}$ and the heatflow of the aggregated model $\hat{\dot{Q}}_{\text{RSS2PCM}}$.

Selected result

The developed aggregation criterium is applied to obtain an optimal PCM sector partitioning, see Figure 1.4. All PCM cells on the RSS shell surface are aggregated into 7 sectors. The PCM cells in one sector are assumed to have the same thermodynamic behavior, which is determined by computing one representative PCM cell. The aggregation criterium leads to a significantly faster co-simulation model while minimizing the error related to the stored enthalpy in the PCM cells. The proposed co-simulation model provides a basis for system analysis, estimation, and control tasks. However, to achieve real-time capability for the latter two tasks, further model reduction is required.

1.5.2 Data-based model reduction

The co-simulation model is not real-time capable and thus a novel model reduction approach is required to reduce computational effort. In a first analysis, the computation of the PCM cell model's Navier-Stokes equations (1.7)-(1.8) was found to be the most time-consuming task. Therefore, a short-cut of the Navier-Stokes equations' laborious solution seems adequate to effectively reduce calculation effort.

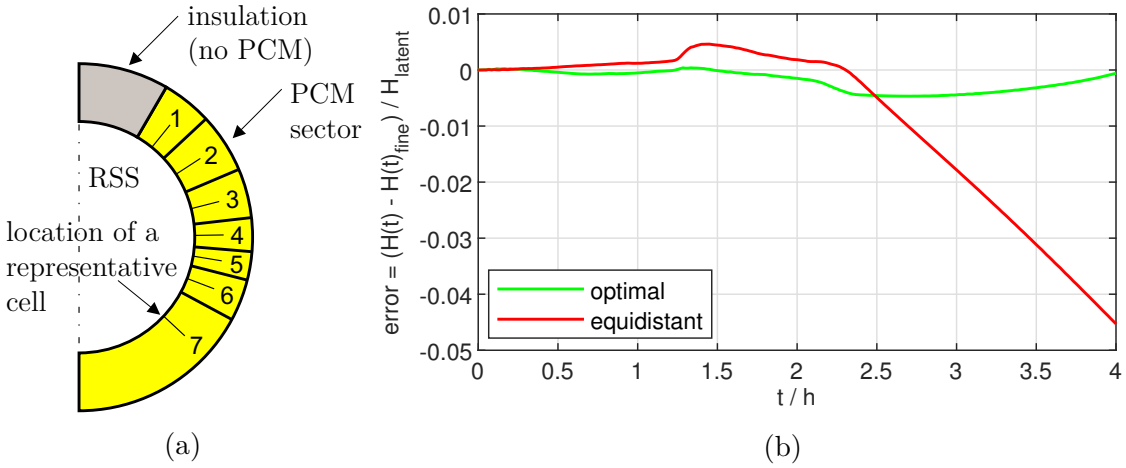

(a) (b)

Figure 1.4: The aggregation criterium leads to the optimal distribution of seven sectors and their representative cells as shown in (a). The error of an optimal PCM sector partitioning can be significantly reduced compared to an equidistant aggregation where all sectors have the same size (b).

Main idea

The main idea is to identify few dominant flow patterns that best explain the effects of natural convection. The reduction approach relies on snapshots of the velocity field obtained from relevant reference simulation studies. The snapshots are decomposed into modes of space and time via singular value decomposition (SVD), and the most dominant modes are extracted. The temporal modes represent the magnitude of the spatial modes and can be modeled as a function of few selected properties of the energy equation, such as minimum/maximum temperature.

Data acquisition and representation via stream functions

First, detailed simulation studies are performed using the PCM cell model from Section 1.5.1 to characterize the thermodynamic behavior in a relevant operating range. Then, snapshots of the velocity fields are generated and represented via stream functions. Stream functions, first introduced in [66], are well known scalar representations for describing planar velocity fields of incompressible fluids, where the velocity components are the partial derivatives of the stream function,

$$v_{\mathrm{PCM},x} = \frac{\partial \Psi}{\partial y} \ , \ v_{\mathrm{PCM},y} = -\frac{\partial \Psi}{\partial x} \ . \tag{1.13}$$

Thus, the stream function Ψ is automatically divergence-free and satisfies the continuity equation (1.8).

Transformation between a flow and a unit domain

Natural convection, and hence non-zero velocity components, can only occur in the liquid area of the PCM, the flow domain $\mathcal{D}_{\text{flow}}$. Due to the melting/solidification process, the flow domain changes over time. To make the stream functions comparable despite the varying flow domain, the stream function snapshots are transformed from the flow domain $\mathcal{D}_{\text{flow}}$ to a solution-independent unit domain $\mathcal{D}_{\text{unit}}$, see Figure 1.5. In the unit domain $\mathcal{D}_{\text{unit}}$ all stream functions have a similar appearing hill shape.

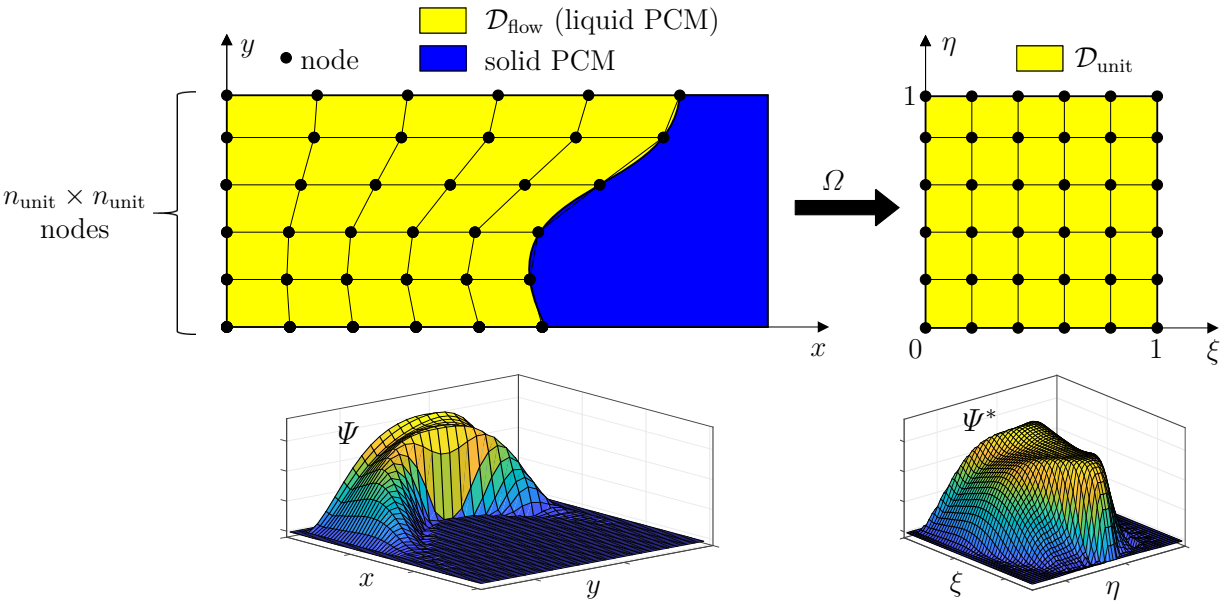

Figure 1.5: The stream function Ψ inside the flow domain (yellow) is transformed to a stream function Ψ^* inside the unit domain via linear interpolation.

Singular value decomposition

The method of snapshots is well-suited for determining POD modes [67]. The time snapshots of collected data contain the spatial distribution of the stream functions and reflect the system dynamics. Given Ψ_i^* as the vector of transformed stream function

values Ψ^* at time t_i, the data matrix

$$\boldsymbol{Z} = \begin{bmatrix} | & | & & | \\ \Psi_1^* & \Psi_2^* & \dots & \Psi_n^* \\ | & | & & | \end{bmatrix} , \tag{1.14}$$

consists of n temporal snapshots (columns) of the stream function's spatial distribution (rows). The data matrix $\boldsymbol{Z}$ is decomposed into dominant space and time modes by means of economy-size SVD,

$$\boldsymbol{Z} = \boldsymbol{U}\boldsymbol{\Sigma}\boldsymbol{V}^T , \tag{1.15}$$

where the snapshots are projected onto an orthonormal basis defined by the left singular vectors $\boldsymbol{U}$. The matrix $\boldsymbol{U}$ contains the shape of the spatial modes (column-wise), whereas the temporal behavior (magnitude) of the spatial modes is given in the matrix $\boldsymbol{V}$ (row-wise). The corresponding singular values are in the diagonal matrix $\boldsymbol{\Sigma}$ and indicate the energy content of each mode. A reduced system representation ($\boldsymbol{U}_{\text{red}}$, $\boldsymbol{\Sigma}_{\text{red}}$ and $\boldsymbol{V}_{\text{red}}$) is obtained by selecting the modes with the highest contributions, denoted by the largest singular values. To obtain a surrogate model from the reduced system representation, the temporal modes must either be replaced by a Galerkin approach, or explained as a function of the energy equation's solution as in this work.

Temporal behavior of the dominant modes

An ARX model is chosen to approximate the most dominant temporal modes,

$$\hat{\boldsymbol{v}}_{\text{red}} = \boldsymbol{r}\boldsymbol{\Theta} , \tag{1.16}$$

wherein $\hat{\boldsymbol{v}}_{\text{red}}$ denotes the current magnitude of the spatial modes (the values of the temporal modes) and $\boldsymbol{r}$ is the regressor containing few selected properties of the energy equation, such as maximum/minimum temperature and proportion of the liquid domain. The parameter vector $\boldsymbol{\Theta}$ is identified using a standard least square algorithm,

$$\boldsymbol{\Theta} = (\boldsymbol{R}^T\boldsymbol{R})^{-1}\boldsymbol{R}^T\boldsymbol{V}_{\text{red}} , \tag{1.17}$$

where the regressor matrix $\boldsymbol{R}$ contains the regressors (columns) evaluated at the n snapshots in time (rows).

Reduced model

The SVD of representative flow field data and the determination of a parameter vector $\boldsymbol{\Theta}$ to reconstruct the dominant temporal modes result in a reduced system model. In the

reduced model, the solution of the Navier-Stokes equations (1.7)-(1.8) is replaced with a stream function model. First, the transformed stream function in the unit domain

$$\hat{\Psi}^* = \boldsymbol{U}_{\mathrm{red}} \boldsymbol{\Sigma}_{\mathrm{red}} \hat{\boldsymbol{v}}_{\mathrm{red}} \tag{1.18}$$

is evaluated at the current temperature field and then back-transformed to a stream function in the flow domain $\hat{\Psi}$. The velocity field is derived from the stream function $\hat{\Psi}$ and substituted into the energy equation (1.6) for the next time step.

Selected results

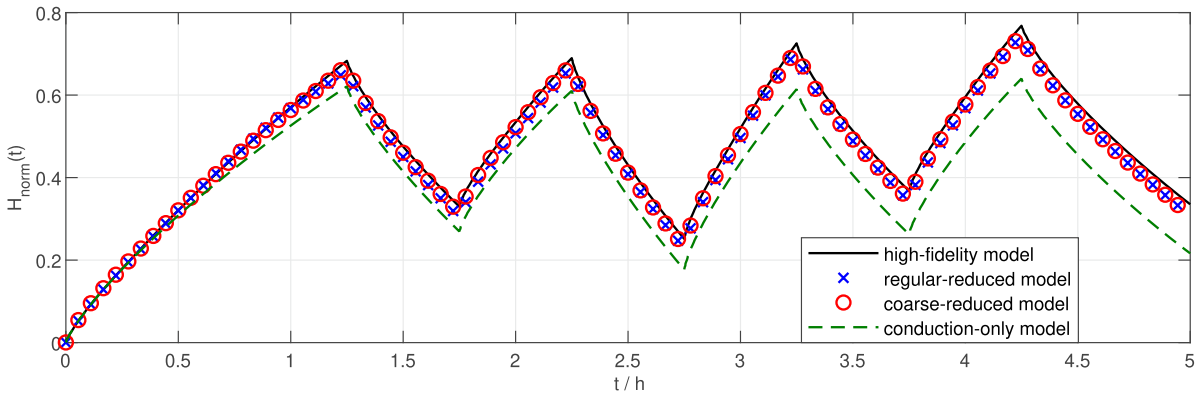

Figure 1.6: The normalized enthalpy content in a PCM cell shows good accuracy of the reduced model during a validation load cycle.

The accuracy of the reduced PCM cell model is less dependent on mesh and time step size than the original model with full Navier-Stokes computation. It is real-time capable with an up to 44-times increased computational speed. The reduction approach provides high accuracy and yields in a maximum error of 7.9 % instead of 35.4 % error caused by a conduction-only model that completely neglects natural convection. The performance of the reduced model is shown in Figure 1.6 and is well suited for both model-based observation and control tasks.

1.5.3 State estimation concept

State estimation in an LHTES is challenging due to the distributed system state and the complex energy-temperature dependence of the PCM. However, knowledge of the distributed system state is crucial as it determines the state of charge and the dynamic behavior of the storage. Therefore, model-based observers are required to obtain accurate state estimations by efficiently combining different types of measurements.

Main idea

The main idea is to apply the highly accurate and real-time capable PCM cell model from Section 1.5.2 to predict (simulate) future system states $\hat{\boldsymbol{x}}^-_{\mathrm{PCM}}$, see Figure 1.7. The predicted model outputs $\hat{\boldsymbol{y}}^-_{\mathrm{PCM}}$ are compared to measurements $\boldsymbol{y}_{\mathrm{PCM}}$ taken from reality, resulting in an innovation residual $\boldsymbol{e}$. The innovation residual and a low-order observer model (dominant-states-only) are fed into an EKF-based observer to compute a state update $\Delta\hat{\boldsymbol{x}}_{\mathrm{PCM}}$ for the high-order PCM cell model. As a result, the observer can only correct the states of the PCM cell model according to the dominant behavior of the system, leading to robust state updates.

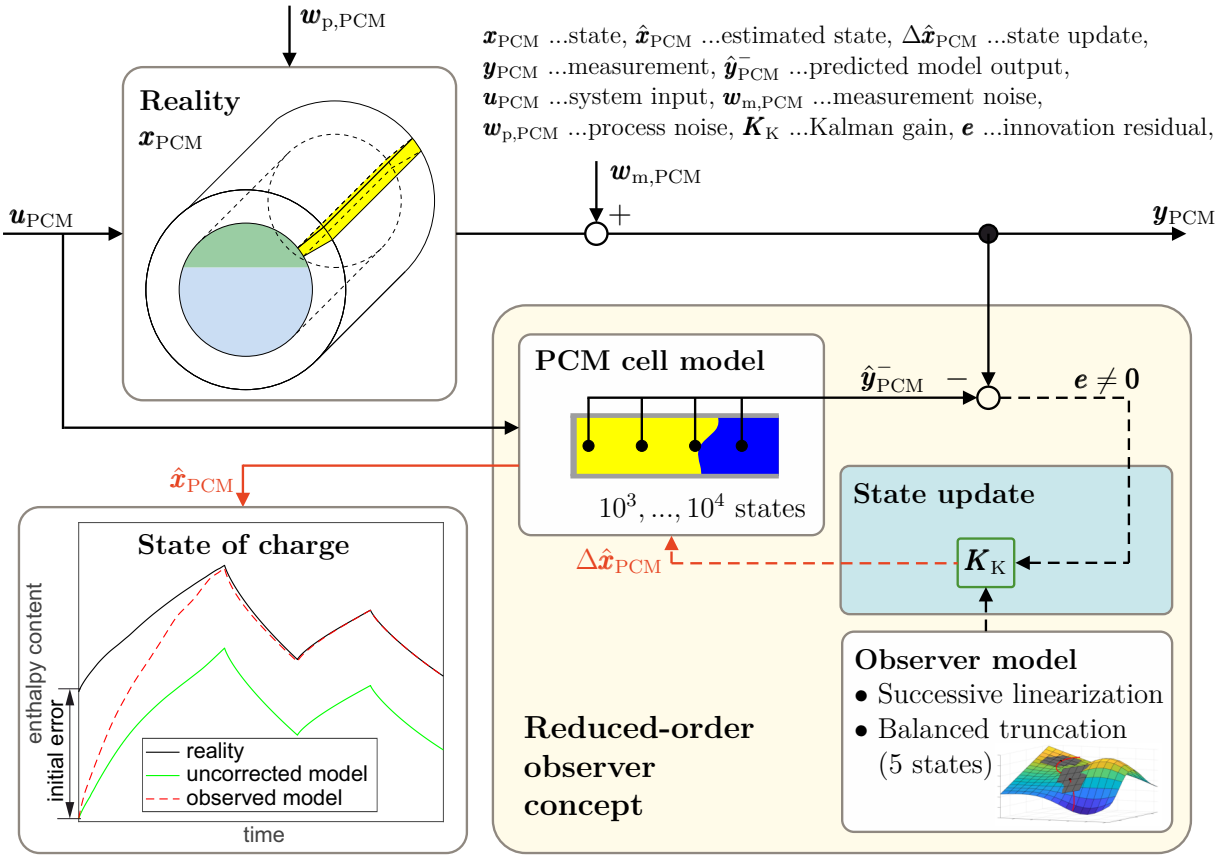

Figure 1.7: The state of the real system is estimated with a model-based observer.

Observer model

The PCM cell model is real-time capable and can thus serve as the basis for a state observer. However, it is still of high order $(10^3, ..., 10^4)$ and cannot be implemented in

an EKF directly. To obtain Jacobians for an efficient EKF implementation, a low-order observer model (dominant-states-only) is built as follows.

The first step to obtain an observer model is successive linearization at the current states and inputs [68]. The linearized system matrices represent the Jacobians of the system, but are still of high-order.

In the second step, the dimensions of the linear system are reduced using balanced truncation [26]. Therefore, the system states are first transformed to an energy-balanced basis in which the states are equally observable and controllable, referred to as the balanced system realization. In the balanced system realization, the controllability and observability Gramians are equal and diagonal [29]. Their eigenvalues represent the Hankel's singular values and serve as an energy measure for evaluating each system state. The states corresponding to the smallest eigenvalues, i.e., the low-energy states, are discarded, while the high-energy states are preserved.

The low-order observer model's system equations serve as Jacobians in an EKF to compute a state update of the PCM cell model.

State update

The extended Kalman filter (EKF) is implemented as described in [69]. The predicted model outputs $\hat{\boldsymbol{y}}_{\mathrm{PCM}}$ from the PCM cell model and the measurements from reality $\boldsymbol{y}_{\mathrm{PCM}}$ result in an innovation residual

$$\boldsymbol{e} = \boldsymbol{y}_{\mathrm{PCM}} - \hat{\boldsymbol{y}}^{-}_{\mathrm{PCM}} \ . \tag{1.19}$$

The EKF uses the innovation residual and computes a state update in the balanced system realization,

$$\Delta\tilde{\boldsymbol{x}}_{\mathrm{PCM}} = \boldsymbol{K}_{\mathrm{K}}\boldsymbol{e} \ . \tag{1.20}$$

The Kalman gain $\boldsymbol{K}_{\mathrm{K}}$ is obtained from the observer model's Jacobians (low order), and covariance matrices for the process and measurement noises. The PCM cell model's states are corrected after back-transforming the state update to the original state space,

$$\Delta\hat{\boldsymbol{x}}_{\mathrm{PCM}} = \tilde{\boldsymbol{V}}\Delta\tilde{\boldsymbol{x}}_{\mathrm{PCM}} \ . \tag{1.21}$$

The projection matrix $\tilde{\boldsymbol{V}}$ is obtained from balanced truncation.

Selected result

The developed state estimation concept accurately estimates the melting front and the state of charge while showing robust behavior against model and initialization errors, see Figure 1.8. The proposed state observer has the potential to serve as the basis for dynamic operations of an LHTES and its integration into thermal energy systems.

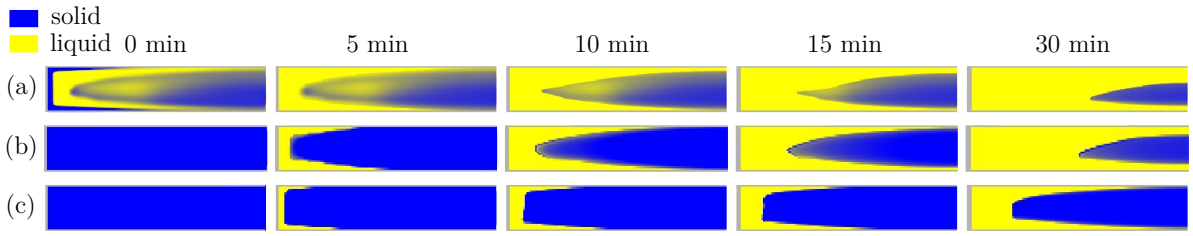

Figure 1.8: The observed model (b) shows the correct melting front of the simulated reality (a), while an uncorrected model differs significantly (c).

1.5.4 Multi-layer control concept

A two-layer operation optimization framework is developed to control an entire thermal energy system. In this concept, an upper optimization layer, before denoted as RTO but here better described as energy hub optimizer (EHO), computes setpoints for all plant components based on economic optimization and static plant models. A lower-layer MPC controls the dynamic plant parts, namely the steam generation process, and tracks the EHO's setpoints. A novel cooperation concept coordinates the interaction between the optimization layers in the presence of disturbances and model mismatches.

Main idea

The challenge is, on the one hand, to have sufficient steam available in the case of disturbances, and on the other hand, not to produce more steam than needed. The basic idea is to solve this trade-off by optimizing the expected plant operating costs. A stochastic MPC tracks the setpoints specified by the EHO with a permitted violation probability. The permitted violation probability depends on the importance of the setpoints. The optimal permitted violation probability is computed in the cooperation concept using a static cost function based on the EHO's cost function sensitivities and stochastic information about the disturbance.

Plant model

The MPC is based on dynamic models incorporated in a receding horizon optimization. The models for the dynamic components and the assembled plant have the state space descriptor form

$$\boldsymbol{M}\left(\boldsymbol{x}\right)\dot{\boldsymbol{x}} = \boldsymbol{f}\left(\boldsymbol{x},\boldsymbol{u},\boldsymbol{z}\right) \ , \tag{1.22}$$

wherein $\boldsymbol{x}$ denotes the state vector, $\boldsymbol{u}$ the input vector, $\boldsymbol{z}$ the disturbance vector, $\boldsymbol{M}$ the mass matrix, and $\boldsymbol{f}$ a function describing the differential equation's right-hand side. The

model outputs are obtained from the nonlinear mapping function $\boldsymbol{g}$,

$$\boldsymbol{y} = \boldsymbol{g}\left(\boldsymbol{x}, \boldsymbol{u}\right) \ . \tag{1.23}$$

The modeling approach is based on a class structure. The component as well as the plant models are constructed by corresponding classes including interface definitions, connecting rules, and assemblation methods. This modular modeling approach is the basis for the developed generic control concept.

All models are calibrated via industrial measurement data and parameter sensitvity analysis as in [70] is applied.

Stochastic control concept

The control concept basically consists of two elements:

- The stochastic MPC controls the multivariable system under chance constraints.
- The observers estimate the true states of the system and the disturbance covariance based on measurements.

The fundamental principle of an MPC is to optimize a trajectory of the controlled system model over a prediction horizon, starting from the present time step into the future. The first value of the optimized control sequence is applied to the real system and the optimization procedure is recomputed at the next time step, starting from a new initial state. To account for stochastic disturbances in the receding horizon optimization problem, chance-constrained MPC methods as described in [71] can be implemented,

$$\begin{aligned}
\min_{\mathbf{u}} \ & J_{\mathrm{MPC},N}\left(\hat{\boldsymbol{x}}_k, \mathbf{u}, \boldsymbol{r}, \beta\right) && (1.24)\\
\text{s.t. } & \Delta\tilde{\boldsymbol{x}}_{k+i+1} = \boldsymbol{A}\Delta\tilde{\boldsymbol{x}}_{k+i} + \boldsymbol{B}\Delta\boldsymbol{u}_{k+i} \ , && (1.25)\\
& \Delta\tilde{\boldsymbol{y}}_{k+i+1} = \boldsymbol{C}\Delta\tilde{\boldsymbol{x}}_{k+i} + \boldsymbol{D}\Delta\boldsymbol{u}_{k+i} \ , && (1.26)\\
& \Pr\left[\tilde{\boldsymbol{y}}_{k+i+1,j} \leq \boldsymbol{r}_{k+i+1,j}\right] \geq 1 - \beta_j \ , && (1.27)\\
\text{with } & i = 0, \ldots, N-1 \ , && (1.28)\\
& j = 1, \ldots, n_y \ . && (1.29)
\end{aligned}$$

The minimization of a cost function $J_{\mathrm{MPC},N}$ over the prediction horizon N leads to an optimal input control sequence $\mathbf{u} = \{\boldsymbol{u}_k, \ldots \boldsymbol{u}_{k+N-1}\}$. The index $k+i+1$ refers to the value of the variable at the corresponding future time step. The optimization is subject to the linearized system's equations (1.25)-(1.26) for the expected predicted state and output vector, respectively (no disturbances assumed). The symbol Δ indicates that all

variables are deviations from the current linearization. The chance constraints for the n_y system outputs are formulated in (1.27), where $\Pr[\cdot]$ represents the probability of an event occurring. The vector $\boldsymbol{r}_{k+i+1}$ contains the desired outputs, which are the EHO's setpoints. The j-th expected predicted system output $\tilde{\boldsymbol{y}}_{k+i+1,j}$ shall satisfy the required setpoints with a permitted violation probability $\beta_j \in (0, 1]$ (1.27). In order to determine (1.27), the disturbance covariance $\Sigma_{z,k}$ can be mapped onto the states and outputs, and be propagated over the prediction horizon N.

However, to control the system as described above, an estimation of the true states and an estimation of the disturbance covariance is required. Therefore, a standard EKF (for example, [69]) is applied as an observer. The disturbance covariance $\Sigma_{z,k}$ is obtained from analyzing the model outputs and measurements.

Cooperation concept

The cooperation concept exploits stochastic information about the disturbance and the EHO's cost function sensitivities to compute an optimal permitted violation probability β for (1.27). The permitted violation probability results from minimizing the expected operating costs (risk costs),

$$\min_{\beta} \quad J_{\text{risk}}\left(c_{\text{fuel}}, c_{\text{viol}}, \beta\right) \ . \tag{1.30}$$

The risk cost function is derived from static considerations of the EHO's optimization problem,

$$J_{\text{risk}}(c_{\text{fuel}}, c_{\text{viol}}, \beta) = c_{\text{fuel}}(\tilde{y} - r) + c_{\text{viol}}\omega \ , \tag{1.31}$$

in which the two terms describe the fuel and violation costs, respectively. In (1.31), c_{fuel} represents the fuel costs per additional output unit and r is the desired setpoint computed by the EHO. The expected output $\tilde{y}$ and the expected violations ω, weighted by severity and frequency, depend on the choice of β. The violation costs per missing output c_{viol} are given by the EHO's cost function sensitivities. They are computed by deriving the cost function of the EHO with respect to the corresponding output,

$$c_{\text{viol}} = \frac{\mathrm{d}J_{\text{EHO}}}{\mathrm{d}r} \ . \tag{1.32}$$

The determined permitted violation probability β leads to optimal plant operation and the best possible trade-off between fuel and violation costs.

Selected result

The operation optimization framework is tested with three different control concepts in the lower operation optimization layer: (1) a standard MPC, (2) a stochastic MPC with a permitted violation probability of 3 %, and (3) a stochastic MPC using the novel cooperation concept. The expected operating costs of the plant are minimized by 54.5 % using the novel cooperation concept in comparison to a standard MPC case. No further expert knowledge is required to control the plant, e.g., to tune control parameters such as the permitted violation probability β.

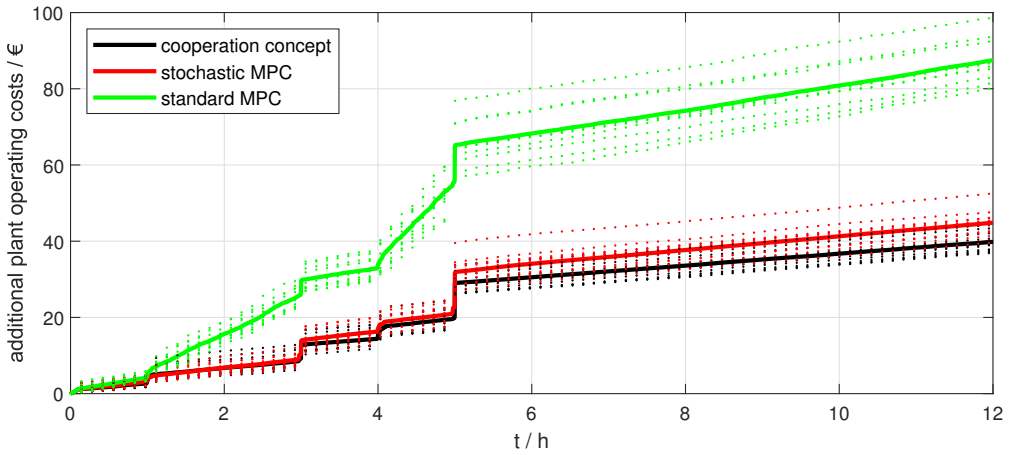

Figure 1.9: The presence of disturbances leads to additional plant operating costs, which can be minimized with the novel cooperation concept. The solid lines are the mean values of the ten simulation runs, whereas the dashed lines represent each individual run.

1.6 Conclusion

The present thesis provides novel model-based optimization methods in the field of thermal energy systems. Therefore, a typical configuration in the energy-intensive industry was studied to develop advanced modeling, observation, and control methods. First, a hybrid thermal energy storage system consisting of an Ruths steam storage (RSS) and a latent heat thermal energy storage (LHTES) was investigated as an exemplary plant component for modeling and state estimation tasks [according **Q.1**, **Q.2**, and **Q.3**]. Then, the overall operation of an entire thermal energy system by means of a hierarchical control scheme was examined [according **Q.4**].

Research question Q.1 is addressed by a co-simulation model using an efficient coupling mechanism and high-level model reduction - For the hybrid thermal energy

storage system, two sub-models of different complexity are combined in a co-simulation model. The co-simulation model uses the exchanged heat flow as coupling mechanism while the global energy conservation is always guaranteed. The sub-models are computed on different time scales to account for their different complexity. The LHTES sub-model is divided into sections called PCM cells, and the number of PCM cells required for the calculation is determined by an optimization criterion. The developed model enables system analysis, but especially serves as foundation for estimation and control tasks.

Research question Q.2 is tackled by considering model reduction for a dominant behavior in a particular use case - The co-simulation model is highly accurate but not real-time capable, as required for advanced control and state estimation tasks. Therefore, the more computing-intensive sub-model, the nonlinear PCM cell model, is brought to real-time capability by a novel reduction method. The developed reduction method is data-based and replaces the laborious solution of the Navier-Stokes equations with a surrogate stream function model. A singular value decomposition extracts dominant modes in space and time from a representative data set. The temporal modes of the surrogate stream function model can be explained by selected properties of the energy equation's solution. The resulting reduced model has significantly increased computational efficiency while maintaining model accuracy, and thus can serve as a basis for observers to estimate the distributed state in a PCM cell.

Research question Q.3 results in a state estimation concept that focuses on the behavior of the dominant states - The reduced PCM cell model is of high order and thus cannot be directly implemented in a standard EKF due to computational complexity and observability issues. Therefore, the presented state estimation approach uses two models of different order. The high-order nonlinear PCM cell model predicts future system states, while a low-order observer model provides the Jacobians for an EKF. The observer model is the linearized and balanced truncated PCM cell model, where only dominant states are considered while weak states are discarded. The EKF computes a state update for the high-order PCM cell model based on the PCM cell model's predicted states, the observer model's Jacobians, and measurements. The observer approach is able to accurately estimate both the melting front as well as the state of charge and shows robust behavior due to the dominant-states-only observer model.

Research question Q.4 is addressed by an operation optimization framework involving a cooperation concept to exchange relevant information between optimization layers - A thermal energy system typically comprises components of different complexity: (1) components with dynamics and disturbances, and (2) components with simpler behavior that can be considered statically. In order to abstract the control of an entire plant into manageable subproblems, a hierarchical optimization structure is often employed in industrial plants. In an upper layer (EHO), the economic characteristics of the overall process are exploited based on static models for all components. In the lower layer (MPC), only the dynamic components are controlled to fulfill the EHO's setpoints

while taking disturbances into account. A cooperation concept between the hierarchical optimization layers is developed to operate the overall plant at optimal expected costs despite the presence of disturbances. In the cooperation concept, stochastic information about the disturbance and the EHO's cost function sensitivities are exploited to compute an optimal permitted violation probability of the EHO's setpoints. A stochastic MPC controls the dynamic plant components to meet the EHO's setpoints with the optimal permitted violation probability. The cooperation concept is demonstrated in simulation studies with models calibrated using industrial measurement data. The plant operation costs caused by disturbances can be significantly reduced with the novel method.

The overarching key objective O. was achieved by successfully exploiting the complex system structures with respect to the underlying specific application domain. To this end, modeling and reduction methods were developed focusing on the dominant system behavior. The complexity of the systems was made manageable by subdivision and selective treatment, with only relevant information being exchanged between subsystems. The different reduction stages were applied in control and observation tasks.

Bibliography

[1] IEA. *World Energy Outlook 2020*. International Energy Agency, 2020. URL: https://www.iea.org/reports/world-energy-outlook-2020.

[2] UN. "Paris Agreement". In: *United Nations Treaty Collection* (2015). URL: https://treaties.un.org/Pages/ViewDetails.aspx?src=IND&mtdsg_no=XXVII-7-d&chapter=27&clang=_en.

[3] A. Gil, M. Medrano, I. Martorell, A. Lázaro, P. Dolado, B. Zalba, and L. F. Cabeza. "State of the art on high temperature thermal energy storage for power generation. Part 1—Concepts, materials and modellization". In: *Renewable and Sustainable Energy Reviews* 14.1 (2010), pp. 31–55. DOI: 10.1016/j.rser.2009.07.035.

[4] R. Scattolini. "Architectures for distributed and hierarchical Model Predictive Control – A review". In: *Journal of Process Control* 19.5 (2009), pp. 723–731. DOI: 10.1016/j.jprocont.2009.02.003.

[5] F. Bai and C. Xu. "Performance analysis of a two-stage thermal energy storage system using concrete and steam accumulator". In: *Applied Thermal Engineering* 31.14 (2011), pp. 2764–2771. DOI: 10.1016/j.applthermaleng.2011.04.049.

[6] W.-D. Steinmann and M. Eck. "Buffer storage for direct steam generation". In: *Solar Energy* 80.10 (2006), pp. 1277–1282. DOI: 10.1016/j.solener.2005.05.013.

[7] V. D. Stevanovic, B. Maslovaric, and S. Prica. "Dynamics of steam accumulation". In: *Applied Thermal Engineering* 37 (2012), pp. 73–79. DOI: 10.1016/j.applthermaleng.2012.01.007.

[8] S. Dusek and R. Hofmann. "A hybrid energy storage concept for future application in industrial processes". In: *Thermal Science* 22.5 (2018), pp. 2235–2242. DOI: 10.2298/TSCI171230270D.

[9] S. Dusek and R. Hofmann. "Modeling of a Hybrid Steam Storage and Validation with an Industrial Ruths Steam Storage Line". In: *Energies* 12.6 (2019), p. 1014. DOI: 10.3390/en12061014.

[10] Y. Dutil, D. R. Rousse, N. B. Salah, S. Lassue, and L. Zalewski. "A review on phase-change materials: Mathematical modeling and simulations". In: *Renewable and Sustainable Energy Reviews* 15.1 (2011), pp. 112–130. DOI: 10.1016/j.rser.2010.06.011.

[11] S. Liu, Y. Li, and Y. Zhang. "Mathematical solutions and numerical models employed for the investigations of PCMs' phase transformations". In: *Renewable and Sustainable Energy Reviews* 33 (2014), pp. 659–674. DOI: 10.1016/j.rser.2014.02.032.

[12] B. Fortunato, S. Camporeale, T. Marco, and M. Albano. "Simple Mathematical Model of a Thermal Storage with PCM". In: *AASRI Procedia* 2 (2012), pp. 241–248. DOI: 10.1016/j.aasri.2012.09.041.

[13] J. Vogel, J. Felbinger, and M. Johnson. "Natural convection in high temperature flat plate latent heat thermal energy storage systems". In: *Applied Energy* 184 (2016), pp. 184–196. DOI: 10.1016/j.apenergy.2016.10.001.

[14] L. Kasper, D. Pernsteiner, M. Koller, A. Schirrer, S. Jakubek, and R. Hofmann. "Numerical studies on the influence of natural convection under inclination on optimal aluminium proportions and fin spacings in a rectangular aluminium finned latent-heat thermal energy storage". In: *Applied Thermal Engineering* 190 (2021), p. 116448. DOI: 10.1016/j.applthermaleng.2020.116448.

[15] V. Voller and C. Prakash. "A fixed grid numerical modelling methodology for convection-diffusion mushy region phase-change problems". In: *International Journal of Heat and Mass Transfer* 30.8 (1987), pp. 1709–1719. DOI: 10.1016/0017-9310(87)90317-6.

[16] R. T. Tenchev, J. A. Mackenzie, T. J. Scanlon, and M. T. Stickland. "Finite element moving mesh analysis of phase change problems with natural convection". In: *International Journal of Heat and Fluid Flow* 26.4 (2005), pp. 597–612. DOI: 10.1016/j.ijheatfluidflow.2005.03.003.

[17] B. Nedjar. "An enthalpy-based finite element method for nonlinear heat problems involving phase change". In: *Computers & Structures* 80.1 (2002), pp. 9–21. DOI: 10.1016/S0045-7949(01)00165-1.

[18] L. Kasper. *Modeling of the Phase Change Material of a Hybrid Storage Using the Finite Element Method*. Wien (Austria): TU Wien Academic Press, 2020. DOI: 10.34727/2020/isbn.978-3-85448-037-2.

[19] B. Seibold. *A compact and fast Matlab code solving the incompressible Navier-Stokes equations on rectangular domains*. retrieved 29th June 2021. 2008. URL: http://math.mit.edu/~gs/cse/codes/mit18086_navierstokes.pdf.

[20] J. Buschle, W.-D. Steinmann, and R. Tamme. "Latent heat storage for process heat applications". In: *10th International Conference on thermal Energy Storage ECOSTOCK 2006*. June 2006. URL: https://elib.dlr.de/55379/.

[21] J. Buschle, W.-D. Steinmann, and R. Tamme. "Analysis of steam storage systems using Modelica". In: *5th International Modelica Conference 2006*. Ed. by M. Association. Sept. 2006. URL: https://elib.dlr.de/47205/.

[22] P. Benner, S. Gugercin, and K. Willcox. "A Survey of Projection-Based Model Reduction Methods for Parametric Dynamical Systems". In: *SIAM Review* 57.4 (2015), pp. 483–531. DOI: 10.1137/130932715.

[23] T. Reis and T. Stykel. "A Survey on Model Reduction of Coupled Systems". In: *Model Order Reduction: Theory, Research Aspects and Applications*. Vol. 13. Berlin (Germany): Springer, Jan. 2008, pp. 133–155. DOI: 10.1007/978-3-540-78841-6_7.

[24] A. Antoulas, D. Sorensen, and S. Gugercin. "A survey of model reduction methods for large systems". In: *Contemp. Math* 280 (2001). DOI: 10.1090/conm/280/04630.

[25] A. Astolfi. "Model Reduction by Moment Matching for Linear and Nonlinear Systems". In: *IEEE Transactions on Automatic Control* 55.10 (2010), pp. 2321–2336. DOI: 10.1109/TAC.2010.2046044.

[26] B. Moore. "Principal component analysis in linear systems: Controllability, observability, and model reduction". In: *IEEE Transactions on Automatic Control* 26.1 (1981), pp. 17–32. DOI: 10.1109/TAC.1981.1102568.

[27] K. Glover. "All optimal Hankel-norm approximations of linear multivariable systems and their error bounds". In: *International Journal of Control* 39.6 (1984), pp. 1115–1193. DOI: 10.1080/00207178408933239.

[28] Y. Liu and B. D. O. Anderson. "Singular perturbation approximation of balanced systems". In: *International Journal of Control* 50.4 (1989), pp. 1379–1405. DOI: 10.1080/00207178908953437.

[29] S. L. Brunton and J. N. Kutz. *Data-Driven Science and Engineering: Machine Learning, Dynamical Systems, and Control*. Cambridge (U.K.): Cambridge University Press, 2019. DOI: 10.1017/9781108380690.

[30] P. J. Schmid. "Dynamic mode decomposition of numerical and experimental data". In: *Journal of Fluid Mechanics* 656 (2010), pp. 5–28. DOI: 10.1017/S0022112010001217.

[31] F. Chinesta, P. Ladeveze, and E. Cueto. "A Short Review on Model Order Reduction Based on Proper Generalized Decomposition". In: *Archives of Computational Methods in Engineering* 18 (Nov. 2011), pp. 395–404. DOI: 10.1007/s11831-011-9064-7.

[32] J. H. Tu, C. W. Rowley, D. M. Luchtenburg, S. L. Brunton, and J. Nathan Kutz. "On dynamic mode decomposition: Theory and applications". In: *Journal of Computational Dynamics* 1.2 (2014), pp. 391–421. DOI: 10.3934/jcd.2014.1.391.

[33] C. W. Rowley and S. T. Dawson. "Model Reduction for Flow Analysis and Control". In: *Annual Review of Fluid Mechanics* 49.1 (2017), pp. 387–417. DOI: 10.1146/annurev-fluid-010816-060042.

[34] T. Lassila, A. Manzoni, A. Quarteroni, and G. Rozza. "Model Order Reduction in Fluid Dynamics: Challenges and Perspectives". In: *Reduced Order Methods for Modeling and Computational Reduction*. Ed. by A. Quarteroni and G. Rozza. Cham (Switzerland): Springer International Publishing, 2014, pp. 235–273. DOI: 10.1007/978-3-319-02090-7_9.

[35] D. A. Bistrian and I. M. Navon. "An improved algorithm for the shallow water equations model reduction: Dynamic Mode Decomposition vs POD". In: *International Journal for Numerical Methods in Fluids* 78.9 (2015), pp. 552–580. DOI: 10.1002/fld.4029.

[36] A. Dumon, C. Allery, and A. Ammar. "Proper general decomposition (PGD) for the resolution of Navier–Stokes equations". In: *Journal of Computational Physics* 230.4 (2011), pp. 1387–1407. DOI: 10.1016/j.jcp.2010.11.010.

[37] E. Liberge and A. Hamdouni. "Reduced order modelling method via proper orthogonal decomposition (POD) for flow around an oscillating cylinder". In: *Journal of Fluids and Structures* 26.2 (2010), pp. 292–311. DOI: 10.1016/j.jfluidstructs.2009.10.006.

[38] J. N. Kutz. "Deep learning in fluid dynamics". In: *Journal of Fluid Mechanics* 814 (2017), pp. 1–4. DOI: 10.1017/jfm.2016.803.

[39] G. Zsembinszki, C. Orozco, J. Gasia, T. Barz, J. Emhofer, and L. F. Cabeza. "Evaluation of the State of Charge of a Solid/Liquid Phase Change Material in a Thermal Energy Storage Tank". In: *Energies* 13.6 (2020), p. 1425. DOI: 10.3390/en13061425.

[40] J. Mohd Ali, N. Ha Hoang, M. Hussain, and D. Dochain. "Review and classification of recent observers applied in chemical process systems". In: *Computers & Chemical Engineering* 76 (2015), pp. 27–41. DOI: 10.1016/j.compchemeng.2015.01.019.

[41] D. Dochain. "State and parameter estimation in chemical and biochemical processes: a tutorial". In: *Journal of Process Control* 13.8 (2003), pp. 801–818. DOI: 10.1016/S0959-1524(03)00026-X.

[42] Z. Hidayat, R. Babuska, B. De Schutter, and A. Núñez. "Observers for linear distributed-parameter systems: A survey". In: *2011 IEEE International Symposium on Robotic and Sensors Environments (ROSE)*. 2011, pp. 166–171. DOI: 10.1109/ROSE.2011.6058523.

[43] M. Bitzer and M. Zeitz. "Design of a nonlinear distributed parameter observer for a pressure swing adsorption plant". In: *Journal of Process Control* 12.4 (2002), pp. 533–543. DOI: 10.1016/S0959-1524(01)00019-1.

[44] D. G. Luenberger. "Observers for multivariable systems". In: *IEEE Transactions on Automatic Control* 11.2 (1966), pp. 190–197. DOI: 10.1109/TAC.1966.1098323.

[45] R. E. Kalman. "A New Approach to Linear Filtering and Prediction Problems". In: *Journal of Basic Engineering* 82.1 (1960), pp. 35–45. DOI: 10.1115/1.3662552.

[46] R. E. Kalman and R. S. Bucy. "New Results in Linear Filtering and Prediction Theory". In: *Journal of Basic Engineering* 83 (1961), pp. 95–108. DOI: 10.1115/1.3658902.

[47] A. Jazwinski. *Stochastic Processes And Filtering Theory*. New York (NY, USA) and London (U.K.): Academic Press, 1970.

[48] R. P. Wishner, J. A. Tabaczynski, and M. Athans. "A comparison of three non-linear filters". In: *Automatica* 5.4 (1969), pp. 487–496. DOI: 10.1016/0005-1098(69)90110-1.

[49] T. Barz, D. Seliger, K. Marx, A. Sommer, S. F. Walter, H. G. Bock, and S. Körkel. "State and state of charge estimation for a latent heat storage". In: *Control Engineering Practice* 72 (2018), pp. 151–166. DOI: 10.1016/j.conengprac.2017.11.006.

[50] C. J. Backi, J. D. Bendtsen, J. Leth, and J. T. Gravdahl. "A heat equation for freezing processes with phase change: stability analysis and applications". In: *International Journal of Control* 89.4 (2016), pp. 833–849. DOI: 10.1080/00207179.2015.1102327.

[51] C. J. Backi, J. Dimon Bendtsen, J. Leth, and J. T. Gravdahl. "Estimation of inner-domain temperatures for a freezing process". In: *2014 IEEE Conference on Control Applications (CCA)*. 2014, pp. 1759–1764. DOI: 10.1109/CCA.2014.6981567.

[52] E. Akkari, S. Chevallier, and L. Boillereaux. "Observer-based monitoring of thermal runaway in microwaves food defrosting". In: *Journal of Process Control* 16.9 (2006), pp. 993–1001. DOI: 10.1016/j.jprocont.2006.05.005.

[53] B.-G. Park, J.-M. Kim, J.-W. Kim, K.-C. Lee, D.-H. Koo, and D.-S. Hyun. "New approach to EKF-based sensorless control using parallel structure for non-salient pole permanent magnet synchronous motors". In: *2013 International Conference on Electrical Machines and Systems (ICEMS)*. 2013, pp. 1099–1104. DOI: 10.1109/ICEMS.2013.6754407.

[54] H. Khodadadi and H. Jazayeri-Rad. "Applying a dual extended Kalman filter for the nonlinear state and parameter estimations of a continuous stirred tank reactor". In: *Computers & Chemical Engineering* 35.11 (2011), pp. 2426–2436. DOI: 10.1016/j.compchemeng.2010.12.010.

[55] J. Lee, O. Nam, and B. Cho. "Li-ion battery SOC estimation method based on the reduced order extended Kalman filtering". In: *Journal of Power Sources* 174.1 (2007), pp. 9–15. DOI: 10.1016/j.jpowsour.2007.03.072.

[56] B. F. Farrell and P. J. Ioannou. "State Estimation Using a Reduced-Order Kalman Filter". In: *Journal of the Atmospheric Sciences* 58.23 (2001), pp. 3666–3680. DOI: 10.1175/1520-0469(2001)058<3666:SEUARO>2.0.CO;2.

[57] P. Tatjewski. "Advanced control and on-line process optimization in multilayer structures". In: *Annual Reviews in Control* 32.1 (2008), pp. 71–85. DOI: 10.1016/j.arcontrol.2008.03.003.

[58] A. Hinojosa, A. Ferramosca, A. Gonzalez, and D. Odloak. "One-layer gradient-based MPC + RTO of a propylene/propane splitter". In: *Computers & Chemical Engineering* 106 (2017), pp. 160–170. DOI: 10.1016/j.compchemeng.2017.06.006.

[59] A. Marchetti, A. Ferramosca, and A. González. "Steady-state target optimization designs for integrating real-time optimization and model predictive control". In: *Journal of Process Control* 24.1 (2014), pp. 129–145. DOI: 10.1016/j.jprocont.2013.11.004.

[60] A. H. González and D. Odloak. "A stable MPC with zone control". In: *Journal of Process Control* 19.1 (2009), pp. 110–122. DOI: 10.1016/j.jprocont.2008.01.003.

[61] M. Z. Jamaludin and C. L. Swartz. "Approximation of closed-loop prediction for dynamic real-time optimization calculations". In: *Computers & Chemical Engineering* 103 (2017), pp. 23–38. DOI: 10.1016/j.compchemeng.2017.02.037.

[62] L. Würth, R. Hannemann, and W. Marquardt. "Neighboring-extremal updates for nonlinear model-predictive control and dynamic real-time optimization". In: *Journal of Process Control* 19.8 (2009), pp. 1277–1288. DOI: 10.1016/j.jprocont.2009.02.001.

[63] J. Kadam and W. Marquardt. "Integration of Economical Optimization and Control for Intentionally Transient Process Operation". In: *Lecture Notes in Control and Information Sciences*. Vol. 358. Berlin (Germany): Springer, 2007, pp. 419–434. DOI: 10.1007/978-3-540-72699-9_34.

[64] J. B. Rawlings, D. Angeli, and C. N. Bates. "Fundamentals of economic model predictive control". In: *2012 IEEE 51st IEEE Conference on Decision and Control (CDC)*. 2012, pp. 3851–3861. DOI: 10.1109/CDC.2012.6425822.

[65] J. Boussinesq. *Theorie Analytique de la Chaleur vol 2 (Paris: Gauthier-Villars)*. 1903.

[66] J. L. Lagrange. "Mémoire sur la théorie du mouvement des fluides, Œuvres complètes". In: *Nouveaux mémoires de l'Académie royale des sciences et belles-lettres de Berlin, année 1781* (1781).

[67] L. Sirovich. "Turbulence and the Dynamics of Coherent Structures Part I: Coherent Structures". In: *Quarterly of Applied Mathematics* XLV (1987), pp. 561–571. DOI: 10.1090/qam/910462.

[68] A. Zhakatayev, B. Rakhim, O. Adiyatov, A. Baimyshev, and H. A. Varol. "Successive linearization based model predictive control of variable stiffness actuated robots". In: *2017 IEEE International Conference on Advanced Intelligent Mechatronics (AIM)*. 2017, pp. 1774–1779. DOI: 10.1109/AIM.2017.8014275.

[69] D. Simon. *Optimal state estimation: Kalman, H∞, and nonlinear approaches*. Hoboken (NJ, USA): John Wiley & Sons, 2006. DOI: 10.1002/0470045345.

[70] D. Ritzberger, J. Höflinger, Z. P. Du, C. Hametner, and S. Jakubek. "Data-driven parameterization of polymer electrolyte membrane fuel cell models via simultaneous local linear structured state space identification". In: *International Journal of Hydrogen Energy* 46.21 (2021), pp. 11878–11893. DOI: 10.1016/j.ijhydene.2021.01.037.

[71] T. A. N. Heirung, J. A. Paulson, J. O'Leary, and A. Mesbah. "Stochastic model predictive control — how does it work?" In: *Computers & Chemical Engineering* 114 (2018), pp. 158–170. DOI: 10.1016/j.compchemeng.2017.10.026.

Chapter 2

Publications

List of selected journal publications

Publication A

Co-simulation methodology of a hybrid latent-heat thermal energy storage unit.

Dominik Pernsteiner, Lukas Kasper, Alexander Schirrer, René Hofmann, and Stefan Jakubek.

Applied Thermal Engineering 178 (2020) p. 115495.

DOI: 10.1016/j.applthermaleng.2020.115495

Publication B

Data-based model reduction for phase change problems with convective heat transfer.

Dominik Pernsteiner, Alexander Schirrer, Lukas Kasper, René Hofmann, and Stefan Jakubek.

Applied Thermal Engineering 184 (2021) p. 116228.

DOI: 10.1016/j.applthermaleng.2020.116228

Publication C

State estimation concept for a nonlinear melting/solidification problem of a latent heat thermal energy storage.

Dominik Pernsteiner, Alexander Schirrer, Lukas Kasper, René Hofmann, and Stefan Jakubek.

Computers & Chemical Engineering 153 (2021) p. 107444.

DOI: 10.1016/j.compchemeng.2021.107444

Publication* D

Efficient sensitivity-based cooperation concept in multi-layer operation optimization architectures.

Dominik Pernsteiner, Verena Halmschlager, Alexander Schirrer, René Hofmann, and Stefan Jakubek.

submitted to Computers & Chemical Engineering (2021).

*in submission

2.1 Publication A

D. Pernsteiner, L. Kasper, A. Schirrer, R. Hofmann, and S. Jakubek. "Co-simulation methodology of a hybrid latent-heat thermal energy storage unit". In: *Applied Thermal Engineering* 178 (2020), p. 115495. DOI: 10.1016/j.applthermaleng.2020.115495

Applicant's contribution [†]

- Dominik Pernsteiner: Conceptualization, Formal analysis, Investigation, Methodology, Software, Visualization, Writing - original draft
- Lukas Kasper: Methodology, Software, Writing - original draft
- Alexander Schirrer: Conceptualization, Methodology, Supervision, Writing - review & editing
- René Hofmann: Funding acquisition, Supervision, Writing - review & editing
- Stefan Jakubek: Funding acquisition, Supervision, Writing - review & editing

[†]According to the Elsevier CRediT author statement: https://www.elsevier.com/authors/policies-and-guidelines/credit-author-statement

Applied Thermal Engineering 178 (2020) 115495

Contents lists available at ScienceDirect

Applied Thermal Engineering

journal homepage: www.elsevier.com/locate/apthermeng

Co-simulation methodology of a hybrid latent-heat thermal energy storage unit

Dominik Pernsteiner[a,*], Lukas Kasper[b], Alexander Schirrer[a], René Hofmann[b,c], Stefan Jakubek[a]

[a] TU Wien, Institute of Mechanics and Mechatronics, Getreidemarkt 9/BA, 1060 Vienna, Austria
[b] TU Wien, Institute for Energy Systems and Thermodynamics, Getreidemarkt 9/BA, 1060 Vienna, Austria
[c] AIT Austrian Institute of Technology GmbH, Center for Energy, Sustainable Thermal Energy Systems, Giefinggasse 2, 1210 Vienna, Austria

HIGHLIGHTS

- A co-simulation method is applied for a hybrid latent heat thermal energy storage.
- Criteria for efficient subsystem aggregation and model reduction are proposed.
- Accurate thermal coupling of models with different complexity is applied.
- The successful model reduction is demonstrated in numerical investigations.

ARTICLE INFO

Keywords:
Co-simulation
Phase change material
Ruths steam storage
Latent heat thermal energy storage
Optimization

ABSTRACT

In a hybrid steam/latent heat storage concept as previously proposed, containers filled with phase change material (PCM) are installed at the shell surface of a Ruths steam storage (RSS) to increase storage capacity through retrofitting. The detailed knowledge of the thermophysical behavior of such a concept is crucial to exploit its full potential. For this purpose, a novel high-fidelity co-simulation model is developed in this work, implementing an efficient and accurate thermal coupling concept of a dynamic RSS model with detailed conduction/convection PCM cell models. It accounts for the significant influence of angular position and orientation of the PCM cells at the RSS shell surface as well as the filling level in the RSS. To reduce computational effort, the PCM cells are logically aggregated to PCM sectors with similar thermodynamic behavior using a new optimization method that minimizes the total error. Therefore, quantitative criteria to find an optimized PCM cell aggregation are formulated. The efficiency and accuracy of the proposed reduced-complexity co-simulation is demonstrated in typical operation modes of the hybrid storage. In the simulation study, the error can be reduced from 4.5% to 0.5% by using the newly developed optimal aggregation criteria. The computation time can be shortened up to 73%, whereby equally accurate results can be achieved compared to a model with high resolution. The developed co-simulation model serves as a foundation for design optimization, model reduction, dynamic state-of-charge estimation, and ultimately enables model-based control.

1. Introduction

1.1. Motivation

Deep decarbonization and greening efforts strongly impact the energy-intensive industries, driving them to continuously increase process efficiency [28]. Many advanced industrial processes rely on the decoupling of energy production and consumption to improve the balancing of supply and demand, resource utilization, and thereby overall energy efficiency. To achieve the necessary flexibility, thermal energy storage systems (TES) are widely used.

There are mainly three types of storage media in TES systems: sensible, latent and chemical [18]. In sensitive storage media, the energy content of a substance increases with rising temperature and is referred to as sensible heat. Latent storage media mainly use the phase transition to store energy in a small temperature range with high energy density. The third storage mechanism is based on chemical reactions and must be completely reversible. The heat generated is used to excite an endothermic chemical reaction and can be fully recovered by the back reaction. The storage systems also can be classified in active or

* Corresponding author at: Institute for Mechanics and Mechatronics, TU Wien, Getreidemarkt 9/E325, 1060 Vienna, Austria.
E-mail address: dominik.pernsteiner@tuwien.ac.at (D. Pernsteiner).

https://doi.org/10.1016/j.applthermaleng.2020.115495
Received 26 November 2019; Received in revised form 14 April 2020; Accepted 14 May 2020
Available online 22 May 2020

Nomenclature

Acronyms

HTC	heat transfer coefficient
LHTES	Latent Heat Thermal Energy Storage
NRMSE	Normalized Root Mean Square Error
PCM	Phase Change Material
RMSE	Root Mean Square Error
RSS	Ruths Steam Storage

Index

0	initial
corr	corrected
env	environment
in	incoming flow
L	liquid
m	melting
out	outgoing flow
ref	reference
RSS, losses	losses to the environment
RSS2PCM	flow from RSS to PCM
S	solid
V	vapour
~	solution of optimization problem
*, **	intermediate solutions of the fractional step approach
i	index for PCM cells in a sector
j	index for PCM sectors on the RSS shell
n	number of simulation/ measurement values
non	number of nodes

Parameters and variables

α	heat transfer coefficient (W/(m^2 K))
β	volumetric thermal expansion coefficient (1/K)
$\boldsymbol{f}$	force density (kg/(m^2 s^2))
$\boldsymbol{g}$	gravitational acceleration vector (m/s^2)
$\boldsymbol{M}$	mass matrix of RSS
$\boldsymbol{u}$	velocity vector (m/s)
$\boldsymbol{w}$	input vector of RSS
$\boldsymbol{x}$	state vector of RSS
$\Delta\Phi_j$	angular distance of PCM sector j (rad)
$\Delta\Phi_{\text{cell}}$	angular distance of a PCM cell (rad)
Δt	time step (s)
Δx_{PCM}	cavity PCM dimension in x direction (m)
Δy_{PCM}	cavity PCM dimension in y direction (m)
$\dot{m}$	mass flow (kg/s)
$\dot{Q}$	total heat flow to RSS (W)
ϵ	mushy region temperature range (K)
γ	water/steam interface angle in RSS (rad)
μ	dynamic viscosity ((Ns)/m^2)
ρ	density (kg/m^3)
Φ	angular position of a PCM sector (rad)
c	specific heat capacity (J/(kg K))
d	inner diameter of RSS (m)
F	liquid filling ratio
H	enthalpy (J)
h	specific enthalpy (J/kg)
k	thermal conductivity (W/(mK))
l	length of RSS (m)
L_x, L_y	length of PCM cell in x, y direction (m)
m	mass of fluid inside RSS (kg)
n_{cell}	number of PCM cells at RSS
n_{sect}	number of PCM sectors at RSS
p	pressure (N/m^2)
q	heat flux (W/m^2)
s	wall thickness of RSS (m)
s_{iso}	wall thickness of insulation (m)
s_{o}	wall thickness of outer panel (m)
T	temperature (°C)
t	time (s)
u, v	velocity components in x, y direction (m/s)
V	volume of RSS (m^3)
x, y	space coordinates (m)
x_{RSS}	vapour mass fraction
N	shape functions

Symbols

Δ	Laplace operator: $\Delta = (\partial^2/\partial x^2 + \partial^2/\partial y^2)$
$\{\cdot\}$	a $non \times 1$ vector of element node point values
$\mathscr{D}$, $\partial\mathscr{D}$	spatial domain, boundary of spatial domain
∇	Nabla operator: $\nabla = (\partial/\partial x, \partial/\partial y)$

passive systems. An active storage system stores the heat transfer medium itself, whereas in a passive storage system the heat transfer medium passes through the storage only for loading and unloading a second material.

An active storage device that stores sensible heat is the well-established and widely used Ruths steam storage (RSS). González-Roubaud et al. [19] emphasize the fast reaction time and the high charging and discharging rates as main advantages of the RSS. Steinmann and Eck [37] analyse the use of RSS as buffer storage in direct steam generation. Biglia et al. [5] consider a design with an RSS in batch food processes. However, storage capacity using RSS is always determined by vessel volume and the allowed system pressure range, which becomes problematic in the case of process requirements that increase during the storage life time.

In order to store energy with a high energy density and at a nearly constant temperature level, phase change material (PCM) in latent heat thermal energy storage (LHTES) is commonly used and represents a passive storage type. Many different PCMs with various properties for application, such as melting points, are available, see Ref. [1,44]. A drawback of PCMs is the low thermal conductivity which determines the charging and discharging rate and poses significant challenges for dynamic operation. Some methods to increase the thermal conductivity are summarized by Tao and He [40] and Ibrahim et al. [22].

Various combinations of RSS with LHTES are mentioned in literature to use the advantages of both storage types and to eliminate their disadvantages. A configuration with PCM inside an RSS was described by Ref. [7,37,39]. Buschle et al. [7] and Tamme et al. [39] also proposed an alternative arrangement of an RSS connected to a tube register which is surrounded by PCM. Underwood et al. [42] and Zhao et al. [46] analyzed the extension of a water tank by integrating PCM inside to increase energy density.

However, most of the above listed hybrid storage concepts are not suited for retrofitting existing industrial systems. Once RSS are built and put into operation, changing operational demands requiring higher storage capacities may have to be met. For this purpose, Dusek and Hofmann [12] and Hofmann et al. [20] presented a novel approach to increase the storage capacity of an existing RSS by attaching phase change material (PCM) containers to its outer shell.

1.2. Innovation

Only very few of these hybrid storage types have been numerically

investigated in detail, most of them were designed via basic model equations and tested experimentally, see Section 1.6. To exploit the full potential of such a complex coupled thermal storage system, dynamic estimation and control algorithms are essential, which in turn rely on accurate numerical models capturing all relevant storage system dynamics. For example, natural convection within liquid PCM can significantly accelerate the melting process. To this end, a novel and efficient high-fidelity co-simulation model of the RSS coupled with detailed conduction/convection PCM models is developed in this work for the concept proposed by Dusek and Hofmann [12] and Hofmann et al. [20]. Quantitative criteria to find an optimized PCM cells to sector aggregation are proposed and used to significantly reduce computational effort. Co-simulation studies are conducted, showing the effectiveness of the proposed co-simulation structure and aggregation criteria. Typical operating ranges for such a storage concept are discussed and the demand for a new control concept is indicated. The model's level of detail, the reduction approach based on optimization to increase computing efficiency as well as the findings from the simulations are a novel contribution of this work and can find application in control (e.g. model predictive control), state of charge estimations and design optimization.

1.3. Hybrid storage concept

The proposed hybrid storage concept comprises an RSS and latent heat thermal energy storages (LHTES), see Fig. 1. The well-known RSS consists of a pressure vessel filled with a two-phase fluid of liquid water and steam at saturation. When charging, steam is injected by a distribution lance into the liquid phase of the vessel to ensure fast condensation. Non-condensing steam rises up and increases the pressure (and therefore temperature) inside the RSS. When demanded by processes, saturated steam is extracted from the top of the vessel, thereby discharging the RSS. Pressure decreases, and a part of the liquid phase evaporates until thermal equilibrium is re-established.

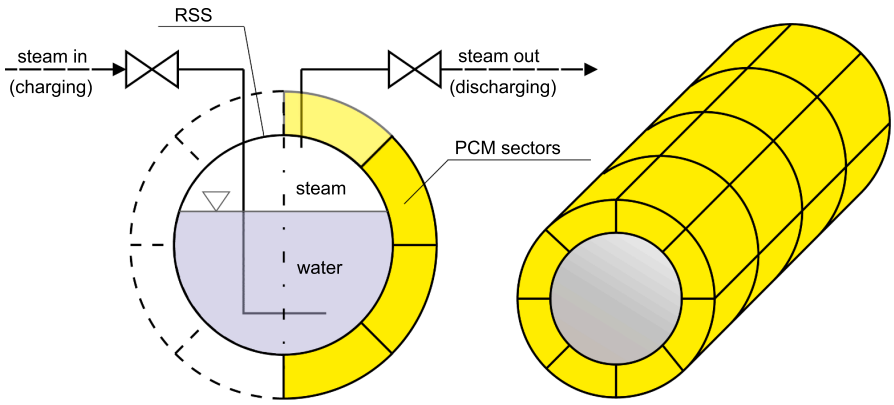

Fig. 1. Hybrid LHTES concept - Ruths steam storage (RSS) with attached phase change material (PCM).

1.4. Modeling approaches for Ruths steam storages

One common way of modeling an RSS is to assume thermodynamic equilibrium between the two phases inside the pressure vessel, which means that the liquid and steam phases have the same temperature [3,37]. Non-equilibrium models for the RSS as used by Stefanovic et al. [38] are not required because in the present work fast transients can be neglected due to the slow heat conduction in the PCM and the resulting long operational time scales of the investigated hybrid LHTES. For this reason, the implemented RSS model is adapted from the equilibrium model presented by Dusek and Hofmann [12], which was successfully validated with operational measurement data from a steel manufacturer.

1.5. Modeling approaches for phase change materials

Relevant heat transfer mechanisms in PCM are conduction and natural convection. The modeling of these materials can be highly complex. Dutil et al. [14] and Liu et al. [27] review options for mathematical modeling and simulation of PCM. Analytical solutions only exist for a limited number of phase change problems, as for example for the one-dimensional Stefan-problem [33]. Typical first modeling approaches are to neglect convective heat transfer in the liquid phase of PCM and use symmetry conditions to reduce the heat transfer problem to one dimension. Zauner et al. [45] formulated a Stefan-problem-based model to calculate the position of the phase interface dynamically for an LHTES where the PCM is enclosed inside tubes and heat transfer fluid flows around these tubes. This simple model provided satisfactory results in comparison with measurement data and was later adapted by Dusek and Hofmann [13] for the simulation of the hybrid LHTES also discussed in this work.

Fortunato et al. [15] state that the effect of natural convection is widely neglected in modeling PCM thermal storage systems due to its complexity. However, the legitimacy of such simplification strongly depends on the type of PCM encapsulation and is potentially violated for low viscosity in the liquid phase. In a numerical study with an experimentally validated model, Vogel et al. [43] analysed the impact of natural convection on melting in so-called flat plate LHTES filled with the common high-temperature PCM sodium nitrate and potassium nitrate (KNO3-NaNO3) also considered in this work. Their investigation results show that heat transfer enhancement due to natural convection increases with greater widths and smaller heights of PCM enclosures. This finding was confirmed by Kasper [25], who numerically investigated the impact of natural convection on melting of a PCM cell depending on its orientation. They found a significant enhancement of melting for upwards-oriented cavities with respect to the heated wall. These facts show that natural convection also has to be considered in modeling of the hybrid LHTES presented by Dusek and Hofmann [12]. The co-simulation approach proposed in the present paper solves this task efficiently.

When considering heat transfer in PCM in more than one dimension, numerical methods, as for example the enthalpy method and the effective heat capacity method, which were summarized by Liu et al. [27], have to be applied. Also, the Stefan-problem is complicated by the fact that, in general, more than one moving phase boundary can occur in PCM [8]. Nedjar [29] states that especially finite element methods are able to handle complex coupled thermomechanical problems with

various and complex boundary conditions. The effective heat capacity method was, for example, applied by Tenchev et al. [41] in a moving-mesh finite element model considering both conduction and natural convection. A similar approach was pursued by Kasper [25], using the effective heat capacity method and an adaptation of the finite difference code published by Seibold [34] to solve the two-dimensional Navier–Stokes equations arising in convection modeling. This provided an experimentally validated coupled finite element/ finite difference model for PCM cavity simulations which is adopted in the present work.

1.6. Co-simulation of hybrid LHTES

There are several simulation approaches in literature for a combination of PCM and a heat transfer fluid as storage systems. Gallego et al. [16] presented a validated mathematical model of a PCM storage tank with water as heat transfer fluid. Bony and Citherlet [6] described a numeric model of PCMs inserted in a water tank storage including convection effects. Underwood et al. [42] and Zhao et al. [46] applied a simple model neglecting natural convection to analyze the design of a water tank with integrated PCM inside for application in buildings. Stamatiou et al. [35] tested a quasi-stationary Tube-PCM model, which is only valid for small Stefan numbers.

Few simulation approaches in literature treat a combined RSS-PCM storage system. Buschle et al. [7] employed a simple dimensioning tool developed by Steinmann and Buschle [36], which neglected convection, to analyze PCM steam storage concepts. For a first analysis of a hybrid LHTES similar to the one investigated in this work, Dusek and Hofmann [12] applied a simplified model in Dymola. In an extension of this model, different heat transfer coefficients for each phase inside the RSS are implemented and the PCM surrounding the RSS is split up into several containers in peripheral direction. The PCM was modeled using the Stefan approach, not fully modeling the heat transfer structure and neglecting convection [13]. It has been shown, however, that natural convection can have a large impact on the melting behavior in PCM cells and should therefore be considered. The PCM sub-model utilized in the present work supports two-dimensional modeling with convection. To the best of the author's knowledge, no RSS-PCM co-simulation approach has yet been presented in the complexity level described here.

The co-simulation model described in this paper combines the two sub-models of the RSS and PCM cells to a hybrid LHTES model, see Fig. 1. To establish an accurate and efficient co-simulation of the coupled sub-models, it is crucial to devise suitable coupling formulations which ensure physically correct subsystem interfaces from a conservation law perspective. For this purpose, the sub-models, which are computed at different time scales, are coupled on a major time grid through wall temperatures respectively the resulting heat flow between the RSS and PCM. The computation at different time scales allows varying complexity of the sub-models.

Several neighboring PCM cells at the circumference of the RSS are combined into and simulated as one sector to improve computational efficiency, see Fig. 2. A cell representative of the sector is selected and used to calculate the behavior of the entire sector. Therefore, criteria for efficient aggregation of PCM cells to sectors while retaining solution accuracy are formulated, accounting for convection effects and the influence of the RSS filling level due to varying heat transfer coefficients. The curvature of the individual PCM cells is neglected because the diameter of the RSS is large compared to the narrow side length of the PCM cell.

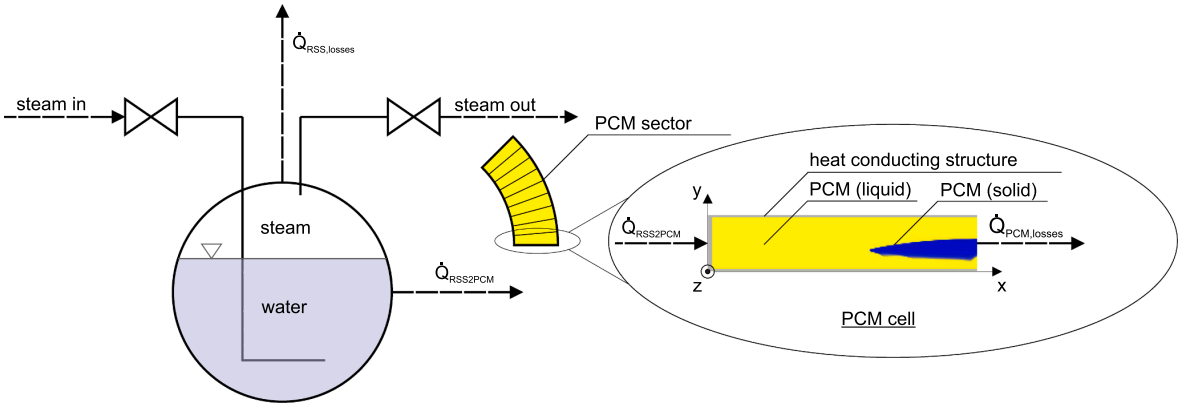

Fig. 2. Hybrid LHTES co-simulation architecture - Ruths steam storage (RSS) and attached phase change material (PCM) containers aggregated to PCM sectors. The liquid phase of the PCM cell is depicted in yellow, the solid phase in blue. Thermodynamic coupling is implemented via heat flows. (For interpretation of the references to colour in this figure legend, the reader is referred to the web version of this article.)

1.7. Main contributions

The main contributions of this paper are as follows:

- A novel and efficient high-fidelity co-simulation model of the considered hybrid latent heat thermal energy storage (LHTES) concept is developed, implementing the coupling of a dynamic RSS simulation model and detailed models of PCM cells (including conduction/ convection and phase change dynamics).
- Quantitative criteria to find an optimized PCM cells to sector aggregation are proposed and applied to significantly reduce computational effort.
- Co-simulation studies are conducted and discussed, showing typical operation of such storage system, as well as the effectiveness of the proposed co-simulation structure and aggregation criteria.

1.8. Paper structure

The paper is organised as follows: In Section 2, the general fundamental equations are presented. In Section 3, the implementation of the mathematical RSS and PCM models as well as the co-simulation coupling is stated. In Section 4, simulation studies to show the significant effects and dependencies are performed and the aggregation of PCM cells to sectors in simulation studies is demonstrated. In Section 5, results and their interpretation towards model reduction, estimation and control aspects are discussed.

2. Fundamental equations

2.1. Ruths steam storage

An RSS contains a two-phase fluid (here, water and steam) in a cylindrical cavity where the phases are considered always in thermodynamic equilibrium in this work (saturated state). This hypothesis is used among others by Steinmann and Eck [37]. The utilized dynamic RSS model is adapted from Dusek and Hofmann [12,13]. Due to the direct correlation between pressure and temperature in vapour-liquid equilibrium, an additional variable besides pressure and temperature is required to fully characterize the state of the system, such as specific enthalpy.

Mass and energy balances are formulated for the combination of the two phases, treating both phases as one fluidic mixture. The implemented governing equations are:

$$\text{energy eq.}: m\frac{dh_{\text{RSS}}}{dt} = \dot{m}_{\text{in}}\left(h_{\text{in}} - h_{\text{RSS}}\right) + \dot{m}_{\text{out}}\left(h_{\text{out}} - h_{\text{RSS}}\right) + \dot{Q} + V\frac{dp_{\text{RSS}}}{dt} \tag{1}$$

$$\text{continuity eq.}: V\frac{d\rho_{\text{RSS}}}{dt} = \dot{m}_{\text{in}} + \dot{m}_{\text{out}} \tag{2}$$

with

$$\text{total heat flow:}\quad \dot{Q} = \dot{Q}_{\text{RSS2PCM}} + \dot{Q}_{\text{RSS,losses}} \tag{3}$$

$$\text{vapour mass fraction:}\quad x_{\text{RSS}} = \frac{m_{\text{V}}}{m_{\text{V}} + m_{\text{L}}} \tag{4}$$

$$\text{mixing law:}\quad h_{\text{RSS}} = x_{\text{RSS}}h_{\text{V}} + (1 - x_{\text{RSS}})h_{\text{L}} \tag{5}$$

Injected and extracted water, steam and heat flows are considered therein. The variables m, $\dot{m}$, h_{RSS} and ρ_{RSS} refer to the mass, mass flow, specific enthalpy, and density of an equivalent water-steam mixture. The pressure p_{RSS} is assumed to be the same for both phases. The volume V and the heat flow $\dot{Q}$ refer to the overall RSS model and are not further subdivided in these balance equations. The indices L and V stands for the liquid and vapour phase, respectively.

The following simplifying assumptions are made:

- Potential and kinetic energies are negligible.
- The properties of the outgoing fluid (extracted steam) are those of the pure vapour phase.
- The material properties are obtained using the steam table implementation “CoolProp”, see Bell et al. [4].
- Heat conduction in the circumferential direction of the RSS steel shell is neglected.

The RSS can be charged and discharged with steam, or the filling level can be controlled by feedwater ($\dot{m}_{\text{in}}$ & $\dot{m}_{\text{out}}$ with h_{in} & h_{out}, respectively). $\dot{Q}$ is composed of the heat losses to the environment and the heat flow to the attached PCM cells (3).

2.2. Phase change material

A detailed multi-phase thermodynamic model including melting/solidification, heat conduction, and natural convection in two dimensions is considered for the PCM, developed and thoroughly documented in Ref. [25]. The PCM model underlies the basic conservation laws of mass, momentum and energy. In order to simplify modeling to the significant occurring phenomena, the following assumptions are made:

- Heat transfer is driven by conduction and natural convection.
- Material properties are constant in each phase but they can take different values for the liquid and solid phases.
- Phase change is modeled by means of the apparent heat capacity method (see, for example Comini et al. [10]), meaning that the phase transition takes place in a small temperature region $T \in [T_{\text{m}} - \varepsilon,\ T_{\text{m}} + \varepsilon]$defined by the melting temperature and mushy region parameter ε.
- Isothermal phase change, although inherently not representable, can be modeled by assuming a small mushy region parameter ε and careful consideration of numerical setup of time step and mesh size [41].
- The phase ratio only depends on T (no temperature hysteresis, no dynamics, no rate dependency, no subcooling).
- No relevant surface effects and dentrite growth occur.
- Density in the liquid phase is assumed constant except for the buoyancy term (Boussinesque approximation), and the only body force arises due to the gravitational acceleration in vertical direction.
- The depth of the rectangular enclosure in z-direction, which is in direction of the RSS cylinder axis, is assumed large enough for wall boundary layer effects to be negligible, hence the problem is reduced to two dimensions (no heat flow or convection in z-direction).

The governing equations within the framework of these assumptions are the energy Eq. (6), continuity Eq. (7) and Navier–Stokes Eqs. (8) and are given as follows:

$$\rho_{\text{PCM}}c\frac{\partial T}{\partial t} = k_{\text{PCM}}\nabla\cdot\left(\nabla T\right) - \rho_{\text{PCM}}c\nabla\left(T\cdot\boldsymbol{u}\right) \tag{6}$$

$$\nabla\cdot\boldsymbol{u} = 0 \tag{7}$$

$$\rho_{\text{PCM}}\left(\frac{\partial\boldsymbol{u}}{\partial t} + \left(\boldsymbol{u}\cdot\nabla\right)\boldsymbol{u}\right) - \mu\nabla\cdot(\nabla\boldsymbol{u}) + \nabla p_{\text{PCM}} = \boldsymbol{f} \tag{8}$$

Therein, the temperature field $T(x, y, t)$ is treated as dependent variable in the energy Eq. (6), and the velocity field $\boldsymbol{u} = [u, v]^T$ with spatial components $u(x, y, t)$ and $v(x, y, t)$ is treated as dependent variable in the Navier–Stokes Eq. (8), see Ref. [9]. The symbols ρ_{PCM}, c, k and μ denote the parameters density, apparent heat capacity

$$c = \begin{cases} c_{\text{S}} & \text{if: } T_{\text{m}} - \varepsilon > T \\ \frac{\Delta l_{\text{m}} + c_{\text{S}}\cdot(T_{\text{m}}+\varepsilon-T) + c_{\text{L}}\cdot(T-(T_{\text{m}}+\varepsilon))}{2\varepsilon} & \text{if: } \begin{matrix} T_{\text{m}} - \varepsilon \le T \\ T \le T_{\text{m}} + \varepsilon \end{matrix} \\ c_{\text{L}} & \text{if: } T > T_{\text{m}} + \varepsilon \end{cases}, \tag{9}$$

heat conductivity and dynamic viscosity, respectively. The force density $\boldsymbol{f}$ formulates the buoyancy force

$$\boldsymbol{f} = \rho_{\text{PCM}}\boldsymbol{g} \cong \rho_0\boldsymbol{g}(1 - \beta(T - T_{\text{ref}})), \tag{10}$$

which is calculated via the Boussinesq approximation as given by Huang et al. [21] by the volumetric thermal expansion coefficient β, the constant (reference) density ρ_0, a reference temperature T_{ref}, and the gravitational standard acceleration vector $\boldsymbol{g}$, $\boldsymbol{g} = -g\begin{bmatrix} cos(\Phi) \\ sin(\Phi) \end{bmatrix}$ with $g = 9.81\ \text{m/s}^2$.

Table 1
Heat Transfer Coefficient α.

Mode	Temperature	Phase	HTC α of	HTC $\frac{\alpha}{\mathrm{Wm^{-2}K^{-1}}}$
charging	$T_{\mathrm{wall}} < T_{\mathrm{RSS}}$	vapour	condensing steam	5000
charging	$T_{\mathrm{wall}} < T_{\mathrm{RSS}}$	liquid	liquid water	700
discharging	$T_{\mathrm{wall}} > T_{\mathrm{RSS}}$	vapour	dry steam	10
discharging	$T_{\mathrm{wall}} > T_{\mathrm{RSS}}$	liquid	boiling water	1000

3. Co-simulation model and implementation

Based on the fundamental equations outlined above, this section details the numeric implementations of the RSS and PCM subsystem dynamic simulation models. Then the co-simulation coupling concept, correction and reduction measures, and the implementation are presented.

3.1. RSS model

The RSS model's underlying differential Eqs. (1) and (2) are represented via an implicit descriptor state-space form with an augmented state vector $\boldsymbol{x}$, an input vector $\boldsymbol{w}$ and a mass matrix $\boldsymbol{M}(\boldsymbol{x})$ ((11)–(13)), adapted from Dusek and Hofmann [12,13]. Given the inputs $\boldsymbol{w}(t)$ and the initial state $\boldsymbol{x}(t = t_0)$, the problem can be solved via the solver `ode15i` in MATLAB®. The state vector consists of the enthalpy of water-steam mixture h_{RSS}, pressure p_{RSS}, enthalpy of the vapour phase h_{V}, enthalpy of the liquid phase h_{L}, heat flow losses $\dot{Q}_{\mathrm{RSS,losses}}$, temperature T_{RSS}, density of the water-steam mixture ρ_{RSS}, density of the vapour phase ρ_{V}, density of the liquid phase ρ_{L}, mass fraction of the vapour phase x_{RSS}, and mass of the water-steam mixture m_{RSS}. The input vector is composed of the mass flows $\dot{m}_{\mathrm{in}}$, $\dot{m}_{\mathrm{out}}$ and enthalpies h_{in}, h_{out} of the water-steam mixture flows (in and out), the total heat flow to PCM sectors $\dot{Q}_{\mathrm{RSS2PCM}}$ and the environment temperature T_{env}.

To determine these 11 states, 2 balance equations and polynomials from material laws are utilized.

$$\text{descriptor system:}\quad \boldsymbol{M}(\boldsymbol{x})\dot{\boldsymbol{x}} = \boldsymbol{f}(\boldsymbol{x}, \boldsymbol{w}) \tag{11}$$

$$\text{state vector:}\quad \boldsymbol{x} = [h_{\mathrm{RSS}}, p_{\mathrm{RSS}}, h_{\mathrm{V}}, h_{\mathrm{L}}, \dot{Q}_{\mathrm{RSS,losses}}, \tag{12}$$

$$T_{\mathrm{RSS}}, \rho_{\mathrm{RSS}}, \rho_{\mathrm{V}}, \rho_{\mathrm{L}}, x_{\mathrm{RSS}}, m_{\mathrm{RSS}}]^T$$

$$\text{input vector:}\quad \boldsymbol{w} = [\dot{m}_{\mathrm{in}}, h_{\mathrm{in}}, \dot{m}_{\mathrm{out}}, h_{\mathrm{out}}, \dot{Q}_{\mathrm{RSS2PCM}}, T_{\mathrm{env}}]^T \tag{13}$$

The RSS is coupled to the PCM cells and the surroundings via heat flows which result from the corresponding heat transfer coefficient α and the temperature difference. In the simulation, different heat transfer coefficients are used for the liquid and vapour phases, and furthermore it is tested whether the wall on the outside of the RSS (T_{wall}) is warmer or colder than the water/steam inside (T_{RSS}), distinguishing charging or discharging operating modes. Table 1 lists the four resulting heat transfer coefficients (HTC) α.

The heat flow thus depends on the position of the water level in the RSS, which is measured by the water/steam interface angle γ as shown in Fig. 3. The relationship between the volumetric liquid filling ratio F and γ is defined as follows:

$$\text{liquid filling ratio:}\quad F = \frac{V_{\mathrm{L}}}{V_{\mathrm{RSS}}} \tag{14}$$

$$\text{liquid volume:}\quad V_{\mathrm{L}} = \frac{m_{\mathrm{L}}}{\rho_{\mathrm{L}}} = \frac{(1 - x_{\mathrm{RSS}})m}{\rho_{\mathrm{L}}} \tag{15}$$

$$\text{interface angle.:}\quad 2\pi F = 2(\pi - \gamma) + sin(2\gamma) \tag{16}$$

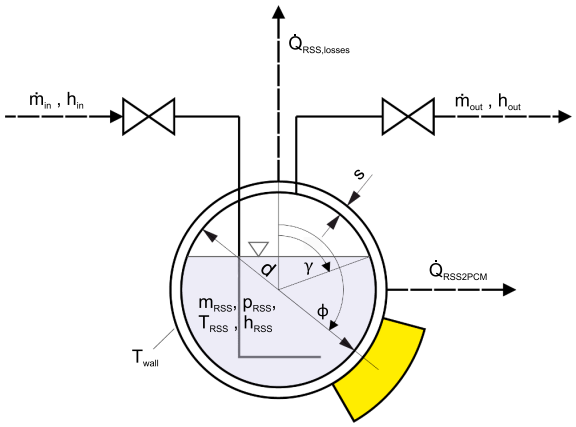

Fig. 3. Relevant variables and parameters of RSS.

3.2. PCM cell conduction/convection model

The PCM cell conduction/convection model summarized in the following was developed by Kasper [25] for a rectangular domain (single cell) and is adapted in this work for the purpose of PCM-RSS co-simulation. The model of the underlying work uses a finite element discretization to model the time-dependent energy equation and applies a finite difference scheme to solve the Navier–Stokes equations in each time step. The obtained velocity field is used for the next time step of the energy equation.

For a rectangular PCM cell in local coordinates (x, y), the modeled two-dimensional spatial domain $\mathcal{D}$ and its boundary $\partial\mathcal{D}$ are defined as shown in Fig. 4 and given as follows:

$$\begin{aligned}
\mathcal{D} &= \{0 \leqslant x \leqslant L_x,\ 0 \leqslant y \leqslant L_y\} \\
\partial\mathcal{D} &= \partial\mathcal{D}_1 \cup \partial\mathcal{D}_2 \cup \partial\mathcal{D}_3 \cup \partial\mathcal{D}_4 \\
\partial\mathcal{D}_1 &= \{x = L_x,\ y \in \mathcal{D}\} \\
\partial\mathcal{D}_2 &= \{x \in \mathcal{D},\ y = L_y\} \\
\partial\mathcal{D}_3 &= \{x = 0,\ y \in \mathcal{D}\} \\
\partial\mathcal{D}_4 &= \{x \in \mathcal{D},\ y = 0\}
\end{aligned} \tag{17}$$

As stated above, Eqs. (6)–(8) combined with the effective heat capacity (9) fully describe the considered behavior of the PCM. The geometry of the regarded PCM cavities, with aluminum fins oriented in the radial-axial plane of the RSS, suggests symmetry reduction of the simulation to single aluminum fin sections. Consequently, the symmetry boundaries, in this case chosen as upper and lower boundaries of the computational domain, are considered as adiabatic:

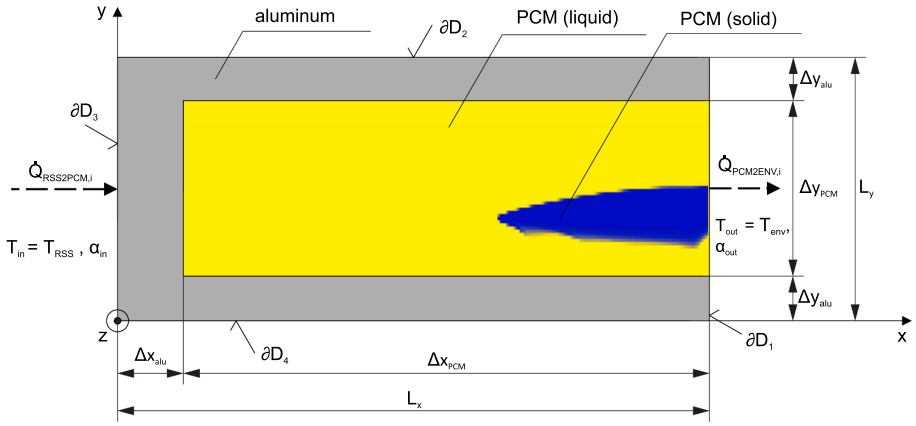

Fig. 4. PCM cell dimensions.

$$\boldsymbol{q}|_{\partial\mathcal{D}_2,\,\partial\mathcal{D}_4} = 0 \tag{18}$$

For the left and right boundaries, i.e. the inner and outer boundaries, type-3 boundary conditions, also known as Robin boundary conditions,

$$\boldsymbol{q}|_{\partial\mathcal{D}_3} = \alpha_{\text{in}}\cdot(T(x,y) - T_{\text{in}}), \tag{19}$$

$$\boldsymbol{q}|_{\partial\mathcal{D}_1} = \alpha_{\text{out}}\cdot(T(x,y) - T_{\text{out}}), \tag{20}$$

are prescribed, where α_{in}, α_{out} are heat transfer coefficients and T_{in}, T_{out} present boundary temperatures at the inner and outer wall surfaces, respectively.

Regarding the velocity field $\boldsymbol{u} = [u, v]^T$, no-slip boundary conditions are set for the domain boundaries,

$$\boldsymbol{u}|_{\partial\mathcal{D}} = 0, \tag{21}$$

as well as at in-domain phase and material boundaries. Furthermore, the velocity is set to zero if the PCM is solid:

$$\boldsymbol{u}|_{T\,<\,T_{\text{m}}-\varepsilon} = 0. \tag{22}$$

This is also done for any non-melting material in the computational domain [25].

3.2.1. Discretization of the energy equation

The energy Eq. (6) is discretised in space using a standard Galerkin finite element method. Four-noded bilinear rectangular elements are used to obtain the finite element representation

$$T = N\cdot\{T\}, \tag{23}$$

of the temperature field $T(x, y, t)$ and analogously for the velocity component fields $u(x, y, t)$, $v(x, y, t)$. In this form, $N = [N_1, N_2, N_3, ..., N_{non}]$ denotes the vector of spatial shape functions whose length is equal to the number of nodes, *non*, and the braces $\{\cdot\}$ denote an $(non \times 1)$ vector of element node point values.

Using this finite element representation and applying Galerkin's method of weighted residuals (see, for example, Pepper and Heinrich [30]) results in a system of ordinary differential equations

$$C\{\dot{T}\} + K\{T\} = R, \tag{24}$$

with the $(non \times non)$ system matrices C, K and the right-hand-side $(non \times 1)$ vector R. To compute these coefficients, the surface and volume integrals are split into the finite element domains. The integrals are then numerically solved applying two-point Gauss–Legendre quadrature and three-point Gauss–Lobatto quadrature for the convection terms. This higher-order quadrature rule was found to be more accurate because of the natural inclusion of boundary conditions and compatibility with the staggered-grid formulation of the Navier–Stokes equations [25].

Time integration is achieved by the backwards Euler method, using the backwards differential quotient

$$\left\{\frac{\partial T}{\partial t}\right\}_{n+1} = \{\dot{T}\}_{n+1} \doteq \frac{\{T\}_{n+1} - \{T\}_n}{\Delta t_{\text{PCM}}}, \tag{25}$$

as approximation of the time derivative of the temperature vector. This leads to the following implicit solution for $\{T\}_{n+1}$ at time level $n+1$ using the current temperature field $\{T\}_n$ at time level $t = n\Delta t_{\text{PCM}}$:

$$\begin{aligned}\{T\}_{n+1} = &\quad \{T\}_n + \Delta t_{\text{PCM}}\{\dot{T}\}_{n+1} = \\ &\{T\}_n + \Delta t_{\text{PCM}}(C + \Delta t_{\text{PCM}}\cdot K)^{-1}\cdot(R - K\{T\}_n)\end{aligned} \tag{26}$$

3.2.2. Solving the Navier–Stokes equation

The set of incompressible two-dimensional Navier–Stokes Eqs. (8) is treated separately from the heat transfer part of the model via a finite difference discretization based on a MATLAB® code available on the course homepage (`http://math.mit.edu/~gs/cse/`) of "Computational Science and Engineering" at the Massachusetts Institute of Technology. This open source code, created and documented by Seibold [34], was implemented and extended to meet specific requirements in Ref. [25]. The main numerical concept used therein is the fractional step method [26], which is applied to split the Navier–Stokes system into equations that are significantly simpler to work with. The solution update is then found by executing a three-step approach, as outlined in the following exemplary for velocity component u and the time steps $n \to n+1 (t \to t + \Delta t_{\text{PCM}})$:

1. Explicit time step for nonlinear convective acceleration terms, solve for u_*:

$$u_* - u_n - \Delta t_{\text{PCM}}\left(\frac{\partial u_n^2}{\partial x} + \frac{\partial u_n v_n}{\partial y}\right) = 0 \tag{27}$$

2. Implicit time step for linear viscosity terms, solve for u_{**}:

$$u_{**} - u_* = \Delta t_{\text{PCM}}\frac{\mu}{\rho_0}\left(\frac{\partial u_{**}}{\partial x^2} + \frac{\partial u_{**}}{\partial y^2}\right) + \Delta t_{\text{PCM}}\frac{f_x}{\rho_0} \tag{28}$$

3. Pressure correction step via projection method, solve for u_{n+1}:

$$u_{n+1} - u_{**} = -\frac{\Delta t_{\text{PCM}}}{\rho_0}\frac{\partial p_{n+1}}{\partial x} \tag{29}$$

The solution update for v are obtained analogously. The PCM pressure p_{n+1} is only given implicitly and can be obtained by solving the linear system

$$\Delta p_{n+1} = \frac{\rho_0}{\Delta t}\nabla \boldsymbol{u}_{**} \tag{30}$$

The pressure correction step is therefore implemented as follows:

(a) Compute the gradient $\nabla \boldsymbol{u}_{**}$

(b) Solve the Poisson equation $\Delta p_{n+1} = \frac{\rho_0}{\Delta t_{\mathrm{PCM}}}\nabla \boldsymbol{u}_{**}$ for p_{n+1}

(c) Compute the pressure gradient ∇p_{n+1}

(d) Update the velocity field $\boldsymbol{u}_{n+1} = \boldsymbol{u}_{**} - \frac{\Delta t_{PCM}}{\rho_0}\nabla p_{n+1}$

Homogenous Neumann boundary conditions are prescribed for the pressure p_{PCM} consistent with the no-slip boundary conditions of the velocity field.

Combining Eqs. (27)–(29) again yields the full Navier–Stokes Eqs. (8) for velocity component u. The spatial discretization via the finite-difference method is conducted using a staggered grid based on the finite element mesh, where the pressure p_{PCM} is defined in the element centers, u values are defined in the middle of the vertical element edges and the values of v are defined in the middle of the horizontal element edges, see Seibold [34] and Kasper [25].

3.3. Co-simulation architecture

The co-simulation model of the hybrid LHTES consists of many single PCM cells as well as an RSS and is assembled as shown in Fig. 2. In this arrangement, the RSS sub-model is located inside and is surrounded by PCM cells. The RSS and the PCM cell sub-models are coupled via the heat flow $\dot{Q}_{\mathrm{RSS2PCM}}$ (detailed in Section 3.3.1). With this coupling, each sub-model can be calculated separately during co-simulation. For this purpose, two different time steps are chosen to account for the different complexity of the sub-models. The RSS is computed on the major time step Δt_{RSS}, which is larger than the minor time step Δt_{PCM} of the PCM (see Fig. 5). The coupling variable heat flow $\dot{Q}_{\mathrm{RSS2PCM}}$ is integrated on minor time step level for the PCM sub-model, passed on to the RSS simulation, and then the major time step is evolved. Together with the incoming and outgoing enthalpy/mass flows, the new states of the RSS are calculated. If the maximum liquid filling ratio or pressure of the RSS is exceeded, the incoming flows are set to zero and the calculation is repeated.

This co-simulation structure creates a simplified coupling between the individual systems. It is based on the assumption that the RSS calculated on the major time step does not significantly change during minor time step simulation. Therefore, it is assumed that the temperature and the filling level of the RSS remain constant within a major time step, while the PCM sub-models calculate the connecting heat flows at the minor time step. This assumption is justified if the capacity of the RSS at the major time step level Δt_{RSS} is much larger than that of the PCM cells at the minor time step level Δt_{PCM}. With such configuration, the calculation of the individual PCM cells can be carried out in parallel, thus significantly saving computation time.

At the beginning of a co-simulation, each sub-model is defined based on its geometry, material properties and initial conditions. Thereby, each individual PCM sub-model represents the thermodynamic behavior of a single PCM cell at the circumference of the RSS. In the investigated hybrid LHTES design, hundreds of such cells are attached along the RSS outer shell. Simulating each cell with a dedicated conduction/convection PCM sub-model would vastly increase computational demand of the co-simulation. It is thus desirable to efficiently aggregate the PCM cell behavior into fewer PCM sectors. Each such sector represents the thermodynamics of several similar cells having the same attributes like heat transfer coefficient or angle-dependent convection (see Fig. 2) resulting in the same temperature $T_{\mathrm{PCM},j}$ of all PCM cells in the PCM sector j, with $j \in \{1, \ldots, n_{\mathrm{sect}}\}$. This reduces computational effort of the entire co-simulation significantly with no or little impact on its overall accuracy. To aggregate the PCM cells surrounding the RSS to PCM sectors, an optimization-based criterion is developed in Section 3.3.2. Each PCM sector j is arranged at the circumference of the RSS covering an angular range $[\Phi_{j,\min}, \Phi_{j,\max}]$. A representative cell of the sector is chosen to describe the melting behavior of all cells in the sector.

3.3.1. Coupling of the RSS and PCM cells via heat flows

To compute the coupling heat flow $\dot{Q}_{\mathrm{RSS2PCM}}$, the water-steam interface angle and the heat transfer coefficients (HTC) for the liquid (L) and vapour (V) phase inside the RSS (Section 3.1) are determined at the beginning of each major time step. The HTC are then assigned to the PCM sectors according to their positions at the RSS:

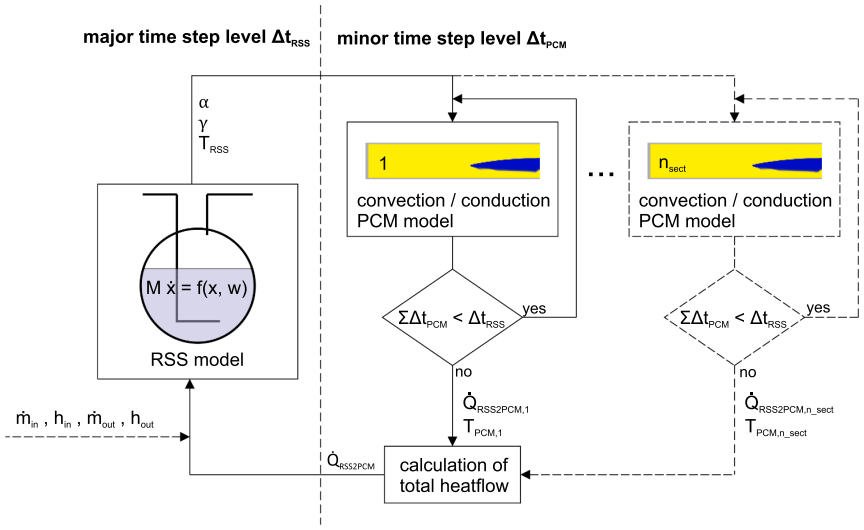

Fig. 5. Coupling mechanism of the hybrid LHTES.

$$\alpha_j = \begin{cases} \alpha_V & \text{if: } \gamma \geqslant \Phi_{j,\max} \\ \alpha_V \frac{\gamma - \Phi_{j,\min}}{\Delta\Phi_j} + \alpha_L \frac{\Phi_{j,\max} - \gamma}{\Delta\Phi_j} & \\ \alpha_L & \text{if: } \gamma \leqslant \Phi_{j,\min} \end{cases} \tag{31}$$

with $\Delta\Phi_j = \Phi_{j,\max} - \Phi_{j,\min}$

Together with the thermal conductivity of the steel shell k_{steel}, an effective HTC, α_{in}, is calculated according to (32). The RSS temperature and the HTC α_{in} are passed on to the PCM sub-model simulation (33). Similarly the losses from the PCM through isolation to the environment are calculated.

With these HTC and the RSS temperature, the PCM sub-models are computed at minor time step level (Fig. 5, right). The total heat flow to the PCM is determined and passed to the RSS simulation at major time step level (Fig. 5, left). For the areas on the RSS not covered with PCM, heat loss is calculated with respect to the environment.

Since there are small deviations between the enthalpy change in the PCM model and the heat flows calculated through temperature change, these must be corrected in order to fulfill the conservation of total energy in the hybrid LHTES. The PCM model itself does not precisely fulfill the energy conservation as can be expected of the underlying FEM code, which is not perfectly consistent with the balance equations due to implementation of the apparent heat capacity method. To ensure energy conservation of the total co-simulation model, the heat flow calculated by the temperature difference between the RSS and PCM is compared with the enthalpy increase of the PCM sectors and corrected accordingly (34). The correction via the enthalpy change of the PCM sectors is necessary to ensure that the system coupling obeys conservation of energy. This measure is considered acceptable because loss heat flow from the PCM to the environment is small compared to the coupling heat flow between the PCM and the RSS and thus the majority of the error can be eliminated.

$$\text{effective HTC:} \quad \alpha_{\text{in},j} = \frac{1}{d\left(\frac{1}{\alpha_j d} + \frac{1}{2k_{\text{steel}}} log\left(\frac{d+2s}{d}\right)\right)} \tag{32}$$

$$\text{coupling:} \quad \dot{Q}_{\text{RSS2PCM},j} = \alpha_{\text{in},j}(T_{\text{RSS}} - T_{\text{wall}}) \tag{33}$$

$$\text{with correction:} \quad \dot{Q}_{\text{RSS2PCM,corr},j} = H_{\text{PCM}}(t + \Delta t_{\text{RSS}}) - H_{\text{PCM}}(t) - \dot{Q}_{\text{PCM,losses}} \tag{34}$$

In the following, only the corrected heat flow is applied.

3.3.2. Optimal PCM cell aggregation

The angular position of an attached PCM cell determines its individual thermodynamic behavior, essentially because of two effects:

- First, convection effects are determined by the direction of the gravitational forces (hence the cell's installation angle) and the location of the heated boundary.
- Second, the heat transfer properties significantly depend on whether liquid water or steam is in contact with the RSS wall at the PCM cell attachment location.

Given the heat flow exchanged between the RSS and the PCM cell i is $\dot{Q}_{\text{RSS2PCM},i}(t)$, with $i \in \{1, \ldots, n_{\text{cell}}\}$, the total heat flow transferred from all PCM cells into the RSS is

$$\dot{Q}_{\text{RSS2PCM}}(t) = -\sum_{i=1}^{n_{\text{cell}}} \dot{Q}_{\text{RSS2PCM},i}(t). \tag{35}$$

Since each PCM cell is represented by an individual sub-model, n_{cell} sub-models would have to be calculated. However, this is highly computationally expensive. Therefore, the cells at the circumference of the RSS are grouped into n_{sect} sectors. The cells, which are reduced into one sector j, with $j \in \{1, \ldots, n_{\text{sect}}\}$, are thereby modeled as having the same properties and boundary conditions and therefore the same melting/solidification behavior.

The error between the heat flow of the complete model $\dot{Q}_{\text{RSS2PCM}}(t)$ (35) and the heat flow estimated from the PCM sectors,

$$\hat{\dot{Q}}_{\text{RSS2PCM}}(t) = -\sum_{j=1}^{n_{\text{sect}}} \dot{Q}_{\text{RSS2PCM},j}(t), \tag{36}$$

should be minimized by optimally choosing the aggregation of the cells into PCM sectors.

3.4. Aggregation criteria to improve co-simulation efficiency

To minimize the aggregated heat flow error between the heat flows of the high-resolution model (35) and the reduced model with PCM cells represented by few PCM sectors (36), a non-uniform resolution of PCM sectors should be selected, see Section 4.2 and 4.3. In order to find a reasonable number and an optimal distribution of the PCM sectors along the circumference, an objective function J is defined and will be minimized.

The objective function (41) is based on the difference between the estimated enthalpy $\widehat{H}(\Phi_j, t)$ by the representative cell of sector j at $\Phi = \Phi_j$, and the actual enthalpy $H(\Phi, t)$ obtained by the cells in sector j, with $\Phi \in [\Phi_{j,\min}, \Phi_{j,\max}]$. The objective function J considers n_Φ different PCM orientation angles and is evaluated at n_t points in time. The optimization problem

$$(\widetilde{\Phi}, \widetilde{\Phi}_{\min}, \widetilde{\Phi}_{\max}) := arg\left(\min_{\mathbf{\Phi}, \mathbf{\Phi}_{\min}, \mathbf{\Phi}_{\max}} J\left(\mathbf{\Phi}, \mathbf{\Phi}_{\min}, \mathbf{\Phi}_{\max}\right)\right) \tag{37}$$

$$\mathbf{\Phi}^T = [\Phi_1, \ldots, \Phi_{n_{\text{sect}}}] \tag{38}$$

$$\mathbf{\Phi}_{\min}^T = [\Phi_{1,\min}, \ldots, \Phi_{n_{\text{sect}},\min}] \tag{39}$$

$$\mathbf{\Phi}_{\max}^T = [\Phi_{1,\max}, \ldots, \Phi_{n_{\text{sect}},\max}] \tag{40}$$

with

$$J = \sqrt{\frac{1}{n_t}\sum_{k=1}^{n_t}\left[\frac{1}{\overline{H}(t_k)}\sqrt{\sum_{j=1}^{n_{\text{sect}}}\int_{\Phi_{j,\min}}^{\Phi_{j,\max}}\left(\frac{\widehat{H}(\Phi_j, t_k) - H(\Phi, t_k)}{\Delta\Phi_{\text{cell}}}\right)^2 d\Phi}\right]^2}, \tag{41}$$

$$\overline{H}(t_k) = \sum_{j=1}^{n_{\text{sect}}}\int_{\Phi_{j,\min}}^{\Phi_{j,\max}} \frac{H(\Phi, t_k)}{\Delta\Phi_{\text{cell}}} d\Phi, \tag{42}$$

$$\Delta\Phi_{\text{cell}} = \frac{2L_y}{d}, \tag{43}$$

$$\text{s. t.} \quad \Phi_{j,\min} \leqslant \Phi_j \leqslant \Phi_{j,\max} \quad j = 1, \ldots, n_{\text{sect}}, \tag{44}$$

$$\Phi_{j,\max} = \Phi_{j+1,\min} \quad j = 1, \ldots, (n_{\text{sect}} - 1), \tag{45}$$

$$\Phi_{1,\min} = \Phi_{\min}, \tag{46}$$

$$\Phi_{n_{\text{sect}},\max} = \Phi_{\max}, \tag{47}$$

is solved in MATLAB® using `fmincon` and greedy initial heuristics to yield an optimized partitioning, $(\widetilde{\Phi}, \widetilde{\Phi}_{\min}, \widetilde{\Phi}_{\max})$, see Fig. 8. In order to render the error between the two aggregation criteria (convection and operation state) comparable, the normalized root mean square error (NRMSE) is used as measure in 41. To do so, the RMSE is scaled with the average enthalpy at a given time $\overline{H}(t_k)$ (42). The angular distance occupied by one PCM cell $\Delta\Phi_{\text{cell}}$ is defined in (43).

The optimization procedure uses data from simulations and is performed in Section 4.4.

4. Simulation studies

This section first addresses the validation of the sub-models and the overall model. The significant effects in co-simulation are highlighted and the implementation of the aggregation criteria is described. Its efficiency is validated by aggregated settings with a high-resolution reference simulation. The functionality of the hybrid LHTES co-simulation model is demonstrated with step-shaped load profiles.

4.1. Basic model validation

The RSS and PCM models adapted were developed and validated by Dusek and Hofmann [13] and Kasper [25] in their respective works.

4.1.1. RSS model

The RSS model was validated using the data from the Austrian steel manufacturer voestalpine Stahl Donawitz GmbH [13]. In their industrial process, a steam generator is connected to three parallel RSS vessels. The RSS vessels are linked and are operated at one common pressure. The validation case shown Dusek and Hofmann [13] has been successfully reproduced and shows good agreement with the measured process data.

4.1.2. PCM cell model

The PCM cell model was validated by experimental data provided by Gau and Viskanta [17], who investigated the melting and solidification behavior of gallium in a rectangular enclosure. Very good agreement of the simulated melted volume fraction compared to this data was found. A comparison of simulated and measured melting fronts of this typical phase change test case at different times is given in Fig. 6a. The minor differences between the experimental data and the numerical results of the implemented model might originate from three-dimensional liquid PCM flow characteristics or slight variations in PCM properties. A further validation approach of the here applied PCM cell model was pursued by Kasper [25], comparing numerical results of melting in an rectangular aluminium finned LHTES to those of the CFD software *ANSYS Fluent*, leading to matching results.

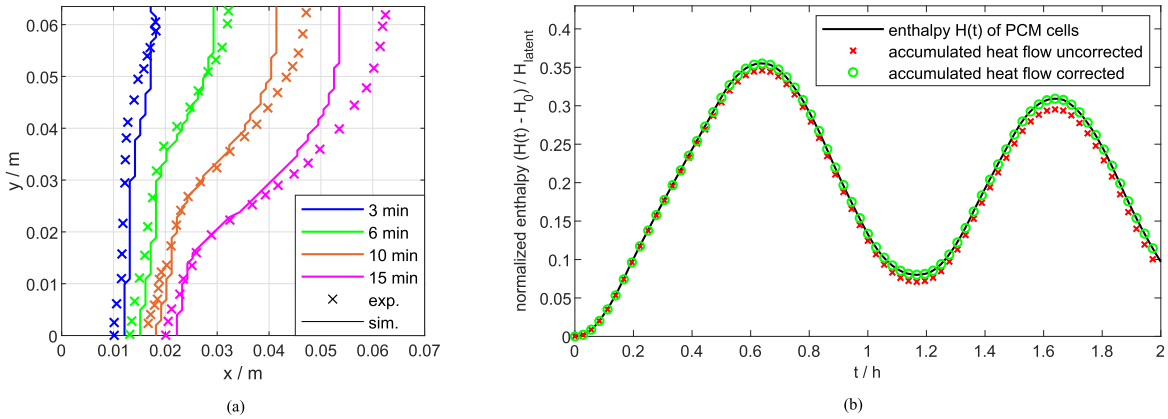

Fig. 6. Validation of the sub-models - simulated (sim.) and experimental (exp.) melting front at different times of the PCM sub-model (a) and the energy conservation balance of the co-simulation model (b).

We consider the small deviations observed during validation as insignificant in the scope of application in this work.

4.1.3. Co-simulation model

The co-simulation model is comprised of the two validated sub-models. For the validation of the co-simulation model, the total energy balance is investigated. Fig. 6b shows the enthalpy change of the PCM sectors and the acccumulated heat flows over time, both scaled with the latent storage enthalpy. With the correction of the coupling heat flow, the conservation of energy across the co-simulation coupling is established. An increasing error would occur if considering only an uncorrected heat flow coupling, see Section 3.3.1.

The coupling of the two sub-models is based on the assumption of an effective HTC as a result of several serial component HTCs, see (31). The implemented boundary conditions of the sub-models are consistent with each other and the resulting heat flow coupling due to temperature difference. An experimental validation to substantiate the assumptions is currently planned.

4.1.4. Scope of validity

Based on the assumptions for the sub-models and the co-simulation model, the scope of validity is characterized as follows:

- Due to the equilibrium model used for the RSS, no conclusions can be drawn about fast storage transients. However, these transients are not relevant for hybrid storage systems with LHTES in the investigated operating regimes.
- Phase transition in the PCM takes place in a small temperature region (mushy region) around the melting temperature with no hysteresis or dynamics.
- Due to the simplified coupling structure (the temperature in the RSS remains constant during a major time step), the capacity of the RSS must be much larger than that of the PCM cells attached.
- In order to eliminate the majority of error by heat flow correction (34), the heat flow loss $\dot{Q}_{\mathrm{PCM,losses}}$ is assumed to be small compared to the coupling heat flow $\dot{Q}_{\mathrm{RSS2PCM}}$ between the RSS and PCM containers.

4.2. Angular dependency of convection effects

The dependence of the thermodynamic behavior of the PCM melting process on the orientation of the heat conducting structure and the PCM enclosure is known in literature (see, for example, Ref. [23,24,47]). To demonstrate and assess this angular effect during melting and solidification for the co-simulation model, several simulations were conducted using the presented PCM cell model and settings described in Section 4.4.1. Fig. 7a shows the angular dependency for different PCM cell orientations during a complete melting/solidification process, with Φ defined as illustrated in Fig. 3. The melting process is significantly dependent on the angle, with convection having a strong influence, especially for PCM cell orientation angles $\Phi < 120°$. For angles $\Phi > 120°$, the convection effects become small for this cell geometry and the melting behavior corresponds to that of a cell with pure heat conduction.

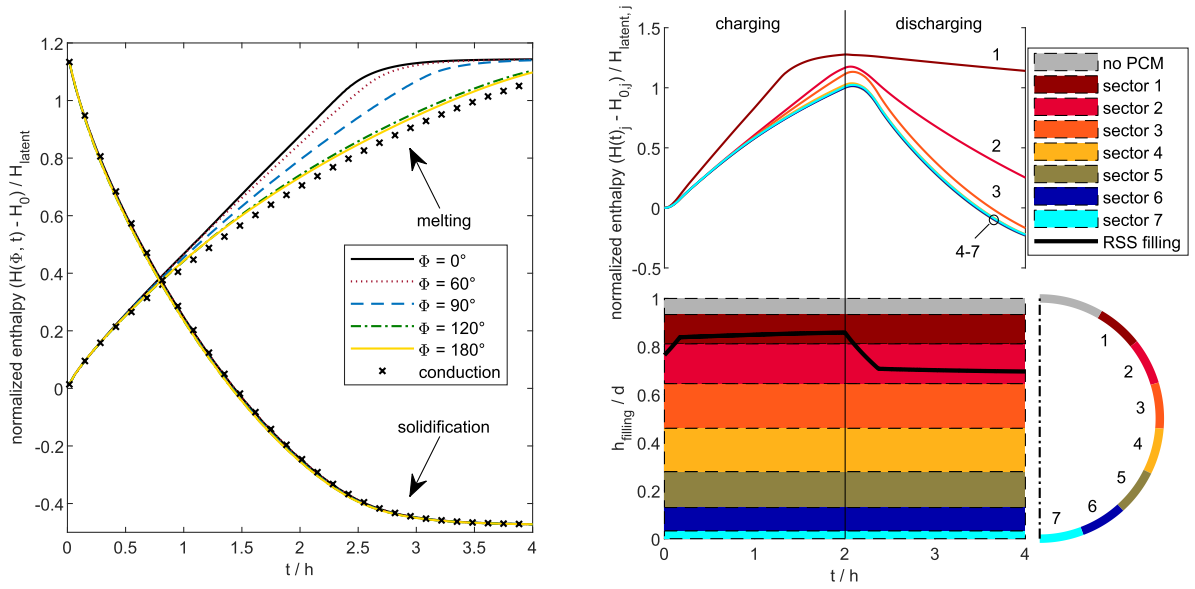

Fig. 7. Angular dependency of convection effects in a PCM cell during melting and solidification (a) and heat transfer dependency on operation state (b).

During the solidification process, natural convection was found negligible regardless the angle Φ, and the solidifying PCM is accurately characterized by heat conduction alone. This is plausible due to the fact that solidification first occurs at the heat-conducting aluminum structure which inhibits further heat transfer and thus the build up of significant temperature/density gradients in the liquid phase. A similar behavior during solidification of PCM was observed by Pourakabar and Darzi [31].

4.3. Heat transfer dependency on operation state

When charging (discharging) an RSS via steam injection (extraction), the water level rises (falls), respectively. The effective HTC for a particular cell varies significantly depending on the local aggregate state of water inside the RSS at the PCM cell's mounting position, as well as on the operation mode, see Table 1).

Fig. 7b depicts a charging/discharging cycle of seven equidistant distributed sectors. The filling level over time as well as the position of the PCM sectors at the RSS are displayed. The enthalpy of each PCM sector is shown thereabove. During the charging process, the filling level rises and a very high HTC applies to cells in contact with condensing steam as well as a moderate one to cells in contact with water. During discharging of the RSS, the filling level sinks and a moderate HTC is valid for cells in contact with water, but a very low HTC value holds for cells in contact with dry steam. Therefore cells in contact with steam can be charged very well but almost not discharged anymore (PCM sectors 1 and 2). Accordingly, the coverage of the RSS with PCM cells above the operation water level would probably not be economically attractive, unless alternative methods to increase the HTC (e.g. active water spraying) are implemented.

4.4. Aggregation

In order to apply the formulated aggregation criteria in 3.4, it is necessary to perform simulations thus collect data for the optimization approach.

4.4.1. Aggregation due to convection

To evaluate the heat flows associated with the different cell orientations due to convection effects, simulation data of a single cell with different orientation angles Φ are collected, $\Phi \in \{0°, ...,180°\}$. The enthalpy of angle Φ and time t is used to find the optimal size and location of the sectors. Furthermore, one cell for each sector is determined, identified by $\tilde{\Phi}_j$, which best represents the thermodynamic behavior of the whole sector (representative cell).

To collect the simulation data, one PCM cell is heated for four hours using the type-3 boundary conditions with 230°C and a heat transfer coefficient (HTC) α of 700 $Wm^{-2}\,K^{-1}$. The initial temperature in the cell is set to 218°C.

The enthalpy at each half hour is evaluated and used for the optimization resulting in eight different scenarios. The enthalpy as a function of Φ is interpolated between the measured values for Φ via splines, see Fig. 8a.

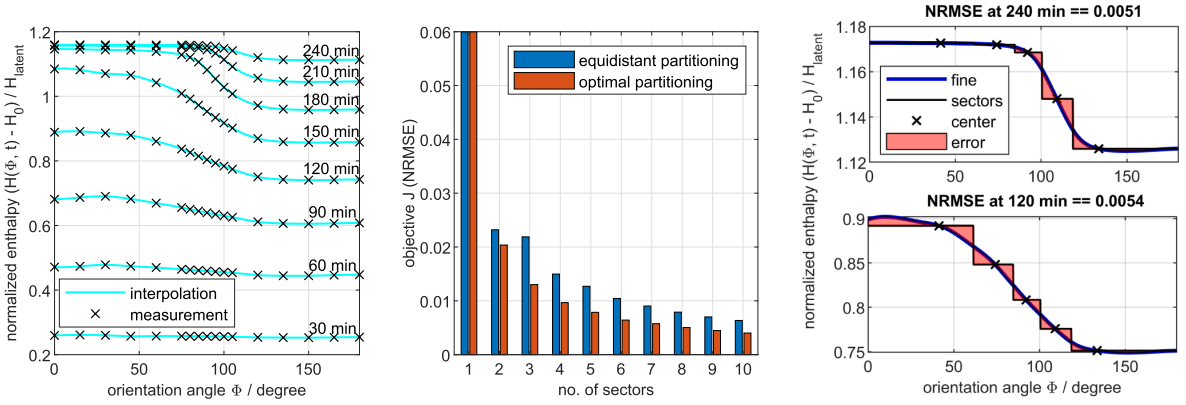

Fig. 8. PCM cell aggregation at the entire circumference due to convection, see Section 4.4.1 - enthalpy at given times for cell orientation angles $\Phi \in \{0°, ...,180°\}$ (a), the objective function J evaluated for various numbers of sectors and equidistant or optimal sector partitioning (b) and the error between five optimally chosen sectors with their representative cells (centers) and a high-resolution case (fine) with cells calculated across the entire range o.f Φ (c).

The optimization (37) is performed to find the optimal sector sizes, locations and representative cells. As seen in Fig. 8b, the NRMSE in the optimized aggregation settings are consistently and significantly lower than in an equidistant partitioning. In Fig. 8c the enthalpy over Φ of five optimally chosen sectors with their representative cells is compared with a high-resolution case.

considered and evaluated in simulations. One case treats a stationary HTC to simulate a water-steam interface which divides a sector of eight vertically arranged PCM cells into two equal halves. In the other case, a dynamic HTC is examined that simulates a linearly decreasing water level over the complete range of the PCM sector, see Fig. 9a.

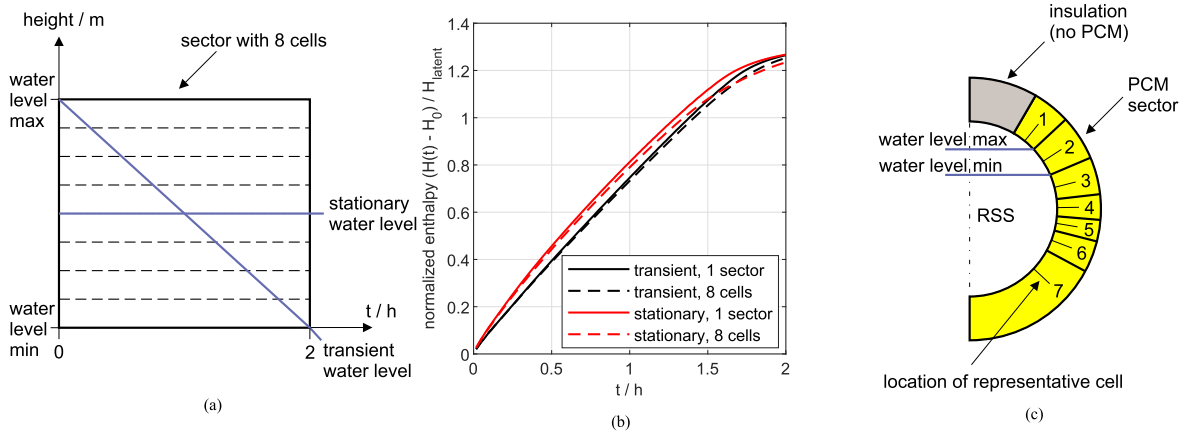

Fig. 9. PCM cell aggregation due to state of charge with the simulation setting for a water steam interface in between a sector, see Section 4.4.2. The water level varies with time (transient HTC) or permanently divides the sector into two equal halves (stationary HTC) (a). The corresponding enthalpy curves are plotted over time with an optimal (8 cells) and reduced resolution (one representative cell for the entire sector) (b). Based on the combined optimum from both criteria the distribution of the sectors and their representative cells are chosen (c).

4.4.2. Aggregation due to operation state

During hybrid LHTES operation, the water level changes and a weighted HTC (31) is applied to the representative cell of the sector. This results in an approximate error because all cells in the sector are considered as having the same thermodynamic behavior as the representative cell.

The HTC is linearly included in the heat flow between the RSS and PCM sectors (33). Accordingly, when performing a single simulation step on minor time step level, no error occurs by weighting the HTC and integrating the heat flow across the entire sector. However, since heat flow, HTC and temperature field in the individual cells are coupled, an error occurs over multiple simulation steps due to the changing PCM cell states and results in a nonlinear behavior.

To assess the influence of the varying HTC, two operating states are

In these simulations the HTC of water and steam is set to 400 and 800 $Wm^{-2}K^{-1}$ respectively. The fluid temperature is 240°C and the initial temperature of the cells 218°C. The total simulation time is two hours.

Fig. 9b shows no significant differences between the different resolution levels for the decreasing water level (transient operation). For the simulation with a stationary water level, an error occurs due to the aggregation of the PCM cells to one sector.

4.4.3. Combination of aggregation criteria for a global optimum

The first aggregation criterion achieves an optimal sector partitioning that accounts for the angular dependency of the convection effect by minimizing the objective function (41). The second aggregation criterion considers the operation state. Therefore, sectors should be

Table 2
Optimal sector dimensions.

Sector j	No. cells	$\Phi_{j,\min}$	$\Phi_{j,\max}$	$\Phi_{j,\text{representative}}$
1	19	30. 0°	47. 6°	39. 2°
2	21	47. 6°	67. 0°	57. 4°
3	17	67. 0°	83. 5°	75. 7°
4	12	83. 5°	94. 6°	89. 1°
5	10	94. 6°	104. 3°	99. 4°
6	15	104. 3°	118. 1°	110. 9°
7	66	118. 1°	180. 0°	133. 0°

Table 3
Material properties of hybrid LHTES.

Property	Steel	Alu.	PCM	Insu.
density $\frac{\rho}{\text{kgm}^{-3}}$	7800	2700	2050 (S) 1959 (L)	80
spec. heat capacity $\frac{c}{\text{J(kgK)}^{-1}}$	540	910	1350 (S) 1492 (L)	840
heat con- ductivity $\frac{k}{\text{W(mK)}^{-1}}$	51	237	0.457 (S) 0.435 (L)	0.062
melting temperature $\frac{T_m}{°C}$	–	–	220	–
mushy region parameter $\frac{\varepsilon}{°C}$	–	–	±0.5	–
spec. latent heat $\frac{h_{\text{latent}}}{\text{kJ(kg)}^{-1}}$	–	–	108	–
thermal expan- sion coefficient $\frac{\beta}{(\text{K})^{-1}}$	–	–	$3.5 \cdot 10^{-4}$	–
dynamic viscosity $\frac{\mu}{\text{Ns(m)}^{-2}}$	–	–	$5.8 \cdot 10^{-4}$	–

Table 4
Geometry of the hybrid LHTES.

Dimension	Part	Value
inner diameter d	RSS	3.1 m
wall thickness s	RSS	0.05 m
length l	RSS	10.7 m
length L_x	PCM	0.12 m
width L_y	PCM	0.025 m
length of cavity Δx_{PCM}	PCM	0.118 m
width of cavity Δy_{PCM}	PCM	0.023 m
insulation layer s_{iso}	RSS & PCM	0.2 m
outer panel s_o	RSS & PCM	0.001 m

chosen in such a way that a stationary water-steam zone is represented by different sectors but transient changes of the HTC do not have to be considered for PCM cell aggregation. The following procedure for a combination of the aggregation criteria is proposed.

1. To estimate the range of the varying water level (minimum and maximum) the RSS without PCM cells is simulated using the desired load profile.
2. Division of the circumference of the RSS occupied by PCM cells into three areas to satisfy the second aggregation criterion: one area exclusively in the steam and water zone respectively (stationary HTC) and one area in the zone where the water level varies (transient HTC).
3. The optimal sector partitioning is determined based on the first aggregation criterion for all three areas separately using the objective function (41) and comparing the resulting NRMSE of each area.

Fig. 9c shows the optimal resolution of sectors and the location of their representative cells for the load profiles A, B and C in Section 4.5. In the upper area of the RSS, for $\Phi < 30°$, no PCM cells are installed and an insulation is attached there. A total of 7 PCM sectors are used to reproduce the behavior of 160 cells. Table 2 lists the dimensions of the sectors.

4.5. Co-simulation studies to demonstrate efficiency and performance

Simulation studies with three load profiles (A, B and C) are carried out to show the performance of the co-simulation model. Case A serves as a base case to show the functionality of the aggregation criterion. Then the reduced co-simulation model is applied to analyze the three cases and compare the simulation results with each other.

4.5.1. Geometry and material

The hybrid LHTES is composed of a cylindric RSS, PCM cells, an insulation layer and an outer panel with the dimensions given in Table 4. For the angular position Φ, $\Phi \in [30°, 330°]$, the RSS is equipped with PCM cells at the circumference. The outside of the PCM cells as well as the upper sixth of the RSS, on which no PCM cells are attached, are covered with an insulating layer. Outside each insulation layer there is a thin outer panel which is in contact with the environment.

The material properties of steel, aluminum, PCM and the insulation are listed in Table 3, as well as the chosen mushy region parameter ε. The RSS vessel and the outer panel are made of steel. The PCM is an eutectic mixture of potassium nitrate and sodium nitrate KNO_3-$NaNO_3$ (see Vogel et al. [43]), enclosed in aluminum cells. The PCM is either liquid (L) or solid (S). The geometry of this aluminum encapsulation is defined in Fig. 4 and Table 4. The assumed heat transfer coefficients are listed in Table 1.

4.5.2. Load profiles

Three different load profiles, denoted as the cases A, B and C, were tested. The three cases differ with the time interval $\Delta t_{\text{interval}}$ during which a steam mass flow of 5 kg/s is supplied or extracted from the storage tank, see Fig. 10a. The chosen intervals for a total simulation time of 4 h are given in Table 5.

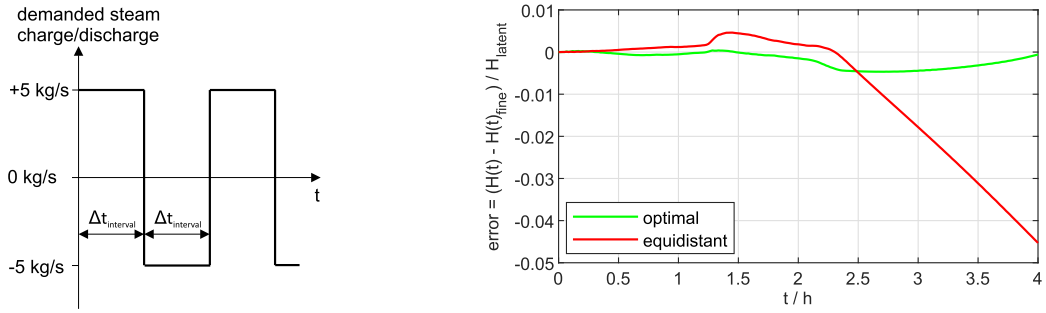

(a) (b)

Fig. 10. The applied steam mass flow to the RSS depending on $\Delta t_{interval}$ for the load cases A, B and C. If the maximum or minimum pressure limit in the RSS is reached, the mass flow is clipped (a). The error for an optimal and equidistant PCM sector partitioning for load case A is evaluated (b).

Table 5
Time intervals of the three load profiles.

Case	A	B	C
Interval $\Delta t_{interval}$ in hours	0.5	1	2

During operation of the RSS, the liquid level in the RSS must be inside the limit range between 0.05 and 0.95. The pressure in the RSS cannot fall below 13 bar or rise above 33 bar, corresponding to a temperature range between 191°C and 239°C. Accordingly, outside the valid operating range, no steam can either be fed into or be withdrawn from the RSS. Fig. 11a shows the temperature profile for load case C.

4.5.3. Evaluation of the aggregation criteria considering case A

In order to proof the functionality of the aggregation criteria, three simulations for load case A are performed. For an optimal case, seven sectors with their representative cells are distributed along the RSS circumference using the developed aggregation criteria, see Fig. 9a and Table 2. This optimal case is compared with a high-resolution reference case with 40 sectors distributed in an equidistant angular spacing along the circumference. Equidistant partitioning means all sectors have the same size and their representative cells are located in the middle of each sector. Another reference simulation includes seven sectors with equidistant partitioning. The total number and geometry of the cells is the same for all simulations.

The enthalpy stored in the PCM cells is used to analyze the results of

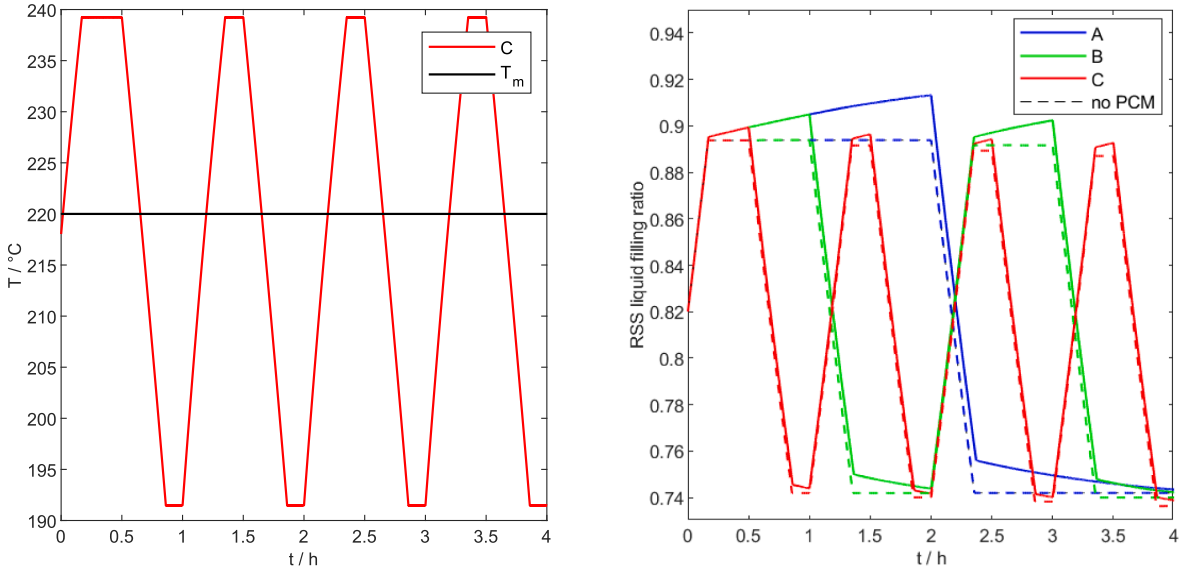

(a) (b)

Fig. 11. The temperature evolution inside the RSS during simulation case C is compared with the melting temperature of a PCM cell T_m (a). The stored energy expressed in terms of liquid filling ratio of the RSS with and without additional PCM energy storage capacity is shown (b).

At the beginning of the simulation, the RSS is initialized with a pressure of 22.35 bar and a liquid fraction of 0.82. The steam available for feeding is slightly overheated with a pressure of 33 bar and a temperature of 250°C. To calculate the losses to the environment, an ambient temperature of 20°C is selected.

the three simulation cases. The scaled error between the high-resolution reference case and the seven sector optimal/equidistant partitioning case is shown in Fig. 10b. The simulation of the optimal case shows a very good agreement with the high-resolution equidistant partitioning case with a maximum error of 0.5%, the case with seven sectors

equidistantly distributed produces a maximum error of 4.5% instead.

4.5.4. Results of load case A, B and C

Simulations of the three different load cases A, B and C are performed with reduction to 7 representative cells and optimal sector partitioning. Fig. 11b shows the stored energy expressed in terms of the liquid filling ratio of the RSS with (solid line) and without (dashed line) attached PCM cells.

PCM cells that are located in the steam zone of the RSS during the discharging period can barely be discharged, as can be seen in Fig. 7b. Therefore, these cells do not represent an useful extension of the storage capacity of the hybrid LHTES, but, on the contrary, are responsible for an initial loss of energy (sectors 1–2). Hence, for an analysis of the behavior of the additional storage capacity by retrofitting, only the enthalpy stored in the PCM sectors 3–7 is considered in Fig. 12a.

Table 6
Additional storage capacity of the three load profiles.

Case	A	B	C
additional storage capacity in %: $\frac{F_{\text{withPCM}} - F_{\text{noPCM}}}{F_{\text{noPCM}} - F_0}$	26.3	15.0	7.5
converted latent heat in %	100	61.5	33.3

additional storage capacity.

In an industrial plant, RSS are used to optimally adapt the steam generation to the subsequent processes. If several RSS are operated in parallel in a storage network, selected RSS units could be retrofitted to a hybrid LHTES.

With regard to a control strategy of the hybrid LHTES, care should

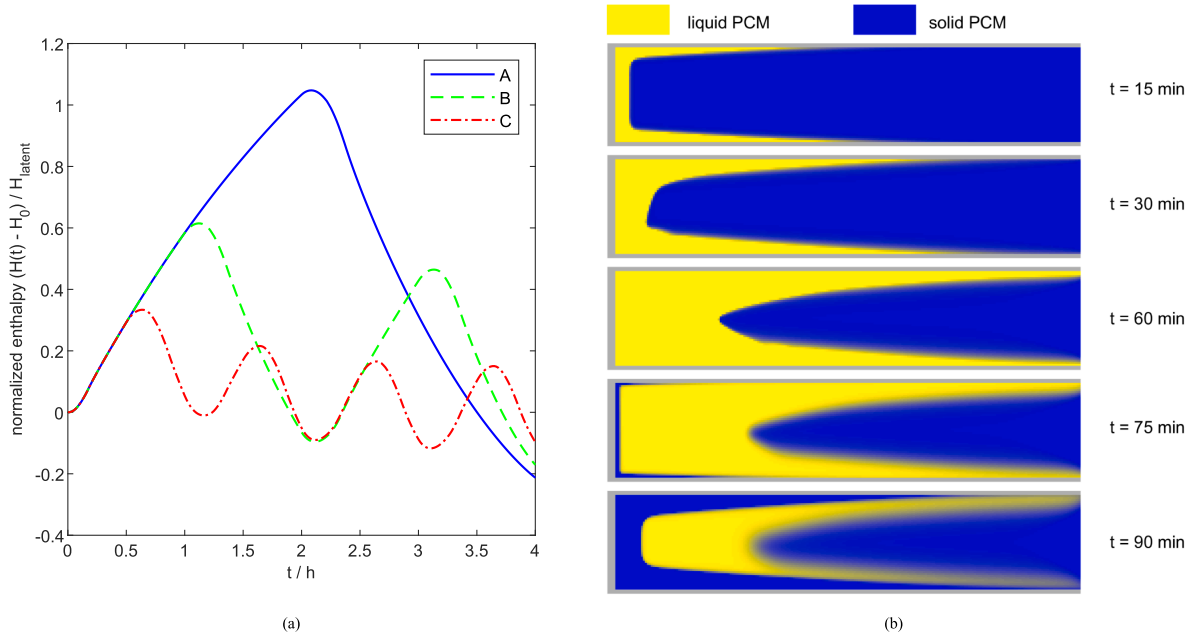

(a) (b)

Fig. 12. Stored enthalpy of sector 3–7 (optimal partitioning) for the three load cases A, B and C are shown (a). The melting behavior of a single PCM cell in sector 3 of load case B is depicted. Liquid PCM is displayed in yellow, solid PCM in blue. Multiple melting fronts are seen at t = 90 min (b). (For interpretation of the references to colour in this figure legend, the reader is referred to the web version of this article.)

5. Discussion and interpretation

5.1. Analysis of load cases A, B and C

The difference between the liquid filling ratio with and without PCM cells, F_{withPCM} and F_{noPCM}, in Fig. 11b characterizes the usable additional PCM storage capacity and is listed in Table 6 for the respective load case. The usable additional storage capacity highly depends on the charging/discharging interval $\Delta t_{\text{interval}}$. While in load case C only 33.3% of the latent enthalpy of the attached PCM cells can be used, in load cases B and A 61.5% and 100% of the additionally available latent heat is converted, see Fig. 12a.

5.2. Application and control strategies

Due to the slow dynamics of the PCM cells compared to the RSS, it is necessary to operate the hybrid LHTES using charging/discharging profiles suitable for the PCM cells. This requires novel control techniques and methods for state of charge estimation to fully exploit the be taken to ensure that the hybrid LHTES is charged or discharged at high temperature differences as long as solid PCM is present. Short-term high charging and discharging rates should be taken over by the pure steam storage devices in the network, if present. Predictive control schemes like model predictive control (MPC) are appropriate to operate such hybrid LHTES in a storage network efficiently. Therefore real-time-capable models are required.

5.3. Model reduction aspects

A first physical model reduction was performed by reducing the number of PCM sub-models. An aggregation criterion was formulated and the 160 cells were successfully aggregated into 7 optimally chosen sectors with representative cells. Using the proposed aggregation method for a simulation duration of 4 h, the computation time can be reduced from 11 days for 40 PCM sectors to 3 days for 7 optimally chosen sectors with equivalent accurate results. However, the reduced model obtained is still not real-time capable by a factor of 18.

The difficulty in further reduction is that the model consists of a

convection and a heat conducting part. Multiple asymmetrically formed melting fronts can occur and influence the further behavior of the hybrid LHTES, see Fig. 12b. Therefore, it is not admissible to simplify the model to a one-dimensional Stefan-problem and neglect the convection effects.

Mathematical methods are needed to reduce the computational effort and identify dominant modes without affecting the solution's accuracy. Techniques such as singular value decomposition (SVD), proper orthogonal decomposition (POD), and dynamic mode decomposition (DMD) can provide approaches for further model reduction and will be investigated, see for example, Dauvergne and del Barrio [11] for POD or Proctor et al. [32] and Alla and Kutz [2] for DMD.

6. Conclusions

The novel co-simulation model of a hybrid LHTES developed in this work consists of sub-models for the RSS and the PCM cells. The RSS model is based on the equilibrium approach for the two phases inside the pressure vessel, and the high-fidelity PCM cell model includes heat conduction and convection effects. The sub-models differ in complexity and time step size and are coupled by wall temperatures and resulting heat flow. Coupling methods to ensure energy conservation between the models have been developed for successful co-simulation. To reduce computational effort, the high number of PCM cells at the circumference of the RSS are aggregated into sectors with one representative cell each. Since the melting behavior depends significantly on the angular position and orientation of the PCM cell as well as on the operation state (liquid filling level inside the RSS), aggregation criteria are formulated to optimize the sector partitioning and produce an efficient and accurate co-simulation model. The performance of PCM cell aggregation is demonstrated using an optimal, and equidistant PCM sector partitioning. The newly developed aggregation criteria for the optimal aggregation of PCM cells into sectors can significantly minimize the simulation error from 4.5% to 0.5%. The computation time can be shortened up to 73%, whereby equally accurate results can be achieved compared to a high-resolution model. With the obtained co-simulation model, three load cases of the hybrid LHTES are analysed. The usable additional storage capacity of the PCM cells highly depends on the operating and control strategy. If the storage is operated optimally, the capacity can be increased up to 25% due to the PCM cells. Therefore, new model-based control techniques and state of charge estimations need to be developed. The model's level of detail, the reduction approach based on optimization to successfully increase computational efficiency as well as the findings from simulations are a novel contribution of this work. The presented coupling concept and the method for model reduction as well as the formulated aggregation criteria can easily be adapted for other co-simulations, such as in other hybrid storage concepts. The developed co-simulation model serves as a foundation for system analysis, but especially for estimation and control tasks. To achieve real-time capability, further model reduction based on mathematical methods for dominant mode identification is required.

Declaration of Competing Interest

None.

Acknowledgements

The Climate and Energy Fund KLIEN/FFG funded a research project in 2018 that has recently started: HyStEPs Grant No. 868842.

Appendix A. Supplementary material

Supplementary data associated with this article can be found, in the online version, at https://doi.org/10.1016/j.applthermaleng.2020.115495.

References

[1] F. Agyenim, N. Hewitt, P. Eames, M. Smyth, A review of materials, heat transfer and phase change problem formulation for latent heat thermal energy storage systems (LHTESS), Renew. Sustain. Energy Rev. 14 (2010) 615–628, https://doi.org/10.1016/j.rser.2009.10.015.
[2] A. Alla, J. Kutz, Nonlinear model order reduction via dynamic mode decomposition, SIAM J. Scient. Comput. 39 (2017) B778–B796, https://doi.org/10.1137/16M1059308.
[3] F. Bai, C. Xu, Performance analysis of a two-stage thermal energy storage system using concrete and steam accumulator, Appl. Therm. Eng. 31 (2011) 2764–2771, https://doi.org/10.1016/j.applthermaleng.2011.04.049.
[4] I.H. Bell, J. Wronski, S. Quoilin, V. Lemort, Pure and Pseudo-pure Fluid Thermophysical Property Evaluation and the Open-Source Thermophysical Property Library CoolProp, Industr. Eng. Chem. Res. 53 (2014) 2498–2508, https://doi.org/10.1021/ie4033999.
[5] A. Biglia, L. Comba, E. Fabrizio, P. Gay, D. Ricauda Aimonino, Steam batch thermal processes in unsteady state conditions: modelling and application to a case study in the food industry, Appl. Therm. Eng. 118 (2017), https://doi.org/10.1016/j.applthermaleng.2017.03.004.
[6] J. Bony, S. Citherlet, Numerical model and experimental validation of heat storage with phase change materials, Energy Build. 39 (2007) 1065–1072, https://doi.org/10.1016/j.enbuild.2006.10.017.
[7] J. Buschle, W.D. Steinmann, R. Tamme, Latent heat storage for process heat applications, in: Proceedings of the 10th International Conference on Thermal Energy Storage ECOSTOCK, 2006.
[8] T.F. Cheng, Numerical analysis of nonlinear multiphase Stefan problems, Comput. Struct. 75 (2000) 225–233, https://doi.org/10.1016/S0045-7949(99)00071-1.
[9] A.J. Chorin, Numerical solution of the Navier-Stokes equations, Math. Comput. 22 (1968) 745–762, https://doi.org/10.1090/S0025-5718-1968-0242392-2.
[10] G. Comini, S. Del Guidice, R.W. Lewis, O.C. Zienkiewicz, Finite element solution of non-linear heat conduction problems with special reference to phase change, Int. J. Numer. Meth. Eng. (1974), https://doi.org/10.1002/nme.1620080314.
[11] J.L. Dauvergne, E.P. del Barrio, Toward a simulation-free POD approach for low-dimensional description of phase-change problems, Int. J. Therm. Sci. 49 (2010) 1369–1382, https://doi.org/10.1016/j.ijthermalsci.2010.02.006.
[12] S. Dusek, R. Hofmann, A hybrid energy storage concept for future application in industrial processes, Therm. Sci. 22 (2018) 270, https://doi.org/10.2298/TSCI171230270D.
[13] S. Dusek, R. Hofmann, Modeling of a Hybrid Steam Storage and Validation with an Industrial Ruths Steam Storage Line, Energies 12 (2019), https://doi.org/10.3390/en12061014.
[14] Y. Dutil, D.R. Rousse, N.B. Salah, S. Lassue, L. Zalewski, A review on phase-change materials: mathematical modeling and simulations, Renew. Sustain. Energy Rev. 15 (2011) 112–130, https://doi.org/10.1016/j.rser.2010.06.011.
[15] B. Fortunato, S. Camporeale, T. Marco, M. Albano, Simple Mathematical Model of a Thermal Storage with PCM, AASRI Proc. 2 (2012) 241–248, https://doi.org/10.1016/j.aasri.2012.09.041.
[16] A. Gallego, A. Ruiz-Pardo, A. Cerezuela-Parish, J. Sanchez, C. Martin-Macareno, L. Cabeza, E. Camacho, E. Oro, Mathematical modeling of a PCM storage tank in a solar cooling plant, Sol. Energy 93 (2013) 1–10, https://doi.org/10.1016/j.solener.2013.03.026.
[17] C. Gau, R. Viskanta, Melting and Solidification of a Pure Metal on a Vertical Wall, J. Heat Transf. - ASME 108 (1986), https://doi.org/10.1115/1.3246884.
[18] A. Gil, M. Medrano, I. Martorell, A. Lázaro, P. Dolado, B. Zalba, L.F. Cabeza, State of the art on high temperature thermal energy storage for power generation. Part 1—Concepts, materials and modellization, Renew. Sustain. Energy Rev. 14 (2010) 31–55, https://doi.org/10.1016/j.rser.2009.07.035.
[19] E. González-Roubaud, D. Pérez-Osorio, C. Prieto, Review of commercial thermal energy storage in concentrated solar power plants: Steam vs. molten salts, Renew. Sustain. Energy Rev. 80 (2017) 133–148, https://doi.org/10.1016/j.rser.2017.05.084.
[20] R. Hofmann, S. Dusek, S. Gruber, G. Drexler-Schmid, Design Optimization of a Hybrid Steam-PCM Thermal Energy Storage for Industrial Applications, Energies 12 (2019), https://doi.org/10.3390/en12050898.
[21] M. Huang, P. Eames, B. Norton, Comparison of a small-scale 3D PCM thermal control model with a validated 2D PCM thermal control model, Sol. Energy Mater. Sol. Cells 90 (2006) 1961–1972, https://doi.org/10.1016/j.solmat.2006.02.001.
[22] N. Ibrahim, F. Al-Sulaiman, S. Rahman, B. Yilbas, A. Sahin, Heat transfer enhancement of phase change materials for thermal energy storage applications: A critical review, Renew. Sustain. Energy Rev. 74 (2017) 26–50, https://doi.org/10.1016/j.rser.2017.01.169.
[23] B. Kamkari, D. Groulx, Experimental investigation of melting behaviour of phase change material in finned rectangular enclosures under different inclination angles, Exp. Therm. Fluid Sci. 97 (2018) 94–108, https://doi.org/10.1016/j.expthermflusci.2018.04.007.
[24] B. Kamkari, H. Shokouhmand, F. Bruno, Experimental investigation of the effect of inclination angle on convection-driven melting of phase change material in a rectangular enclosure, Int. J. Heat Mass Transf. 72 (2014) 186–200, https://doi.org/10.1016/j.ijheatmasstransfer.2014.01.014.
[25] L. Kasper, Modeling of the Phase Change Material of a Hybrid Storage Using the Finite Element Method, TU Wien Academic Press, Wien, 2020, https://doi.org/10.34727/2020/isbn.978-3-85448-037-2 (in press).
[26] H.P. Langtangen, K.A. Mardal, R. Winther, Numerical methods for incompressible viscous flow, Adv. Water Resour. 25 (2002) 1125–1146, https://doi.org/10.1016/

S0309-1708(02)00052-0.
[27] S. Liu, Y. Li, Y. Zhang, Mathematical solutions and numerical models employed for the investigations of PCMs phase transformations, Renew. Sustain. Energy Rev. 33 (2014) 659–674, https://doi.org/10.1016/j.rser.2014.02.032.
[28] T. Napp, A. Gambhir, T. Hills, N. Florin, P. Fennell, A review of the technologies, economics and policy instruments for decarbonising energy-intensive manufacturing industries, Renew. Sustain. Energy Rev. 30 (2014) 616–640, https://doi.org/10.1016/j.rser.2013.10.036.
[29] B. Nedjar, An enthalpy-based finite element method for nonlinear heat problems involving phase change, Comput. Struct. 80 (2002) 9–21, https://doi.org/10.1016/S0045-7949(01)00165-1.
[30] D. Pepper, J. Heinrich, The Finite Element Method: Basic Concepts and Applications. Series in Computational and Physical Processes in Mechanics and Thermal Sciences, CRC Press, 2005.
[31] A. Pourakabar, A.R. Darzi, Enhancement of phase change rate of PCM in cylindrical thermal energy storage, Appl. Therm. Eng. 150 (2019) 132–142, https://doi.org/10.1016/j.applthermaleng.2019.01.009.
[32] J. Proctor, S. Brunton, J. Kutz, Dynamic Mode Decomposition with Control, SIAM J. Appl. Dynam. Syst. 15 (2016) 142–161, https://doi.org/10.1137/15M1013857.
[33] K. Radhakrishnan, A. Balakrishnan, Heat transfer analysis of thermal energy storage using phase change materials, Heat Recov. Syst. CHP 12 (1992) 427–435, https://doi.org/10.1016/0890-4332(92)90064-O.
[34] B. Seibold, A compact and fast Matlab code solving the incompressible Navier-Stokes equations on rectangular domains. <http://math.mit.edu/gs/cse/codes/mit18086_navierstokes.pdf>, 2008.
[35] A. Stamatiou, S. Maranda, F. Eckl, P. Schuetz, L. Fischer, J. Worlitschek, Quasi-stationary modelling of solidification in a latent heat storage comprising a plain tube heat exchanger, J. Energy Storage 20 (2018) 551–559, https://doi.org/10.1016/j.est.2018.10.019.
[36] W. Steinmann, J. Buschle, Analysis of thermal storage systems using Modelica. < https://elib.dlr.de/19172/. LIDO-Berichtsjahr = 2005 > , 2005.
[37] W.D. Steinmann, M. Eck, Buffer storage for direct steam generation, Sol. Energy 80 (2006) 1277–1282, https://doi.org/10.1016/j.solener.2005.05.013.
[38] V. Stevanovic, B. Maslovaric, S. Prica, Dynamics of steam accumulation, Appl. Therm. Eng. 37 (2012) 73–79, https://doi.org/10.1016/j.applthermaleng.2012.01.007.
[39] R. Tamme, T. Bauer, J. Buschle, D. Laing, H. Müller-Steinhagen, W.D. Steinmann, Latent heat storage above 120 °C for applications in the industrial process heat sector and solar power generation, Int. J. Energy Res. 32 (2008) 264–271, https://doi.org/10.1002/er.1346.
[40] Y. Tao, Y.L. He, A review of phase change material and performance enhancement method for latent heat storage system, Renew. Sustain. Energy Rev. 93 (2018) 245–259, https://doi.org/10.1016/j.rser.2018.05.028.
[41] R. Tenchev, J. Mackenzie, T. Scanlon, M. Stickland, Finite element moving mesh analysis of phase change problems with natural convection, Int. J. Heat Fluid Flow 26 (2005) 597–612, https://doi.org/10.1016/j.ijheatfluidflow.2005.03.003.
[42] C. Underwood, T. Shepherd, S. Bull, S. Joyce, Hybrid thermal storage using coil-encapsulated phase change materials, Energy Build. 159 (2018) 357–369, https://doi.org/10.1016/j.enbuild.2017.10.095.
[43] J. Vogel, J. Felbinger, M. Johnson, Natural convection in high temperature flat plate latent heat thermal energy storage systems, Appl. Energy 184 (2016) 184–196, https://doi.org/10.1016/j.apenergy.2016.10.001.
[44] B. Zalba, J.M. Marin, L.F. Cabeza, H. Mehling, Review on thermal energy storage with phase change: materials, heat transfer analysis and applications, Appl. Therm. Eng. 23 (2003) 251–283, https://doi.org/10.1016/S1359-4311(02)00192-8.
[45] C. Zauner, F. Hengstberger, B. Mörzinger, R. Hofmann, H. Walter, Experimental characterization and simulation of a hybrid sensible-latent heat storage, Appl. Energy 189 (2017) 506–519, https://doi.org/10.1016/j.apenergy.2016.12.079.
[46] J. Zhao, J. Yasheng, Z. Zhang, J. Lu, Energy-Saving Analysis of Solar Heating System with PCM Storage Tank, Energies 2018 (2018), https://doi.org/10.3390/en11010237.
[47] J. Zhao, J. Zhai, Y. Lu, N. Liu, Theory and experiment of contact melting of phase change materials in a rectangular cavity at different tilt angles, Int. J. Heat Mass Transf. 120 (2018) 241–249, https://doi.org/10.1016/j.ijheatmasstransfer.2017.12.006.

2.2 Publication B

D. Pernsteiner, A. Schirrer, L. Kasper, R. Hofmann, and S. Jakubek. "Data-based model reduction for phase change problems with convective heat transfer". In: *Applied Thermal Engineering* 184 (2021), p. 116228. DOI: 10.1016/j.applthermaleng.2020.116228

Applicant's contribution [†]

- Dominik Pernsteiner: Conceptualization, Formal analysis, Investigation, Methodology, Software, Visualization, Writing - original draft
- Alexander Schirrer: Conceptualization, Methodology, Supervision, Writing - review & editing
- Lukas Kasper: Software, Writing - review & editing
- René Hofmann: Funding acquisition, Supervision, Writing - review & editing
- Stefan Jakubek: Funding acquisition, Conceptualization, Supervision, Writing - review & editing

[†]According to the Elsevier CRediT author statement: https://www.elsevier.com/authors/policies-and-guidelines/credit-author-statement

Applied Thermal Engineering 184 (2021) 116228

Contents lists available at ScienceDirect

Applied Thermal Engineering

journal homepage: www.elsevier.com/locate/apthermeng

Data-based model reduction for phase change problems with convective heat transfer

Dominik Pernsteiner [a,*], Alexander Schirrer [a], Lukas Kasper [b], René Hofmann [b,c], Stefan Jakubek [a]

[a] TU Wien, Institute of Mechanics and Mechatronics, Getreidemarkt 9/BA, 1060 Vienna, Austria
[b] TU Wien, Institute for Energy Systems and Thermodynamics, Getreidemarkt 9/BA, 1060 Vienna, Austria
[c] AIT Austrian Institute of Technology GmbH, Center for Energy, Sustainable Thermal Energy Systems, Giefinggasse 2, 1210 Vienna, Austria

ARTICLE INFO

Keywords:
Phase change material
Model reduction
Convective and conductive heat transfer
Singular value decomposition
Stream function

ABSTRACT

Latent heat thermal energy storages (LHTES) exploit the high energy density of phase change material (PCM). The typically low thermal conductivity of PCM limits the charging and discharging rates and poses considerable challenges for dynamic storage operation. To operate LHTES efficiently and to exploit their full potential, new methods are required to obtain accurate and fast models for state of charge estimation and control tasks. In LHTES the heat transfer in low viscosity PCM is driven by conduction and also significantly by convective transport. In previous works, various high-precision models have been developed which employ finite element, difference and volume methods to solve the coupled Navier–Stokes and energy equations, but they incur large computational effort. In the present work, a novel, high-fidelity model reduction technique is proposed to achieve real-time capability while preserving high model accuracy. The idea is to short-cut the laborious solution of the Navier–Stokes equations by an efficiently parametrized, data-based model which approximates the stream function of the typical convection flow pattern by singular value decomposition. To account for the complexity of the solution-dependent flow domain, a suitable transformation method is proposed. The efficiency and accuracy of the proposed reduction method is demonstrated in typical operating modes.

1. Introduction

1.1. Motivation

Due to the volatile nature of renewable energy sources, their efficient use requires the application of thermal energy storage systems (TES). TES are essential to decouple energy supply and consumption, which in turn improves the performance and reliability of energy systems as a whole [28]. In particular, the energy-intensive industries rely on balancing energy supply and demand to achieve the necessary flexibility for an effective use of resources and to incorporate renewable energy sources.

There are three main types of storage media in TES systems: sensible, latent and chemical, see Gil et al. [24]. In sensible TES, the energy is stored with increasing/decreasing temperature of the storage media, e.g. in the packed rock bed thermal storage. Latent heat thermal energy storage (LHTES) mainly use the phase transition to store energy in a small temperature range. The third storage mechanism is based on completely reversible chemical reactions to store and fully recover thermal energy, e.g. in oxidation–reduction reactions.

LHTES consist of phase change material (PCM) to store energy with high energy density and at an almost constant temperature level, see Agyenim et al. [1] and Zalba et al. [62]. A drawback of many PCMs is their low thermal conductivity which limits the charging and discharging rates and poses significant challenges for dynamic operation of the storage. Some methods to increase the thermal conductivity are summarized by Tao and He [56] and Ibrahim et al. [28]. Bondareva et al. [9] investigated the addition of nanoparticles in PCM to increase conduction. Typical LHTES configurations incorporate aluminum fins in PCM for thermal conductivity enhancement, such as the setup shown in Fig. 1. Due to the complex dependency of the temperature distribution on the total energy content and the low thermal conductivity of PCM, the thermodynamic state is distributed over the domain and thus the state of charge cannot be measured directly. For an efficient implementation of LHTES in industrial energy systems, knowledge of the distributed thermodynamic state and its dynamic behavior is of crucial importance. In order to realize state of charge estimation with an

* Corresponding author at: Institute for Mechanics and Mechatronics, TU Wien, Getreidemarkt 9/E325, 1060 Vienna, Austria.
E-mail address: dominik.pernsteiner@tuwien.ac.at (D. Pernsteiner).

https://doi.org/10.1016/j.applthermaleng.2020.116228
Received 25 May 2020; Received in revised form 14 October 2020; Accepted 15 October 2020
Available online 27 October 2020

Nomenclature

Acronyms

ARX	Auto regressive model with exogenous input
DMD	Dynamic Mode Decomposition
LHTES	Latent Heat Thermal Energy Storage
PCM	Phase Change Material
PGD	Proper General Decomposition
POD	Proper Orthogonal Decomposition
SVD	Singular Value Decomposition
TES	Thermal Energy Storage

Index

$\hat{}$	estimated quantity
0	initial
in	incoming flow
L	liquid
out	outgoing flow
ref	reference
S	solid
*	transformed quantity
con	constant
cub	cubic
lin	linear
max	maximal
min	minimal
norm	normalized
qu	quadratic
red	reduced system

Parameters and variables

α	heat transfer coefficient $\left(\mathrm{W}/(\mathrm{m}^2\mathrm{K})\right)$
β	volumetric thermal expansion coefficient $(1/\mathrm{K})$
$\hat{\nu}_{\mathrm{red}}$	estimation of the current magnitude of the spatial modes in the reduced system
$\boldsymbol{\Sigma}$	matrix with singular values
$\boldsymbol{\Theta}$	parameter vector
$\boldsymbol{f}$	force density $\left(\mathrm{kg}/(\mathrm{m}^2\mathrm{s}^2)\right)$
$\boldsymbol{g}$	gravitational acceleration vector $\left(\mathrm{m}/\mathrm{s}^2\right)$
$\boldsymbol{R}$	regressor matrix
$\boldsymbol{r}$	regressor using current measurement values
$\boldsymbol{U}$	left singular vector
$\boldsymbol{u}$	velocity vector (m/s)
$\boldsymbol{V}$	right singular vector
Δt	time step (s)
Δx_{PCM}	cavity PCM dimension in x direction (m)
Δy_{PCM}	cavity PCM dimension in y direction (m)
$\dot{Q}$	heat flow (W)
$\in$	mushy region temperature range (K)
γ	activation function
μ	dynamic viscosity $\left((\mathrm{Ns})/\mathrm{m}^2\right)$
ρ	density $\left(\mathrm{kg}/\mathrm{m}^3\right)$
Ω	coordinate transformation
Ψ	stream function $\left(\mathrm{m}^2/\mathrm{s}\right)$
ξ, η	transformed space coordinates (m)
c	specific heat capacity $(\mathrm{J}/(\mathrm{kgK}))$
H	enthalpy (J)
h	specific enthalpy (J/kg)
k	thermal conductivity $(\mathrm{W}/(\mathrm{mK}))$
L_x, L_y	length of PCM cell in x, y direction (m)
n	number of simulation/ measurement values
q	heat flux $\left(\mathrm{W}/\mathrm{m}^2\right)$
RTF	real-time factor
T	temperature $(^\circ\mathrm{C})$
t	time (s)
t_{comp}	computation time of simulation (s)
T_{corner}	temperature near the heated wall $(^\circ\mathrm{C})$
t_{end}	end time of simulation (s)
T_{m}	melting temperature of PCM $(^\circ\mathrm{C})$
T_{spread}	maximum temperature difference $(^\circ\mathrm{C})$
u, v	velocity components in x, y direction (m/s)
x, y	space coordinates (m)
x_{liquid}	primary flow liquid ratio
x_{switch}	liquid ratio which accounts for a switching flow regime

Symbols

$\mathcal{D}, \partial\mathcal{D}$	spatial domain, boundary of spatial domain
$\mathcal{D}_{\mathrm{flow}}$	primary flow domain
$\mathcal{D}_{\mathrm{unit}}$	unit domain
∇	Nabla operator: $\nabla = (\partial/\partial x, \partial/\partial y)$
∂	partial derivative

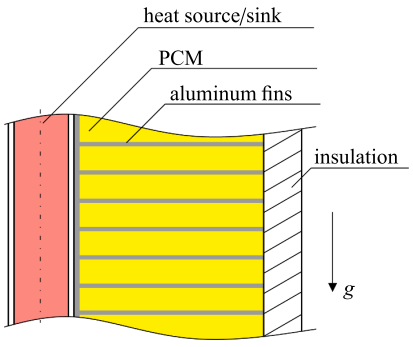

Fig. 1. Scheme of a typical LHTES configuration with PCM and aluminum fins for heat transfer enhancement.

observer such as the extended Kalman filter as well as to enable model-based control, an accurate and real-time capable model is required that contains all relevant effects. The two most relevant effects that occur when modeling the heat transfer of low-viscosity PCMs are conduction and convection. The computation of these effects with finite element, finite difference or finite volume methods for the coupled energy equation and the Navier–Stokes equations requires high computational effort and leads to simulation models which typically cannot be computed in or faster than real-time, see Kasper [29].

1.2. PCM modeling approach

Relevant heat transfer mechanisms in PCM are conduction and natural convection. Dutil et al. [21] and Liu et al. [35] review options for mathematical modeling and simulation of PCM. Analytical solutions only exist for a limited number of phase change problems, as for example for the one-dimensional Stefan-problem, see Radhakrishnan and Balakrishnan [44].

Fortunato et al. [23] state that the effect of natural convection is widely neglected in modeling PCM thermal storage systems due to its complexity. However, the legitimacy of such simplification strongly

depends on the type of PCM encapsulation and is potentially violated for PCM with low viscosity in the liquid phase. Bondareva and Sheremet [10] investigated the influence of geometric parameters of fins such as length and width on convection modes and thus on the melting rate. In a numerical study with an experimentally validated model, Vogel et al. [59] analysed the impact of natural convection on melting in so-called flat plate LHTES filled with the common high-temperature PCM sodium nitrate and potassium nitrate (KNO3-NaNO3) and found a significant heat transfer enhancement depending on the geometry of PCM enclosures due to convective transport. This finding was confirmed by Kasper [29], who numerically investigated the impact of natural convection on melting of PCM in an encapsulation depending on its orientation.

When considering heat transfer due to conduction in PCM in more than one dimension, numerical methods, as for example the enthalpy method and the effective heat capacity method, which were summarized by Liu et al. [35], have to be applied. Nedjar [40] state that especially finite element methods are able to handle complex coupled thermo-mechanical problems with various and complex boundary conditions. The effective heat capacity method was, for example, applied by Tenchev et al. [57] in a moving-mesh finite element model considering both conduction and natural convection. A similar approach was pursued by Kasper [29], using the effective heat capacity method and an adaptation of the finite difference code published by Seibold [51] to solve the two-dimensional Navier–Stokes equations arising in convection modeling. This provided an experimentally validated coupled finite element/ finite difference model for PCM cavity simulations and is adopted in the present work as a reference model for the model reduction approach.

1.3. Innovation

The modeling approaches for PCMs described in the above section are computationally highly demanding and not suitable for real-time models. Fig. 2 outlines the main contribution of this work - a model reduction method aiming to cut down computational requirements strongly while retaining high accuracy. The energy and the Navier–Stokes equations are coupled via the velocity field $\boldsymbol{u}$. A first analysis of the method proposed by Kasper [29] showed that the Navier–Stokes equations require about 80% of the computation time. Therefore, in this work a novel reduction method is developed to model the relevant convection effects in PCM in a simplified form without fully solving the Navier–Stokes equations. The model reduction approach is data-based and relies on the stream function derived from the velocity field obtained in a reference simulation. A suitable transformation is introduced to map the active flow domain (whose shape depends on the solution itself) to a unit domain to account for the changing flow domain of the PCM. The stream function snapshots are decomposed into modes of space and time using singular value decomposition (SVD). It is found that the temporal behavior of the dominant modes of the velocity field can be obtained from thermal properties of the domain, such as liquid ratio and temperature gradient. The resulting reduced model is able to reconstruct the stream function and thus the velocity field without solving the Navier–Stokes equations in the real-time simulation. The new model reduction method is evaluated based on simulations of typical storage operating modes and shows highly accurate results achieved with considerably lower computation times.

1.4. Model reduction methods

1.4.1. Overview

Model reduction methods have been a major research topic in recent decades and have been addressed in numerous reviews. Benner et al. [5] conducted a survey of model reduction methods for linear systems and Reis and Stykel [45] provided an overview of approaches in coupled systems. Antoulas et al. [2] divided the reduction methods into two main categories: moment matching based methods and SVD-based methods. The former group can be implemented iteratively but does not have global error bounds, see Antoulas et al. [2] for an overview of linear implementations and Astolfi [4] for the nonlinear enhancement of this method. The approach developed in this paper is based on the latter group. An example of SVD-based reduction methods in linear systems is balanced truncation, where the system is transformed via principal component analysis to a basis in which the hard-to-reach states are simultaneously difficult to observe and are simply truncated for the reduced model. This method was first introduced by Moore [38], and a short overview of implementations is given by Gugercin and Antoulas

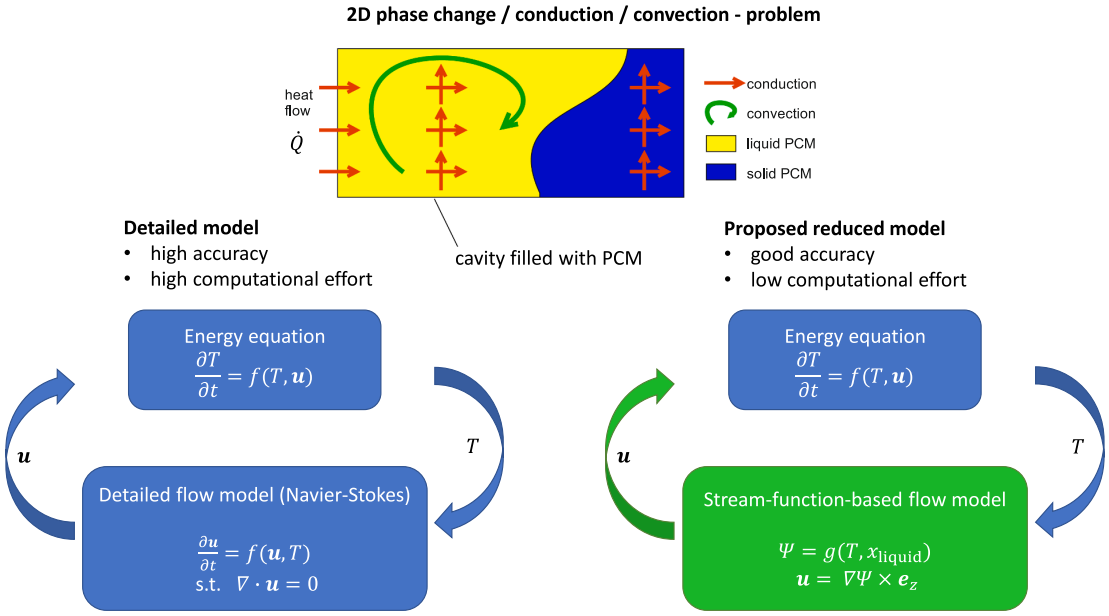

Fig. 2. Coupling of the dominant effects in the detailed and reduced model.

[26]. Other SVD-based methods for linear systems are the Hankel-norm approximation and the singular pertubation, see Glover [25] and Liu and Anderson [36], respectively. Proper orthogonal decomposition (POD), first introduced by Lumley [37], is a popular method for nonlinear complexity reduction problems. The basic idea is to extract the most significant characteristics of a system's behavior and represent them in a set of orthonormal basis vectors. For this purpose, the POD basis vectors are determined empirically by examining sample data collected over a range of relevant system dynamics and identifying the most energetic modes. The system's governing equations are projected onto the reduced-order subspace defined by the POD basis vectors. This low-dimensional description of the system's dynamics is obtained directly from the Galerkin projection of the governing equations on the POD modes. This yields an explicit POD reduced model that can be solved instead of the original system, see Chinesta et al. [14] and Volkwein [60].

More recent methods for model reduction of nonlinear systems are the dynamic mode decomposition (DMD) developed by Schmid [50] and the proper generalized method (PGD), see Chinesta et al. [15] and Néron and Ladeveze [41]. In contrast to the POD method, the PGD technique is an "a priori" iterative model reduction method which does not rely on particular bases. DMD is data-driven and, in contrast to POD, the DMD modes attempt to describe the dynamics in the timeseries rather than best reconstructing a dataset, see Tu et al. [58]. Brunton et al. [13] proposed the data-based regression method SINDY, combining DMD and sparse regression and exemplified it in applications of uniform flow vortex shedding and discovering the sparse equations structure in a noisy Lorentz system. Other model reduction techniques are based on the combination of machine learning and SVD, which demands a lot of training data, see e.g. Prasad and Bequette [43]. Furthermore, Swischuk et al. [55] demonstrate the importance of embedding physical constraints as well as of incorporating knowledge such as conservation laws within the learned models.

1.4.2. Model reduction in fluid dynamics

Particularly in the field of fluid dynamics, modeling often reaches the limits of computing power and is therefore the subject of current research regarding model reduction methods. The coupled partial differential equations to be solved in this area represent a particular challenge. Rowley and Dawson [48] and Lassila et al. [32] summarized model reduction approaches in flow analysis. Bistrian and Navon [7] compared the DMD and POD approaches to derive a reduced model for the shallow water equation. Rowley et al. [47] presented a framework for applying POD to compressible fluids with small temperature gradients and moderate Mach numbers. Rowley [46] successfully applied a balanced POD method to a channel flow. Dumon et al. [20] used the PGD method to solve the Navier–Stokes equations in the case of a lid-driven cavity for different Reynolds numbers. Liberge and Hamdouni [34] applied the POD technique to a flow around an oscillating cylinder using a fictitious domain. Stabile and Rozza [54] compared two different pressure stabilisation strategies for POD methods in a lid-driven cavity problem and in a flow around a circular cylinder for moderate Reynolds number. Kutz [30] emphasized the potential of deep learning in fluid dynamics, but also pointed out unresolved issues such as the number of layers/nodes and the amount of training data required. Applicatons of reduction techniques using neural nets in fluid dynamics can be found in Wang et al. [61] for forced convection and in San and Maulik [49] for natural convection.

Most of the model reduction approaches for fluid dynamics presented are highly complex and laborious to adapt. One research gap is the lack of methods to efficiently reduce dominant flow patterns to a simple model. In the present work, an easy-to-implement data-based approach is developed to address this issue.

1.4.3. Model reduction with varying domains

A large number of problems is found on partial differential equations with time-varying spatial domains, such as melting/solidification processes, crystal growth, and hydraulic fracturing. However, only a few model reduction approaches have been developed specifically considering this aspect so far.

Armaou and Christofides [3] expressed the partial differential equation system of a diffusion–reaction process with respect to an appropriate time-invariant coordinate derived from an analytical expression. A POD method was applied to the resulting transformed time-invariant system. Fogleman et al. [22] applied the POD to flows of an engine combustion process within a time-varying domain. They transformed the velocity fields to a fixed domain in such a way that the divergence-free property remained preserved, which is relevant also in the present context. Dauvergne and del Barrio [18] presented a simulation-free POD model reduction method for multidimensional heat conduction problems with phase change. They decomposed the problem into a heat conduction and source-term problem for the phase change. Narasingam and Kwon [39] partitioned the domain into multiple subdomains and then applied POD to each local domain. Recently Sidhu et al. [52] developed a model reduction method for the fracture propagation in a hydraulic fracturing process with moving boundaries. They could consider the time-varying spatial domain as a time-invariant one by assuming the fraction width zero where the fraction has not propagated into the domain.

Our newly developed model reduction method solves the problem of varying flow domains by first converting the velocity field into the stream function which preserves the continuity of the flow per definition. Then the stream function is mapped to a unit domain in which the dominant modes can be efficiently identified.

1.5. Main contributions

To the best of the authors' knowledge, no model reduction technique for convection problems with phase change and the associated problem of a varying flow domain has been presented so far. The main contributions of this paper are as follows:

- A novel and efficient high-fidelity model reduction concept for convective heat transfer in phase change problems is developed, which takes changing flow domains into account.
- The new approach considerably reduces the computational effort and realizes the real-time capability of the model.
- Simulation studies are conducted and discussed, showing the effectiveness and accuracy of the proposed model reduction in typical operation modes of an LHTES application.
- In contrast to the solution of the complete Navier–Stokes equations, the accuracy of the reduced model is less dependent on the time step and mesh size.

1.6. Paper structure

The paper is organised as follows: In Section 2, the detailed model and its fundamental equations are presented. Section 3 describes the model reduction approach through stream functions, transformation and SVD as well as the assumptions made. In Section 4, simulation studies to demonstrate the effectiveness of the proposed model reduction are performed. In Section 5 the results of the model reduction are compared and different aspects are discussed.

2. Detailed model

The reduction approach is demonstrated using a two-dimensional rectangular PCM domain with aluminum fins as heat conducting structures. For reasons of symmetry, modelling of a LHTES configuration as illustrated in Fig. 3 is reduced to a single, so called PCM cell, consisting only of one fin section of the storage.

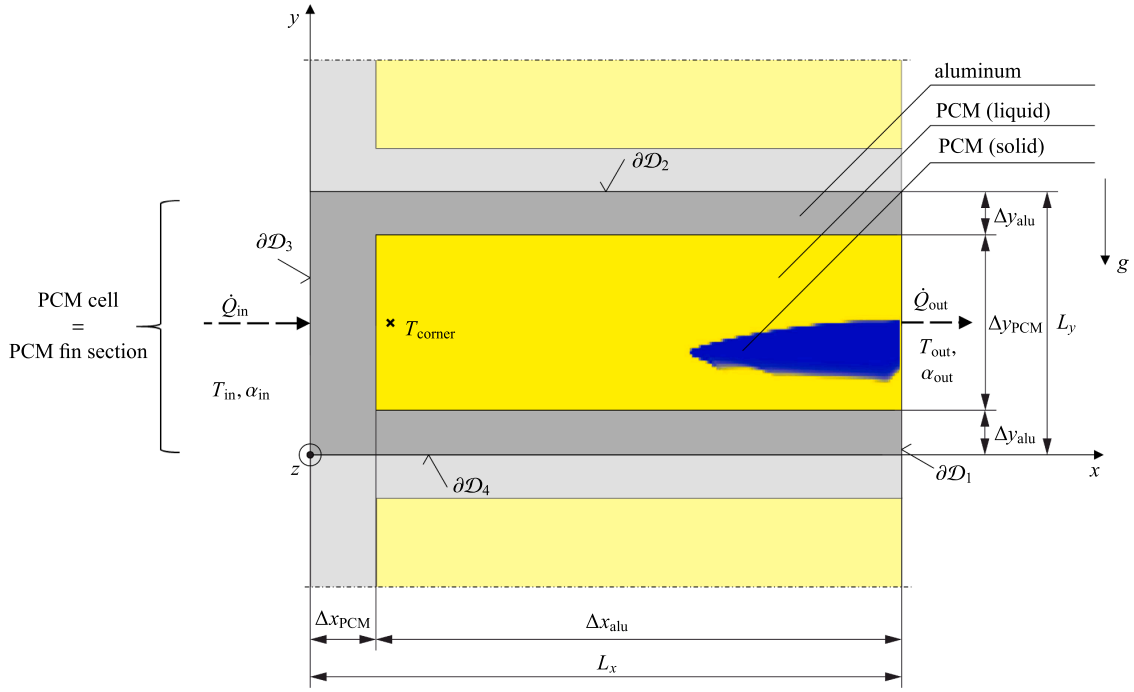

Fig. 3. PCM cell dimensions.

2.1. Fundamental Equations

A detailed multi-phase thermodynamic model including melting/solidification, heat conduction, and natural convection in two dimensions is considered for the PCM cell, developed and thoroughly documented in Kasper [29]. It underlies the basic conservation laws of mass, momentum and energy. Multiple PCM cell models were successfully coupled with a Ruths steam storage in a co-simulation in Pernsteiner et al. [42]. In order to simplify modeling of a PCM cell to the significant occurring phenomena, the following assumptions are made therein:

- Heat transfer is driven by conduction and natural convection, both being relevant phenomena.
- Material properties, apart from density, are constant in each phase but they can take on different values for the liquid and solid phases.
- Density is assumed constant and the same for both phases except for the buoyancy term in the liquid domain (Boussinesq approximation). Therein, the only body force arises due to the gravitational acceleration in vertical direction. This is a common and widely used approach, see Vogel et al. [59].
- Phase change is modeled by means of the apparent heat capacity method (see [8,17]), meaning that the phase transition takes place in a small temperature region $T \in [T_m - \varepsilon, T_m + \varepsilon]$ defined by the melting temperature T_m and mushy region parameter ε.
- The phase ratio only depends on T (no temperature hysteresis, no dynamics, no rate dependency, no subcooling).
- No relevant surface effects nor dentrite growth occur.
- Dissipation and pressure terms are neglected in the energy Eq. (1) due to small Eckert numbers, $Ec \ll 1$.
- The depth of the PCM enclosure in z-direction, is assumed large enough for wall boundary layer effects to be negligible, hence the problem is reduced to two dimensions (no heat flow or convection in z-direction).

The governing equations within the framework of these assumptions are the energy Eq. (1), continuity Eq. (2) and Navier–Stokes Eqs. (3) as follows:

$$\rho_{PCM} c \frac{\partial T}{\partial t} = k_{PCM} \nabla\cdot(\nabla T) - \rho_{PCM} c (\boldsymbol{u}\cdot\nabla) T \tag{1}$$

$$\nabla\cdot\boldsymbol{u} = 0 \tag{2}$$

$$\rho_{PCM} \frac{\partial \boldsymbol{u}}{\partial t} + \rho_{PCM} (\boldsymbol{u}\cdot\nabla)\boldsymbol{u} - \mu\nabla\cdot(\nabla\boldsymbol{u}) = \boldsymbol{f}(T) - \nabla p_{PCM} \tag{3}$$

Therein, the temperature field $T = T(x,y,t)$ is treated as dependent variable in the energy Eq. (1), and the velocity field $\boldsymbol{u} = [u,v]^T$ with spatial components $u(x,y,t)$ and $v(x,y,t)$ is treated as dependent variable in the Navier–Stokes Eq. (3), see Chorin [16]. The variable p_{PCM} stands for the pressure in the PCM. The symbols ρ_{PCM}, c, k and μ denote the parameters density, apparent heat capacity

$$c(T) = \begin{cases} c_S & \text{if}: T < T_m - \varepsilon \\ \dfrac{\Delta l_m + c_S\cdot(T_m + \varepsilon - T) + c_L\cdot(T - (T_m + \varepsilon))}{2\varepsilon} & \text{if}: T_m - \varepsilon \leqslant T T \leqslant T_m + \varepsilon \\ c_L & \text{if}: T > T_m + \varepsilon \end{cases}, \tag{4}$$

heat conductivity and dynamic viscosity, respectively. The force density $\boldsymbol{f}$ describes the buoyancy force

$$\boldsymbol{f} = \rho\boldsymbol{g} \cong \rho_0 \boldsymbol{g}\big(1 - \beta(T - T_{ref})\big), \tag{5}$$

which is calculated via the Boussinesq approximation [11] as given in Huang et al. [27] by the volumetric thermal expansion coefficient β, the constant (reference) density ρ_0, a reference temperature T_{ref}, and the gravitational standard acceleration vector $\boldsymbol{g}, \boldsymbol{g} = g\begin{bmatrix} 0 \\ -1 \end{bmatrix}$ with $g = 9.81$ m/s^2.

2.2. Discretization

The PCM cell conduction/convection model developed by Kasper [29] uses a finite element discretization to model the time-dependent energy Eq. (1) and applies a finite difference scheme to solve the incompressible Navier–Stokes Eqs. (2) and (3) in each time step. The obtained velocity field is used for the next time step of the energy equation.

The finite element method uses a standard Galerkin finite element approach with four-noded bilinear rectangular elements for the energy Eq. (1). The set of incompressible two-dimensional Navier–Stokes Eqs. (2) and (3) is treated separately from the heat transfer part of the model via a finite difference discretization based on a MATLAB® code available on the course homepage(http://math.mit.edu/~gs/cse/) of "Computational Science and Engineering" at the Massachusetts Institute of Technology. This open source code, created and documented by Seibold [51], was implemented and extended to meet specific requirements in the diploma thesis of Kasper [29]. The main numerical concept used therein is the fractional step method [16,19], which is applied to split the Navier–Stokes system into equations that are significantly simpler to work with.

2.3. Boundary conditions

The geometry of the considered PCM cell suggests symmetry reduction of the simulation to single aluminum fin sections. Consequently, the symmetry boundaries, in this case chosen as upper and lower boundaries of the computational domain, are treated as adiabatic:

$$\boldsymbol{q}|_{\partial\mathcal{D}_2,\,\partial\mathcal{D}_4} = 0 \tag{6}$$

For the left and right boundaries type-3 boundary conditions, also known as Robin or heat-transfer boundary conditions,

$$\boldsymbol{q}|_{\partial\mathcal{D}_3} = \alpha_{\text{in}}\cdot(T(x,y,t) - T_{\text{in}}), \tag{7}$$

$$\boldsymbol{q}|_{\partial\mathcal{D}_1} = \alpha_{\text{out}}\cdot(T(x,y,t) - T_{\text{out}}), \tag{8}$$

are prescribed following Newton's law of cooling, where $\alpha_{\text{in}}, \alpha_{\text{out}}$ are heat transfer coefficients, q is the specific heat flux across the boundary, and $T_{\text{in}}, T_{\text{out}}$ present boundary temperatures at the left and right wall surfaces, respectively.

Regarding the velocity field $\boldsymbol{u} = [u,v]^T$, no-slip boundary conditions are set for the domain boundaries,

$$\boldsymbol{u}|_{\partial\mathcal{D}} = 0. \tag{9}$$

Furthermore, the velocity is set to zero if the PCM is not completely liquefied:

$$\boldsymbol{u}|_{T<T_{\text{m}}+\varepsilon} = 0. \tag{10}$$

This is also done for any solid material (here, aluminum) in the computational domain, see Kasper [29].

2.4. Features of the model

The model presented above is able to model heat transfer by convection and conduction in PCM. It fully solves the Navier–Stokes equations, thus providing a highly accurate velocity field in the liquid domain. It was validated in Kasper [29] against experimental data from Brent et al. [12], resulting in an error of 3% in the liquid fraction. However, for realistic problem sizes it is not real-time capable by a factor of 5 or more and it is found that the computation of the Navier–Stokes equations consumes about 80% of the time. To achieve real-time capability, a model for high accuracy heat transfer and good accuracy of the velocity field is developed, utilized to determine the convection terms in the energy equation and hence achieve the overall solution quickly. This enables a model suitable for estimating the state of charge and controlling an LHTES.

3. Reduced model

The basic idea is to replace the solution of the Navier–Stokes equations by a simplified data-driven model, that explains the velocity field from few selected properties of the energy equation, such as the size of the relevant domain in which convection acts and the temperature distribution driving the convection. The reduction relies on snapshots of data of the velocity field derived from high-fidelity simulation studies. First, the assumptions under which the proposed model reduction is admissible are discussed. Then the pre-processing of the sampled data is described: flow domain identification, representation of the velocity field via the stream function and the transformation to a unit domain. The data is decomposed into dominant modes of space and time through SVD. A model for the magnitude of the dominant modes is developed and the reduced model is presented, see Fig. 4.

3.1. Assumptions

The proposed model reduction approach is based on the following assumptions:

- The flow phenomena consist of one or only a few dominant flow patterns.
- The fluid is incompressible and its motion can be fully described in two dimensions, so a scalar stream function exists which defines the velocity field.
- The flow domain varies slowly compared to the time step size. This assumption is justified due to the low thermal conductivity and the high latent heat of PCMs.
- Convection can be neglected during solidification, see Pernsteiner et al. [42]. During discharging, the PCM solidifies on the heat-conducting structure where it acts as an insulator due to its low thermal conductivity. Therefore the temperature gradient in the remaining liquid domain is low and convection becomes negligible.

3.2. Flow domain identification

Representative simulations in Kasper [29] and Pernsteiner et al. [42] show that relevant convection phenomena only occur in a specific region within the entire domain which will be called "primary flow domain" in the following. This primary flow domain $\mathcal{D}_{\text{flow}} = \mathcal{D}_{\text{flow}}(t)$ is identified in the overall domain $\mathcal{D}$ according to the following properties:

- The primary flow domain $\mathcal{D}_{\text{flow}}$ is comprised of liquid PCM, $T(x,y,t) \geqslant T_{\text{m}} + \epsilon$.
- The primary flow domain $\mathcal{D}_{\text{flow}}$ is only considered during charging, since only then relevant convection occurs. This is the case if the temperature at the boundary condition on the left side of the cell domain is greater than the liquidus temperature of the PCM, $T_{\text{in}} \geqslant T_{\text{m}} + \epsilon$. Natural convection is neglected during discharging.
- In case of several melting fronts, only the area directly adjacent to the heated wall with a high temperature gradient is treated as the primary flow domain $\mathcal{D}_{\text{flow}}$. Natural convection is seen to be only relevant in this area. This is characterized by the condition that a simple path must exist in liquid PCM from the lower left corner in the PCM domain $(x,y)_{\text{PCMorigin}}$ to any point in the primary flow domain $(x,y) \in \mathcal{D}_{\text{flow}}$.

The primary flow domain $\mathcal{D}_{\text{flow}}(t) \subseteq \mathcal{D}$ is thus defined as follows:

$$\begin{aligned}\mathcal{D}_{\text{flow}}(t) = \{(x,y) \in \mathcal{D} : T(x,y,t) \geqslant T_{\text{m}} + \epsilon \wedge T_{\text{in}}(t) \geqslant T_{\text{m}} + \epsilon \\ \wedge \exists \text{ simple path in liquid PCM from} (x,y)_{\text{PCMorigin}} \\ \text{to} (x,y) \in \mathcal{D}_{\text{flow}}(t)\}.\end{aligned} \tag{11}$$

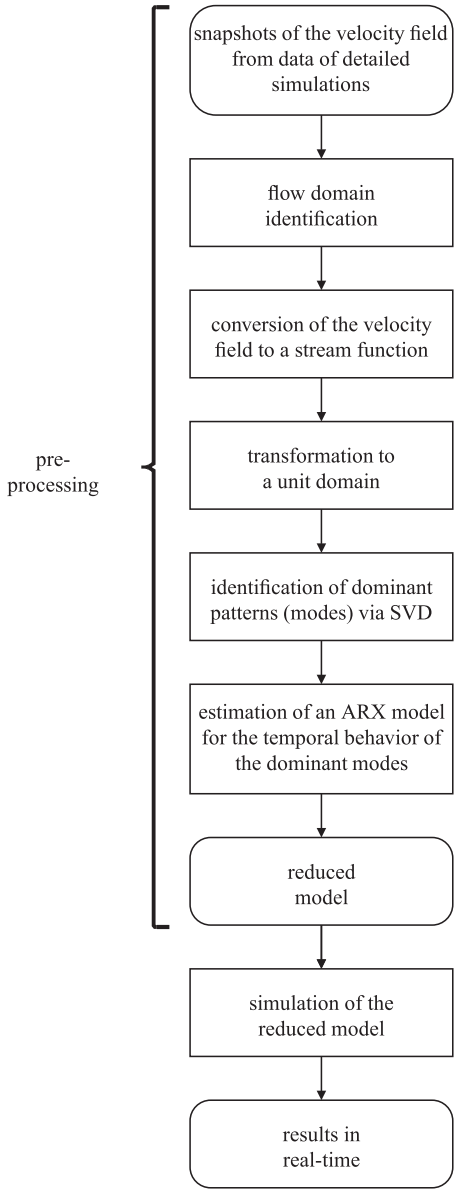

Fig. 4. Flow chart of reduced model creation.

The primary flow domain is the definition area of the stream function and the starting point of the transformation into a unit domain. The proportion of the liquid PCM in the primary flow domain to the entire domain x_{liquid}, with $x_{\text{liquid}} \in [0, 1]$, is introduced as primary flow liquid ratio:

$$x_{\text{liquid}} = \frac{|\mathcal{D}_{\text{flow}}|}{|\mathcal{D}|}. \tag{12}$$

3.3. Stream function

The stream function is a well-known scalar representation to describe a planar velocity field of an incompressible fluid and was first introduced by Lagrange [31]. Partial derivatives of the stream function yield the velocity field, which in turn is automatically divergence-free and thus satisfies the continuity Eq. (2), see Bestehorn [6]. Therefore, the stream function is chosen as a representation of the velocity field and is derived from snapshots of simulation data in this work. The stream function $\Psi = \Psi(x, y, t) : \mathcal{D}_{\text{flow}} \to \mathbb{R}$ is defined through

$$u = \frac{\partial \Psi}{\partial y}, v = -\frac{\partial \Psi}{\partial x}. \tag{13}$$

Therein, u and v are the spatial components of the velocity field $\boldsymbol{u}$ in the spatial x and y-directions.

3.4. Transformation

To account for the varying liquid area of the PCM, the stream function in the time-dependent primary flow domain $\Psi = \Psi(x, y, t) : \mathcal{D}_{\text{flow}}(t) \to \mathbb{R}$ is mapped to a stream function in a time-invariant unit domain $\Psi^* = \Psi^*(\xi, \eta, t) : \mathcal{D}_{\text{unit}} \to \mathbb{R}$ via the coordinate transformation $\Omega : \mathcal{D}_{\text{flow}}(t) \to \mathcal{D}_{\text{unit}}$,

$$\mathcal{D}_{\text{unit}} = \{(\xi, \eta) : 0 \leqslant \xi \leqslant 1, 0 \leqslant \eta \leqslant 1\}, \tag{14}$$

$$(\xi, \eta) = \Omega(x, y), (x, y) = \Omega^{-1}(\xi, \eta), \tag{15}$$

$$\Psi^*(\xi, \eta, t) = \Psi(\Omega(x, y), t), \Psi(x, y, t) = \Psi^*(\Omega^{-1}(\xi, \eta), t), \tag{16}$$

see Fig. 5. The transformation itself depends on the shape of $\mathcal{D}_{\text{flow}}$ and hence ultimately on the temperature field of the solution and is evaluated using equally spaced nodes in x-direction and linear interpolation. This is done with the aim to simplify the flow patterns and ease their treatment as Ψ^* is now defined on a domain of constant shape.

3.5. Singular value decomposition

Sirovich [53] introduced the method of snapshots to efficiently determine POD modes. Therefore, the data set is selected as time snapshots containing the spatial distribution and reflecting the system dynamics. Indicating by Ψ_i^* the vector of values of Ψ^* at the time t_i, the data matrix $\boldsymbol{Z}$,

$$\boldsymbol{Z} = \begin{bmatrix} | & | & & | \\ \Psi_1^* & \Psi_2^* & \dots & \Psi_n^* \\ | & | & & | \end{bmatrix}, \tag{17}$$

consists of n snapshots in time (columns) from the spatial distribution of the stream function values (rows). Dominant modes in time and space are identified from the snapshots. The economy-size SVD is utilized to decompose the snapshot matrix,

$$\boldsymbol{Z} = \boldsymbol{U}\boldsymbol{\Sigma}\boldsymbol{V}^T, \tag{18}$$

by projecting it onto an orthonormal basis given by the left singular vectors $\boldsymbol{U}$. The matrix $\boldsymbol{U}$ contains column-wise the spatial modes, and $\boldsymbol{V}$ represents the temporal behavior of each mode row-wise. The diagonal matrix $\boldsymbol{\Sigma}$ comprises the singular values which indicate the signal energy content of each mode. Identified by the largest singular values, typically only a few modes, represent the major contributions. Their dominant modes can be used as a reduced description of the relevant behavior of the system. The reduced model ($\boldsymbol{U}_{\text{red}}, \boldsymbol{\Sigma}_{\text{red}}$ and $\boldsymbol{V}_{\text{red}}$) is obtained by selecting the corresponding rows/columns from $\boldsymbol{U}, \boldsymbol{\Sigma}and\boldsymbol{V}$, respectively.

3.6. Temporal behavior of the spatial modes

To establish the temporal behavior of the spatial modes, it is common to apply the Galerkin method to project the partial differential equation system onto the spatial basic functions, yielding a system of ordinary differential equations for the modal coordinates. As these projections (numeric integration over the domain) are cumbersome, a different, data-based approach is chosen in this work. The temporal behavior of

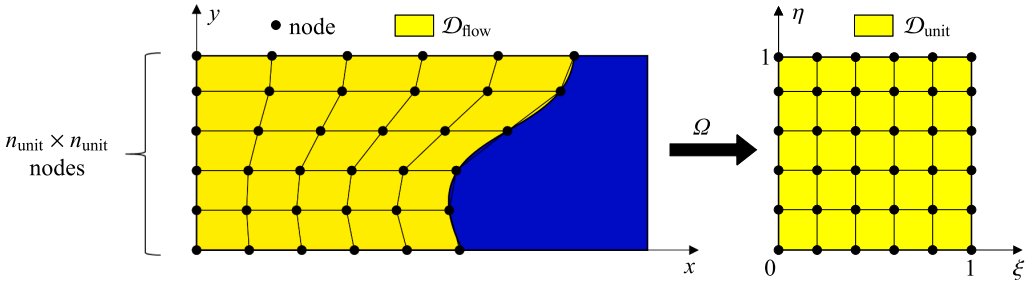

Fig. 5. Transformation of the stream function inside the flow domain (yellow) to a unit domain via linear interpolation. (For interpretation of the references to colour in this figure legend, the reader is referred to the web version of this article.)

the dominant modes given by the matrix V_{red} as well as the magnitude of the velocity field itself seems to depend on quantities of the energy equation, such as the temperature distribution in the PCM or the size of the primary flow domain. Therefore, it is attempted to explain the temporal behavior of the spatial modes V_{red} by the primary flow liquid ratio x_{liquid}, the maximum temperature in the flow domain T_{max}, the maximum temperature difference in the domain T_{spread},

$$T_{\text{spread}} = T_{\text{max}} - T_{\text{min}} \tag{19}$$

with T_{min} as minimum temperature in the domain, and the temperature near the heated wall (left side) in the horizontal symmetry plane of the PCM cell T_{corner}, see Fig. 3. These four measurements,

$$r_1 = T_{\text{spread}}, r_2 = T_{\text{corner}}, r_3 = T_{\text{max}} \ , \textit{and} \ r_4 = x_{\text{liquid}}, \tag{20}$$

form the basis of a cubic polynomial approach for a regressor matrix $\boldsymbol{R}$. In order to consider a switching flow regime in the regressor $\boldsymbol{R}$ at a certain liquid ratio x_{switch}, an activation function γ,

$$\gamma = \frac{1}{1 + \exp\big((x_{\text{switch}} - x_{\text{liquid}}) \cdot 100\big)}, \tag{21}$$

is introduced. The regressor matrix $\boldsymbol{R}$ consists of 62 regressors (columns) at the n snapshots in time (rows) and is defined as follows:

$$\boldsymbol{R} = \begin{bmatrix} | & | & | & | & | & | & | & | \\ r_{\text{con}} & \boldsymbol{r}_{\text{lin}} & \boldsymbol{r}_{\text{qu}} & \boldsymbol{r}_{\text{cub}} & \gamma r_{\text{con}} & \gamma \boldsymbol{r}_{\text{lin}} & \gamma \boldsymbol{r}_{\text{qu}} & \gamma \boldsymbol{r}_{\text{cub}} \\ | & | & | & | & | & | & | & | \end{bmatrix} \tag{22}$$

with

$$r_{\text{con}} = [1], \tag{23}$$

$$\boldsymbol{r}_{\text{lin}} = [r_1 \ r_2 \ r_3 \ r_4], \tag{24}$$

$$\boldsymbol{r}_{\text{qu}} = [r_1^2 \ r_2^2 \ r_3^2 \ r_4^2 \ r_1 r_2 \ r_1 r_3 \tag{25}$$

$$\boldsymbol{r}_{\text{cub}} = [r_1^3 \ r_2^3 \ r_3^3 \ r_4^3 \ r_1^2 r_2 \ r_1^2 r_3 \ r_1^2 r_4 \ r_2^2 r_1 \ r_2^2 r_3 \ r_1 r_4 \ r_2 r_3 \ r_2 r_4 \ r_3 r_4], \tag{26}$$

$$r_2^2 r_4 \ r_3^2 r_1 \ r_3^2 r_2 \ r_3^2 r_4 \ r_4^2 r_1 \ r_4^2 r_2 \ r_4^2 r_3].$$

A matrix $\boldsymbol{\Theta}$ containing the parameter vectors is identified for an ARX model using a least square algorithm:

$$\boldsymbol{\Theta} = (\boldsymbol{R}^T \boldsymbol{R})^{-1} \boldsymbol{R}^T \boldsymbol{V}_{\text{red}}. \tag{27}$$

The estimation of the current magnitude of the spatial modes is then given by

$$\widehat{\boldsymbol{v}}_{\text{red}} = \boldsymbol{r}\boldsymbol{\Theta}, \tag{28}$$

with $\boldsymbol{r}$ as regressor using the current measurement values,

$$\boldsymbol{r} = [\, r_{\text{con}} \quad \boldsymbol{r}_{\text{lin}} \quad \boldsymbol{r}_{\text{qu}} \quad \boldsymbol{r}_{\text{cub}} \quad \gamma r_{\text{con}} \quad \gamma \boldsymbol{r}_{\text{lin}} \quad \gamma \boldsymbol{r}_{\text{qu}} \quad \gamma \boldsymbol{r}_{\text{cub}} \,]. \tag{29}$$

3.7. Reduced model architecture

The reduced model described above consists of an offline pre-processing and an online real-time capable part.

During pre-processing, dominant modes are identified by the SVD of stream function data to obtain a reduced system, $\boldsymbol{U}_{\text{red}}, \boldsymbol{\Sigma}_{\text{red}}$ and $\boldsymbol{V}_{\text{red}}$. An ARX model approximates the modal coordinates $\widehat{\boldsymbol{v}}_{\text{red}}$ of the dominant spatial modes $\boldsymbol{U}_{\text{red}}$ based on four characteristic measurements (20).

Fig. 6 shows the online architecture of the reduced model developed in the section above. It consists of the finite element code of the detailed model for the energy equation. The finite difference approach for the Navier–Stokes equations is replaced by the reduced stream function model,

$$\widehat{\Psi}^* = \boldsymbol{U}_{\text{red}} \boldsymbol{\Sigma}_{\text{red}} \widehat{\boldsymbol{v}}_{\text{red}}^T. \tag{30}$$

After back-transforming the stream function $\widehat{\Psi}^*$ within the unit domain to the stream function $\widehat{\Psi}$ within the primary flow domain, the velocity field is obtained by numeric differentiation and inserted into the energy Eq. (1).

4. Simulation studies

As described in the previous section, our reduction method consists of two parts: the pre-processing/model creation and the real-time model. To demonstrate the novel method, a suitable geometry is first defined and the material parameters are determined. Then simulations are performed to generate training data for the creation of the reduced model. Two additional load profiles are defined to validate the reduced model against the detailed high-fidelity model. Finally it is shown that the reduced model can be calculated on a coarser grid and larger time step without significantly compromising the result.

4.1. Simulation setup

The simulation setup is based on Pernsteiner et al. [42]. The size and shape of a PCM cell has been chosen to allow load profiles on an industrially relevant scale.

In order to demonstrate the capability of the model reduction approach, five different model instances are simulated. The high-fidelity model, which completely solves the Navier–Stokes and energy Eqs. (1)–(3), relies on the code developed by Kasper [29] and is described in Section 2. In addition, it is used to generate training and validation data for the model reduction method. The regular-reduced model fully solves the energy equation, but uses a reduced stream function model instead of the Navier–Stokes equations. The coarse-reduced model is computed on a coarser mesh and larger time step to demonstrate mesh and time step independency of the model reduction approach and is compared to a coarse-high-fidelity model. A conduction-only model, which completely neglects natural convection, acts as a reference simulation.

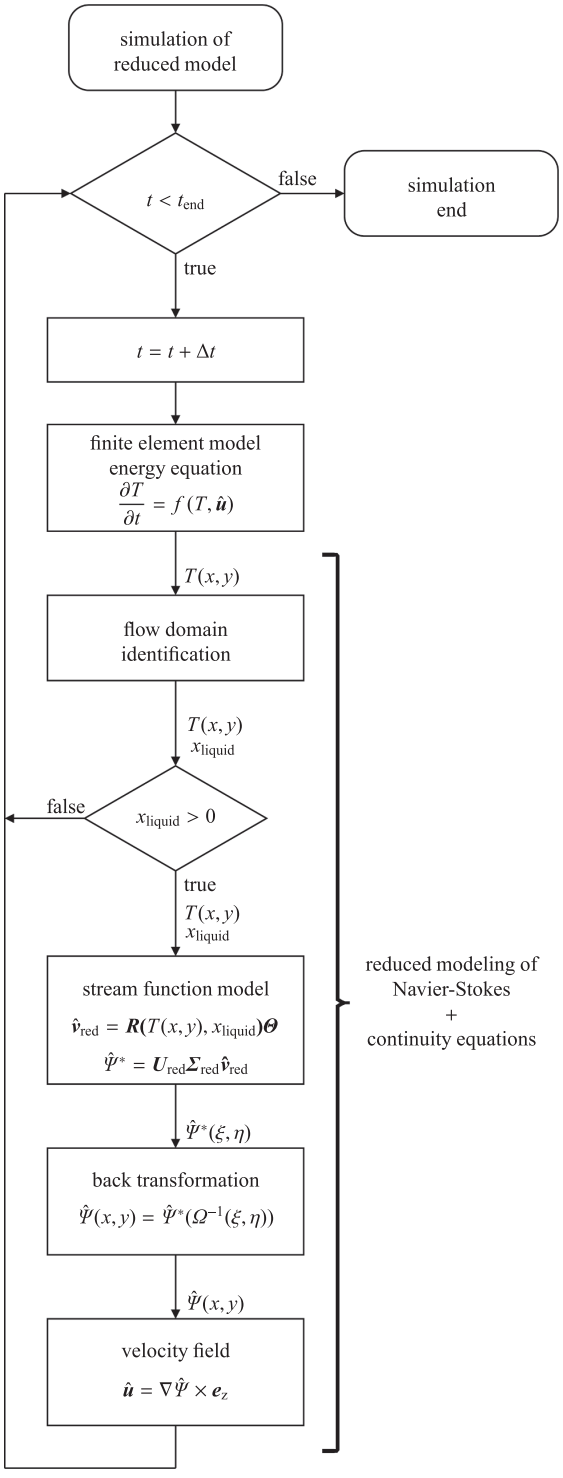

Fig. 6. Flow chart of reduced model architecture.

4.1.1. Geometry

The geometry of the PCM cell is defined in Fig. 3 and Table 1.

An insulation layer is attached to the right side of the PCM cell to reduce heat loss to the environment. The left side of the PCM cell has good heat transfer properties for charging and discharging via heat flows. The assumed heat transfer coefficients are listed in Table 2.

4.1.2. Material parameters

The PCM is an eutectic mixture of potassium nitrate and sodium nitrate KNO_3-$NaNO_3$ (see [59]), enclosed in an aluminum encapsulation. The PCM is either liquid (L) or solid (S). The material properties of the aluminum encapsulation and the PCM are listed in Table 3. The density of solid PCM is used for both phases. A mushy region parameter of $\varepsilon = \pm 0.5$K was chosen. Influence of the variation of this parameter on the result of the high-fidelity simulation was studied in Kasper [29].

4.1.3. Load profiles

The PCM cell is charged/discharged by a heat flow resulting from the temperature difference on its left side (7). The input temperature on the left side, T_{in}, is set as shown in Fig. 7 to generate training and validation data. Five different load profiles are used to train the reduced model: Four load profiles with a constant temperature for 4-h operation time and one load profile with a varying cycle for 5-h operation time. The performance of the reduced model is demonstrated using two 5-h validation load cycles. The right side of the PCM cell is insulated and the temperature responsible for the heat loss, T_{out}, is fixed at 20 °C for all load profiles (8). The initial temperature in the PCM cell is $T_0 = 218$ °C.

4.1.4. Mesh and time step size

A mesh of square elements with a side length of $\Delta x = \Delta y = 0.5$ mm discretizes the geometry of the PCM cell of the high-fidelity model, the conduction-only model and the regular-reduced model. A time step of $\Delta t = 0.1$s is applied for the temporal discretization. These settings resulted as optimal values from an independence study of mesh size and time step. In order to demonstrate the capability of calculating the reduced model on a coarser mesh and larger time step, the side length of the elements and the time step is doubled for the coarse-reduced model. The properties of the different models are summarized in Table 4.

4.1.5. Settings of the reduced model

The reduced model was created as described in Section 3. The data from the high-fidelity simulations are used and only the charging intervals for the model training are considered (since natural convection during discharging is neglected). The SVD of the stream function data results in a single dominant spatial mode, see Fig. 8a. The temporal behavior of this dominant mode is characterized by the ARX model (28)–(21) using properties of the domain, e.g. temperature spread or liquid ratio in the PCM cell. The parameter for a switching flow regime in (21) is set to $x_{switch} = 0.5$ and the excellent fit of the ARX model is shown in Fig. 8b.

4.1.6. Stream function in the original/unit domain

Fig. 9 shows the stream function of the PCM cell using the constant load profile for training ($T_{in} = 235$ °C) at two different times in the original domain and the unit domain. While the shape and expansion of the stream function in the original flow domain differs significantly

Table 1
Geometry of the LHTES.

Dimension	Part	Value
Length L_x	Encapsulation	0.12 m
Width L_y	Encapsulation	0.025 m
Length of cavity Δx_{PCM}	PCM	0.118 m
Width of cavity Δy_{PCM}	PCM	0.023 m

Table 2
Heat transfer coefficient α.

Heat transfer coefficent	Value
For charging/discharging heat flow (left side of PCM cavity) $\frac{\alpha_{\text{in}}}{Wm^{-2}K^{-1}}$	700
For heat losses through insulation (right side of PCM cavity) $\frac{\alpha_{\text{out}}}{Wm^{-2}K^{-1}}$	0.01

Table 3
Material properties of the LHTES.

Property	Alu.	PCM
Density $\frac{\rho}{\text{kgm}^{-3}}$	2700	2050 (S) 1959 (L)
Specific heat capacity $\frac{c}{\text{J(kgK)}^{-1}}$	910	1350 (S) 1492 (L)
Heat conductivity $\frac{k}{\text{W(mK)}^{-1}}$	237	0.457 (S) 0.435 (L)
Melting temperature $\frac{T_{\text{m}}}{^{\circ}\text{C}}$	-	220
Mushy region parameter $\frac{\epsilon}{^{\circ}\text{C}}$	-	± 0.5
Specific latent heat $\frac{h_{\text{latent}}}{\text{kJ(kg)}^{-1}}$	-	108
Thermal expansion coefficient $\frac{\beta}{(\text{K})^{-1}}$	-	$3.5 \cdot 10^{-4}$
Dynamic viscosity $\frac{\mu}{\text{Ns(m)}^{-2}}$	-	$5.8 \cdot 10^{-4}$

between the two time points, the two stream functions are very similar in the unit domain. Such a stream function results in a nearly circular shaped vortex.

4.2. Results

The results are evaluated under two aspects: accuracy and computational effort. These criteria are compared between the five different models listed in Table 4.

4.2.1. Solution accuracy

The stored enthalpy in the PCM cell is essential in order to assess the state of charge and to control the LHTES. Therefore, Fig. 11 compares the stored normalized enthalpy,

$$H_{\text{norm}}(t) = \frac{H(t) - H_0}{H_{\text{latent}}} \tag{31}$$

of the different models for the training and validation load cases, respectively. In (31) H_0 is the initial enthalpy and H_{latent} the latent heat of the PCM cell. The overall error is listed in Table 5. As a second criterion, the shape and progression of the melting fronts in the PCM are evaluated qualitatively, see Fig. 12.

4.2.2. Computational effort

The computational effort is assessed through the real-time factor,

$$RTF = \frac{t_{\text{comp}}}{t_{\text{end}}}, \tag{32}$$

which is listed for the different models in Table 5. Eq. (32) consists of the computation time t_{comp} required to simulate a PCM cell until the end time t_{end}. The computation was performed using MATLAB® on the processor Intel® Core™; i7-8550U with a base frequency of 1.8 GHz.

Table 4
Model characterization, mesh and time step size.

Type	Energy equation	Navier–Stokes equations	Mesh size $\frac{\Delta x}{\text{mm}}$	Time step $\frac{\Delta t}{\text{s}}$
High-fidelity model	Finite element	Finite difference	0.5	0.1
Conduction-only model	Finite element	Neglected	0.5	0.1
Regular-reduced model	Finite element	Stream function reduction method	0.5	0.1
Coarse-reduced model	Finite element	Stream function reduction method	1	0.2
Coarse-high-fidelity model	Finite element	Finite difference	1	0.2

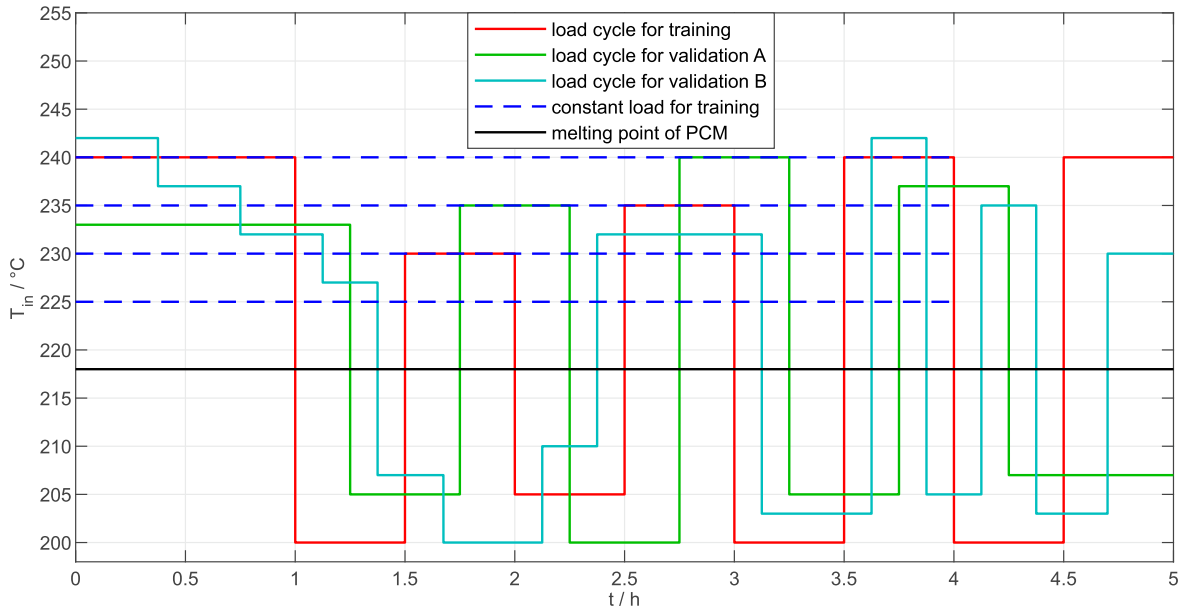

Fig. 7. Load profiles for training and validation of the reduced order model in the simulation studies.

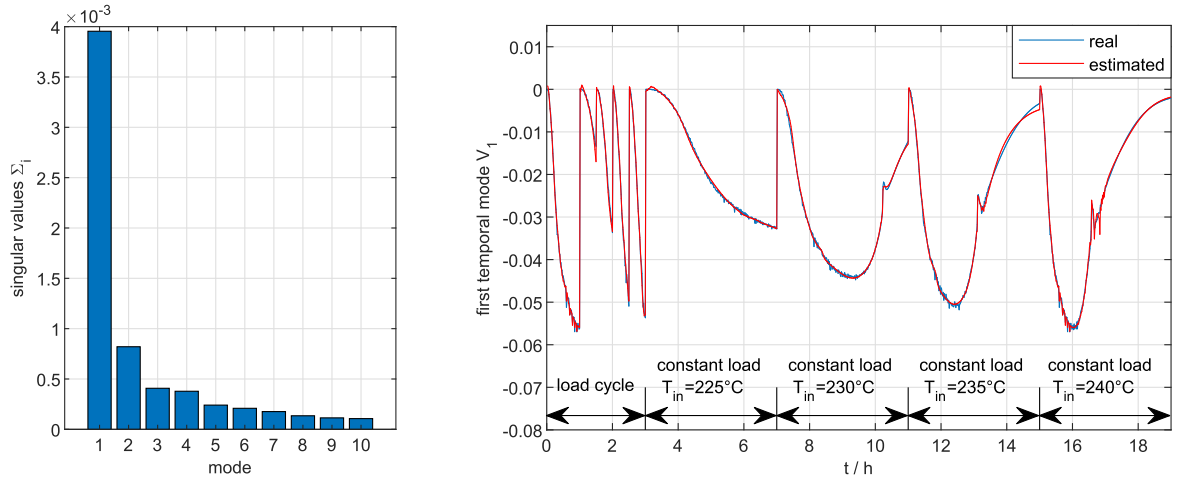

Fig. 8. Singular values Σ_i of the first ten modes (a) and the first temporal mode V_1 as well as its estimation by the ARX model for the training data (b).

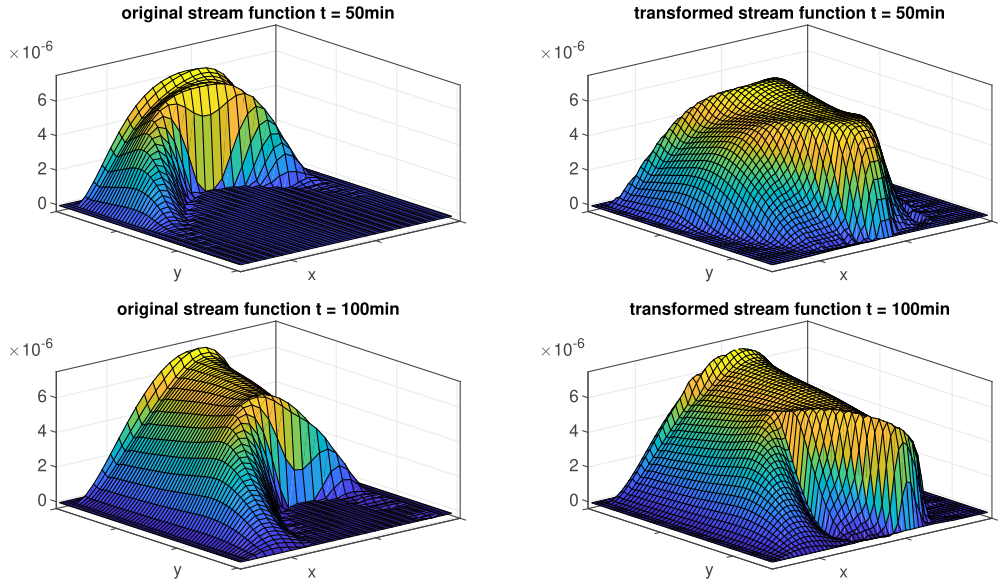

Fig. 9. Stream function of the PCM cell using the constant load profile ($T_{in} = 235$ °C) after 50 min (above) and 100 min (below) in the original domain (left) and in the unit domain (right).

5. Discussion

At the end, the stored enthalpy of the regular-reduced model and the coarse-reduced model is 7.9% and 7.1% lower for the validation load cycle A as well as 3.3% and 5.8% lower for the validation load cycle B than of the high-fidelity model, respectively. The coarse-high-fidelity model differs by 6.3% and 3.7% and the conduction-only model shows an error of 35.4% and 26.5% for the validation load cycles A and B, respectively, see Fig. 11 and Table 5. The coarse-reduced model is as good as the regular-reduced model, but more than 8 times faster and even 44 times faster than the high-fidelity model. Therefore, the coarse-reduced model requires only 0.65 h instead of 28.6 h computation time for 5 h simulation time. Fig. 10 shows a comparison between accuracy and computation time. A coarsening of the grid and an enlargement of the time step causes a significant decrease in accuracy in the high-fidelity model, but not in the reduced model. The shape and progression of the melting fronts is slightly different between the reduced and the high-fidelity models, but still in good agreement after multiple charging/discharging cycles, see Fig. 12 for the validation load cycle A. Therefore, the reduced models are able to accurately estimate the state of charge, determine the location of the melting fronts, as well as serve as a basis to control the LHTES in real-time.

5.1. Mesh coarsening and time step enlargement

Solving the Navier–Stokes equations is often sensitive with respect to the chosen spatial discretization $\Delta x = \Delta y$ of the high-fidelity model. The spatial discretization, in turn, determines the discrete time step Δt of the

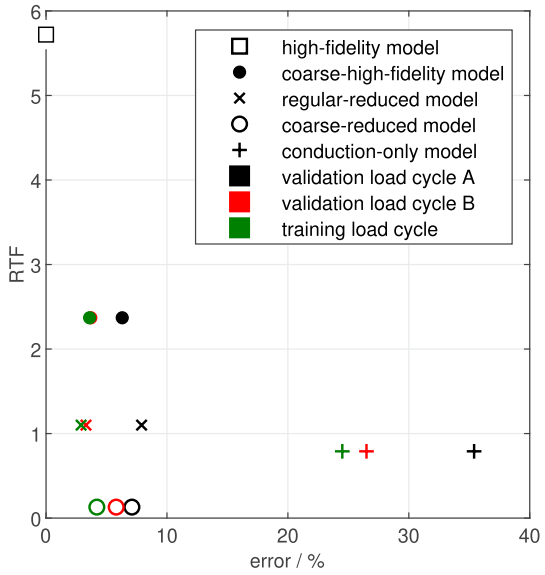

Fig. 10. Pareto efficiency - a comparison of accuracy and computation speed (*RTF*) of the different models.

simulation. The relationship between $\Delta t, \Delta x$ and the velocity u is given by the Courant-Friedrich-Lewy number,

$$CFL = \frac{u\Delta t}{\Delta x}, \tag{33}$$

which should be less than 1 to correctly resolve convective heat transfer, see Lewy [33]. The *CFL* number indicates the maximum number of cells which a considered quantity passes through per time step. In the novel model reduction approach, the computation of the Navier–Stokes equations is replaced by a stream function model. Mesh and time step sizes are therefore only limited by the solution of the energy equation through the finite element model. As a result it is seen that the mesh can be significantly coarsened and the time step can be enlarged. This reduces the computational effort enormously while maintaining high accuracy.

Table 5
Real-time factor *RTF* and error of the different models according to validation load cycle A and B.

Model	*RTF*	Error in % case A	Error in % case B
High-fidelity (reference)	5.72	0	0
Coarse-high-fidelity	2.37	6.3	3.7
Conduction-only	0.79	35.4	26.5
Regular-reduced	1.1	7.9	3.3
Coarse-reduced	0.13	7.1	5.8

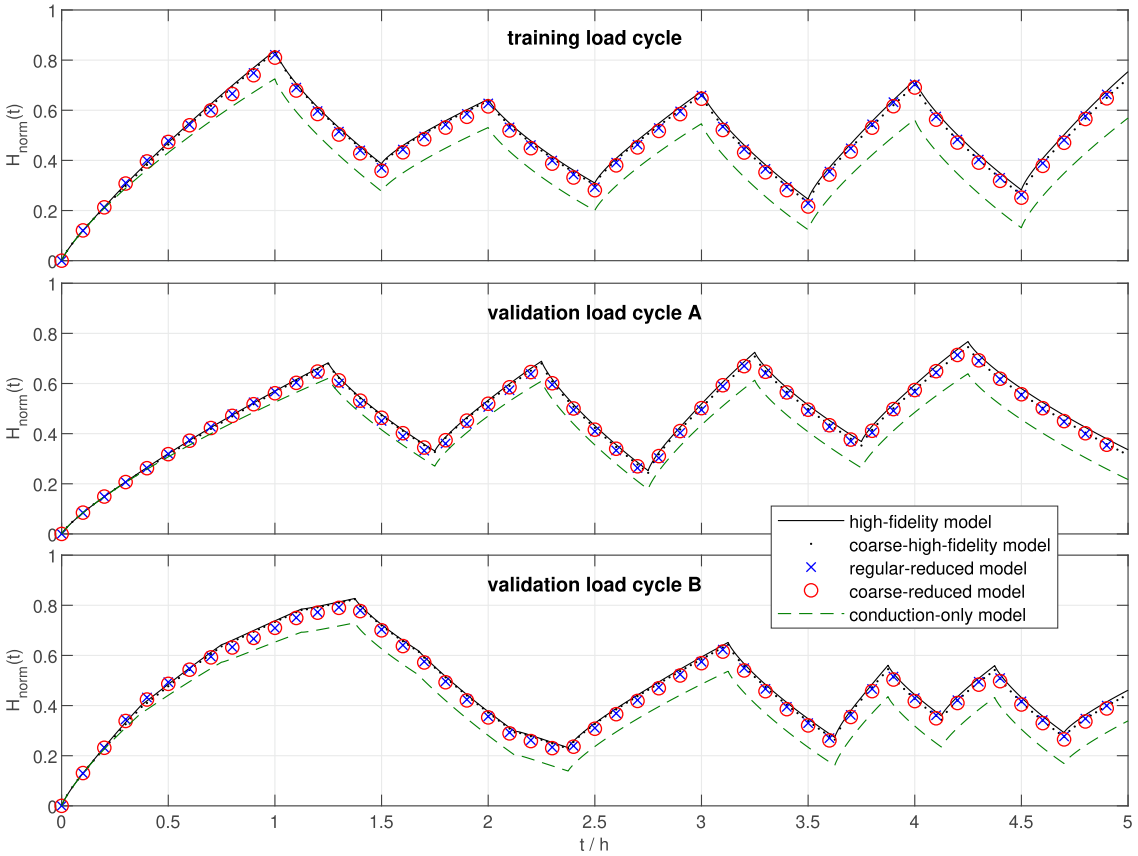

Fig. 11. Normalized enthalpy content of the four models in the training load cycle (top) and the validation load cycles A and B (beneath).

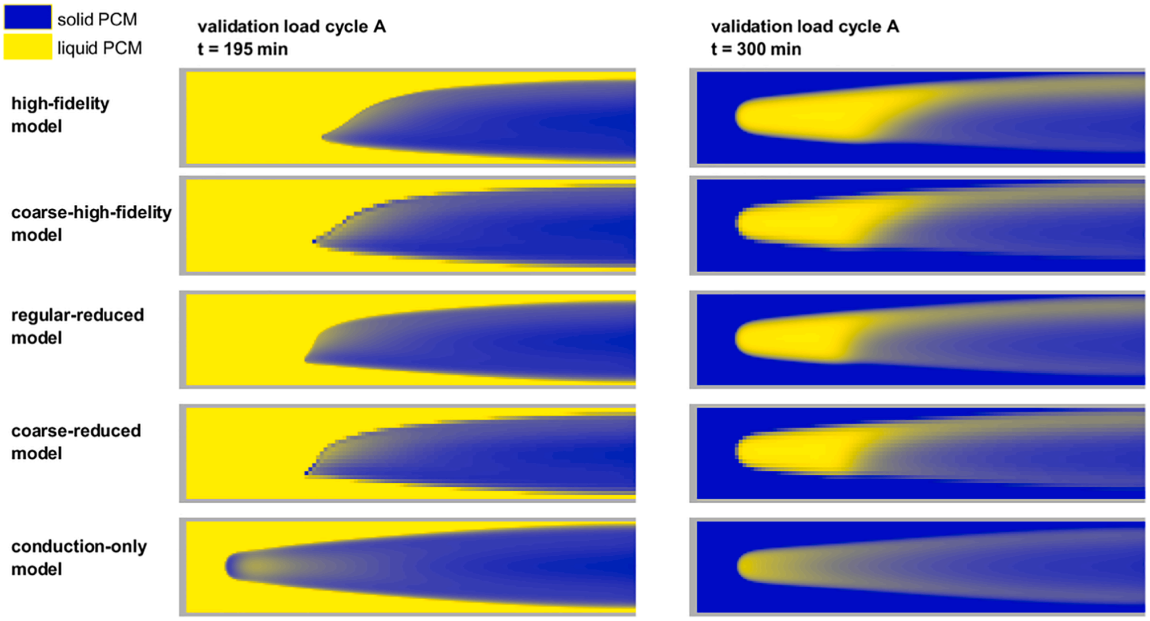

Fig. 12. Melting fronts in the PCM cell after 195 min (left) and 300 min (right) of the simulation of the validation load cycle A.

5.2. Further improvements

As seen above, the results of the proposed model reduction method are highly satisfactory. In order to further improve the model reduction approach in future work, two aspects are highlighted below: the transformation of the stream function into a unit domain and the decomposition of the stream function using SVD.

5.2.1. Transformation

The transformation of the stream function into a unit domain utilizes a simple and robust linear interpolation. This distributes the arising distortions evenly, but also leads to a distorted mapping of the flow's boundary layers. Additionally, the authors studied piecewise-linear mapping approaches that are designed to keep the boundary layers undistorted, but the similarity of the transformed stream function could not be further improved yet. Still, more complex transformations that seek to accurately represent the boundary layer structure while compressing the wake interior could yield a simpler stream function representation via the SVD method and should thus be studied deeper in the future.

5.2.2. Radial basis functions

The dominant modes are extracted from the stream function via SVD. The dominant modes approximate the grid values of the stream function optimally. For the proposed model reduction approach, however, the velocities, i.e., the spatial partial derivatives of the stream function are the actual quantities of interest. Selecting more than one mode for the model reduction approach improves the grid values but not necessarily their derivatives. In an improvement of the presented method, the SVD weighting could be adjusted to focus on the precision of representing the partial derivatives of the stream function and radial basis functions could be utilized to represent the stream function modes and allow to evaluate accurate derivatives of the stream function.

6. Conclusions

The model reduction method for dominant flow patterns developed in this work replaces the Navier–Stokes equations with a reduced stream function model. The stream function model is data-based and parametrized from simulations of a high-fidelity model. In order to consider the solution-dependent flow region (melting and solidification processes), the stream function is mapped from the original flow domain to a unit domain. While the shape and size of the stream function differ greatly in the original domain at different times, the transformed stream functions show similar shape. The reduction of the stream function model is SVD-based and the velocity field of the flow domain can be reconstructed solely from properties of the flow domain, e.g. the temperature distribution. The reduced model can be computed on a coarser grid and therefore on a larger time step without significantlydecreasing its accuracy.

The novel contribution of this work is the easily adaptable reduction technique for problems with varying domains. Its accuracy and computational speed is demonstrated in simulation studies. The reduced model can be computed up to 44 times faster than the high-fidelity model. In the validation cases, the reduced models yielded a maximum error of 7.9% instead of 35.4% error caused by a conduction-only model that completely neglects natural convection. Thus the reduced model is sufficient for the intended applications of state of charge estimation and model-based control of an LHTES. The model captures the dominant dynamics and the remaining uncertainties, which are in the range of the actual accuracy of the numerical model of 3%, can be compensated by an observer or a controller, respectively. To further improve the reduction efficiency, radial basis functions and an advanced transformation of the stream function are emphasized.

Declaration of Competing Interest

The authors declare that they have no known competing financial interests or personal relationships that could have appeared to influence the work reported in this paper.

Acknowledgements

The Climate and Energy Fund KLIEN/FFG funded a research project in 2018 that has recently started: HyStEPs Grant No. 868842. The authors also want to acknowledge the support provided by the doctoral

school Smart Industrial Concept [SIC!] (https://sic.tuwien.ac.at). The authors would furthermore like to thank Professor Stefan Braun for the helpful suggestions and valuable discussions on this topic.

References

[1] F. Agyenim, N. Hewitt, P. Eames, M. Smyth, A review of materials, heat transfer and phase change problem formulation for latent heat thermal energy storage systems (LHTESS), Renew. Sustain. Energy Rev. 14 (2010) 615–628, https://doi.org/10.1016/j.rser.2009.10.015.

[2] A. Antoulas, D. Sorensen, S. Gugercin, A survey of model reduction methods for large systems, Contemporary Mathe. 280 (2001), https://doi.org/10.1090/conm/280/04630.

[3] A. Armaou, P.D. Christofides, Computation of empirical eigenfunctions and order reduction for nonlinear parabolic PDE systems with time-dependent spatial domains, Nonlinear Anal.: Theory Methods Appl. 47 (2001) 2869–2874, https://doi.org/10.1016/S0362-546X(01)00407-2.

[4] A. Astolfi, Model reduction by moment matching for linear and nonlinear systems, IEEE Trans. Autom. Control 55 (2010) 2321–2336, https://doi.org/10.1109/TAC.2010.2046044.

[5] P. Benner, S. Gugercin, K. Willcox, A survey of projection-based model reduction methods for parametric dynamical systems, SIAM Rev. 57 (2015) 483–531, https://doi.org/10.1137/130932715.

[6] M. Bestehorn, Hydrodynamik und Strukturbildung, Springer-Verlag, Berlin, 2006.

[7] D. Bistrian, I. Navon, An improved algorithm for the shallow water equations model reduction: Dynamic Mode Decomposition vs POD, Int. J. Numer. Meth. Fluids 78 (2015) 552–580, https://doi.org/10.1002/fld.4029.

[8] C. Bonacina, G. Comini, A. Fasano, M. Primicerio, Numerical solution of phase-change problems, Int. J. Heat Mass Transf. 16 (1973) 1825–1832, https://doi.org/10.1016/0017-9310(73)90202-0.

[9] N.S. Bondareva, B. Buonomo, O. Manca, M.A. Sheremet, Heat transfer inside cooling system based on phase change material with alumina nanoparticles, Appl. Therm. Eng. 144 (2018) 972–981, https://doi.org/10.1016/j.applthermaleng.2018.09.002.

[10] N.S. Bondareva, M.A. Sheremet, Conjugate heat transfer in the PCM-based heat storage system with finned copper profile: Application in electronics cooling, Int. J. Heat Mass Transf. 124 (2018) 1275–1284, https://doi.org/10.1016/j.ijheatmasstransfer.2018.04.040.

[11] J. Boussinesq, Theorie analytique de la chaleur, vol. 2, Gauthier-villars, Paris, 1903.

[12] A.D. Brent, V.R. Voller, K.J. Reid, Enthalpy-porosity technique for modeling convection-diffusion phase change: Application to the melting of a pure metal, Numerical Heat Transfer 13 (1988) 297–318, https://doi.org/10.1080/10407788808913615.

[13] S. Brunton, J. Proctor, J. Kutz, Discovering governing equations from data: Sparse identification of nonlinear dynamical systems, Proc. Nat. Acad. Sci. 113 (2015) 3932–3937, https://doi.org/10.1073/pnas.1517384113.

[14] F. Chinesta, A. Huerta, G. Rozza, K. Willcox, Model Reduction Methods, American Cancer Society, 2017, pp. 1–36, https://doi.org/10.1002/9781119176817.ecm2110.

[15] F. Chinesta, P. Ladeveze, E. Cueto, A short review on model order reduction based on proper generalized decomposition, Arch. Comput. Methods Eng. 18 (2011) 395–404, https://doi.org/10.1007/s11831-011-9064-7.

[16] A.J. Chorin, Numerical solution of the Navier-Stokes equations, Mathe. Comput. 22 (1968) 745–762, https://doi.org/10.1090/S0025-5718-1968-0242392-2.

[17] G. Comini, S. Del Guidice, R.W. Lewis, O.C. Zienkiewicz, Finite element solution of non-linear heat conduction problems with special reference to phase change, Int. J. Numer. Meth. Eng. (1974), https://doi.org/10.1002/nme.1620080314.

[18] J.L. Dauvergne, E.P. del Barrio, Toward a simulation-free POD approach for low-dimensional description of phase-change problems, Int. J. Therm. Sci. 49 (2010) 1369–1382, https://doi.org/10.1016/j.ijthermalsci.2010.02.006.

[19] J. Donea, S. Giuliani, H. Laval, L. Quartapelle, Finite element solution of the unsteady navier-stokes equations by a fractional step method, Comput. Methods Appl. Mech. Eng. 30 (1982) 53–73, https://doi.org/10.1016/0045-7825(82)90054-8.

[20] A. Dumon, C. Allery, A. Ammar, Proper general decomposition (PGD) for the resolution of Navier-Stokes equations, J. Comput. Phys. 230 (2011) 1387–1407, https://doi.org/10.1016/j.jcp.2010.11.010.

[21] Y. Dutil, D.R. Rousse, N.B. Salah, S. Lassue, L. Zalewski, A review on phase-change materials: Mathematical modeling and simulations, Renew. Sustain. Energy Rev. 15 (2011) 112–130, https://doi.org/10.1016/j.rser.2010.06.011.

[22] M. Fogleman, J. Lumley, D. Rempfer, D. Haworth, Application of the proper orthogonal decomposition to datasets of internal combustion engine flows, J. Turbul. 5 (2004) N23, https://doi.org/10.1088/1468-5248/5/1/023.

[23] B. Fortunato, S. Camporeale, T. Marco, M. Albano, Simple mathematical model of a thermal storage with PCM, AASRI Procedia 2 (2012) 241–248, https://doi.org/10.1016/j.aasri.2012.09.041.

[24] A. Gil, M. Medrano, I. Martorell, A. Lázaro, P. Dolado, B. Zalba, L.F. Cabeza, State of the art on high temperature thermal energy storage for power generation. Part 1—Concepts, materials and modellization, Renew. Sustain. Energy Rev. 14 (2010) 31–55, https://doi.org/10.1016/j.rser.2009.07.035.

[25] K. Glover, All optimal Hankel-norm approximations of linear multivariable systems and their error bounds, Int. J. Control 39 (1984) 1115–1193, https://doi.org/10.1080/00207178408933239.

[26] S. Gugercin, A.C. Antoulas, A survey of model reduction by balanced truncation and some new results, Int. J. Control 77 (2004) 748–766, https://doi.org/10.1080/00207170410001713448.

[27] M. Huang, P. Eames, B. Norton, Comparison of a small-scale 3D PCM thermal control model with a validated 2D PCM thermal control model, Sol. Energy Mater. Sol. Cells 90 (2006) 1961–1972, https://doi.org/10.1016/j.solmat.2006.02.001.

[28] N. Ibrahim, F. Al-Sulaiman, S. Rahman, B. Yilbas, A. Sahin, Heat transfer enhancement of phase change materials for thermal energy storage applications: A critical review, Renew. Sustain. Energy Rev. 74 (2017) 26–50, https://doi.org/10.1016/j.rser.2017.01.169.

[29] L. Kasper, Modeling of the Phase Change Material of a Hybrid Storage Using the Finite Element Method, TU Wien Academic Press, Wien, 2020, https://doi.org/10.34727/2020/isbn.978-3-85448-037-2 (in press).

[30] J.N. Kutz, Deep learning in fluid dynamics, J. Fluid Mech. 814 (2017) 1–4, https://doi.org/10.1017/jfm.2016.803.

[31] J.L. Lagrange, Mémoire sur la théorie du mouvement des fluides, Œuvres complètes. Nouveaux mémoires de l'Académie royale des sciences et belles-lettres de Berlin, année 1781, 1781.

[32] T. Lassila, A. Manzoni, A. Quarteroni, G. Rozza, Model order reduction in fluid dynamics, Challenges Perspect. 9 (2014), https://doi.org/10.1007/978-3-319-02090-7_9.

[33] H. Lewy, K. Friedrichs, R. Courant, Über die partiellen differenzengleichungen der mathematischen physik, Math. Ann. 100 (1928) 32–74, https://doi.org/10.1007/BF01448839.

[34] E. Liberge, A. Hamdouni, Reduced order modelling method via proper orthogonal decomposition (POD) for flow around an oscillating cylinder, J. Fluids Struct. 26 (2010) 292–311, https://doi.org/10.1016/j.jfluidstructs.2009.10.006.

[35] S. Liu, Y. Li, Y. Zhang, Mathematical solutions and numerical models employed for the investigations of PCMs phase transformations, Renew. Sustain. Energy Rev. 33 (2014) 659–674, https://doi.org/10.1016/j.rser.2014.02.032.

[36] Y. Liu, B.D.O. Anderson, Singular perturbation approximation of balanced systems, Int. J. Control 50 (1989) 1379–1405, https://doi.org/10.1080/00207178908953437.

[37] J.L. Lumley, The structure of inhomogeneous turbulence, Atmosph. Turbulence Wave Propagat. (1967) 166–178.

[38] B. Moore, Principal component analysis in linear systems: Controllability, observability, and model reduction, IEEE Trans. Autom. Control 26 (1981) 17–32, https://doi.org/10.1109/TAC.1981.1102568.

[39] A. Narasingam, J.S.I. Kwon, Development of local dynamic mode decomposition with control: Application to model predictive control of hydraulic fracturing, Comput. Chem. Eng. 106 (2017) 501–511, https://doi.org/10.1016/j.compchemeng.2017.07.002.

[40] B. Nedjar, An enthalpy-based finite element method for nonlinear heat problems involving phase change, Comput. Struct. 80 (2002) 9–21, https://doi.org/10.1016/S0045-7949(01)00165-1.

[41] D. Néron, P. Ladeveze, Proper Generalized Decomposition for Multiscale and Multiphysics Problems, Arch. Comput. Methods Eng. 17 (2010) 351–372, https://doi.org/10.1007/s11831-010-9053-2.

[42] D. Pernsteiner, L. Kasper, A. Schirrer, R. Hofmann, S. Jakubek, Co-simulation methodology of a hybrid latent-heat thermal energy storage unit, Appl. Therm. Eng. (2020), https://doi.org/10.1016/j.applthermaleng.2020.115495.

[43] V. Prasad, B. Bequette, Nonlinear system identification and model reduction using artificial neural networks, Comput. Chem. Eng. 27 (2003) 1741–1754, https://doi.org/10.1016/S0098-1354(03)00137-6.

[44] K. Radhakrishnan, A. Balakrishnan, Heat transfer analysis of thermal energy storage using phase change materials, Heat Recovery Syst. CHP 12 (1992) 427–435, https://doi.org/10.1016/0890-4332(92)90064-O.

[45] T. Reis, T. Stykel, A survey on model reduction of coupled systems. 13 (2008) 133–155. doi:10.1007/978-3-540-78841-6_7.

[46] C.W. Rowley, Model reduction for fluids, using balanced proper orthogonal decomposition, Int. J. Bifurcat. Chaos 15 (2005) 997–1013, https://doi.org/10.1142/S0218127405012429.

[47] C.W. Rowley, T. Colonius, R.M. Murray, Model reduction for compressible flows using POD and Galerkin projection, Physica D 189 (2004) 115–129, https://doi.org/10.1016/j.physd.2003.03.001.

[48] C.W. Rowley, S.T. Dawson, Model reduction for flow analysis and control, Annu. Rev. Fluid Mech. 49 (2017) 387–417, https://doi.org/10.1146/annurev-fluid-010816-060042.

[49] O. San, R. Maulik, Machine learning closures for model order reduction of thermal fluids, Appl. Math. Model. 60 (2018) 681–710, https://doi.org/10.1016/j.apm.2018.03.037.

[50] P.J. Schmid, Dynamic mode decomposition of numerical and experimental data, J. Fluid Mech. 656 (2010) 5–28, https://doi.org/10.1017/S0022112010001217.

[51] B. Seibold, A compact and fast Matlab code solving the incompressible Navier-Stokes equations on rectangular domains, http://math.mit.edu/gs/cse/codes/mit18086_navierstokes.pdf, 2008.

[52] H.S. Sidhu, A. Narasingam, P. Siddhamshetty, J.S.I. Kwon, Model order reduction of nonlinear parabolic PDE systems with moving boundaries using sparse proper orthogonal decomposition: Application to hydraulic fracturing, Comput. Chem. Eng. 112 (2018) 92–100, https://doi.org/10.1016/j.compchemeng.2018.02.004.

[53] L. Sirovich, Turbulence and the dynamics of coherent structures Part I: coherent structures, Q. Appl. Math. XLV (1987) 561–571, https://doi.org/10.1090/qam/910462.

[54] G. Stabile, G. Rozza, Finite volume POD-Galerkin stabilised reduced order methods for the parametrised incompressible Navier-Stokes equations, Comput. Fluids 173 (2018) 273–284, https://doi.org/10.1016/j.compfluid.2018.01.035.

[55] R. Swischuk, L. Mainini, B. Peherstorfer, K. Willcox, Projection-based model reduction: Formulations for physics-based machine learning, Comput. Fluids 179 (2019) 704–717, https://doi.org/10.1016/j.compfluid.2018.07.021.
[56] Y. Tao, Y.L. He, A review of phase change material and performance enhancement method for latent heat storage system, Renew. Sustain. Energy Rev. 93 (2018) 245–259, https://doi.org/10.1016/j.rser.2018.05.028.
[57] R. Tenchev, J. Mackenzie, T. Scanlon, M. Stickland, Finite element moving mesh analysis of phase change problems with natural convection, Int. J. Heat Fluid Flow 26 (2005) 597–612, https://doi.org/10.1016/j.ijheatfluidflow.2005.03.003.
[58] J.H. Tu, C.W. Rowley, D.M. Luchtenburg, S.L. Brunton, J. Nathan Kutz, On dynamic mode decomposition: Theory and applications, J. Comput. Dyn. 1 (2014) 391–421, https://doi.org/10.3934/jcd.2014.1.391.
[59] J. Vogel, J. Felbinger, M. Johnson, Natural convection in high temperature flat plate latent heat thermal energy storage systems, Appl. Energy 184 (2016) 184–196, https://doi.org/10.1016/j.apenergy.2016.10.001.
[60] S. Volkwein, Model reduction using proper orthogonal decomposition, 2011. Lecture Notes, University of Konstanz. http://www.math.uni-konstanz.de/numerik/personen/volkwein/teaching/POD-Vorlesung.pdf, 2011.
[61] Z. Wang, D. Xiao, F. Fang, R. Govindan, C.C. Pain, Y. Guo, Model identification of reduced order fluid dynamics systems using deep learning, Int. J. Numer. Meth. Fluids 86 (2018) 255–268, https://doi.org/10.1002/fld.4416.
[62] B. Zalba, J.M. Marin, L.F. Cabeza, H. Mehling, Review on thermal energy storage with phase change: materials, heat transfer analysis and applications, Appl. Therm. Eng. 23 (2003) 251–283, https://doi.org/10.1016/S1359-4311(02)00192-8.

2.3 Publication C

D. Pernsteiner, A. Schirrer, L. Kasper, R. Hofmann, and S. Jakubek. "State estimation concept for a nonlinear melting/solidification problem of a latent heat thermal energy storage". In: *Computers & Chemical Engineering* 153 (2021), p. 107444. DOI: 10.1016/j.compchemeng.2021.107444

Applicant's contribution [†]

- Dominik Pernsteiner: Conceptualization, Formal analysis, Investigation, Methodology, Software, Visualization, Writing - original draft
- Alexander Schirrer: Conceptualization, Supervision, Writing - review & editing
- Lukas Kasper: Software, Writing - review & editing
- René Hofmann: Funding acquisition, Supervision, Writing - review & editing
- Stefan Jakubek: Conceptualization, Funding acquisition, Supervision, Writing - review & editing

[†]According to the Elsevier CRediT author statement: https://www.elsevier.com/authors/policies-and-guidelines/credit-author-statement

Computers and Chemical Engineering 153 (2021) 107444

Contents lists available at ScienceDirect

Computers and Chemical Engineering

journal homepage: www.elsevier.com/locate/compchemeng

State estimation concept for a nonlinear melting/solidification problem of a latent heat thermal energy storage

Dominik Pernsteiner[a,c,d,*], Alexander Schirrer[a,c], Lukas Kasper[b,c], René Hofmann[b,c], Stefan Jakubek[a,c]

[a] TU Wien, Institute of Mechanics and Mechatronics, Getreidemarkt 9/BA, Vienna 1060, Austria
[b] TU Wien, Institute for Energy Systems and Thermodynamics, Getreidemarkt 9/BA, Vienna 1060, Austria
[c] TU Wien, Austria
[d] Institute for Mechanics and Mechatronics, TU Wien, Getreidemarkt 9/E325, Vienna 1060, Austria

ARTICLE INFO

Article history:
Received 18 February 2021
Revised 1 July 2021
Accepted 4 July 2021
Available online 7 July 2021

Keywords:
Extended Kalman filter
Phase change material
Nonlinear distributed-parameter system
Singular value decomposition
Balanced truncation

ABSTRACT

Latent heat thermal energy storages (LHTES) utilize a material's phase transition to store energy at an almost constant temperature. To fully exploit their high energy density, reliable state estimation is essential, which requires a suitable model-based observer. In previous works, high-precision and real-time-capable models have been developed to solve the arising coupled Navier-Stokes and energy equations. In the present work, these high-order nonlinear models are applied to predict (simulate) the states of the LHTES one time step ahead. Then, an extended Kalman filter uses a reduced-order observer model derived from the prediction model by linearization and balanced truncation to compute a state update based on measurements. This approach increases both, computational efficiency and performance, since the observer can only update the state of the prediction model compliant to its dominant behavior. Different types of measurements can be accurately combined in the observer, resulting in fast convergence despite model errors.

1. Introduction

1.1. Motivation

More than two-thirds of the energy consumed in the industry is generated by the conversion of fossil fuels and thus contributes to the increase in carbon dioxide emissions, see Napp et al. (2014). Thermal energy storage systems (TES) are essential to replace these fossil fuels with renewable energy sources despite their volatile nature. TES decouple energy supply and consumption, which leads to greater flexibility and thus to higher performance of the entire energy system.

TES can rely on different physical and chemical principles, depending on the required operating conditions, see Gil et al. (2010). This work focuses on latent heat thermal energy storages (LHTES), which consist of phase change material (PCM) to store energy through phase transition processes at an almost constant temperature. PCM has high energy density but low thermal conductivity, see Agyenim et al. (2010) and Zalba et al. (2003). To increase the low thermal conductivity, heat-conducting structures are often integrated, as summarized by Tao and He (2018) and Ibrahim et al. (2017). Such a heat conduction enhancement by aluminum fins is shown in a typical LHTES configuration in Fig. 1. In this configuration, a section bounded by two adjacent fins is referred to as PCM cell, whose state estimation is the subject of this work. The above-mentioned characteristics of complex energy-temperature dependency and low conductivity pose a significant challenge to the state estimation, which in turn is crucial for an efficient implementation of LHTES in industrial applications. The task of the state observer developed within this work is to estimate the distributed system state (temperature distribution and enthalpy content) by only a few measurements on the basis of an accurate model. Moreover, the observation should show high performance despite the expected presence of model errors.

1.2. Innovation

In this work, an observer based on the extended Kalman filter (EKF) is developed, which can accurately reconstruct the thermodynamic state of an LHTES using only a few measurements of

* Corresponding author at: Institute for Mechanics and Mechatronics, TU Wien, Getreidemarkt 9/E325, 1060 Vienna, Austria.
E-mail address: dominik.pernsteiner@tuwien.ac.at (D. Pernsteiner).

https://doi.org/10.1016/j.compchemeng.2021.107444

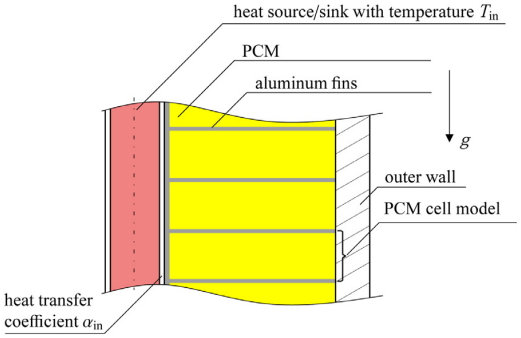

Fig. 1. scheme of a typical LHTES configuration with PCM and aluminum fins for heat transfer enhancement.

temperature and other measures such as PCM volume. In contrast to the standard EKF, two different model complexities are employed. The observer uses a nonlinear real-time-capable PCM cell model for prediction. This high-order prediction model is comprised of the Navier-Stokes and the energy equations to represent the dominant effects of natural convection and conduction in the melting/solidification problem. In order to update the state predictions, a linear low-order observer model is incorporated in the EKF. The observer model is obtained by successively linearizing the high-order prediction model and reducing it via balanced truncation to increase the computational efficiency and improve the performance of the observer. In order to account for parameter mismatches and allow a targeted intervention of the observer, the states of the observer model are extended by selected parameters to be estimated, such as the heat transfer coefficient α_{in} between the heat source/sink and the PCM cell. An EKF-based observer uses the system matrices of the low-order observer model as the system equations' Jacobians, resulting in accurate and well-converging state estimates. The newly proposed observer structure for the nonlinear melting/solidification problem is tested with both, an incorrect initialization and an incorrect model parameterization, under realistic load conditions. The method is able to find the correct state of charge and accurately estimates the melting front in different test scenarios, using only a few temperature sensors and a PCM volume measurement. The observer is tested with simulated measurements generated by a more detailed, but not real-time-capable, high-fidelity model, which produces a slightly different temperature distribution. Furthermore, the sensor selection is discussed, and a mode-shape-based placement criterion for temperature sensors is provided. The novel contributions of this work are the proposed observer concept for high-order nonlinear melting/solidification problems, its insensitivity against model errors, and the considered simulation study.

In the following literature overview, relevant observer approaches for nonlinear distributed-parameter systems are presented. Then, the state of the art regarding phase change models, which serve as the basis for the observer, is highlighted. Finally, reduction techniques to efficiently tackle high-order systems in observation and control tasks are outlined.

1.3. Observers for distributed-parameter systems

Observers/estimators (used synonymously in this work) can be divided into two main categories according to their underlying system dynamics: (1) lumped-parameter systems are described by ordinary differential equations, and (2) distributed-parameter systems are described by partial differential equations and are thus, here, space- and time-dependent. Both types of systems can show linear or nonlinear behavior.

The most well-known observer techniques for linear systems are the Luenberger observer (Luenberger (1966)) and the Kalman filter in its discrete and continuous forms (Kalman (1960) and Kalman and Bucy (1961)), in which white Gaussian noise for model and measurement errors is considered. Many subsequently developed observers are modifications thereof. For nonlinear system extensions of these observers, see, e.g., Jazwinski (1970) and Wishner et al. (1969).

In general, observers have been addressed in numerous reviews, see, e.g., Mohd Ali et al. (2015) and Dochain (2003) for chemical process systems. Daum (2005) compares nonlinear filters in a tutorial-style work, while Patwardhan et al. (2012) focussed on the development of Bayesian estimators, both involving different types of the Kalman filter. Afshar et al. (2015) analyzed different observer designs for the heat equation.

There are two main approaches for distributed-parameter systems: early- and late-lumping. For the early-lumping approach, the infinite-dimensional solutions of the system are approximated by a finite-dimensional spatial representation, such as finite elements or other discretization methods, resulting in a system of ordinary differential equations. For the late-lumping approach, the infinite-dimensional character is retained to analyze the system but also to design controllers or observers. In early-lumping, the Kalman filter is a well-known method. An unscented Kalman filter is reviewed by Julier and Uhlmann (2004), and a broad overview of different unscented Kalman filter formulations is given by Kolås et al. (2009). Examples for an EKF with unknown inputs, where the unknown inputs are considered as part of the states, can be found in Yang et al. (2007) and Ghahremani and Kamwa (2011). Another well-known early-lumping observer type is based on the sliding mode approach, which provides robustness to possible discrepancies between the model and the actual system, see, for example, Drakunov and Utkin (1992). In late-lumping, on the other hand, Bitzer and Zeitz (2002) based their observer design on the injection of correction functions into the model equations and boundary conditions. Other promising late-lumping designs have been found in the backstepping method, see Jadachowski et al. (2014).

A comparison of early-lumping, in the form of an unscented Kalman filter, versus late-lumping, using a distributed-parameter observer, is conducted by Kreuzinger et al. (2008) to estimate the state of a stratified storage tank. In Marko et al. (2018), an early-lumping EKF outperformed two late-lumping observers, in the form of a Lyapunov-based and a backstepping-based design. In this work, an early-lumping approach is employed for state estimation of the phase change problem by first discretizing the characterizing equations via finite elements and then applying an EKF to the discretized system.

In previous approaches for state estimation of phase change processes, Akkari et al. (2006) successfully applied an EKF to microwave defrosting using a finite volume model. Backi et al. (2014) and Backi et al. (2016) presented a state observer for freezing processes based on the EKF and a finite difference model. Barz et al. (2018) designed a nonlinear state observer for a liquid/solid LHTES using an EKF, a collocation method to model the energy balance equations, and temperature sensors. Zsembinszki et al. (2020) summed up the common practices to evaluate the state of charge of liquid/solid LHTES. However, the state estimators developed so far are based on modeling simplifications, such as the neglect of convection. They would therefore not fully describe the dominant system behavior in the present general phase change problem. The observer approach applied in this work can handle high-order models and thus consider all relevant heat transfer effects.

The problem associated with the EKF and high-order systems is, first, computational complexity (see, e.g., Mohd Ali et al. (2015)) and, second, that most systems are not observable when the full state dimension is considered. Therefore, reduced-order EKFs were the subject of various research projects. Park et al. (2013) developed a reduced-order EKF, in which two EKFs with reduced-order models were operated in parallel, instead of one high-order EKF. Lee et al. (2007) combined the reduced model of the EKF with a measurement noise model and data rejection to account for model errors caused by the model simplification. Khodadadi and Jazayeri-Rad (2011) applied a dual EKF design to estimate states and parameters separately, and turned off the parameter estimator after reaching the optimal values to reduce the computational load. Potocki and Tharp (1993) reduced the model order of the EKF by balanced truncation to estimate the temperature distribution in hyperthermia treatment of cancer. In order to track storms, Farrell and Ioannou (2001) applied a Kalman filter to a high-order model by computing a Kalman gain obtained from a reduced system, which was derived from balanced truncation.

The observer approach presented in this work combines already existing techniques to estimate the states in a phase change process (such as an LHTES) while taking into account all relevant heat transfer effects, such as natural convection and conduction. Therefore, the phase change problem is first described by a real-time-capable high-order nonlinear model already existing in the literature. In order to apply the EKF to the high-order system, reduction via balanced truncation is made. The main procedure is to use the fine-grained, but real-time-capable, nonlinear simulation model to predict and a successively linearized reduced-order (dominant-states only) model to update the simulated model state via an appropriate EKF-based estimator. This approach leads to an increased computational speed and renders the estimation insensitive against model errors. Different types of measurements, such as temperature and volume, are combined in the observer to estimate the state efficiently.

1.4. PCM modeling approach

The two most relevant heat transfer mechanisms occurring in low-viscosity PCMs are conduction and natural convection. Dutil et al. (2011) and Liu et al. (2014) review options for mathematical modeling of PCM. Analytical solutions only exist for a limited number of melting/solidification problems, such as the one-dimensional Stefan-problem, see Radhakrishnan and Balakrishnan (1992). Fortunato et al. (2012) state that the effect of natural convection is widely neglected in modeling PCM thermal storage systems due to its complexity. However, Vogel et al. (2016) and Kasper et al. (2021) found a significant heat transfer enhancement due to convection for low-viscosity PCM depending on the geometry of its enclosure.

When modeling multidimensional heat conduction in PCMs, numerical methods such as the enthalpy method or the effective heat capacity method, summarized in Liu et al. (2014), must be applied. Nedjar (2002) states that especially finite element methods are able to handle coupled thermomechanical problems with complex boundary conditions. The effective heat capacity method and finite elements were, for example, applied by Tenchev et al. (2005) to solve a conduction and natural convection phase change problem. In a similar approach, Kasper (2020) used the effective heat capacity method and an adaptation of the finite difference code, published by Seibold (2008), for the two-dimensional Navier-Stokes equations in convection modeling. This experimentally validated coupled finite element/difference model was adapted in Kasper et al. (2021) to study the melting and solidification process of different PCM geometries, and in Pernsteiner et al. (2020), for a co-simulation methodology of a Ruths steam storage surrounded by PCM cells.

The computation of the relevant heat transfer effects with finite element and finite difference methods, as proposed by Kasper (2020), requires high computational effort and leads to simulation models which typically cannot be computed in or faster than real-time as needed for observation and control tasks. Therefore, Pernsteiner et al. (2021) developed a model reduction approach to short-cut the laborious solution of the Navier-Stokes equations by a data-based stream function model with high accuracy, which is adopted and built on in this work.

1.5. Reduction methods for high-order systems

To efficiently model, analyze and simulate systems with high order, model reduction approaches are used to reduce the system dynamics' complexity while maintaining their dominant behavior. Especially model reduction in linear systems is well established, and the research topic has been covered in numerous reviews, see, e.g., Antoulas (2004) and Benner et al. (2015). The preferred method in this work is the balanced truncation, where the system is transformed to a basis in which the hard-to-reach states are simultaneously difficult to observe and are simply eliminated by truncation to obtain the reduced model. This method was first introduced by Moore (1981), and a short overview of implementations is given by Gugercin and Antoulas (2004). Other model reduction methods for linear systems are the Hankel-norm approximation and the singular perturbation methods, see Glover (1984) and Liu and Anderson (1989), respectively. It is noted that in this work the balanced realization is constructed for linearized implicit system equations with sparse coefficient matrices, for which special numerical tools as in Castagnotto et al. (2017) are available.

1.6. Main contributions

To the best of the authors' knowledge, no observer approach has been presented so far to estimate the state of a complex melting/solidification phase change problem, taking into account the effects of conduction and convection. The main contributions of this paper are as follows:

- An efficient observer approach for a high-order nonlinear distributed-parameter phase change problem is developed based on a combination of existing modeling, reduction, and observer design methods.
- The observer shows high performance and robust behavior, as it can update the system only according to its dominant behavior and combines different types of measurements.
- A mode-shape-based sensor placement criterion by analyzing sensitivities is applied and discussed.
- Simulation studies are conducted and analyzed, showing the effectiveness and accuracy of the proposed method, even despite model errors. The new approach leads to excellent convergence and is able to find both, the correct state of charge and the melting front.

1.7. Paper structure

The paper is organized as follows: In Section 2, the PCM cell model and its fundamental equations are presented. Section 3 describes the overall observer structure as well as the reduction of the linearized high-order model and the EKF. In Section 4, a sensor placement strategy using mode shapes is devised. In Section 5, simulation studies to demonstrate the effectiveness of the proposed observer framework are performed.

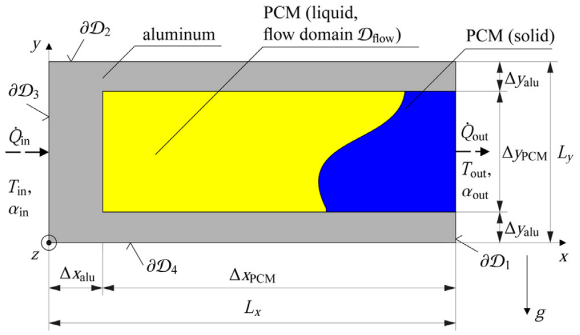

Fig. 2. illustration of the considered PCM cell with dimensions and modeled heat flows $\dot{Q}_{\text{in}}$ and $\dot{Q}_{\text{out}}$ (resulting from heat transfer boundary conditions with temperatures T_{in} and T_{out} as well as heat transfer coefficients α_{in} and α_{out}, respectively).

2. PCM cell model

The observer approach is demonstrated using a two-dimensional rectangular PCM domain with aluminum fins as heat-conducting structures. For reasons of symmetry, modeling of an LHTES configuration, as illustrated in Fig. 1, is reduced to a single so-called PCM cell, consisting only of one fin section of the storage, see Fig. 2. The high-fidelity PCM cell model, developed by Kasper (2020) and described in Section 2.1, is the basis for the model reduction approach from Pernsteiner et al. (2021). This reduced nonlinear model, described in Section 2.2, is real-time-capable with high accuracy and is therefore implemented in the observer to predict the state.

2.1. High-fidelity PCM cell model

A detailed multi-phase thermodynamic model, including melting/solidification, heat conduction, and natural convection in two dimensions, is considered for the PCM cell, developed and thoroughly documented in Kasper (2020). It is based on the conservation laws of energy, mass, and momentum resulting in the energy Eq. (1), continuity Eq. (2), and Navier-Stokes Eq. (3) as follows:

$$\rho c \frac{\partial T}{\partial t} = \lambda \nabla \cdot (\nabla T) - \rho c (\boldsymbol{v} \cdot \nabla) T, \tag{1}$$

$$\nabla \cdot \boldsymbol{v} = 0, \text{ and} \tag{2}$$

$$\rho \frac{\partial \boldsymbol{v}}{\partial t} + \rho (\boldsymbol{v} \cdot \nabla) \boldsymbol{v} - \mu \nabla \cdot (\nabla \boldsymbol{v}) = \boldsymbol{f}(T) - \nabla p_{\text{PCM}}. \tag{3}$$

Therein, the temperature field $T = T(x, y, t)$ is treated as the dependent variable in the energy Eq. (1), and the velocity field $\boldsymbol{v} = [u, v]^T$ with spatial components $u(x, y, t)$ and $v(x, y, t)$ is treated as the dependent variable in the Navier-Stokes Eqs. (2)–(3), see Chorin (1968). The variable p_{PCM} represents the pressure in the PCM. The symbols ρ, c, λ, and μ denote the parameters density, apparent heat capacity

$$c(T) = \begin{cases} c_{\text{S}} & \text{if: } T < T_{\text{m}} - \varepsilon \\ \frac{\Delta l_{\text{m}} + c_{\text{S}} \cdot (T_{\text{m}} + \varepsilon - T) + c_{\text{L}} \cdot (T - (T_{\text{m}} + \varepsilon))}{2\varepsilon} & \text{if: } T_{\text{m}} - \varepsilon \leq T \\ & \quad T \leq T_{\text{m}} + \varepsilon \\ c_{\text{L}} & \text{if: } T > T_{\text{m}} + \varepsilon \end{cases}, \tag{4}$$

thermal conductivity, and dynamic viscosity, respectively. The phase transition takes place in a small temperature range referred to as "*mushy region*" $[T_{\text{m}} - \varepsilon, T_{\text{m}} + \varepsilon]$, which is defined by the melting temperature T_{m} and the mushy region width parameter ε. The force density $\boldsymbol{f}$ describes the buoyancy force

$$\boldsymbol{f} = \rho \boldsymbol{g} \cong \rho_0 \boldsymbol{g} (1 - \beta (T - T_{\text{ref}})), \tag{5}$$

which is calculated via the Boussinesq approximation by the volumetric thermal expansion coefficient β, the constant (reference) density ρ_0, a reference temperature T_{ref}, and the gravitational standard acceleration vector $\boldsymbol{g}$.

The time-dependent energy Eq. (1) is discretized using a standard Galerkin finite element (FE) approach with four-noded bilinear rectangular elements, and the incompressible Navier-Stokes Eqs. (2)–(3) are solved via finite differences. The obtained velocity field is applied in the next time step of the energy equation.

2.1.1. Boundary conditions

On the upper and lower sides of the PCM cell, the domain boundaries are modeled as adiabatic,

$$\boldsymbol{q}|_{\partial\mathcal{D}_2,\, \partial\mathcal{D}_4} = \boldsymbol{0}. \tag{6}$$

For the left and right boundaries, type-3 boundary conditions, also known as Robin or heat-transfer boundary conditions,

$$\boldsymbol{q}|_{\partial\mathcal{D}_3} = \alpha_{\text{in}} (T(x, y, t) - T_{\text{in}}) \text{ and} \tag{7}$$

$$\boldsymbol{q}|_{\partial\mathcal{D}_1} = \alpha_{\text{out}} (T(x, y, t) - T_{\text{out}}), \tag{8}$$

are prescribed following Newton's law of cooling, where $\alpha_{\text{in}}, \alpha_{\text{out}}$ are heat transfer coefficients, $\boldsymbol{q}$ is the specific heat flux across the boundary, and $T_{\text{in}}, T_{\text{out}}$ present boundary temperatures at the left and right wall surfaces, respectively.

Regarding the velocity field $\boldsymbol{v} = [u, v]^T$, no-slip boundary conditions are set for the domain boundaries,

$$\boldsymbol{v}|_{\partial\mathcal{D}} = \boldsymbol{0}. \tag{9}$$

Furthermore, the velocity is set to zero wherever the PCM temperature lies below its liquidus temperature,

$$\boldsymbol{v}|_{T < T_{\text{m}} + \varepsilon} = \boldsymbol{0}. \tag{10}$$

2.2. Reduced nonlinear and real-time-capable model

The model presented above is able to simulate heat transfer by convection and conduction in PCM with high accuracy. Still, it cannot be computed in real-time for adequate problem sizes and on standard computing units. To achieve real-time capability, the model reduction method developed by Pernsteiner et al. (2021) is applied. This reduction method is applicable when the system exhibits simple convective dominant flow patterns. Then, the Navier-Stokes and continuity equations are replaced by a simplified data-based stream function model, but the energy equation is fully solved via the FE model, see Fig. 3. Therein, the state vector $\boldsymbol{x}_k$ contains the temperatures at the nodes of the FE model for the time step k. The input vector $\boldsymbol{u}$ is composed of the temperatures at the boundary surfaces $T_{\text{in},k}$ and $T_{\text{out},k}$, and the approximated velocity field $\hat{\boldsymbol{v}}_{k-1}$ is derived from the stream function model.

In order to develop the data-based stream function model, snapshots of the stream function Ψ, defined by

$$\begin{aligned} u = \frac{\partial \Psi}{\partial y},\ v = -\frac{\partial \Psi}{\partial x}, \\ \Psi = \Psi(x, y, t) : \mathcal{D}_{\text{flow}}(t) \to \mathbb{R}, \text{ and} \\ \mathcal{D}_{\text{flow}}(t) = \left\{ (x, y) \in \mathcal{D} : T(x, y, t) \geq T_{\text{m}} + \epsilon \wedge T_{\text{in}}(t) \geq T_{\text{m}} + \epsilon \right\}, \end{aligned} \tag{11}$$

are derived from the velocity field obtained in reference simulation studies using the high-fidelity model from Section 2.1. In order to consider the solution-dependent flow region due to melting and solidification processes, the stream function is mapped from the original flow domain to a solution-independent unit domain. Then, the stream function snapshots are decomposed into modes of space and time using singular value decomposition (SVD). The temporal behavior $\boldsymbol{V}_{\text{red}}$ of the dominant spatial modes $\boldsymbol{U}_{\text{red}}$ can

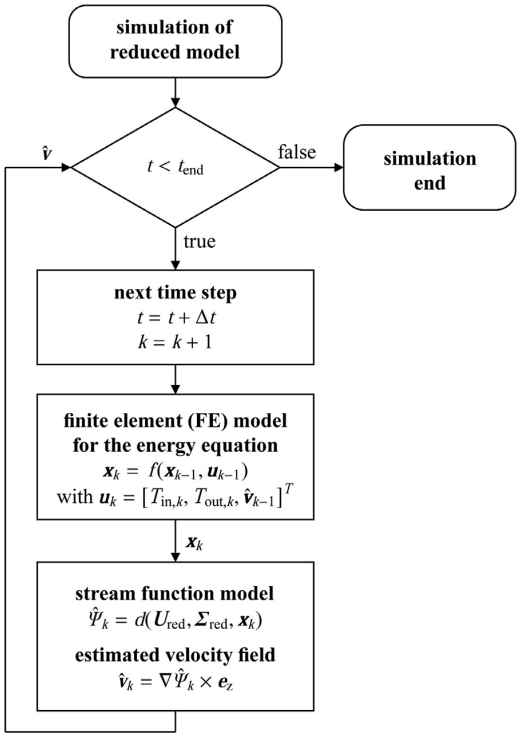

Fig. 3. flow chart of reduced model architecture.

be reconstructed by the temperature field solution of the energy equation. As a result, the estimated stream function $\hat{\Psi}_k$ is a function of the dominant spatial modes $\boldsymbol{U}_{\text{red}}$ with their singular values $\boldsymbol{\Sigma}_{\text{red}}$ and the states resulting from the solution of the energy equation $\boldsymbol{x}_k$,

$$\hat{\Psi}_k = d(\boldsymbol{U}_{\text{red}}, \boldsymbol{\Sigma}_{\text{red}}, \boldsymbol{x}_k). \tag{12}$$

The stream function model can replace the Navier-Stokes and continuity equations. The reduced model is no longer limited by the solver requirements of the Navier-Stokes equations and is therefore robust with respect to mesh and time step enlargement. Thus, a real-time capable model is available that serves as the prediction model in the observer framework and is suitable for reliable state estimation.

3. Observer framework

In contrast to the standard EKF, two different model complexities are employed. Therefore, the presented observer approach uses a high-order nonlinear, but real-time-capable, prediction model to predict (simulate) the states of the PCM cell one time step ahead. Then, a low-order observer model is derived from the prediction model by linearizing it around the current trajectory (state estimate), subsequently reducing it to its dominant behavior via balanced truncation, and finally augmenting its states by selected parameters to be additionally estimated. The observer model system matrices serve as Jacobians in an EKF. The EKF computes a state update of the prediction model according to the difference between the measurements taken from reality and the predicted model outputs, see Fig. 4. This structure leads to a reliable state estimation with increased computational speed and improved performance because the observer intervention is restricted to the dominant behavior of the system.

In the following Section, predicted quantities are denoted by the superscript "$^-$" and estimated quantities by "$\hat{}$", so that the predicted state estimates are denoted by $\hat{\boldsymbol{x}}^-$, for example. To estimate the state of a PCM cell as described above, the following steps are carried out in the observer structure as illustrated in Fig. 4.

3.1. Measurements

Measurements are taken from an LHTES system (reality) and provided to the observer along with the predicted (simulated) model outputs to compute updated state estimates.

3.2. Prediction model

The discrete-time prediction model is simulated forward in time to evolve the model states $\boldsymbol{x}$ and outputs $\boldsymbol{y}$,

$$\boldsymbol{x}_k = f(\boldsymbol{x}_{k-1}, \boldsymbol{u}_{k-1}) \text{ and} \tag{13}$$

$$\boldsymbol{y}_k = h(\boldsymbol{x}_k), \tag{14}$$

where k is the time step index with a chosen time step length Δt, so $t_k = k\Delta t$, and signals with subscript k denote their values at time $t = t_k = k\Delta t$. The function $f(\boldsymbol{x}_{k-1}, \boldsymbol{u}_{k-1})$ expresses the state updates at the next time step based on the first-order differential equations of the model, and $h(\boldsymbol{x}_k)$ is the nonlinear function mapping the states to the model outputs $\boldsymbol{y}_k$, which correspond to the available measurements.

The underlying equations of (13) are based on the reduced nonlinear model described in Section 2.2, which are solved with a backward Euler scheme. Using the finite-element representation and applying Galerkin's method of weighted residuals (see Pepper and Heinrich (2005)), the phase change problem (1)–(13) results in a continous-time implicit system of high-order ordinary differential equations of the form

$$\boldsymbol{J}(\boldsymbol{x}, \boldsymbol{u})\dot{\boldsymbol{x}} + \boldsymbol{K}(\boldsymbol{x}, \boldsymbol{u})\boldsymbol{x} = \boldsymbol{R}(\boldsymbol{x}, \boldsymbol{u}), \tag{15}$$

with the large but sparse system matrices $\boldsymbol{J}$, $\boldsymbol{K}$ and the right-hand-side vector $\boldsymbol{R}$.

3.3. Observer model

The prediction model is nonlinear and of high order m, $m \in \mathcal{O}(10^{3\ldots4})$. To obtain Jacobians for an efficient EKF implementation, a linear low-order observer model is derived from the prediction model by first linearizing it around the current trajectory. Then, balanced truncation reduces the observer model to r remaining dominant modes, $r \in \mathcal{O}(10^1)$. Finally, the reduced model states are extended by a selected parameter to be estimated. The system matrices of this observer model serve as the Jacobians of the EKF. Since they evolve slowly in the present phase change problem, they are only recomputed every n_{lin}th time steps, $n_{\text{lin}} \in \mathbb{N}^+$. For the observer model system matrices, the time index is omitted for reasons of brevity.

3.3.1. Linearization

The successive linearization (see Zhakatayev et al. (2017)) of (15) at the current states and inputs $\left(\boldsymbol{x}(t_{k-1}), \boldsymbol{u}(t_{k-1})\right)$ leads to the continuous-time system in descriptor form,

$$\boldsymbol{E}_c \Delta\dot{\boldsymbol{x}} = \boldsymbol{A}_c \Delta\boldsymbol{x} + \boldsymbol{B}_c \Delta\boldsymbol{u} \text{ and} \tag{16}$$

$$\Delta\boldsymbol{y} = \boldsymbol{C}_c \Delta\boldsymbol{x}, \tag{17}$$

where Δ indicates the deviations from the current trajectory, $\boldsymbol{x}$ is the state vector consisting of the temperature field represented by

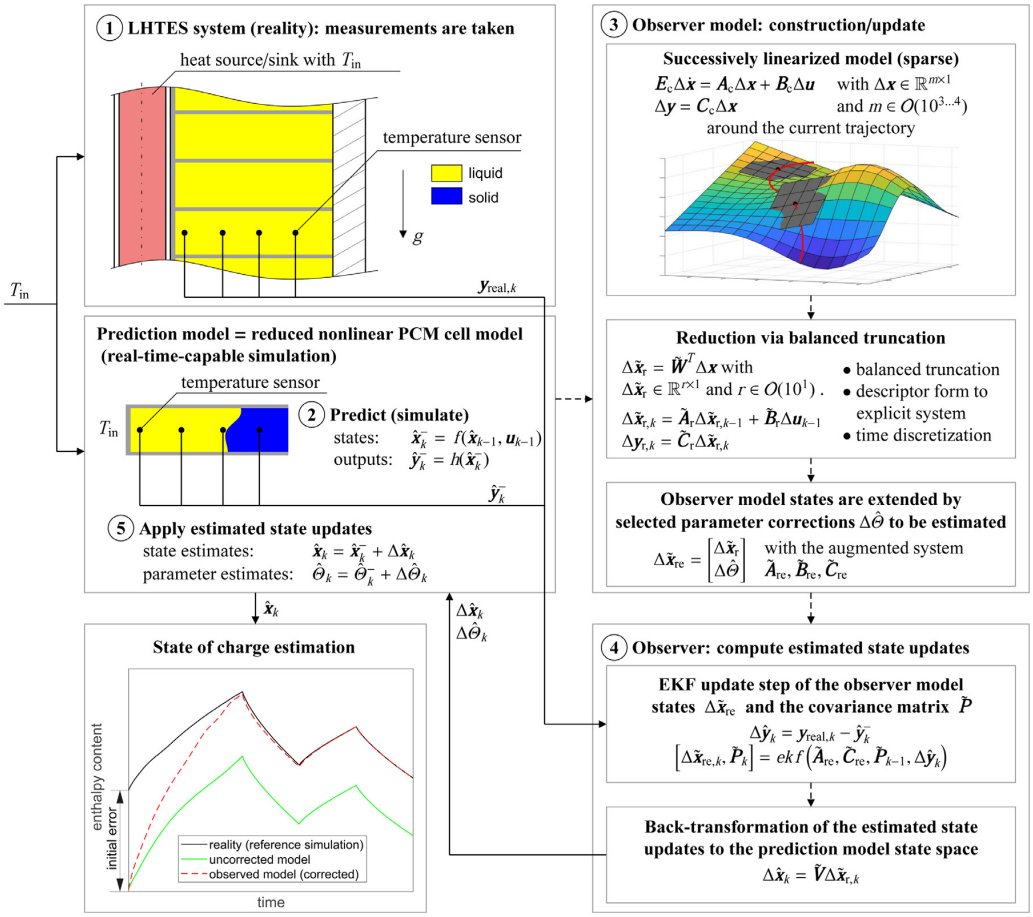

Fig. 4. structure of the observer with signal (solid line) and process flow (dashed line). The circled numbers illustrate the processing order.

the FE nodal temperatures, and $\boldsymbol{y}$ the output vector modeling the measurements. The input vector $\boldsymbol{u}$ consists of the temperature at the left wall T_{in}, the temperature at the right wall T_{out}, and a selected parameter to be estimated Θ, such as the potentially unknown heat transfer coefficient α_{in}. In (16)–(17), the matrices are

$$\boldsymbol{A}_c = -\boldsymbol{K}(\boldsymbol{x}(t_{k-1}), \boldsymbol{u}(t_{k-1})), \tag{18}$$

$$\boldsymbol{E}_c = \boldsymbol{J}(\boldsymbol{x}(t_{k-1}), \boldsymbol{u}(t_{k-1})), \tag{19}$$

and the observation matrix $\boldsymbol{C}_c$, which maps the states to the outputs. The input matrix $\boldsymbol{B}_c$ is comprised of

$$\boldsymbol{B}_c = \begin{bmatrix}\boldsymbol{b}_i & \dots & \boldsymbol{b}_{n_u}\end{bmatrix} \text{ with} \tag{20}$$

$$\boldsymbol{b}_i = \left(\frac{d\boldsymbol{R}}{du_i}\bigg|_{\substack{\boldsymbol{x}(t_{k-1})\\ \boldsymbol{u}(t_{k-1})}} - \frac{d\boldsymbol{K}}{du_i}\bigg|_{\substack{\boldsymbol{x}(t_{k-1})\\ \boldsymbol{u}(t_{k-1})}}\boldsymbol{x}(t_{k-1}) - \frac{d\boldsymbol{J}}{du_i}\bigg|_{\substack{\boldsymbol{x}(t_{k-1})\\ \boldsymbol{u}(t_{k-1})}}\dot{\boldsymbol{x}}(t_{k-1})\right) \text{ and} \tag{21}$$

$$\dot{\boldsymbol{x}}_{k-1} = \boldsymbol{J}^{-1}(\boldsymbol{x}(t_{k-1}), \boldsymbol{u}(t_{k-1}))\Big(-\boldsymbol{K}(\boldsymbol{x}(t_{k-1}), \boldsymbol{u}(t_{k-1}))\boldsymbol{x}(t_{k-1}) + \boldsymbol{R}(\boldsymbol{x}(t_{k-1}), \boldsymbol{u}(t_{k-1}))\Big). \tag{22}$$

The obtained successively linearized model is of high order, $\Delta\boldsymbol{x} \in \mathbb{R}^{m\times 1}$, $m \in \mathcal{O}(10^{3...4})$, with the sparse but large system matrices $\boldsymbol{A}_c$, $\boldsymbol{B}_c$, $\boldsymbol{C}_c$, and $\boldsymbol{E}_c$.

3.3.2. Reduction using balanced truncation

The matrices of the linearized system $\boldsymbol{A}_c$, $\boldsymbol{B}_c$, $\boldsymbol{C}_c$, and $\boldsymbol{E}_c$ from Section 3.3.1 are of high order and thus, as also pointed out by Mohd Ali et al. (2015), cannot be implemented in an EKF for real-time applications due to its computational complexity. Therefore, the system is reduced via balanced truncation (see Moore (1981)) to r dominant modes.

In balanced truncation, the system states are first transformed to an energy-balanced basis, in which the states are equally controllable and observable as evident in the corresponding Gramians

$$\boldsymbol{W}_c = \int_0^\infty e^{\boldsymbol{A}_c\tau}\boldsymbol{B}_c\boldsymbol{B}_c^T e^{\boldsymbol{A}_c^T\tau}d\tau \text{ and} \tag{23}$$

$$\boldsymbol{W}_o = \int_0^\infty e^{\boldsymbol{A}_c^T\tau}\boldsymbol{C}_c^T\boldsymbol{C}_c e^{\boldsymbol{A}_c\tau}d\tau, \tag{24}$$

respectively. In such a transformed representation, the controllability and observability Gramians are equal and correspond to a diagonal matrix, see Brunton and Kutz (2019). The balanced Gramians' eigenvalues are the system's Hankel singular values and provide an energy measure for each state, so that the high-energy states can be preserved in the reduced system while the low-energy states are eliminated by truncating them entirely.

In order to perform the balanced truncation of the descriptor-form high-order system (16)–(17) efficiently, it is necessary

to exploit the sparsity of the matrices. Therefore, Castagnotto et al. (2017) developed a MATLAB® toolbox to analyze and reduce large-scale linear dynamic systems in sparse state-space representations, see also the sparse algorithms developed by Davis (2006), Duff et al. (1986), Saad (2003), and Gilbert et al. (1992). In this work, the toolbox is used to preserve the sparsity of the high-order system and exploit it for the computations of the balanced truncation. This is achieved by applying the Petrov-Galerkin projections of the form

$$\tilde{\boldsymbol{W}}^T \boldsymbol{E}_c \tilde{\boldsymbol{V}} \dot{\tilde{\boldsymbol{x}}}_r = \tilde{\boldsymbol{W}}^T \boldsymbol{A}_c \tilde{\boldsymbol{V}} \tilde{\boldsymbol{x}}_r + \tilde{\boldsymbol{W}}^T \boldsymbol{B}_c \boldsymbol{u} \text{ and} \tag{25}$$

$$\boldsymbol{y}_r = \boldsymbol{C}_c \tilde{\boldsymbol{V}} \tilde{\boldsymbol{x}}_r, \tag{26}$$

with the projection matrices $\tilde{\boldsymbol{V}}$ and $\tilde{\boldsymbol{W}}^T$. These projection matrices result from the balanced realization, see Castagnotto et al. (2017).

Subsequently, in the vastly reduced form, the descriptor form is resolved to an explicit state space representation and discretized in time, resulting in the state-space representation

$$\Delta\tilde{\boldsymbol{x}}_{r,k} = \tilde{\boldsymbol{A}}_r \Delta\tilde{\boldsymbol{x}}_{r,k-1} + \tilde{\boldsymbol{B}}_r \Delta\boldsymbol{u}_{k-1} \text{ and} \tag{27}$$

$$\Delta\boldsymbol{y}_{r,k} = \tilde{\boldsymbol{C}}_r \Delta\tilde{\boldsymbol{x}}_{r,k}, \tag{28}$$

with the system matrices $\tilde{\boldsymbol{A}}_r$, $\tilde{\boldsymbol{B}}_r$ and $\tilde{\boldsymbol{C}}_r$. The reduced states

$$\Delta\tilde{\boldsymbol{x}}_r = \tilde{\boldsymbol{W}}^T \Delta\boldsymbol{x} \tag{29}$$

can be obtained through the $(r \times m)$ projection matrix $\tilde{\boldsymbol{W}}^T$, which retains the r most controllable and observable modes, $\Delta\tilde{\boldsymbol{x}}_r \in \mathbb{R}^{r\times 1}$ with $r \in \mathcal{O}(10^1)$.

3.3.3. Augmentation of the system matrix with unknown inputs

The reduced system states are augmented by a selected parameter Θ that should be estimated along with the states in order to deal with parameter mismatch or uncertainty as well as to introduce a targeted correction option for the observer. Previously, in Section 3.3.1, the selected parameter to be estimated, such as a potentially unknown heat transfer coefficient α_{in}, was treated as an input to the system. Now the reduced system matrices are reassembled so that the selected parameter to be estimated is subsequently part of the system vector

$$\Delta\tilde{\boldsymbol{x}}_{\text{re},k} = \begin{bmatrix} \Delta\tilde{\boldsymbol{x}}_{r,k} \\ \Delta\hat{\Theta}_k \end{bmatrix}. \tag{30}$$

Then, the augmented system matrices have the following form

$$\tilde{\boldsymbol{A}}_{\text{re}} = \begin{bmatrix} \tilde{\boldsymbol{A}}_r & \tilde{\boldsymbol{b}}_{r,\Theta} \\ \boldsymbol{0} & 1 \end{bmatrix}, \tag{31}$$

$$\tilde{\boldsymbol{B}}_{\text{re}} = \begin{bmatrix} \tilde{\boldsymbol{b}}_i & \cdots & \tilde{\boldsymbol{b}}_{n_u-1} \\ & \boldsymbol{0} & \end{bmatrix}, \text{ and} \tag{32}$$

$$\tilde{\boldsymbol{C}}_{\text{re}} = \begin{bmatrix} \tilde{\boldsymbol{C}}_r & \boldsymbol{0} \end{bmatrix}, \tag{33}$$

and serve as the Jacobians of the EKF to determine an update for the augmented state vector $\Delta\tilde{\boldsymbol{x}}_{\text{re},k}$.

3.4. Observer

First, in Section 3.4.1, the formulation of the EKF based on Simon (2006) is recapitulated. Then, aspects of the EKF's temporal evolution across different state-space representations are highlighted in Section 3.4.2.

3.4.1. Extended Kalman filter formulation

The discrete-time nonlinear system model (13)–(14) with process noise $\boldsymbol{w}_k$ and measurement noise $\boldsymbol{v}_k$, both assumed to be Gaussian uncorrelated and white, is given as

$$\boldsymbol{x}_k = f(\boldsymbol{x}_{k-1}, \boldsymbol{u}_{k-1}) + \boldsymbol{w}_k \text{ and} \tag{34}$$

$$\boldsymbol{y}_k = h(\boldsymbol{x}_k) + \boldsymbol{v}_k. \tag{35}$$

It is further assumed that the zero-mean Gaussian noises,

$$\boldsymbol{w}_k \sim \mathcal{N}(\boldsymbol{0}, \boldsymbol{Q}_k) \text{ and } \boldsymbol{v}_k \sim \mathcal{N}(\boldsymbol{0}, \boldsymbol{R}_k), \tag{36}$$

have the known covariance matrices $\boldsymbol{Q}_k$ and $\boldsymbol{R}_k$.

In general, the EKF consists of two steps, the prediction and update step. In the prediction step of the EKF, the predicted state vector and error covariance matrix are determined a priori. Thus, the predicted state vector

$$\hat{\boldsymbol{x}}_k^- = f(\hat{\boldsymbol{x}}_{k-1}, \boldsymbol{u}_{k-1}) \tag{37}$$

is computed using the high-order nonlinear prediction model. The predicted error covariance matrix

$$\tilde{\boldsymbol{P}}_k^- = \tilde{\boldsymbol{A}}_{\text{re}} \tilde{\boldsymbol{P}}_{k-1} \tilde{\boldsymbol{A}}_{\text{re}}^T + \tilde{\boldsymbol{Q}}_k \tag{38}$$

is obtained in the low-order observer model state space using the observer model's system matrix $\tilde{\boldsymbol{A}}_{\text{re}}$ as Jacobian of the EKF with the corresponding matrix $\tilde{\boldsymbol{Q}}$.

In the update step of the EKF, an estimated state vector and error covariance matrix in the low-order observer model state space are computed a posteriori based on the innovation

$$\Delta\hat{\boldsymbol{y}}_k = \boldsymbol{y}_{\text{real},k} - h(\hat{\boldsymbol{x}}_k^-, \boldsymbol{u}_k), \tag{39}$$

which is defined by the difference between the measurements $\boldsymbol{y}_{\text{real}}$ taken from reality and the nonlinear prediction model output. The innovation covariance

$$\tilde{\boldsymbol{S}}_k = \tilde{\boldsymbol{C}}_{\text{re}} \tilde{\boldsymbol{P}}_k^- \tilde{\boldsymbol{C}}_{\text{re}}^T + \tilde{\boldsymbol{R}}_k \tag{40}$$

is computed using the matrix $\tilde{\boldsymbol{C}}_{\text{re}}$ of the observer model as Jacobian of the EKF and the corresponding matrix $\tilde{\boldsymbol{R}}$. Together with the Kalman gain

$$\tilde{\boldsymbol{K}}_k = \tilde{\boldsymbol{P}}_k^- \tilde{\boldsymbol{C}}_{\text{re}}^T \tilde{\boldsymbol{S}}_k^{-1}, \tag{41}$$

the updated state vector estimation of the observer model

$$\Delta\tilde{\boldsymbol{x}}_{\text{re},k} = \tilde{\boldsymbol{K}}_k \Delta\hat{\boldsymbol{y}}_k \tag{42}$$

is obtained. The state estimates of the observer model are used to update the prediction model states after back-transformation into the high-order state representation of the prediction model, see Section 3.5. The estimation error covariance matrix update of the observer model can be formulated as

$$\tilde{\boldsymbol{P}}_k = \left(\boldsymbol{I} - \tilde{\boldsymbol{K}}_k \tilde{\boldsymbol{C}}_{\text{re}}\right) \tilde{\boldsymbol{P}}_k^-, \tag{43}$$

where $\boldsymbol{I}$ is the identity matrix of appropriate size. The updated estimation error covariance evolves over time, which requires special considerations of the different model state-space representations, see Section 3.4.2.

3.4.2. Consistent covariance mapping over different observer model representations

Since the Jacobians of the EKF change only slowly in the present phase change problem, the successive linearization and thus the observer model matrices are not recomputed in each time step but are considered constant for n_{lin} time steps. With each new linearization step, the observer model and its balanced realization are newly built. Thus, not only the choice of states changes, but also the representation of the corresponding error covariance matrix of the EKF.

Therefore, in order to correctly evolve the error covariance matrix across different state representations, it must be transformed between two observer model representations (reduced state choice "1" → "2"). To do so, the covariance matrix $\tilde{\boldsymbol{P}}_1$ of the representation "1" is first transformed into the common high-order prediction model state space via the projection matrix $\tilde{\boldsymbol{V}}_1$, and then brought into the low-order state space of the observer model representation "2" using the projection matrix $\tilde{\boldsymbol{W}}_2$. The resulting covariance matrix reads

$$\tilde{\boldsymbol{P}}_2 = \left(\tilde{\boldsymbol{W}}_2^T \tilde{\boldsymbol{V}}_1\right) \tilde{\boldsymbol{P}}_1 \left(\tilde{\boldsymbol{V}}_1^T \tilde{\boldsymbol{W}}_2\right). \tag{44}$$

This mapping avoids the actual computation of a large, dense $(m \times m)$ matrix.

3.5. State update of the prediction model

The observer in Section 3.4 computes updated state estimates of the observer model. This updated augmented state vector estimate $\Delta\tilde{\boldsymbol{x}}_{\mathrm{re},k}$ is first decomposed into the reduced states $\Delta\tilde{\boldsymbol{x}}_{\mathrm{r},k}$ and the parameter $\Delta\hat{\Theta}_k$ (30). Then, the reduced state vector estimate $\Delta\tilde{\boldsymbol{x}}_{\mathrm{r},k}$ is transformed from the balanced realization of the observer model back into the original state representation of the prediction model using the $(m \times r)$ projection matrix $\tilde{\boldsymbol{V}}$,

$$\Delta\hat{\boldsymbol{x}}_k = \tilde{\boldsymbol{V}} \Delta\tilde{\boldsymbol{x}}_{\mathrm{r},k}. \tag{45}$$

In this original state representation, both, the states as well as the selected parameter, are updated accordingly,

$$\hat{\boldsymbol{x}}_k = \hat{\boldsymbol{x}}_k^- + \Delta\hat{\boldsymbol{x}}_k \text{ and} \tag{46}$$

$$\hat{\Theta}_k = \hat{\Theta}_k^- + \Delta\hat{\Theta}_k. \tag{47}$$

The performance of the developed observer structure is shown in Section 5. It is seen that for the present system, an observer of this form is robust and converges well. The reduction of states restricts the intervention options of the observer. The observer computes the update of the nonlinear prediction model based on the reduced states and thus can only correct the system according to its dominant behavior.

4. Sensor selection

In many applications, only a few sensors can be realized for space and cost reasons, so an efficient choice of few sensor locations to maximize observability measures is required.

Appropriate observability measures are proposed in the literature based on mode shapes (Clark et al. (2020)), system Gramians (Vaidya et al. (2012), Gawronski and Lim (1996)), information content (Hanis and Hromcik (2012)), or closed-loop simulation performance indices (Hemedi et al. (2012)), for example.

In the following, a data-based approach is proposed to select s efficient temperature sensor locations based on simulated temperature field time-series data for representative operation scenarios. The sensors and their corresponding measurements,

$$\boldsymbol{Y} = \mathcal{C}\boldsymbol{x}, \tag{48}$$

are defined by the selection matrix $\mathcal{C}$, where the rows of $\mathcal{C} \in \mathbb{R}^{s\times m}$ are unit vectors picking out rows of the state vector $\boldsymbol{x} \in \mathbb{R}^{m\times 1}$. The basic idea of the presented model-free, and thus conservative, approach is to reconstruct the dominant modal coordinates by only measuring few selected states. The sensor positions that explain the dominant modes best over time are obtained by analyzing the corresponding sensitivity matrix.

First, a data matrix containing the temperature field time-series data from representative reference simulations is constructed and decomposed via singular value decomposition (SVD),

$$\begin{Bmatrix} \boldsymbol{x}_1 & \boldsymbol{x}_2 & \dots \end{Bmatrix} = \mathcal{X} = \boldsymbol{U}\boldsymbol{\Sigma}\boldsymbol{V}^T, \tag{49}$$

whereby the state vector $\boldsymbol{x}_k$ contains the temperatures at the m nodes of the FE model at timestep k, $\boldsymbol{\Sigma} = \mathrm{diag}(\sigma_i)$ is the diagonal matrix of singular values $\sigma_1 \geq \sigma_2 \geq \ldots \geq 0$, and $\boldsymbol{U}$ and $\boldsymbol{V}$ contain the left and right singular vectors, respectively. The ith mode shape of the temperature field is found in the ith column of $\boldsymbol{U}$, starting with the most dominant mode (for $i = 1$). Its normalized modal coordinate time-series is contained in the ith row of $\boldsymbol{V}^T$. Truncating the SVD representation to the first q dominant modes is indicated by $\boldsymbol{U}_q$, $\boldsymbol{\Sigma}_q$, and $\boldsymbol{V}_q$, respectively.

The basic idea is to find sensors whose information allows a direct reconstruction of the q most dominant modes' modal coordinate values. For a given sensor selection defined by the index vector $l = \{l_1, ., l_s\}$, the output selection matrix $\mathcal{C}$ reads

$$\mathcal{C}_l = \begin{bmatrix} \mathrm{e}_{l_1}^T \\ \vdots \\ \boldsymbol{e}_{l_s}^T \end{bmatrix}. \tag{50}$$

The resulting sensitivity matrix expresses the gains from the considered modal coordinates to the measured outputs as

$$\mathcal{F}_l = [\mathcal{C}_l(\boldsymbol{U}_q\boldsymbol{\Sigma}_q)]^T [\mathcal{C}_l(\boldsymbol{U}_q\boldsymbol{\Sigma}_q)]. \tag{51}$$

Finally, a suitable matrix measure on the sensitivity matrix F_l is formulated to evaluate the studied sensor combination. To discriminate well between the different modes, the choice

$$\eta(l) = \min \mathrm{eig}(\mathcal{F}_l), \tag{52}$$

that is, the minimal eigenvalue of the sensitivity matrix $\mathcal{F}_l$, is an appropriate utility function to be maximized over a considered (large) set of candidate sensor combinations $\mathcal{L}$. The optimal sensor choice of s sensors reads

$$\arg\max_{l\in\mathcal{L}} \eta(l). \tag{53}$$

This combinatorial optimization problem is solved with appropriate search algorithms, usually in an approximated or heuristic way.

This data-based sensor selection approach does not utilize modeled system dynamics, so the number of sensors s must be at least as large as the number of reconstructed modes q, i.e., $q \leq s$. In this work, the proposed method will be applied for the most important temperature sensor only ($s = 1$) to ensure high observability of the most relevant mode ($q = 1$). Moreover, besides temperature measurements, any sensor type with a linear output Eq. (48) can be considered directly in the sensor selection process. In the present application, a PCM volume measurement is found to improve estimation robustness in the presence of model errors. Its output function is, however, nonlinear in $\boldsymbol{x}$ and it is not considered in the selection process of temperature sensors.

5. Demonstration of the observer & discussion

The performance of the developed observer is demonstrated in this section via simulation studies. First, the simulation setup is defined. Then, the observer is tested under two scenarios: an incorrect initialization and an incorrect parameterization of the model, respectively.

5.1. Simulation setup

The setup for the simulation studies and the parameters of the observer are specified below. The geometry of the PCM cell, the material parameters, and the discretization correspond to the values in Pernsteiner et al. (2021).

Table 1
Geometry of the LHTES.

Dimension	Part	Value
length L_x	encapsulation	0.12 m
width L_y	encapsulation	0.025 m
length of cavity Δx_{PCM}	PCM	0.118 m
width of cavity Δy_{PCM}	PCM	0.023 m

5.1.1. Geometry

The geometry of the PCM cell is defined in Fig. 2 and Table 1. The heated wall (left) side of the PCM cell has good heat transfer properties for charging and discharging via heat flows. On the outer wall (right) side, the PCM cell is isolated to reduce heat loss to the environment, see Fig. 2. The assumed heat transfer coefficients are listed in Table 2.

5.1.2. Material parameters

As in Vogel et al. (2016), the PCM is chosen as a eutectic mixture of potassium nitrate and sodium nitrate KNO_3-$NaNO_3$, enclosed in an aluminum encapsulation. The PCM is either liquid (L), solid (S), or mushy (M). The material properties of the aluminum encapsulation and the PCM are listed in Table 3. The density of solid PCM is used for both phases. The thermal expansion coefficient is only used to compute the buoyancy force (Boussinesq approximation) (5) and, together with the assumed expansion due to phase change, to determine the PCM volume.

5.1.3. Mesh and time step size

The geometry of the high-fidelity model is discretized by a mesh of square elements with a side length of $\Delta x = \Delta y = 0.5$ mm, and the time step is set to $\Delta t = 0.1$ s. These mesh resolutions resulted as optimal values from a mesh convergence study, see Kasper et al. (2021). The reduction method described in Section 2.2 enables a coarser mesh and larger time step. Therefore, the time step and mesh sizes are doubled to $\Delta x = \Delta y = 1$ mm and $\Delta t = 0.2$ s for the prediction model that is implemented in the observer, see Table 4.

5.1.4. Observer parameters

The observer is realized as described in Section 3. The linearization and thus the creation of the observer model is executed every $\Delta t_{\text{lin}} = 60$ s. The balanced truncation leads to a model with $r = 5$ reduced states. This model is then extended by the selected parameter to be estimated, the heat transfer coefficient α_{in}. The volume measurement is scaled by 10^7. The matrices $\boldsymbol{Q}$ and $\boldsymbol{R}$ in the observer are selected to be diagonal and constant. All diagonal components of the matrix $\boldsymbol{Q}$ are set to 10^{-1}. The diagonal components of the matrix $\boldsymbol{R}$ are 10^3 for the temperature measurements and 10^{-1} for the volume measurement. The values of $\boldsymbol{Q}$ and $\boldsymbol{R}$ have been adjusted to balance convergence speed and performance in the presence of model errors.

5.1.5. Load profile

The performance of the observer is demonstrated using a 5-hour load profile with varying amplitude. Consequently, the PCM cell is charged/discharged by a heat flow resulting from the temperature difference between its heated (left) wall and the domain interior (7). The load profile's input temperature on the left side T_{in} of (7) is set as shown in Fig. 5, while the temperature responsible for the heat loss on the outer (right) wall T_{out} of (8) is fixed at 20 °C. The initial temperature in the PCM cell is $T_0 = 218$ °C, just below the solidus temperature of the PCM.

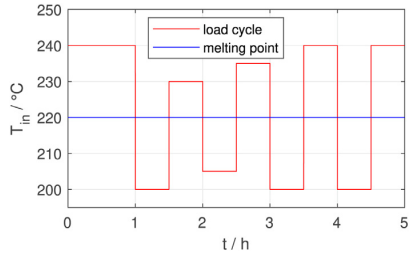

Fig. 5. input temperature T_{in} of the load profile on the left side of the PCM cell.

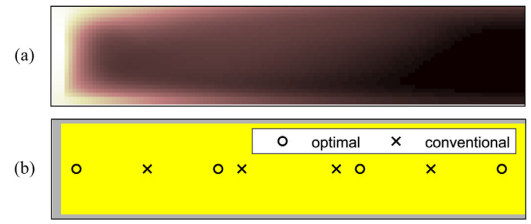

Fig. 6. (a) optimal placement of one temperature sensor - light areas have a high and dark areas a low temperature sensitivity (b) temperature sensor positions for the optimal and conventional placement.

5.1.6. Optimized sensor selection

The optimized sensor selection is derived from the method presented in Section 4. The sensor candidate positions are located in the symmetry plane of the PCM cell. One ($s = 1$) temperature sensor is selected optimally for $q = 1$ dominant mode. Fig. 6a shows the temperature sensitivity for the considered load case, and Fig. 6b depicts the optimized sensor placement (left-most sensor is optimized, three additional temperature sensors are distributed equidistantly due to application constraints).

Simulation studies show that the optimized sensor placement is preferable to the conventional one. During the melting process, a sensor located close to the left heated wall quickly detects the beginning of the melting process and thus provides information to the observer. If the left-most sensor is too far away from this heated wall, however, as in the case of the conventional sensor placement, it remains much longer in the solid region, where it only measures an almost constant temperature (the melting temperature). Therefore the sensor does not provide the observer with significant information until the melting front reaches the first sensor and the temperature changes. These relations are also depicted in the data matrix outlined in Section 4. The following additional observations were made:

- The total enthalpy of the PCM cell and the melting front characteristics are estimated more accurately and with faster convergence with the optimized sensor placement compared to the conventional one.
- The parameter α_{in} can be determined correctly with the optimized sensor placement but not with the conventional one when no model error is assumed.

Therefore, in the following simulation studies, the optimized temperature sensor placement is applied. Additionally, a measurement of the total PCM volume,

$$V_{\text{PCM}} = \int_M \frac{1}{\rho_{\text{PCM}}} dm, \tag{54}$$

with total PCM mass M, is assumed and considered in the observer. The additional measurement of PCM volume helps to make the observer insensitive to model errors and extends the field of appli-

Table 2
Heat transfer coefficient α.

Heat transfer coefficent	Value
for charging/discharging heat flow (heated wall (left) side of PCM cell) $\frac{\alpha_{\text{in}}}{\text{Wm}^{-2}\text{K}^{-1}}$	700
for heat losses through isolation (outer wall (right) side of PCM cell) $\frac{\alpha_{\text{out}}}{\text{Wm}^{-2}\text{K}^{-1}}$	0.01

Table 3
Material properties of the LHTES, phases in solid (S) and liquid (L) state.

Property	Alu.	PCM
density $\frac{\rho}{\text{kgm}^{-3}}$	2700	2050 (S)
specific heat capacity $\frac{c}{\text{J(kgK)}^{-1}}$	910	1350 (S) 1492 (L)
thermal conductivity $\frac{\lambda}{\text{W(mK)}^{-1}}$	237	0.457 (S) 0.435 (L)
melting temperature $\frac{T_{\text{m}}}{\text{C}_\circ}$	-	220
mushy region parameter $\frac{\varepsilon}{\text{C}_\circ}$	-	±0.5
specific latent heat $\frac{h_{\text{latent}}}{\text{kJ(kg)}^{-1}}$	-	108
dynamic viscosity $\frac{\mu}{\text{Ns(m)}^{-2}}$	-	$5.8 \cdot 10^{-4}$ (L)
thermal expansion coefficient $\frac{\beta}{(\text{K})^{-1}}$	-	$3.5 \cdot 10^{-4}$ (L)
expansion due to phase change	-	10% (M)

Table 4
Mesh and time step size.

Type	mesh size $\frac{\Delta x}{\text{mm}}$	time step $\frac{\Delta t}{\text{s}}$
high-fidelity model	0.5	0.1
reduced nonlinear model	1	0.2

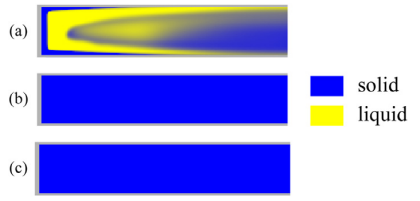

Fig. 7. initial melting front distribution of the wrong-initialization scenario for the (a) simulated reality, (b) the observed model, and (c) the uncorrected model.

cation to pure substances as well as eutectics, where the melting process takes place without temperature change.

5.1.7. Simulation scenarios

Two different scenarios are evaluated in the simulation study:

- wrong initialization - The initial temperature field of the simulated reality is set to a complex temperature distribution with parts in liquid and solid state, see Fig. 7.
- wrong parameterization - The heat transfer coefficient of the simulated reality is set to 900 $\text{Wm}^{-2}\text{K}^{-1}$.

The measurements used by the observer come from the perturbed high-fidelity model, which hence serves as simulated reality. This model is different from the prediction model implemented in the observer and exhibits a moderately different temperature distribution, especially in the liquid phase of the PCM. This model error occurs in the prediction model due to the substitution of the Navier-Stokes Eqs. (2)–(3) by a stream function model, which is optimized to accurately reconstruct the correct total enthalpy content as well as position of the melting front but not the exact temperature distribution.

The measurements from the simulated reality are subject to Gaussian noise. For this purpose, the standard deviation of the temperature sensors is assumed to be 1 K and of the volume measurement 1% of the PCM domain size.

The simulated reality allows an analysis of the entire distributed state of the PCM cell to evaluate the performance of the observer.

5.2. Results

The results are evaluated under two aspects: the state of charge as well as the location and shape of the melting front. These criteria are compared between the simulated reality, the observed model, and an uncorrected model (i.e., the prediction model simulation only).

5.2.1. State of charge

Knowing the state of charge and its distribution in the PCM cell is essential to control the LHTES. One representative formulation of the state of charge is the stored normalized enthalpy,

$$H_{\text{norm}}(t) = \frac{H(t) - H_0}{H_{\text{latent}}}. \tag{55}$$

In (55), $H(t)$ is the total enthalpy at time t, H_0 the initial total enthalpy, and H_{latent} the latent heat of the PCM cell. Figure 8 compares the stored normalized enthalpy of the different models for the wrong-initialization and wrong-parameterization scenarios, respectively. The total enthalpy can be estimated with high accuracy for both simulation cases, and only small offsets are seen. Therefore the developed observer is considered suitable to estimate the state of charge.

5.2.2. Melting front

As a second criterion, the shape and progression of the melting fronts in the PCM are evaluated qualitatively, see Fig. 9 for an illustration in the wrong-initialization scenario. The location of the melting front is accurately estimated and its shape is being retained correctly. Such a good estimate of the melting front is essential as it determines, for example, how quickly the stored enthalpy can be retrieved from the PCM cell.

These results are highly promising in terms of robustness and performance, especially considering the large initialization error of the first test scenario and the model error in the observer leading to temperature deviations in the liquid phase between the prediction model and the simulated reality. With such a state observer, it is also possible to dynamically operate the LHTES and integrate it into complex storage systems using modern control methods.

5.2.3. Joint state and parameter estimation

The augmented parameter Θ, in this case the heat transfer coefficient α_{in}, was correctly estimated when using measurements from the real-time-capable nonlinear prediction model. However, when using measurements from the high-fidelity model (the simulated reality), that is, in the presence of a model error, the parameter to be estimated showed oscillating behavior rather than smooth convergence. Still, the augmented parameter can be used by the observer as an additional correction variable and is therefore considered a valuable design tool.

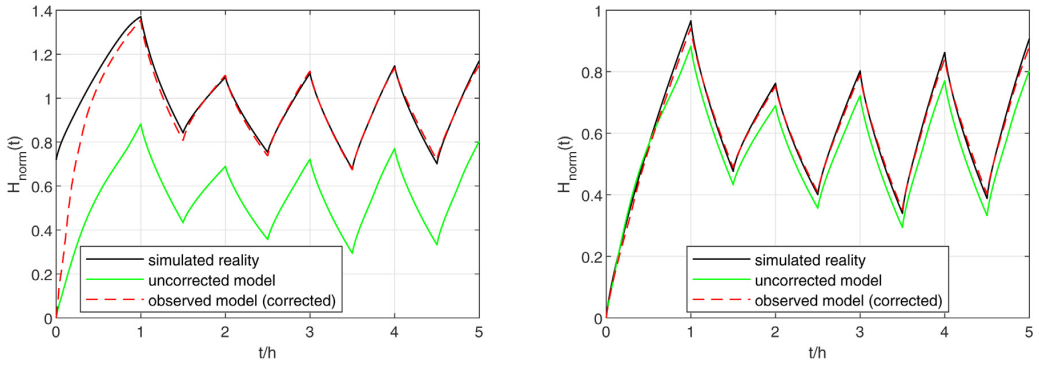

(a) wrong-initialization scenario (b) wrong-parameterization scenario

Fig. 8. the normalized enthalpy content $H_{\text{norm}}(t)$ of the observed model shows an excellent convergence over time t in both test scenarios of wrong-initialization (a) and wrong-parameterization (b), even despite model errors.

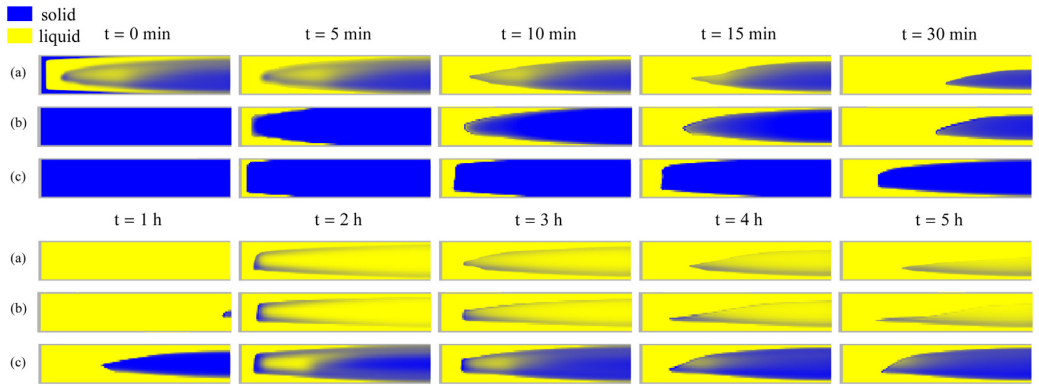

Fig. 9. in the wrong-initialization scenario, the observed model (b) estimates accurately the melting front location and shape of the simulated reality (a) compared to the uncorrected model (c).

6. Conclusions

The developed observer framework for melting/solidification phase change problems with conduction/convection is able to handle nonlinear distributed-parameter systems. The method is based on a high-order but real-time-capable finite element model, which is used to predict future states. This prediction model is linearized around the current trajectory and then efficiently reduced via balanced truncation to obtain an observer model with dominant modes only. The low-order observer model's states are augmented by selected parameters that should be estimated along with the states in order to deal with parameter mismatch or uncertainty. The observer model system matrices serve as Jacobians in an extended Kalman filter, and a state update of the prediction model is computed according to the difference between the measurements and the predicted model outputs. Thereby the observer combines temperature and volume measurements.

It is seen that an observer of this form converges well and is insensitive against model errors. The reduction of states restricts the intervention options of the observer. The observer computes the update of the nonlinear prediction model based on the reduced states and thus can only correct the system according to its dominant behavior. The temperature sensor placement is optimized using a proposed mode-shape-based selection criterion.

The observer can be computed in real-time and its performance is demonstrated in simulation studies of two scenarios: a wrong-initialization and a wrong-parameterization case. It is tested with simulated measurements generated by a detailed (but not real-time-capable) high-fidelity reference model, which exhibits a slightly different temperature distribution. The results are satisfactory, especially considering the large initialization error of the first test scenario and the modeling error of the temperature distribution between the prediction model and the simulated reality. The total enthalpy and thus the state of charge can be estimated with high accuracy. Also, the location and shape of the melting front are estimated accurately.

Credit Author Statement

- Dominik Pernsteiner: concept, development and implementation
- Alexander Schirrer: concept, development
- Lukas Kasper: consultation, code base review
- René Hofmann: consultation, senior researcher guidance (thermodynamics)
- Stefan Jakubek: concept, senior researcher guidance (state estimation)

Declaration of Competing Interest

The authors declare that they have no known competing financial interests or personal relationships that could have appeared to influence the work reported in this paper.

Acknowledgements

The Climate and Energy Fund KLIEN/FFG funded a research project started in 2018: HyStEPs grant number 868842. The authors also want to acknowledge the support provided by the doctoral school Smart Industrial Concept [SIC!] (https://sic.tuwien.ac.at).

References

Afshar, S., Morris, K., Khajepour, A., 2015. Comparison of different observer designs for heat equation. In: 2015 54th IEEE Conference on Decision and Control (CDC), pp. 1136–1141. doi:10.1109/CDC.2015.7402364.

Agyenim, F., Hewitt, N., Eames, P., Smyth, M., 2010. A review of materials, heat transfer and phase change problem formulation for latent heat thermal energy storage systems (LHTESS). Renew. Sustain. Energy Rev. 14 (2), 615–628. doi:10.1016/j.rser.2009.10.015.

Akkari, E., Chevallier, S., Boillereaux, L., 2006. Observer-based monitoring of thermal runaway in microwaves food defrosting. J. Process Control 16, 993–1001. doi:10.1016/j.jprocont.2006.05.005.

Antoulas, A.C., 2004. Approximation of large-scale dynamical systems: an overview. IFAC Proc. Vol. 37 (11), 19–28. doi:10.1016/S1474-6670(17)31584-7.

Backi, C.J., Bendtsen, J.D., Leth, J., Gravdahl, J.T., 2016. A heat equation for freezing processes with phase change: stability analysis and applications. Int. J. Control 89 (4), 833–849. doi:10.1080/00207179.2015.1102327.

Backi, C.J., Dimon Bendtsen, J., Leth, J., Gravdahl, J.T., 2014. Estimation of inner-domain temperatures for a freezing process. In: 2014 IEEE Conference on Control Applications (CCA), pp. 1759–1764. doi:10.1109/CCA.2014.6981567.

Barz, T., Seliger, D., Marx, K., Sommer, A., Walter, S.F., Bock, H.G., Körkel, S., 2018. State and state of charge estimation for a latent heat storage. Control Eng. Pract. 72, 151–166. doi:10.1016/j.conengprac.2017.11.006.

Benner, P., Gugercin, S., Willcox, K., 2015. A survey of projection-based model reduction methods for parametric dynamical systems. SIAM Rev. 57 (4), 483–531. doi:10.1137/130932715.

Bitzer, M., Zeitz, M., 2002. Design of a nonlinear distributed parameter observer for a pressure swing adsorption plant. J. Process Control 12 (4), 533–543. doi:10.1016/S0959-1524(01)00019-1.

Brunton, S.L., Kutz, J.N., 2019. Data-Driven Science and Engineering: Machine Learning, Dynamical Systems, and Control. Cambridge University Press, Cambridge (U.K.) doi:10.1017/9781108380690.

Castagnotto, A., Varona, M.C., Jeschek, L., Lohmann, B., 2017. sss & sssMOR: analysis and reduction of large-scale dynamic systems in MATLAB. at - Automatisierungstechnik 65 (2), 134–150. doi:10.1515/auto-2016-0137.

Chorin, A.J., 1968. Numerical solution of the Navier-Stokes equations. Math. Comput. 22 (104), 745–762. doi:10.1090/S0025-5718-1968-0242392-2.

Clark, E., Kutz, J.N., Brunton, S.L., 2020. Sensor selection with cost constraints for dynamically relevant bases. IEEE Sens. J. 20 (19), 11674–11687. doi:10.1109/JSEN.2020.2997298.

Daum, F., 2005. Nonlinear filters: beyond the Kalman filter. IEEE Aerosp. Electron. Syst. Mag. 20 (8), 57–69. doi:10.1109/MAES.2005.1499276.

Davis, T.A., 2006. Direct Methods for Sparse Linear Systems. Society for Industrial and Applied Mathematics, Philadelphia (PA, USA.) doi:10.1137/1.9780898718881.

Dochain, D., 2003. State and parameter estimation in chemical and biochemical processes: a tutorial. J. Process Control 13 (8), 801–818. doi:10.1016/S0959-1524(03)00026-X.

Drakunov, S.V., Utkin, V.I., 1992. Sliding mode control in dynamic systems. Int. J. Control 55 (4), 1029–1037. doi:10.1080/00207179208934270.

Duff, I.S., Erisman, A.M., Reid, J.K., 1986. Direct Methods for Sparse Matrices. Oxford University Press, Oxford (U.K.).

Dutil, Y., Rousse, D.R., Salah, N.B., Lassue, S., Zalewski, L., 2011. A review on phase-change materials: mathematical modeling and simulations. Renew. Sustain. Energy Rev. 15 (1), 112–130. doi:10.1016/j.rser.2010.06.011.

Farrell, B.F., Ioannou, P.J., 2001. State estimation using a reduced-order Kalman filter. J. Atmos. Sci. 58 (23), 3666–3680. doi:10.1175/1520-0469(2001)058<3666:SEUARO>2.0.CO;2.

Fortunato, B., Camporeale, S., Marco, T., Albano, M., 2012. Simple mathematical model of a thermal storage with PCM. AASRI Procedia 2, 241–248. doi:10.1016/j.aasri.2012.09.041.

Gawronski, W., Lim, K.B., 1996. Balanced actuator and sensor placement for flexible structures. Int. J. Control 65 (1), 131–145. doi:10.1080/00207179608921690.

Ghahremani, E., Kamwa, I., 2011. Dynamic state estimation in power system by applying the extended Kalman filter with unknown inputs to phasor measurements. IEEE Trans. Power Syst. 26. doi:10.1109/TPWRS.2011.2145396.

Gil, A., Medrano, M., Martorell, I., Lázaro, A., Dolado, P., Zalba, B., Cabeza, L.F., 2010. State of the art on high temperature thermal energy storage for power generation. Part 1–concepts, materials and modellization. Renew. Sustain. Energy Rev. 14 (1), 31–55. doi:10.1016/j.rser.2009.07.035.

Gilbert, J.R., Moler, C., Schreiber, R., 1992. Sparse matrices in MATLAB: design and implementation. SIAM J. Matrix Anal. Appl. 13 (1), 333–356. doi:10.1137/0613024.

Glover, K., 1984. All optimal Hankel-norm approximations of linear multivariable systems and their error bounds. Int. J. Control 39 (6), 1115–1193. doi:10.1080/00207178408933239.

Gugercin, S., Antoulas, A.C., 2004. A survey of model reduction by balanced truncation and some new results. Int. J. Control 77 (8), 748–766. doi:10.1080/00207170410001713448.

Hanis, T., Hromcik, M., 2012. Optimal sensors placement and spillover suppression. Mech. Syst. Signal Process. 28, 367–378. doi:10.1016/j.ymssp.2011.12.007.

Hemedi, M., Schirrer, A., Kozek, M., 2012. Comparison of LQ-optimal actuator/sensor selection approaches for flexible structure systems. In: AIP Conference Proceedings, vol. 1493. American Institute of Physics, pp. 459–466. doi:10.1063/1.4765529.

Ibrahim, N., Al-Sulaiman, F., Rahman, S., Yilbas, B., Sahin, A., 2017. Heat transfer enhancement of phase change materials for thermal energy storage applications: a critical review. Renew. Sustain. Energy Rev. 74, 26–50. doi:10.1016/j.rser.2017.01.169.

Jadachowski, L., Meurer, T., Kugi, A., 2014. Backstepping observers for linear PDEs on higher-dimensional spatial domains. Automatica 51. doi:10.1016/j.automatica.2014.10.108.

Jazwinski, A., 1970. Stochastic Processes And Filtering Theory. Academic Press, New York (NY, USA) and London (U.K.).

Julier, S.J., Uhlmann, J.K., 2004. Unscented filtering and nonlinear estimation. Proc. IEEE 92 (3), 401–422. doi:10.1109/JPROC.2003.823141.

Kalman, R.E., 1960. A new approach to linear filtering and prediction problems. J. Basic Eng. 82 (1), 35–45. doi:10.1115/1.3662552.

Kalman, R.E., Bucy, R.S., 1961. New results in linear filtering and prediction theory. J. Basic Eng. 83, 95–108. doi:10.1115/1.3658902.

Kasper, L., 2020. Modeling of the Phase Change Material of a Hybrid Storage Using the Finite Element Method. TU Wien Academic Press, Wien (Austria) doi:10.34727/2020/isbn.978-3-85448-037-2.

Kasper, L., Pernsteiner, D., Koller, M., Schirrer, A., Jakubek, S., Hofmann, R., 2021. Numerical studies on the influence of natural convection under inclination on optimal aluminium proportions and fin spacings in a rectangular aluminium finned latent-heat thermal energy storage. Appl. Therm. Eng. 190, 116448. doi:10.1016/j.applthermaleng.2020.116448.

Khodadadi, H., Jazayeri-Rad, H., 2011. Applying a dual extended Kalman filter for the nonlinear state and parameter estimations of a continuous stirred tank reactor. Comput. Chem. Eng. 35 (11), 2426–2436. doi:10.1016/j.compchemeng.2010.12.010.

Kolås, S., Foss, B., Schei, T., 2009. Constrained nonlinear state estimation based on the UKF approach. Comput. Chem. Eng. 33 (8), 1386–1401. doi:10.1016/j.compchemeng.2009.01.012.

Kreuzinger, T., Bitzer, M., Marquardt, W., 2008. State estimation of a stratified storage tank. Control Eng. Pract. 16 (3), 308–320. doi:10.1016/j.conengprac.2007.04.013.

Lee, J., Nam, O., Cho, B., 2007. Li-ion battery SOC estimation method based on the reduced order extended Kalman filtering. J. Power Sources 174 (1), 9–15. doi:10.1016/j.jpowsour.2007.03.072.

Liu, S., Li, Y., Zhang, Y., 2014. Mathematical solutions and numerical models employed for the investigations of PCMs' phase transformations. Renew. Sustain. Energy Rev. 33, 659–674. doi:10.1016/j.rser.2014.02.032.

Liu, Y., Anderson, B.D.O., 1989. Singular perturbation approximation of balanced systems. Int. J. Control 50 (4), 1379–1405. doi:10.1080/00207178908953437.

Luenberger, D.G., 1966. Observers for multivariable systems. IEEE Trans. Automat. Control 11 (2), 190–197. doi:10.1109/TAC.1966.1098323.

Marko, L., Mennemann, J.-F., Jadachowski, L., Kemmetmüller, W., Kugi, A., 2018. Early- and late-lumping observer designs for long hydraulic pipelines: application to pumped-storage power plants. Int. J. Robust Nonlinear Control 28 (7), 2759–2779. doi:10.1002/rnc.4049.

Mohd Ali, J., Ha Hoang, N., Hussain, M., Dochain, D., 2015. Review and classification of recent observers applied in chemical process systems. Comput. Chem. Eng. 76, 27–41. doi:10.1016/j.compchemeng.2015.01.019.

Moore, B., 1981. Principal component analysis in linear systems: controllability, observability, and model reduction. IEEE Trans. Automat. Control 26 (1), 17–32. doi:10.1109/TAC.1981.1102568.

Napp, T.A., Gambhir, A., Hills, T.P., Florin, N., Fennell, P.S., 2014. A review of the technologies, economics and policy instruments for decarbonising energy-intensive manufacturing industries. Renew. Sustain. Energy Rev. 30, 616–640. doi:10.1016/j.rser.2013.10.036.

Nedjar, B., 2002. An enthalpy-based finite element method for nonlinear heat problems involving phase change. Comput. Struct. 80 (1), 9–21. doi:10.1016/S0045-7949(01)00165-1.

Park, B.-G., Kim, J.-M., Kim, J.-W., Lee, K.-C., Koo, D.-H., Hyun, D.-S., 2013. New approach to EKF-based sensorless control using parallel structure for non-salient pole permanent magnet synchronous motors. In: 2013 International Conference on Electrical Machines and Systems (ICEMS), pp. 1099–1104. doi:10.1109/ICEMS.2013.6754407.

Patwardhan, S.C., Narasimhan, S., Jagadeesan, P., Gopaluni, B., L. Shah, S., 2012. Nonlinear Bayesian state estimation: a review of recent developments. Control Eng. Pract. 20 (10), 933–953. doi:10.1016/j.conengprac.2012.04.003.

Pepper, D.W., Heinrich, J.C., 2005. The finite element method: basic concepts and applications. Computational and Physical Processes in Mechanics and Thermal Sciences. CRC Press, Boca Raton (FL, USA).

Pernsteiner, D., Kasper, L., Schirrer, A., Hofmann, R., Jakubek, S., 2020. Co-simulation methodology of a hybrid latent-heat thermal energy storage unit. Appl. Therm. Eng. 178, 115495. doi:10.1016/j.applthermaleng.2020.115495.

Pernsteiner, D., Schirrer, A., Kasper, L., Hofmann, R., Jakubek, S., 2021. Data-based model reduction for phase change problems with convective heat transfer. Appl. Therm. Eng. 184, 116228. doi:10.1016/j.applthermaleng.2020.116228.

Potocki, J.K., Tharp, H.S., 1993. Concurrent hyperthermia estimation schemes based on extended Kalman filtering and reduced-order modelling. Int. J. Hyperthermia 9 (6), 849–865. doi:10.3109/02656739309034987.

Radhakrishnan, K.B., Balakrishnan, A.R., 1992. Heat transfer analysis of thermal energy storage using phase change materials. Heat Recovery Syst. CHP 12 (5), 427–435. doi:10.1016/0890-4332(92)90064-O.

Saad, Y., 2003. Iterative Methods for Sparse Linear Systems. Society for Industrial and Applied Mathematics, Philadelphia (PA, USA) doi:10.1137/1.9780898718003.

Seibold, B., 2008. A compact and fast Matlab code solving the incompressible Navier-Stokes equations on rectangular domains. Retrieved 29th June 2021.

Simon, D., 2006. Optimal State Estimation: Kalman, H∞, and Nonlinear Approaches. John Wiley & Sons, Hoboken (NJ, USA) doi:10.1002/0470045345.

Tao, Y.B., He, Y.-L., 2018. A review of phase change material and performance enhancement method for latent heat storage system. Renew. Sustain. Energy Rev. 93, 245–259. doi:10.1016/j.rser.2018.05.028.

Tenchev, R.T., Mackenzie, J.A., Scanlon, T.J., Stickland, M.T., 2005. Finite element moving mesh analysis of phase change problems with natural convection. Int. J. Heat Fluid Flow 26 (4), 597–612. doi:10.1016/j.ijheatfluidflow.2005.03.003.

Vaidya, U., Rajaram, R., Dasgupta, S., 2012. Actuator and sensor placement in linear advection PDE with building system application. J. Math. Anal. Appl. 394 (1), 213–224. doi:10.1016/j.jmaa.2012.03.046.

Vogel, J., Felbinger, J., Johnson, M., 2016. Natural convection in high temperature flat plate latent heat thermal energy storage systems. Appl. Energy 184, 184–196. doi:10.1016/j.apenergy.2016.10.001.

Wishner, R.P., Tabaczynski, J.A., Athans, M., 1969. A comparison of three non-linear filters. Automatica 5 (4), 487–496. doi:10.1016/0005-1098(69)90110-1.

Yang, J.N., Pan, S., Huang, H., 2007. An adaptive extended Kalman filter for structural damage identifications II: unknown inputs. Struct. Control Health Monit. 14 (3), 497–521. doi:10.1002/stc.171.

Zalba, B., Marin, J.M., Cabeza, L.F., Mehling, H., 2003. Review on thermal energy storage with phase change: materials, heat transfer analysis and applications. Appl. Therm. Eng. 23 (3), 251–283. doi:10.1016/S1359-4311(02)00192-8.

Zhakatayev, A., Rakhim, B., Adiyatov, O., Baimyshev, A., Varol, H.A., 2017. Successive linearization based model predictive control of variable stiffness actuated robots. In: 2017 IEEE International Conference on Advanced Intelligent Mechatronics (AIM), pp. 1774–1779. doi:10.1109/AIM.2017.8014275.

Zsembinszki, G., Orozco, C., Gasia, J., Barz, T., Emhofer, J., Cabeza, L.F., 2020. Evaluation of the state of charge of a solid/liquid phase change material in a thermal energy storage tank. Energies 13 (6). doi:10.3390/en13061425.

2.4 Publication* D

D. Pernsteiner, V. Halmschlager, A. Schirrer, R. Hofmann, and S. Jakubek. "Efficient sensitivity-based cooperation concept in multi-layer operation optimization architectures". In: *submitted to Computers & Chemical Engineering* (2021)

Applicant's contribution †

- Dominik Pernsteiner: Conceptualization, Formal analysis, Investigation, Methodology, Software, Visualization, Writing - original draft
- Verena Halmschlager: Formal analysis, Methodology, Software, Writing - original draft
- Alexander Schirrer: Conceptualization, Supervision, Writing - review & editing
- René Hofmann: Funding acquisition, Supervision, Writing - review & editing
- Stefan Jakubek: Funding acquisition, Supervision, Writing - review & editing

*in submission

†According to the Elsevier CRediT author statement: `https://www.elsevier.com/authors/policies-and-guidelines/credit-author-statement`

Highlights

Efficient sensitivity-based cooperation concept in multi-layer operation optimization architectures

Dominik Pernsteiner, Verena Halmschlager, Alexander Schirrer, René Hofmann, Stefan Jakubek

- Multi-layer optimization of a chipboard manufacturing plant.
- Efficient cooperation strategy between hierarchical optimization layers.
- The expected operating costs are minimized in a stochastic manner.
- The approach is generic and can be easily adapted.
- Proof of concept through simulation models calibrated by industrial measurement data.

Efficient sensitivity-based cooperation concept in multi-layer operation optimization architectures

Dominik Pernsteiner[a,*], Verena Halmschlager[b], Alexander Schirrer[a], René Hofmann[b], Stefan Jakubek[a]

TU Wien, Austria

[a] *TU Wien, Institute of Mechanics and Mechatronics, Getreidemarkt 9/BA, 1060 Vienna, Austria*
[b] *TU Wien, Institute for Energy Systems and Thermodynamics, Getreidemarkt 9/BA, 1060 Vienna, Austria*

Abstract

Hierarchical optimization architectures are typically employed to manage industrial processes efficiently. The key challenge today is to find a near global optimum despite these subdivided control structures. This paper proposes a novel cooperation concept between hierarchical layers. In the upper layer, optimal static setpoints are computed for economic operation schedules of the entire plant. In the lower layer, a model predictive controller realizes these schedules, regulates the dynamic plant parts, and treats occurring disturbances optimally in a stochastic manner. To adequately overcome limitations due to mismatches between the optimization layers (caused by model mismatches or disturbances), it is essential to establish an efficient cooperation concept. Therefore, the presented concept exchanges specific sensitivity information between the optimization layers, where it is exploited in the interest of global control objectives, resulting in optimal expected operating costs. The novel concept is demonstrated via simulation studies calibrated with industrial measurements of a chipboard manufacturer.

Keywords:
hierarchical operation optimization, mixed-integer linear programming, model predictive control, stochastic control, sensitivity-based cooperation

1. Introduction

1.1. Motivation

The IEA (2020) annually publishes the *World Energy Outlook*, in which various scenarios provide an overview of tomorrow's energy sector. Of particular interest are two scenarios that envisage compliance with the Paris climate targets (UN (2015)), or even more ambitious zero net emissions by 2050. Both scenarios rely on renewable energy sources.

The goal of achieving a climate-neutral energy sector through the integration of renewable energies requires greater flexibility on the supply and demand sides of industrial processes while also increasing their efficiency. In energy-intensive industries, steam plays a major role in converting heat to power or distributing thermal energy throughout the plant to drive its mechanical and chemical processes. Additionally, industrial plants are facing new challenges in the transition to climate-friendly energy systems, such as the task of feeding power into electricity grids at peak times or supplying district heating to their neighborhoods. In order to operate industrial steam processes effectively, hierarchical optimization architectures are employed. In these concepts, operation optimization is decomposed into several parts (layers) to abstract the complex optimization problem into manageable subproblems. The optimization layers can be therefore divided according to different dynamics and time scales. Other reasons for subdivision include various types of optimization goals, such as economic optimization or control purposes. However, for an effective implementation of hierarchical optimization concepts, it is essential to establish an efficient cooperation between the optimization layers in order to adequately consider the effects of modeling mismatches between layers (static and dynamic models), disturbances, or plant limitations. A sensitivity-based stochastic method is developed in this work to do so.

In the present work, a novel two-layer optimization framework is proposed and demonstrated in a chipboard manufacturing plant use case. The main energetic process in the plant is steam generation that supplies heat to a chipboard production. In addition, a steam turbine generates electricity, and heat can be fed into a district heating network that supplies a hospital. In the upper optimization layer, an energy hub optimizer (EHO) computes static setpoints for economic optimal plant operation schedules. In the lower optimization layer, a model predictive controller (MPC) tracks these setpoints, efficiently compensates for stochastic disturbances, and controls the system based on nonlinear dynamic models for the crucial parts of the plant.

Due to stochastic fluctuations in the combustion process, the steam requirements cannot always be met exactly. In order to have sufficient steam available at all times, more steam must be generated and thus more fuel must be consumed. In this work, an efficient cooperation concept between the EHO and the MPC

*Corresponding author at: Institute for Mechanics and Mechatronics, TU Wien, Getreidemarkt 9/E325, 1060 Vienna, Austria.
E-mail address: dominik.pernsteiner@tuwien.ac.at (D.Pernsteiner).

is developed to optimally solve the trade-off between fuel consumption and steam demand satisfaction, in which stochastic information and true costs are optimally exploited. Thus, a complex coupled plant operation can be better managed in terms of overall costs and also emissions.

To do so, the EHO passes the (time-varying) sensivities of its economic cost function to a cooperation concept. In the cooperation concept, optimal expected costs (risk costs) determine a permitted violation probabilities of the EHO's setpoints. The MPC uses the desired setpoints of the EHO and their permitted violation probability computed by the cooperation concept to efficiently produce and distribute the steam over the entire plant, even without knowledge of all plant-wide components and the global economic optimization goal. The occuring process disturbances are handled by the MPC in a stochastic manner, and the plant is operated at optimal expected cost. The developed approach is generic and therefore can be easily adapted to other processes.

The investigated use case is based on plant models that are calibrated with real industrial measurement data. The simulation studies are performed with these validated models.

1.2. Paper structure

The paper is organized as follows: In Section 1, a literature review is performed and the main contributions of the present work are formulated. Section 2 describes the use case and the purpose of the different optimization layers in more detail, followed by the description of the static model and the EHO approach in Section 3. The dynamic models of the plant are introduced in Section 4, and their parameters are identified from the chipboard manufacturer's data using parameter sensitivity analysis. Section 5 describes the control concept for the chipboard production process, including the nonlinear stochastic MPC, the state observer, and the disturbance covariance estimation. The cooperation concept between the EHO and the MPC is stated in Section 6. In Section 7, simulation studies to demonstrate the effectiveness of the proposed framework are performed.

1.3. Optimization of industrial plants

The operation optimization of industrial plants is conventionally approached through a hierarchical multi-layer process automation structure, see for example Scattolini (2009), Tatjewski (2008), Engell (2007), and Qin and Badgwell (2003). Thereby, an economic optimization problem for scheduling is solved in the upper layer (usually referred to as real-time optimization - RTO) while control methods for ongoing operations are applied in the lower layer.

The hierarchical control/optimization problem is usually decomposed according to the different dynamics of states and disturbances. The sampling time and optimization horizon decreases in the lower layers due to faster process dynamics, disturbances and real-time computation requirements. Typically, the RTO in the upper layer exploits the economic characteristics of the process while accounting for significant changes in operating conditions, such as price factors and slowly varying disturbances that strongly affect plant profitability. It provides either stationary setpoints or dynamic trajectories as well as additional information on economically optimal operation to the control layer beneath. The control layer applies the information provided to match the output variables as closely as possible to the optimal setpoints/trajectories in the presence of disturbances or model mismatches. The control layer may be comprised of advanced model predictive controllers (MPCs), simple PID controllers, or a combination of those (Vega et al. (2014), Tatjewski (2008)). The following RTO/MPC strategies can be distinguished based on their temporal characteristics.

The static RTO/dynamic MPC strategy uses a steady-state plant-wide model for its economic optimization in the upper layer and dynamic models of particular sub-systems for control in the lower layer. The static RTO in the upper layer can only provide steady-state setpoints and is thus less frequently executed. In general, this approach does not consider the economic performance of the plant during the transition from one steady state to another, leading to suboptimal operation for processes that have slow dynamics, experience frequent transitions, or are constantly affected by fast disturbances (Jamaludin and Swartz (2017), Tatjewski (2008)). Additionally, the plant's economic performance suffers since the RTO and MPC solve two different optimization problems, each with different models, objectives, and on different time scales. The conflict between these optimization layers can lead to both infeasibility and unreachability of the economic setpoints in the control layer, resulting in poor economic performance. Consequently, an appropriate strategy to unify these (likely competing) objectives is highly desirable (Hinojosa et al. (2017)).

To address this shortcoming, a new optimization layer was added between the RTO and MPC referred to as steady-state target optimizer (Hinojosa et al. (2017), Jamaludin and Swartz (2017)). This layer computes feasible setpoint updates for the MPC to which the system must be stabilized, using a steady-state model that is consistent in its formulation as well as frequency with the dynamic MPC, and taking into account information from the RTO, see for example, Marchetti et al. (2014), González and Odloak (2009), Muske (1997). However, this approach is limited with respect to transient operations or fast disturbances.

In other approaches, instead of RTO based on steady-state models, dynamic real-time optimization (DRTO) is performed, which takes into account disturbances and process dynamics and provides target trajectories (rather than steady-state setpoints) to the lower layer, see e.g. Biegler (2009) and Kadam and Marquardt (2007). Tosukhowong et al. (2004) propose a DRTO approach for the upper optimization layer, which is designed to capture only the dominant slow modes that describe the effective plant-wide dynamics but are not affected by local fast disturbances. Kadam et al. (2002) decompose the operation of chemical processes into a two-layer architecture, where in the upper layer a DRTO optimizes the dynamic trajectory, which is tracked by the controller of the lower layer. Instead of performing the trajectory optimization at a fixed interval, the DRTO computation in the upper layer is performed only when external disturbances exceed a certain

limit. Würth et al. (2011) implement a neighboring-extremal control strategy in the lower layer control problem, designed to update the economically optimal control trajectory based on sensitivity information computed at the DRTO level, see also the works of Würth et al. (2009b), Würth et al. (2009a), and Kadam and Marquardt (2004). Vega et al. (2014) present a benchmarking of different hierarchical control structures consisting of RTO, DRTO and MPC for wastewater treatment plants. Jamaludin and Swartz (2017) developed a closed-loop DRTO-MPC formulation along with approximations thereof to manage the computational load and tested their approaches on a polystyrene reactor. Nevertheless, DRTO-MPC multilayer methods remain computationally expensive, and the use of plant-wide implementation does not appear reasonable as it is too complex and too demanding for real-time requirements.

Other strategies aim to approximate the RTO problem setting in the lower-layer MPC, which is considered as economic MPC, see for example Rawlings et al. (2012), Amrit et al. (2013) and Ellis et al. (2014)

In the present work a two-layer optimization and control architecture for an industrial steam process is presented. The upper layer, before denoted as RTO, is better described in this context as energy hub optimization (EHO), the lower layer is chosen as MPC. The cooperation concept between the two layers is based on the sensitivities of the economic cost function and the optimal expected plant operating costs.

1.4. Lower optimization layer: control approaches for industrial steam plants

A brief overview of advanced process control and its role in the industry is given in Hofmann et al. (2020) and Willis and Tham (1994). Basic process controls, such as classical PID-based control methods, are designed and implemented within the process components themselves to provide the foundation for operation as well as automation. Advanced process controls are usually added at a higher level, often later, to exploit optimization potential by combining process knowledge with control techniques.

Numerous control methods, from basic to advanced schemes, have been applied in literature for the control of steam-powered systems. A review using both conventional and advanced methods was conducted by Wu et al. (2015) and includes academic studies as well as industrial practice. In a hierarchical approach with underlying PID controllers, Prasad et al. (2000) and Prasad et al. (2002) have presented a nonlinear MPC concept based on successive linearization. Hlava et al. (2013) compared a multi-model and a nonlinear MPC (non-convex optimal control problem) with traditional PID controllers.

In the present work, an MPC (see, for example Rawlings and Mayne (2009)) is chosen for the control layer. The MPC computes optimal control actions in order to regulate the plant as close as possible to the optimal setpoints while taking constraints into account. The MPC employs a nonlinear dynamic plant model successively linearized around the current trajectory, see for example, Zhakatayev et al. (2017) and Lawrynczuk (2014). In order to account for disturbances and ensure sufficient steam quality, stochastic MPC methods as in Heirung et al. (2018) are adopted. The permitted violation probability of the stochastic MPC is obtained from the cooperation concept, which determines optimal expected operating costs (risk costs) based on the sensitivities of the EHO's cost function and stochastic information of the disturbances. Thus, an efficient cooperation between the control layer and a higher-level optimization layer is ensured.

1.5. Upper optimization layer: operation optimization approaches for industrial steam plants

To determine the optimal operation strategy of industrial processes, the optimal commitment – which defines if a unit is on or off – and the loading level of relevant units of the process need to be determined. This optimization problem is typically called Unit Commitment (UC) problem and originated in 1949 in power systems research (Abdou and Tkiouat, 2018). Since then, the UC problem has been the focus of many studies and is also widely applied to thermal processes (Abdi, 2021).

To solve the UC problem, a variety of methods and algorithms have been proposed. For example, they include priority list, dynamic programming, Lagrangian relaxation, simulated annealing, fuzzy systems, artificial neural networks, genetic algorithms, and integer and linear programming. Out of these methods, mixed-integer linear programming (MILP) is an operation research method in which specific variables are integers (Abdi, 2021). This solution technique yields feasible solutions, however, large optimization problems lead to high computational complexity and long run times (van den Bergh et al., 2014). Nevertheless, the MILP formulation has become one of the state-of-the-art solutions for the UC problem and is still widely applied.

A concept that goes one step further than traditional operation optimization approaches is the Energy Hub (EH), introduced in Favre-Perrod (2005). The EH is a concept for optimal energy management of multi-energy-carrier systems, including electrical and thermal energy, water, and gas. It describes a system where multiple energy carriers can be converted, conditioned, and stored. Thus, this concept emphasized a global view of energy systems, not taking into account one energy carrier in one process, but multiple energy carriers, possibly in a network of energy systems (Mohammadi et al., 2017). Although the EH concept is more far-reaching than traditional optimization approaches, it can basically be seen as an extension of the UC problem. Thus, for the formulation and solution of EHs, also methods and algorithms of the UC problem can be used, MILP amongst others (Halmschlager and Hofmann, 2021).

In this work, the operation optimization of the use case is formulated as MILP-UC problem based on the EH concept, providing the upper optimization layer. In this optimization layer, the entire chipboard manufacturing plant is optimized, considering heat, electricity, and interactions with the district heating network and the electrical grid. In addition to the traditionally used EH concept, the product streams and production units of the chipboard manufacturing plant are included in the optimization, according to Halmschlager and Hofmann (2021). To this end, this upper optimization layer is further referred to as energy hub optimization (EHO).

1.6. Main contributions

In the proposed method, the EHO in the upper layer computes optimal setpoints for plant operation based on economic cost functions and static models. The MPC in the lower layer uses these setpoints and additional information from the cooperation concept to compute optimal trajectories for the dynamic plant parts in the presence of disturbances. The cooperation concept exploits stochastic information of the disturbance and the EHO's cost function sensitivities so that the plant is operated at an optimum of expected costs (risk costs).

To the best of the authors' knowledge, no such operation optimization framework for industrial steam processes has been presented so far. The main contributions of this paper are as follows:

- A novel multi-layer operation optimization framework for industrial steam processes is proposed in a stochastic setting, employing a hierarchical structure, resulting in minimal expected operating costs (risk costs).
- The developed cooperation strategy between the two optimization layers ensures efficient cooperation between the higher-layer energy hub optimization (EHO) and the lower-layer model predictive controller (MPC) by computing a permitted violation probability of the EHO's setpoints based on its sensitivity and stochastic information.
- The operation optimization framework is based on a generic architecture and is easy to adapt.
- The underlying static and dynamic models are presented and their parameters are identified from real industrial measurement data of a chipboard manufacturing plant.
- Simulation studies are conducted with these calibrated models, showing the effectiveness and accuracy of the proposed method.

2. Use case

2.1. Plant design

The investigated plant of the chipboard manufacturer is operated with steam, see Figure 1. First, the steam is generated and superheated. From the steam generation unit, the steam is distributed throughout the plant via two extraction ports. The steam at the lower enthalpy level is used in a heated press to harden the adhesives in the chipboards. The steam at the higher enthalpy level is expanded in a turbine and generates electricity. The turbine has two extraction ports at different pressure levels. At the intermediate-pressure stage, the steam can be extracted and supplied to a chip dryer or to district heating. At the low-pressure stage, the steam can only be used for district heating (if it's temperature level is high enough, depending on the season and turbine settings), or is condensed and returned to the plant's water cycle. The plant is modeled in terms of dynamics at two complexity levels:

- The static part consists of models for all components in the entire plant. The models are simplified, do not contain any dynamics and represent the main behavior and couplings of the plant. The static component models are implemented in an EHO to compute cost-optimal setpoints.
- The dynamic part decomposes the steam generation process into multiple detailed (sub)models. This dynamic models are implemented in a controller (MPC) to follow the setpoints computed by the EHO.

2.2. Plant operation

The EHO computes optimal static setpoints for the entire plant, exploiting its economic characteristics while accounting for significant changes in operating conditions such as price factors or other slowly varying disturbances.

The MPC stabilizes the dynamic plant components and follows the EHO's cost-optimal setpoints by minimizing a quadratic cost function that describes the deviations of the states from their desired values.

In a trivial scenario, where no disturbances occur and the operating conditions do not change, the MPC realizes the setpoints of the EHO and performs optimally. However, during a realistic plant operation situation, disturbances and time-varying operating conditions occur. In such situations, an MPC that only tracks the static setpoints with a quadratic penalty on deviations yields suboptimal economic efficiency. Thus, the question arises: How can a global optimum be achieved?

As a solution, a cooperation concept based on the sensitivities of the economic cost function and stochastic information is developed. The proposed cooperation concept manages the interaction between the EHO and the MPC most efficiently in the presence of disturbances.

3. Energy hub optimization

The upper energy hub optimization layer EHO is based on the previous work, Halmschlager and Hofmann (2021), where we developed a MILP optimization framework for industrial (manufacturing) processes and applied it to the chipboard manufacturing plant. Using the MILP optimization framework, relevant units of the use-case and their interactions are formulated by linear constraints and objectives, and the models are aggregated to form the final static plant model. This static plant model includes all relevant units of the chipboard production plant, in contrast to the dynamic control concept model that only represents the steam generation process. After the formulation of the static plant model, the optimization of the plant can be carried out, resulting in optimal trajectories of all units' energy flows. These trajectories are the final results of the EHO layer and specify the setpoints to be followed by the lower control layer. Because the control concept only considers the steam generation process, the relevant setpoints define the steam flows for the press and for the steam turbine, see Figure 1.

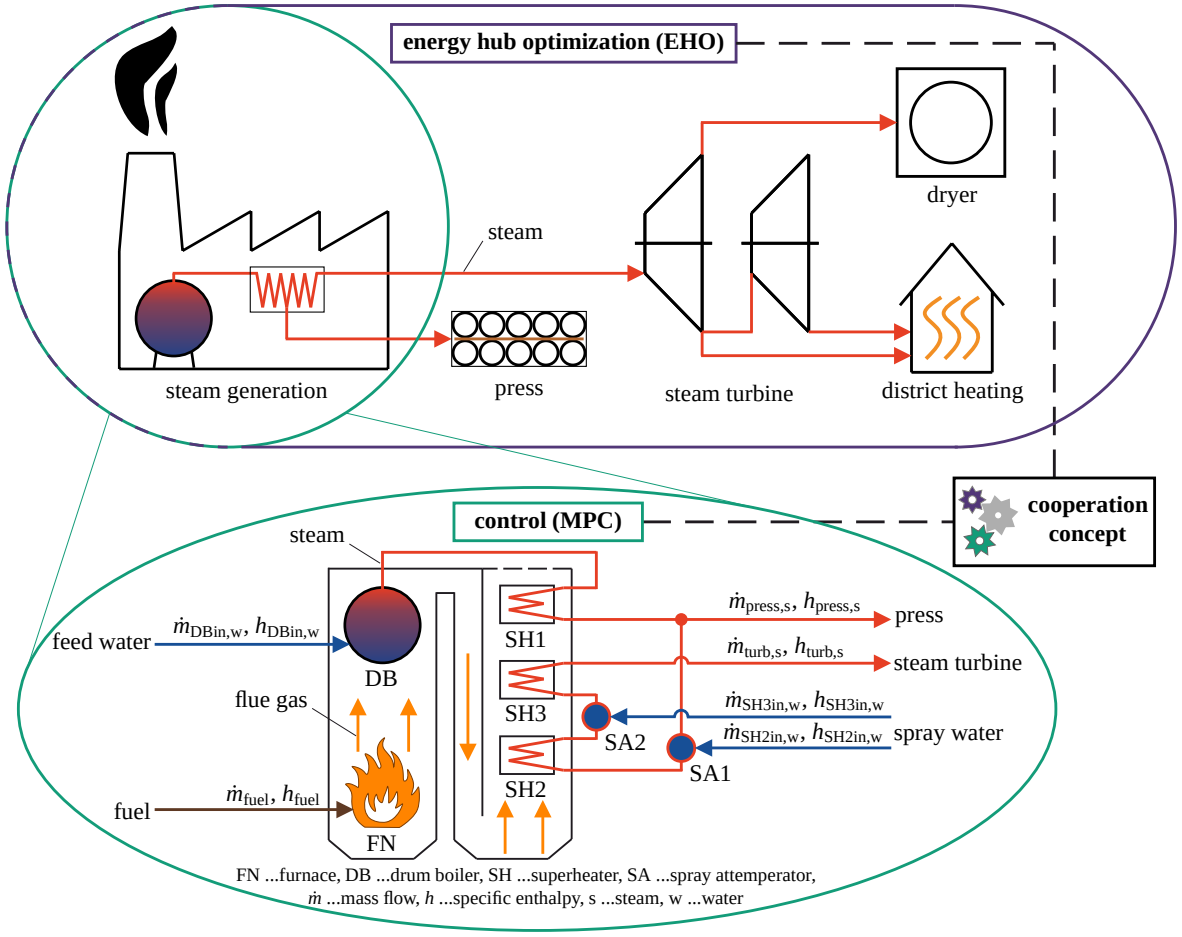

Figure 1: Illustration of the main components and energy flows - the operation of the chipboard manufacturing plant is divided between the optimization and control layers according to its dynamic behavior.

As the entire formulation and description of the EHO of the chipboard production plant would exceed the scope of this work, we refer to Halmschlager and Hofmann (2021) for a detailed description. However, in this Section, we briefly summarize the used constraints and objectives, the modeled units of the static plant model, and relevant optimization features.

3.1. Constraints and objectives

The static plant model of the chipboard manufacturing plant is based on a cost-based UC approach using three binary variables to describe the behavior of one unit, according to Chang et al. (2004). Every unit can have an arbitrary number of streams (energy or product streams) entering or leaving. Using the following constraints, a unit itself and its corresponding streams can be described:

- **Conversion constraints** describe the linear relation between different streams of a device, e.g., between input and output. If required, non-linear behavior can be approximated by piecewise linear segments, using additional binary variables.
- **Start-up constraints** define that a unit can either be *on* or *off*, and can not be started up and shut down simultaneously.
- **Maximum/minimum generation constraints** set a maximum/minimum value for a stream of a unit.
- **Ramp-up/ramp-down constraints** limit the maximal positive/negative gradient of a stream of a unit.
- **Minimum up-/ downtime constraints** define the minimal up-/downtime of a device after it was started/shut down.
- **Storage constraints** are implemented to model the use of (limited) storage.
- **External requirement constraints** define a desired fulfillment of external requirements at every time-step, e.g., district heating demand.
- **Production schedule constraints** also define a desired fulfillment, however, along a specified time interval. Thus,

these constraints can be used to define a production schedule of a manufacturing plant.

The considered objective function J_{EHO}, is comprised of the sum of all fuel costs C_{EHO}, rewards R_{EHO}, and penalties E_{EHO} over an optimization horizon H_{EHO}. With k denoting the time step index, the optimization objective is to minimize

$$J_{EHO} = \sum_{k=1}^{H_{EHO}} (C_{EHO,k} + E_{EHO,k} - R_{EHO,k}) \,, \tag{1}$$

subject to plant constraints as outlined above.

3.2. Static plant model

In contrast to the dynamic model that only includes the steam generation process with the medium steam, the static plant model contains all relevant parts of the chipboard production plant and the mediums steam, electricity, and product. In addition, two district heating demands need to be met by the plant operators, electricity can be sold to the grid, and a specified production schedule needs to be fulfilled. Thus, in the static plant model, the following units are modeled by the constraints outlined above: Steam producer, steam turbine, presses, dryers, district heating heat exchangers, air condenser (after the turbine), and two additional smaller steam producers that are only used if required.

The unit models are aggregated by connecting their input and output streams with corresponding other units' streams to form the entire static plant model. The static models were applied to process input data to validate the aggregated plant model, and their results were compared to process output data. The analysis showed that the aggregated static plant model can approximate the behavior of the plant well, showing an average error of only 2.4 % for all energy and product flows, see Halmschlager and Hofmann (2021). Nevertheless, this was tested over a time interval of one month and does not allow conclusions to be drawn about the plant's dynamic short-term behavior.

3.3. Optimization approach

The optimization of the static plant model is conducted with the developed EHO framework using the YALMIP (Löfberg (2004)) toolbox in MATLAB® (MATLAB (2018)) with the solver GUROBI™ (Gurobi (2021)). The horizon of the optimization is set to 12 h using hourly time-steps. The optimization identifies the optimal operating behavior of the plant to achieve minimal costs - which also includes the best possible fulfillment of the plant's external requirements. As a result, the optimal trajectories of all modeled units' streams are determined, including the info whether these units are *on* or *off*. Additionally, sensitivities are exported for the cooperation concept. The trajectories can then be handed to the control concept, which aims to follow the setpoints based on dynamic component models, and the sensitivities are used for the control concept.

4. Dynamic modeling and parameter identification

In this section, the dynamic component models for the control concept are introduced and their assembly into a plant model of the steam generation process is outlined. The implemented models are mechanistic and their parameters are identified and validated using actual industrial measurement data from a chipboard manufacturer. The models serve as simulated reality of the process and are the basis of the MPC.

4.1. General model structure

The general model structure of both the dynamic component models and the plant model is given by an implicit nonlinear state space descriptor form and reads

$$\boldsymbol{M}(\boldsymbol{x})\,\dot{\boldsymbol{x}} = \boldsymbol{f}(\boldsymbol{x}, \boldsymbol{u}, \boldsymbol{z}) \,, \tag{2}$$

wherein $\boldsymbol{x} \in \mathbb{R}^{n_x \times 1}$ denotes the state vector, $\boldsymbol{u} \in \mathbb{R}^{n_u \times 1}$ the input vector, $\boldsymbol{z} \in \mathbb{R}^{n_z \times 1}$ the disturbance vector, $\boldsymbol{\Theta} \in \mathbb{R}^{n_\Theta \times 1}$ the parameter vector, and $\boldsymbol{M}$ the mass matrix. The outputs of the model are given by

$$\boldsymbol{y} = \boldsymbol{g}(\boldsymbol{x}, \boldsymbol{u}) \,. \tag{3}$$

In (2) and (3), the function $\boldsymbol{f}$ describes the differential equation's right-hand side, and $\boldsymbol{g}$ is the function mapping the states and inputs to the outputs. The mass matrix $\boldsymbol{M}$ and the function $\boldsymbol{f}$ depend on the parameter vector $\boldsymbol{\Theta} \in \mathbb{R}^{n_\Theta \times 1}$.

4.2. Plant model

The models are implemented in MATLAB® employing a class structure for each type of component and the assembled plant. The component classes construct the corresponding models and specify their properties, state equations, interface definitions, as well as connection rules to other components. The plant class contains the instances of the component classes as well as information concerning their assembly and is responsible for calling the components' methods. By calling the components' methods, the plant class computes their state equations, connects the components to each other through flow variables (e.g. steam, flue gas), and updates their state vectors. Thereby, the plant class has methods for simulation (via the MATLAB® solver `ode15s`), linearization, and control. The plant model is composed of the component models described in the following section.

4.3. Component models

The main components of the steam generation are illustrated in the lower part of Figure 1. The furnace "FN" (symbolized by a flame) generates flue gas, which distributes thermal energy throughout the process. Thereby, water evaporates in the drum boiler "DB" and is then further heated in the superheaters "SH". Finally, the resulting steam is directed to the consumers "C" (press and steam turbine). The component models are mechanistic and derived from literature.

Basically, there are two flows that drive the steam generation process and connect the components: flue gas and water/steam. The evaluation of these flows is executed through the plant model, which contains the assembled component models.

The flue gas is produced in the furnace and emits heat to the drum boiler "DB" and superheaters "SH", further also referred to as steam components "SC". The temperature of the flue gas at the outlet of the previous steam component corresponds to the inlet temperature of the flue gas of the following steam component.

The water/steam flows from one steam component ("SC1") to the next ("SC2") due to the pressure difference between "SC1" and "SC2",

$$\dot{m}_{\mathrm{SC1out}} = K_{\mathrm{SC2}} \sqrt{p_{\mathrm{SC1}} - p_{\mathrm{SC2}}} \, . \tag{4}$$

Therein $\dot{m}_{\mathrm{SC1out}}$ denotes the mass flow out of steam component "SC1", K_{SC2} the flow constant of the following steam component "SC2", and p_{SC1} and p_{SC2} the pressure of "SC1" and "SC2", respectively.

The components in the steam generation process are modeled as follows.

4.3.1. Furnace

The furnace "FN" combusts the fuel, e.g. wood, and releases thermal energy, which is distributed in the process by the flue gas. The initial flue gas temperature (combustion temperature) T_{FN} and the heat capacity $c_{p,\mathrm{FG}}$ is affected by the composition of the fuel, e.g. the moisture content of the wood, and thus subject to disturbances. The time response of the furnace is modeled assuming a linear PT1 behavior of the available power P_{FN},

$$\dot{P}_{\mathrm{FN}} = \frac{1}{K_{\mathrm{FN,PT1}}} \left(P_{\mathrm{FN,nom}} u_{\mathrm{FN}} - P_{\mathrm{FN}} \right) \, . \tag{5}$$

Therein, $K_{\mathrm{FN,PT1}}$ is the time constant of the PT1 behavior, $P_{\mathrm{FN,nom}}$ is the nominal power and $u_{\mathrm{FN}} \in [0, 1]$ the utilization factor of the furnace. The available power P_{FN} determines the mass flow $\dot{m}_{\mathrm{FG}}$ of the flue gas "FG",

$$P_{\mathrm{FN}} = \dot{m}_{\mathrm{FG}} c_{p,\mathrm{FG}} T_{\mathrm{FN}} \, . \tag{6}$$

As indicated by the chipboard manufacturer's measurement data, the heat flow from the flue gas "FG" to a steam component "SC" $\dot{Q}_{\mathrm{SC}}$ arises primarily due to convection,

$$\dot{Q}_{\mathrm{SC}} = \tilde{\alpha}_{\mathrm{SC}} \Delta T_{\mathrm{SC,log}} \, . \tag{7}$$

Therein, $\tilde{\alpha}_{\mathrm{SC}}$ is the heat transfer coefficient that determines the heat transfer properties of the corresponding steam component. $T_{\mathrm{SC,log}}$ stands for the mean logarithmic temperature difference which depends on the type of heat exchanger, either parallel such as for the drum boiler "DB", superheater "SH2" and "SH3" or countercurrent such as for the superheater "SH1". The mean logarithmic temperature difference reads

$$T_{\mathrm{SC,log}} = \frac{\Delta T_{\mathrm{SC,max}} - \Delta T_{\mathrm{SC,min}}}{\log\left(\frac{\Delta T_{\mathrm{SC,max}}}{\Delta T_{\mathrm{SC,min}}}\right)} \text{ with} \tag{8}$$

$$\Delta T_{\mathrm{SC,max}} = \begin{cases} T_{\mathrm{FGin}} - T_{\mathrm{SCin}} & \text{for parallel,} \\ T_{\mathrm{FGin}} - T_{\mathrm{SCout}} & \text{for countercurrent,} \end{cases} \tag{9}$$

$$\Delta T_{\mathrm{SC,min}} = \begin{cases} T_{\mathrm{FGout}} - T_{\mathrm{SCout}} & \text{for parallel,} \\ T_{\mathrm{FGout}} - T_{\mathrm{SCin}} & \text{for countercurrent.} \end{cases} \tag{10}$$

The properties of the incoming and outgoing flows are denoted by the indices "in" and "out", respectively.

In addition to (7), the energy balance for the flue gas must hold,

$$\dot{Q}_{\mathrm{SC}} = \dot{m}_{\mathrm{FG}} c_{p,\mathrm{FG}} \left(T_{\mathrm{FGin}} - T_{\mathrm{FGout}} \right) \, . \tag{11}$$

4.3.2. Drum boiler

In the drum boiler "DB", the water circulates in risers connected to the furnace. The water evaporates at saturation temperature and leaves the boiler as steam towards the superheaters. Meanwhile, feed water is constantly supplied to the drum boiler.

To model the dominating drum boiler dynamics, the well-known and validated second-order model of Åström and Bell (2000) is adopted. It captures the overall behavior of the steam boiler well, but does not describe the behavior of the drum level. If the latter is of interest, other higher-order models from Åström and Bell (2000) could be implemented instead. In this work, the second-order model is employed.

The dynamic system equations are derived from the mass and energy balances of the drum boiler,

$$\begin{bmatrix} e_{11} & e_{12} \\ e_{21} & e_{22} \end{bmatrix} \begin{bmatrix} \frac{dV_{\mathrm{DB,w}}}{dt} \\ \frac{dp_{\mathrm{DB}}}{dt} \end{bmatrix} = \begin{bmatrix} \dot{m}_{\mathrm{DBin,w}} - \dot{m}_{\mathrm{DBout,s}} \\ \dot{Q}_{\mathrm{DB}} + \dot{m}_{\mathrm{DBin,w}} h_{\mathrm{DBin,w}} - \dot{m}_{\mathrm{DBout,s}} h_{\mathrm{DB,s}} \end{bmatrix} \tag{12}$$

$$\begin{aligned} \text{with } e_{11} &= \rho_{\mathrm{DB,w}} - \rho_{\mathrm{DB,s}} \, , \\ e_{12} &= V_{\mathrm{DB,s}} \frac{\partial \rho_{\mathrm{DB,s}}}{\partial p_{\mathrm{DB}}} + V_{\mathrm{DB,w}} \frac{\partial \rho_{\mathrm{DB,w}}}{\partial p_{\mathrm{DB}}} \, , \\ e_{21} &= \rho_{\mathrm{DB,w}} h_{\mathrm{DB,w}} - \rho_{\mathrm{DB,s}} h_{\mathrm{DB,s}} \, , \\ e_{22} &= V_{\mathrm{DB,s}} \left(h_{\mathrm{DB,s}} \frac{\partial \rho_{\mathrm{DB,s}}}{\partial p_{\mathrm{DB}}} + \rho_{\mathrm{DB,s}} \frac{\partial h_{\mathrm{DB,s}}}{\partial p_{\mathrm{DB}}} \right) \\ &\quad + V_{\mathrm{DB,w}} \left(h_{\mathrm{DB,w}} \frac{\partial \rho_{\mathrm{DB,w}}}{\partial p_{\mathrm{DB}}} + \rho_{\mathrm{DB,w}} \frac{\partial h_{\mathrm{DB,w}}}{\partial p_{\mathrm{DB}}} \right) \\ &\quad - \left(V_{\mathrm{DB,s}} + V_{\mathrm{DB,w}} \right) + m_{\mathrm{DB,m}} c_{\mathrm{DB,m}} \frac{\partial T_{\mathrm{sat}}}{\partial p_{\mathrm{DB}}} \, . \end{aligned}$$

Therein, V denotes the volume, p the pressure, $\dot{m}$ the mass flow, $\dot{Q}$ the heat flow, h the specific enthalpy and ρ the density. The different phases steam and water are described by the indices "s" and "w", respectively. The influence of the drum boiler's metal parts in (12) depends on its total mass $m_{\mathrm{DB,m}}$ (drum, tubes, and risers), the metal's specific heat capacity $c_{\mathrm{DB,m}}$, and the metal temperature, which is strongly correlated with the saturation temperature T_{sat}.

The input to the system (12) is the valve position u_{DB} which defines the incoming feed water

$$\dot{m}_{\mathrm{DBin,w}} = u_{\mathrm{DB}} K_{\mathrm{DB,w}} \sqrt{p_{\mathrm{DB}} - p_{\mathrm{DB,w}}} \, , \tag{13}$$

wherein $K_{\mathrm{DB,w}}$ is the flow constant and $p_{\mathrm{DB,fw}}$ the pressure of the feed water supply. The connection variables to other components are the heat flow to the drum boiler $\dot{Q}_{\mathrm{DB}}$ evaluated in (7) and the steam flow $\dot{m}_{\mathrm{DBout,s}}$ to the component downstream (4).

4.3.3. Superheater and spray attemperator

In the superheaters "SH", the steam supplied by the drum boiler absorbs the heat from the combustion gases of the furnace. Usually, there are multiple superheater stages in which the steam is brought to the desired temperature and is then delivered for further use, e.g. to a steam turbine. Spray attemperators "SA" support the precise control of the steam temperature and are integrated in the corresponding superheater model. The state equations are derived by means of the energy and mass balances (Boman et al. (2010)),

$$\begin{bmatrix} e_{11} & e_{12} \\ e_{21} & e_{22} \end{bmatrix} \begin{bmatrix} \frac{dp_{\mathrm{SH}}}{dt} \\ \frac{dT_{\mathrm{SH}}}{dt} \end{bmatrix} = \begin{bmatrix} \dot{Q}_{\mathrm{SH}} + \dot{m}_{\mathrm{SHin,w}} h_{\mathrm{SHin,w}} + \dot{m}_{\mathrm{SHin,s}} h_{\mathrm{SHin,s}} - \dot{m}_{\mathrm{SHout,s}} h_{\mathrm{SH,s}} \\ \dot{m}_{\mathrm{SHin,s}} + \dot{m}_{\mathrm{SHin,w}} - \dot{m}_{\mathrm{SHout,s}} \end{bmatrix} \tag{14}$$

$$\begin{aligned} \text{with } e_{11} &= V_{\mathrm{SH}} \left(h_{\mathrm{SH,s}} \frac{\partial \rho_{\mathrm{SH,s}}}{\partial p_{\mathrm{SH}}} + \rho_{\mathrm{SH,s}} \frac{\partial h_{\mathrm{SH,s}}}{\partial p_{\mathrm{SH}}} - 1 \right) , \\ e_{12} &= V_{\mathrm{SH}} \left(h_{\mathrm{SH,s}} \frac{\partial \rho_{\mathrm{SH,s}}}{\partial T_{\mathrm{SH}}} + \rho_{\mathrm{SH,s}} \frac{\partial h_{\mathrm{SH,s}}}{\partial T_{\mathrm{SH}}} \right) , \\ e_{21} &= V_{\mathrm{SH}} \frac{\partial \rho_{\mathrm{SH,s}}}{\partial p_{\mathrm{SH}}} , \\ e_{22} &= V_{\mathrm{SH}} \frac{\partial \rho_{\mathrm{SH,s}}}{\partial T_{\mathrm{SH}}} . \end{aligned}$$

Therein V denotes the total volume, p the pressure, T the temperature, $\dot{m}$ the mass flow, $\dot{Q}$ the heat flow, h the specific enthalpy and ρ the density. The different phases steam and water are described by the indices "s" and "w", respectively. The incoming and outgoing quantities are indicated by the index "in" and "out", respectively.

The input to the system (14) is the valve position $u_{\mathrm{SH,w}} \in [0, 1]$ of the spray attemperator which determines the incoming spray mass flow

$$\dot{m}_{\mathrm{SHin,w}} = u_{\mathrm{SH,w}} K_{\mathrm{SH,w}} \sqrt{p_{\mathrm{SH}} - p_{\mathrm{SH,w}}} , \tag{15}$$

wherein $K_{\mathrm{SH,w}}$ is the flow constant and $p_{\mathrm{SH,w}}$ the pressure of the spray attemperator. The connection variables to other components are the heat flow to the superheater $\dot{Q}_{\mathrm{SH}}$ evaluated in (7), and the incoming and outgoing steam flows $\dot{m}_{\mathrm{SHin,s}}$ and $\dot{m}_{\mathrm{SHout,s}}$ (4), respectively.

4.3.4. Consumer

The consumer model "C" represents the press and the steam turbine. It is assumed as static and its properties determine the steam mass flow out of the steam generation process,

$$\dot{m}_{\mathrm{SCout,s}} = u_{\mathrm{C}} K_{\mathrm{C}} \sqrt{p_{\mathrm{SC}} - p_{\mathrm{C}}} , \tag{16}$$

wherein p_{SC} denotes the pressure in the steam component "SC", K_{C} is the flow constant, and p_{C} the pressure of the consumer "C". The input to the consumer model is the valve opening $u_{\mathrm{C}} \in [0, 1]$. The required steam mass flow to the consumers is determined by the EHO, and the MPC attempts to realize the EHO's setpoints.

4.4. Parameter identification

The parameters of the models described in Section 4.3 are obtained either from data sheets or through parameter estimation of the chipboard manufacturing plant. For the latter, parameter sensitvity analysis is applied utilizing real industrial measurements from the chipboard manufacturer. A viable summary of the steps required for parameter estimation can be found in Ritzberger et al. (2021).

4.4.1. Parameter estimation

Table 1: Plant parameters (dynamic model)

Dimension		**Value**	**scaled Fisher information F_{s}**
time constant	$K_{\mathrm{FN,PT1}}$	537 s	-
total volume	V_{DB}	14 m^3	-
metal mass	$m_{\mathrm{DB,m}}$	26000 kg	-
metal specific heat capacity	$c_{\mathrm{DB,m}}$	0.5 $\frac{\mathrm{kJ}}{\mathrm{kg\ K}}$	-
heat transfer coefficient	$\tilde{\alpha}_{\mathrm{DB}}$	34.10 $\frac{\mathrm{kW}}{\mathrm{K}}$	10^{12}
flow constant feed water	$K_{\mathrm{DB,w}}$	13.94 $\frac{\mathrm{kg}}{\mathrm{s}\sqrt{\mathrm{bar}}}$	10^{12}
flow constant steam in	$K_{\mathrm{SH1,s}}$	9.05 $\frac{\mathrm{kg}}{\mathrm{s}\sqrt{\mathrm{bar}}}$	10^{15}
flow constant spray in	$K_{\mathrm{SH1,w}}$	0 $\frac{\mathrm{kg}}{\mathrm{s}\sqrt{\mathrm{bar}}}$	-
heat transfer coefficient	$\tilde{\alpha}_{\mathrm{SH1}}$	41.09 $\frac{\mathrm{kW}}{\mathrm{K}}$	10^{16}
volume	V_{SH1}	3.2 m^3	-
flow constant steam in	$K_{\mathrm{SH2,s}}$	9.05 $\frac{\mathrm{kg}}{\mathrm{s}\sqrt{\mathrm{bar}}}$	10^{15}
flow constant spray in	$K_{\mathrm{SH2,w}}$	0.30 $\frac{\mathrm{kg}}{\mathrm{s}\sqrt{\mathrm{bar}}}$	10^{12}
heat transfer coefficient	$\tilde{\alpha}_{\mathrm{SH2}}$	6.08 $\frac{\mathrm{kW}}{\mathrm{K}}$	10^{16}
volume	V_{SH2}	0.9 m^3	-
flow constant steam in	$K_{\mathrm{SH3,s}}$	9.07 $\frac{\mathrm{kg}}{\mathrm{s}\sqrt{\mathrm{bar}}}$	10^{8}
flow constant spray in	$K_{\mathrm{SH3,w}}$	0.14 $\frac{\mathrm{kg}}{\mathrm{s}\sqrt{\mathrm{bar}}}$	10^{13}
heat transfer coefficient	$\tilde{\alpha}_{\mathrm{SH3}}$	17.28 $\frac{\mathrm{kW}}{\mathrm{K}}$	10^{16}
volume	V_{SH3}	1.7 m^3	-
flow constant steam in	$K_{\mathrm{O,s}}$	9.14 $\frac{\mathrm{kg}}{\mathrm{s}\sqrt{\mathrm{bar}}}$	10^{15}

To estimate the unknown parameters not found in data sheets, a suitable quadratic cost function is defined,

$$J_{\mathrm{id}}(\boldsymbol{\theta}) = \mathrm{Tr}\left(\left(\boldsymbol{Y}(\boldsymbol{\theta}) - \tilde{\boldsymbol{Y}} \right)^T \boldsymbol{Q}_{\mathrm{y}} \left(\boldsymbol{Y}(\boldsymbol{\theta}) - \tilde{\boldsymbol{Y}} \right) \right) . \tag{17}$$

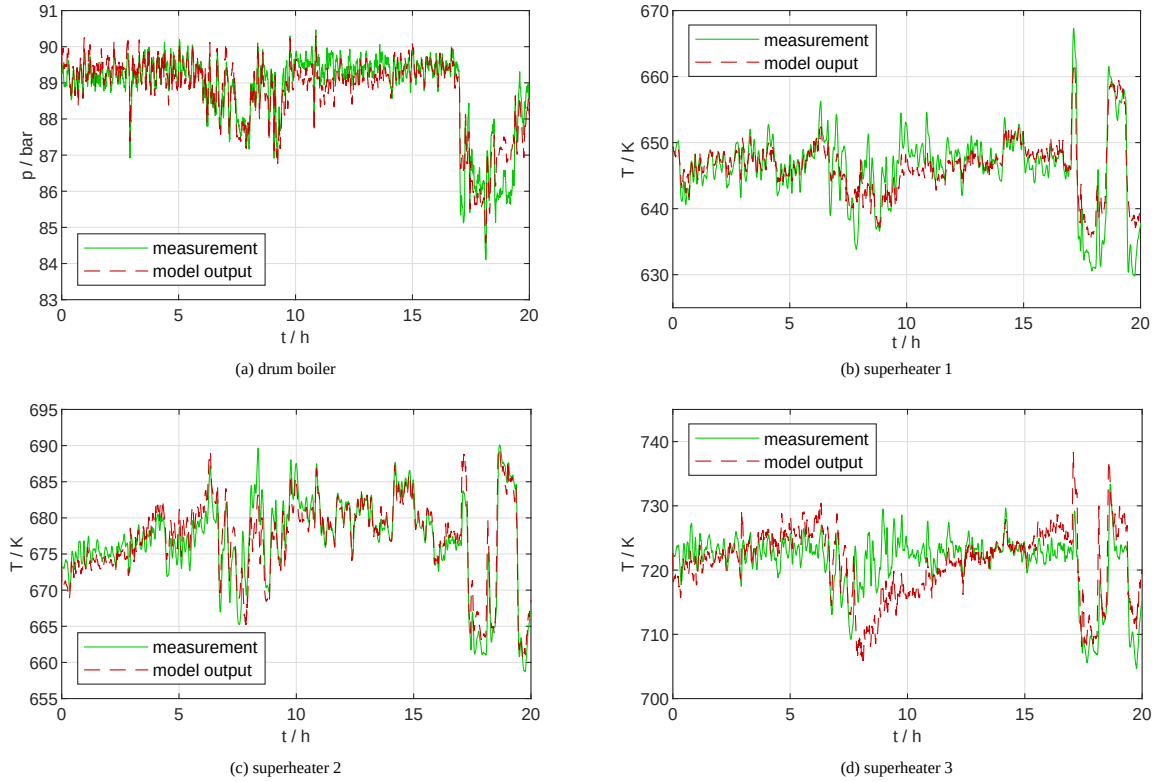

(a) drum boiler

(b) superheater 1

(c) superheater 2

(d) superheater 3

Figure 2: The models show an accurate fit using the optimal parameter estimates.

Here, $\mathrm{Tr}(\cdot)$ stands for the trace of a square matrix, representing the sum of its diagonal elements. The vector $\boldsymbol{\theta}$ contains all model parameters. The matrix $\tilde{\boldsymbol{Y}} \in \mathbb{R}^{m \times n_y}$ contains the n_y measurement channels at m measurement samples. The corresponding simulated model outputs are in the matrix $\boldsymbol{Y}(\boldsymbol{\theta}) \in \mathbb{R}^{m \times n_y}$. The residuals of the different measurement types are scaled by the weighting matrix $\boldsymbol{Q}_y$. The optimal parameter estimates are given by

$$\hat{\boldsymbol{\theta}} = \arg\min_{\boldsymbol{\theta}} \left(J_{\mathrm{id}}(\boldsymbol{\theta}) \right) . \tag{18}$$

The parameter estimations are performed separately for each component, treating them in either a static or a dynamic optimization problem.

The static parameter estimation of the flow constants in (4), (13), (15) and (16) yields a standard least-squares regression problem.

In order to solve the dynamic parameter estimation problem, the dynamic component models are simulated forward in time. The optimal parameter estimates $\hat{\boldsymbol{\theta}}$ are found using the solver `fmincon` of MATLAB® and minimizing the cost function $J(\boldsymbol{\theta})$ (17). To ensure good quality and significance of the parameter estimates, parameter sensitivity analysis is performed.

4.4.2. Parameter sensitivity analysis

Many works have dealt with parameter estimation along with the related problems of optimal experiment design (Baltes et al. (1994)), identifiability analysis (Guillaume et al. (2019), Miao et al. (2011)), and measures of estimation quality (Varella et al. (2010)). In this work, the approach described by Ritzberger et al. (2021) for characterizing estimation quality as well as significance is recapitulated and applied.

Given a consistent estimator and the correct model structure, the parameter estimates approach their true values as the number of measurement samples grows, $\hat{\boldsymbol{\theta}} \rightarrow \mathrm{E}(\boldsymbol{\theta})$. Consequently, the entries of the covariance matrix approach zero as well, $\boldsymbol{\Sigma}_{\hat{\theta}} = \mathrm{cov}\left(\hat{\boldsymbol{\theta}}\right) \rightarrow \boldsymbol{0}$. Hence, in order to assess the accuracy of the parameter estimates $\hat{\boldsymbol{\theta}}$, the associated parameter covariance matrix,

$$\boldsymbol{\Sigma}_{\hat{\theta}} = \mathrm{cov}\left(\hat{\boldsymbol{\theta}}\right) = \mathrm{E}\left[\left(\hat{\boldsymbol{\theta}} - \mathrm{E}[\boldsymbol{\theta}]\right) \left(\hat{\boldsymbol{\theta}} - \mathrm{E}[\boldsymbol{\theta}]\right)^T \right] \tag{19}$$

is evaluated. Thereby, $\mathrm{E}[\cdot]$ stands for the expected value, and thus $\mathrm{E}[\boldsymbol{\theta}]$ represents the actual parameter.

In general, however, a numerical approximation directly of equation (19) is not feasible, but a lower bound can be obtained from the Cramér-Rao inequality (Cramér (1999)),

$$\boldsymbol{\Sigma}_{\hat{\theta}} \geq \boldsymbol{F}^{-1} . \tag{20}$$

The Fisher information matrix $\boldsymbol{F}$ in (20) can be defined as in

(Zullo (1991)) and (Ljung (1999)):

$$\boldsymbol{F} = \boldsymbol{F}(\boldsymbol{\Theta}, m) = \sum_{k=1}^{m} \boldsymbol{\phi}^T(k, \boldsymbol{\Theta}) \boldsymbol{\Sigma}_\mathrm{e}^{-1} \boldsymbol{\phi}(k, \boldsymbol{\Theta}) \ . \tag{21}$$

In (21) $\boldsymbol{\Sigma}_\mathrm{e}$ denotes the error covariance matrix and $\boldsymbol{\phi}(k, \boldsymbol{\Theta})$ is seen as the parametric output sensitivity of the n_p parameters,

$$\boldsymbol{\phi}(k, \boldsymbol{\Theta}) = \left[\frac{d}{d\Theta_1} \boldsymbol{y}(k, \boldsymbol{\Theta}) \ , \cdots , \ \frac{d}{d\Theta_{n_\mathrm{p}}} \boldsymbol{y}(k, \boldsymbol{\Theta}) \right] . \tag{22}$$

The Fisher information matrix is formed by applying finite differences at the optimal parameter estimates $\hat{\boldsymbol{\Theta}}$. In order to render the Fisher information matrix comparable for different types of measurements, it is scaled using a diagonal matrix $\hat{\boldsymbol{\Omega}}$ containing the optimal parameter estimates,

$$\boldsymbol{F}_\mathrm{s} = \hat{\boldsymbol{\Omega}}^T \boldsymbol{F} \hat{\boldsymbol{\Omega}} \ . \tag{23}$$

If $\boldsymbol{F}_{\mathrm{s,ii}} \to 0$ the m measurement samples of the n_y measurement channels do not provide enough information to estimate the parameter Θ_i, $i \in [1, \ldots, n_\mathrm{p}]$.

4.4.3. Parameters

All parameters and their corresponding scaled Fisher information of the components in Figure 1 are listed in Table 1.

The geometry and material parameters of the drum boiler and the superheaters, namely $V_\mathrm{DB,t}$, $m_\mathrm{DB,t}$, $c_\mathrm{DB,t}$, V_SH1, V_SH2, and V_SH3, are obtained from data sheets. The time constant of the furnace is derived from a step response recorded in the chipboard manufacture.

The flow constants K of the steam flow between two consecutive components (4), the feedwater to the drum boiler (13), the spray attemperator (15) and the outlet (16) are obtained from static parameter estimation.

The other parameters are estimated using dynamic simulations, (17), and MATLAB®'s `fmincon` solver.

Fits of the model outputs using the optimal parameter estimates are shown in Figure 2. The Fisher information indicates an excellent suitability of the available data for estimating the parameters not given by data sheets.

5. Control concept

The lower-layer control concept is composed of the stochastic MPC, the successive linearization, and the observer for state and disturbance covariance estimation, see Figure 3. The MPC computes optimal control actions to fulfill the setpoints specified by the EHO for a given permitted violation probability β appropriately, taking stochastic disturbances into account. The permitted violation probability β is obtained by the cooperation concept. In the cooperation concept, stochastic information about the disturbances and the EHO's cost function sensitivities are exploited to compute the permitted violation probability β that leads to optimal expected plant operating costs (risk costs).

To control the steam generation process with its dynamics as well as disturbances, the stochastic control concept is implemented as shown in Figure 3. In the control concept, a nonlinear steam generation model predicts the future state trajectories online using the current control inputs but assuming no disturbances. Then, the steam generation model is successively linearized around this trajectory and discretized in time. A stochastic MPC implements the obtained linear model and computes optimal control inputs based on chance constraints to follow desired reference setpoints from the EHO in a probabilistic manner. In order to provide the stochastic MPC with up-to-date information, an observer estimates the true states from measurements and computes their estimation error covariances. Additionally, the covariance of the disturbance is estimated. The measurements are taken from a nonlinear model, which serves as simulated reality and is subject to disturbances.

In the following Section, k is the time step index with a chosen time step length Δt, so $t_k = k\ \Delta t$, and signals with subscript k denote their values at time $t = t_k = k\ \Delta t$.

5.1. Simulated reality

The simulated reality's model is based on Section 4. The process equations with disturbances and the measurement output equations with noise have the form

$$\boldsymbol{M}\left(\boldsymbol{x}_\mathrm{p}\right) \dot{\boldsymbol{x}}_\mathrm{p} = \boldsymbol{f}\left(\boldsymbol{x}_\mathrm{p}, \boldsymbol{u}_k, \boldsymbol{z}_k\right) \tag{24}$$

$$\boldsymbol{y}_{\mathrm{p},k} = \boldsymbol{g}\left(\boldsymbol{x}_\mathrm{p}(t_k), \boldsymbol{u}_k, \boldsymbol{v}_k\right) \ . \tag{25}$$

Therein, the disturbances $\boldsymbol{z}_k$ and the measurement noise $\boldsymbol{v}_k$ are both assumed Gaussian and white.

5.2. Nonlinear steam generation model

The nonlinear steam generation model corresponds to the simulated reality's model, except no disturbances are assumed,

$$\boldsymbol{M}(\boldsymbol{x}_\mathrm{m}) \dot{\boldsymbol{x}}_\mathrm{m} = \boldsymbol{f}(\boldsymbol{x}_\mathrm{m}, \boldsymbol{u}_k, \boldsymbol{z}_k = \boldsymbol{0}) \tag{26}$$

$$\boldsymbol{y}_{\mathrm{m},k} = \boldsymbol{g}(\boldsymbol{x}_\mathrm{m}(t_k), \boldsymbol{u}_k, \boldsymbol{v}_k = \boldsymbol{0}) \ . \tag{27}$$

The nonlinear steam generation model predicts the future state trajectories based on the current states and inputs $(\boldsymbol{x}_\mathrm{m}(t_{k+1}), \boldsymbol{u}_k)$. The predicted states form the basis for linearization and state estimation of the observer.

5.3. Linear model

The dynamic model equations (2)-(3) are discretized and successively linearized (see, e.g., Zhakatayev et al. (2017)) around the trajectory obtained from the nonlinear steam generation model,

$$\Delta \boldsymbol{x}_{k+1} = \boldsymbol{A} \Delta \boldsymbol{x}_k + \boldsymbol{B} \Delta \boldsymbol{u}_k + \boldsymbol{E} \Delta \boldsymbol{z}_k \tag{28}$$

$$\Delta \boldsymbol{y}_k = \boldsymbol{C} \Delta \boldsymbol{x}_k + \boldsymbol{D} \Delta \boldsymbol{u}_k \ , \tag{29}$$

where Δ indicates the deviations from the state trajectories. The system matrices $\boldsymbol{A} \in \mathbb{R}^{n_x \times n_x}$, $\boldsymbol{B} \in \mathbb{R}^{n_x \times n_u}$, $\boldsymbol{C} \in \mathbb{R}^{n_y \times n_x}$, $\boldsymbol{D} \in \mathbb{R}^{n_y \times n_u}$, and $\boldsymbol{E} \in \mathbb{R}^{n_x \times n_z}$ are derived using finite differences and their time index is omitted for reasons of brevity. The system (28)-(29) can be implemented in a standard MPC or an extended Kalman filter (observer) formulation.

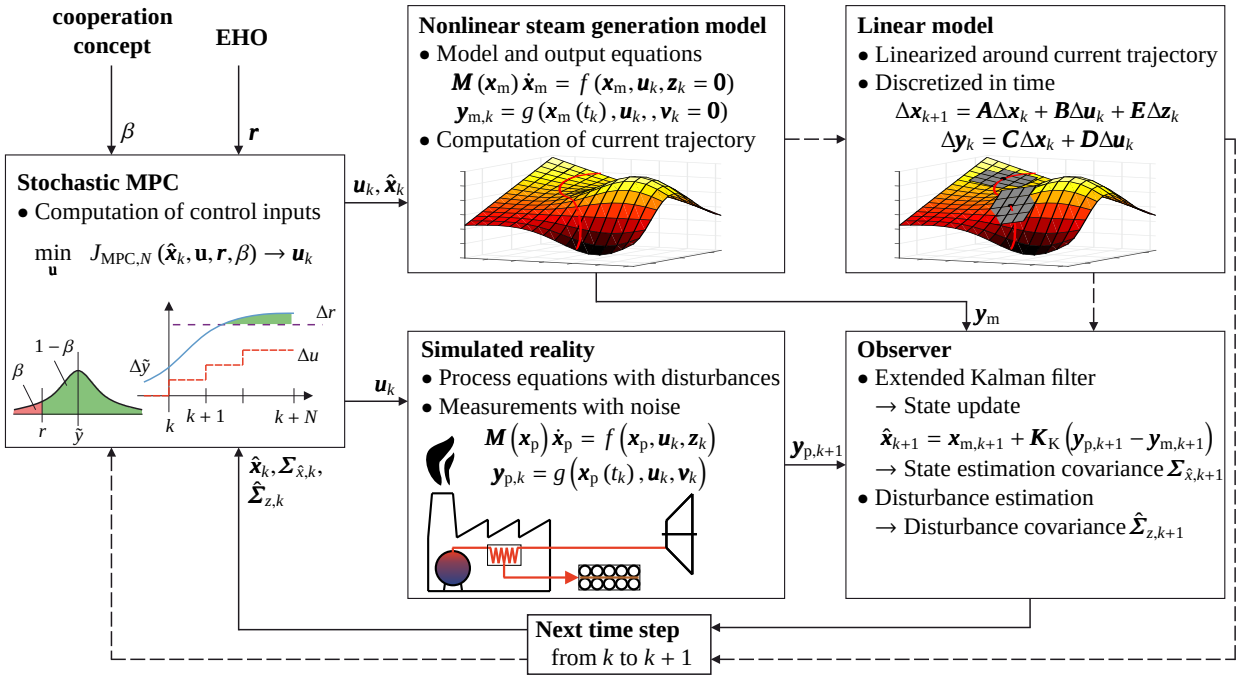

β ...permitted violation probability, $\boldsymbol{r}$ ...reference setpoints, $\boldsymbol{\Sigma}$ ...covariance matrix, $\hat{}$...estimated quantity

Figure 3: Scheme of the control concept with signal (solid line) and process flow (dashed line)

5.4. Observer

In the control concept, observers are used to estimate the true states, their estimation error covariances, and the disturbance covariance from measurements.

5.4.1. Extended Kalman filter

A standard extended Kalman filter (EKF), as described in Simon (2006), is implemented to estimate the true states and their estimation error covariances. The state update,

$$\hat{\boldsymbol{x}}_{k+1} = \boldsymbol{x}_{\mathrm{m},k+1} + \boldsymbol{K}_{\mathrm{K}} \left(\boldsymbol{y}_{\mathrm{p},k+1} - \boldsymbol{y}_{\mathrm{m},k+1} \right) , \tag{30}$$

is determined using measurements $\boldsymbol{y}_{\mathrm{p}}$ from the simulated reality and the predicted nonlinear model outputs $\boldsymbol{y}_{\mathrm{m}}$. The Kalman gain $\boldsymbol{K}_{\mathrm{K}}$ is computed from the Jacobians of (26)-(27), the evolution of the estimation error covariance $\boldsymbol{\Sigma}_{\hat{x},k}$, and the process as well as measurement noise. The process noise is obtained by estimating the disturbance covariance $\hat{\boldsymbol{\Sigma}}_{z,k}$ as described in Section 5.4.2 and the measurement covariance $\boldsymbol{R}$ is assumed to be known.

5.4.2. Disturbance covariance estimation

The disturbance covariance estimation is based on the EKF's assumptions and the definition of the state covariance matrix. First, the differences of the measurements and the model outputs are computed,

$$\boldsymbol{s}_{k+1} = \boldsymbol{y}_{\mathrm{p},k+1} - \boldsymbol{y}_{\mathrm{m},k+1} . \tag{31}$$

This current ouput residual is collected with n_{s} older residuals in the innovation matrix,

$$\boldsymbol{S}_{k+1} = \left[\begin{array}{c|c|c|c} & & & \\ \boldsymbol{s}_{k-n_{\mathrm{s}}+2} & \boldsymbol{s}_{k-n_{\mathrm{s}}+3} & \cdots & \boldsymbol{s}_{k+1} \\ & & & \end{array} \right] \text{ with } \boldsymbol{S}_k \in \mathbb{R}^{n_y \times n_{\mathrm{s}}} , \tag{32}$$

whereby n_{s} is the window size of the estimator. Then, the covariance matrix of the measurements is defined as

$$\hat{\boldsymbol{\Sigma}}_{yz,k+1} = \frac{\boldsymbol{S}_{k+1} \boldsymbol{S}_{k+1}^{T}}{n_{\mathrm{s}} - 1} . \tag{33}$$

The disturbance variance's influence on the states is given by

$$\hat{\boldsymbol{\Sigma}}_{xz,k+1} = \boldsymbol{C} \backslash \left(\hat{\boldsymbol{\Sigma}}_{yz,k+1} - \boldsymbol{R} \right) / \boldsymbol{C}^{\mathrm{T}} - \boldsymbol{A} \boldsymbol{\Sigma}_{\hat{x},k} \boldsymbol{A}^{T} , \tag{34}$$

and the disturbance error covariance results in

$$\hat{\boldsymbol{\Sigma}}_{z,k+1} = \boldsymbol{E} \backslash \hat{\boldsymbol{\Sigma}}_{xz,k+1} / \boldsymbol{E}^{T} , \tag{35}$$

where \ and / denote left- and right-pseudo inverses. The quality of estimation significantly depends on the window size n_{s}. A large window size is required for good convergence, whereas a small window size is better suited to account for a (slowly) varying disturbance covariance and thus reduces effective bias estimation. A recursive estimation algorithm for disturbance covariance estimation can be found in Ma et al. (2020), which, however, cannot consider a varying disturbance covariance.

5.5. Chance-constrained model predictive control

MPCs are widely used to control multivariable systems under constraints. The key idea is to compute an optimal trajectory of the controlled system model, predicted over a chosen horizon from the current time into the future. The first control signal value is applied and the whole optimization is repeated at the next time step, based on an updated initial state. In order to account for disturbances and ensure sufficient steam quality, stochastic MPC methods as described in Heirung et al. (2018) are adapted. The formulations of Heirung et al. (2018) result in the following deterministic optimal control problem of the linearized model (28)-(29),

$$\min_{\mathbf{u}} \quad J_{\mathrm{MPC},N}\left(\hat{\boldsymbol{x}}_k, \mathbf{u}, \boldsymbol{r}, \beta\right) \tag{36}$$

$$\text{s.t.} \quad \Delta\tilde{\boldsymbol{x}}_{k+i+1} = \boldsymbol{A}\Delta\tilde{\boldsymbol{x}}_{k+i} + \boldsymbol{B}\Delta\boldsymbol{u}_{k+i}\,, \tag{37}$$

$$\Delta\tilde{\boldsymbol{y}}_{k+i+1} = \boldsymbol{C}\Delta\tilde{\boldsymbol{x}}_{k+i} + \boldsymbol{D}\Delta\boldsymbol{u}_{k+i}\,, \tag{38}$$

$$\Pr\left[\tilde{\boldsymbol{y}}_{k+i+1,j} \leq \boldsymbol{r}_{k+i+1,j}\right] \geq 1-\beta_j\,, \tag{39}$$

$$\boldsymbol{u}_{k+i} \leq \boldsymbol{u}_{\mathrm{con}}\,, \tag{40}$$

$$\Delta\tilde{\boldsymbol{x}}_{k+i} = \mathrm{E}[\Delta\boldsymbol{x}_{k+i}]\,, \tag{41}$$

$$\text{with } i = 0,\ldots,N-1\,, \tag{42}$$

$$j = 1,\ldots,n_y\,. \tag{43}$$

Therein, the cost function $J_{\mathrm{MPC},N}$ is minimized over the prediction horizon N to compute an optimal input control sequence $\mathbf{u} = \{\boldsymbol{u}_k, \ldots \boldsymbol{u}_{k+N-1}\}$. The first input $\boldsymbol{u}_k$ of the control sequence is applied to the system, and then the optimization problem is recomputed at the next time step. In (36)–(43) the subscript $k+i+1$ denotes the value at the corresponding future time step based on the current knowledge. The expected deterministic value of the predicted state and output vector (no disturbances assumed) is given by $\Delta\tilde{\boldsymbol{x}}_{k+i+1}$ and $\Delta\tilde{\boldsymbol{y}}_{k+i+1}$, respectively. Here, Δ indicates deviations from the trajectory computed by the nonlinear steam generation model, so that the effective predicted state and output vector is the sum of the two.

When the disturbances $\Delta\boldsymbol{z}_k$ in (28) are modeled as random variables, the system dynamics are described in a probalistic sense. In the chance constraint (39), $\Pr[\cdot]$ stands for the probability of an event. The vectors $\boldsymbol{r}_{k+i+1}$ and $\boldsymbol{u}_{\mathrm{con}}$ contain the desired outputs (setpoints) and the input constraints, respectively. In (39), the probability of violating an output constraint j should not exceed a permitted probability $\beta_j \in (0, 1]$.

The chance constraints (39) can be expressed in terms of the expected deterministic predicted output variable $\tilde{\boldsymbol{y}}_{k+i+1,j}$ and the inverse cumulative density function $F^{-1}_{k+i+1,j}$ for each output constraint j,

$$\tilde{\boldsymbol{y}}_{k+i+1,j} \geq \boldsymbol{r}_{k+i+1,j} + F^{-1}_{k+i+1,j}\left(1-\beta_j\right) \tag{44}$$

The complexity of computing (44) depends on the underlying probability distribution of the stochastic disturbances $\Delta\boldsymbol{z}_k$ as well as the specific nonlinearity characteristics of the plant behavior. Assuming $\Delta\boldsymbol{z}_k$ as Gaussian and the plant behavior to be approximately linear with respect to disturbance propagation over the prediction horizon N, the state and output covariance can be propagated over the prediction horizon,

$$\boldsymbol{\Sigma}_{\tilde{x},k+i+1} = \boldsymbol{A}\boldsymbol{\Sigma}_{\tilde{x},k+i}\boldsymbol{A}^T + \boldsymbol{E}\boldsymbol{\Sigma}_{z,k}\boldsymbol{E}^T\,, \tag{45}$$

$$\boldsymbol{\Sigma}_{\tilde{y},k+i+1} = \boldsymbol{C}\boldsymbol{\Sigma}_{\tilde{x},k+i+1}\boldsymbol{C}^T \text{ with } i = 0,\ldots,N-1\,. \tag{46}$$

In (45), $\boldsymbol{\Sigma}_{z,k}$ is the disturbance covariance matrix,

$$\boldsymbol{\Sigma}_{z,k} = \mathrm{E}\left[\Delta\boldsymbol{z}_k\ \Delta\boldsymbol{z}_k^T\right]\,. \tag{47}$$

Since the disturbance covariance matrix is unknown and needs to be estimated as described in Section 5.4.2, the predicted state vector and thus the output vector is modeled via the Student's t-distribution $\boldsymbol{x}_{k+i+1|k} \sim \mathcal{T}\left(\tilde{\boldsymbol{x}}_{k+i+1|k}, \boldsymbol{\Sigma}_{\tilde{x},k+i+1}, \nu\right)$, whereby ν is the number of degrees of freedom of the Student's t-distribution.

The cumulative density function F and its inverse can be obtained with initial condition $\boldsymbol{\Sigma}_{\tilde{x},k} = \boldsymbol{\Sigma}_{\hat{x},k}$ and $\tilde{\boldsymbol{x}}_k = \hat{\boldsymbol{x}}_k$, both obtained from the EKF in Section 5.4.1.

The cost function $J_{\mathrm{MPC},N}$ in (36) is designed to track the desired setpoints $\mathbf{r} = \{\boldsymbol{r}_{k+1}, \ldots \boldsymbol{r}_{k+N}\}$ with $\boldsymbol{r}_i \in \mathbb{R}^{n_y \times 1}$,

$$J_{\mathrm{MPC},N} = \sum_{i}^{N}\left(\left(\tilde{\boldsymbol{y}}_{k+i} - \boldsymbol{r}_i\right)^T \boldsymbol{Q}_y \left(\tilde{\boldsymbol{y}}_{k+i} - \boldsymbol{r}_i\right)\right) + \sum_{i}^{N-1}\left(\boldsymbol{u}_{k+i}^T \boldsymbol{Q}_u \boldsymbol{u}_{k+i}\right) \tag{48}$$

wherein $\boldsymbol{Q}_y$ and $\boldsymbol{Q}_u$ are weighting matrices.

By minimizing equation (48), the MPC is able to optimally track the setpoints given by the EHO with a given permitted violation probability β. The permitted violation probability β of (39) is obtained from the cooperation concept in Section 6 using the EHO's cost function sensitivities.

6. Cooperation concept

The basic idea of the following cooperation concept is to compute a permitted violation probability β of the desired setpoints $\boldsymbol{r}$ to obtain optimal expected plant operating costs (risk costs). Therefore, the EHO passes the cost function's sensitivities with respect to the desired setpoints to the cooperation concept. In the cooperation concept, the EHO's sensitivities are implemented in a risk cost function based on a probability distribution. The risk cost function's minimization leads to an optimal permitted violation probability β.

6.1. Risk cost function

The risk cost function is based on static considerations of the EHO's cost function and consists of two terms, one for fuel costs and one for violation costs,

$$J_{\mathrm{risk}}(c_{\mathrm{fuel}}, c_{\mathrm{viol}}, \beta) = c_{\mathrm{fuel}}(\tilde{y} - r) + c_{\mathrm{viol}}\omega\,. \tag{49}$$

Therein, c_{fuel} denotes the fuel costs per additional output unit and r is a desired setpoint. The expected deterministic output $\tilde{y}$ and the expected violations ω depend on the choice of β, see (39) and Figure 4. The violation costs per missing output c_{viol}

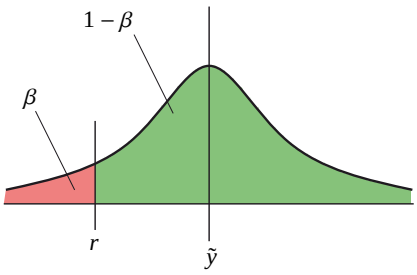

Figure 4: The properties of the chosen stochastic probability distribution are used to compute a permitted violation probability β for optimal expected operating costs.

are obtained by deriving the EHO's cost function with respect to the corresponding setpoint

$$c_{\text{viol}} = \frac{\mathrm{d}J_{\text{EHO}}}{\mathrm{d}r} \,. \tag{50}$$

The permitted violation probability is found by minimizing the risk cost function,

$$\min_{\beta} \quad J_{\text{risk}}\left(c_{\text{fuel}}, c_{\text{viol}}, \beta\right) \,. \tag{51}$$

6.2. Expected violations

As in Section 5.5, the probability density function f_X is chosen as Student's t-distribution. The permitted violation probability is found by evaluating the cumulative density function

$$\beta = \int_{-\infty}^{r} f_X dx \,. \tag{52}$$

The expected violations are given by

$$\omega = \int_{-\infty}^{r} (r - x)\, f_X dx \,. \tag{53}$$

6.3. Multiple outputs

In the case of multiple outputs, the corresponding permitted violation probabilities can be evaluated separately if there are no other constraints. If the maximum available power is limitted, for example due to plant restrictions, the optimization for determining the permitted violation probabilities for multiple outputs must be performed with respect to complementary constraints.

7. Demonstration of the novel operation optimization framework

The performance of the developed information-exchange concept (sensitivity-based) is demonstrated via simulation studies. First, the settings of the operation optimization framework are described. Then, the effectiveness of the stochastic control concept is shown. Finally, simulations are performed using the multi-layer control architecture with and without the cooperation concept.

7.1. Settings

7.1.1. Settings of the EHO

The economic plant operation is optimized via the EHO from Section 3 using the YALMIP (Löfberg (2004)) toolbox in MATLAB® (MATLAB (2018)) with the solver GUROBI™ (Gurobi (2021)). The EHO's optimization horizon is set to 12 h using hourly time-steps, $T_{\text{EHO,s}} = 1$ h. The optimization is performed under real industrial constraints for district heating demand, production schedules, the electricity market and cost factors.

7.1.2. Settings of the control concept

The control concept from Section 5 follows the EHO's setpoints with the permitted violation probability β provided by the cooperation concept. The sampling time of the control concept is chosen to be $T_{\text{MPC,s}} = 10$ s. The observer for disturbance estimation has a window size of $n_{\text{s}} = 3000$ simulation steps. The MPC controls the water volume of the drum boiler, as well as the enthalpy flow to the steam turbine and the press. The weighting matrices of the MPC are chosen diagonal. The entries of the output weighting matrix $\boldsymbol{Q}_y$ are 10^5 for the water volume and 10^1 for the demanded enthalpy flow. The entries of the input weighting matrix $\boldsymbol{Q}_u$ are 10^4 for all steam/water valves and 10^6 for the utilization factor of the furnace. The degrees of freedom of the Student's t-distribution are $\nu = n_{\text{s}} - 1$. Nonlinear simulation results are obtained via the MATLAB® solver `ode15s` (MATLAB (2018)).

The optimization problems of the MPC are solved using MOSEK® (MOSEK (2019)) and YALMIP (Löfberg (2004)).

7.1.3. Settings of the simulation

The simulation contains the models as described in Sections 4 and 5.1. A stochastic disturbance with a standard deviation of $\sigma_{\text{z}} = 0.15$ is applied to the input of the furnace $u_{\text{FN}} \in [0, 1]$, which can be interpreted as fluctuating fuel quality (e.g., due to the moisture content of wood).

7.2. Demonstration of the stochastic control concept

The performance of the stochastic control concept is demonstrated using a stepwise heat demand of the steam turbine and a permitted violation probability of 10%.

In the case of a linear reference simulation, the system was able to accurately meet the demand (realized violation probability 9.8%). However, when considering the nonlinear plant, the constraints get violated in 17.3% of the cases. The deviations in the permitted violation probability occur due to nonlinear plant behavior and the successive linearization. Therefore, the chance constraints (44) are modified by adding a nonlinear correction term Δ_{nonlin},

$$\tilde{\boldsymbol{y}}_{k+i+1,j} \geq \boldsymbol{r}_{k+i+1,j} + F^{-1}_{k+i+1,j}\left(1 - \beta_j\right) + \Delta_{\text{nonlin}} \,. \tag{54}$$

The nonlinear correction term Δ_{nonlin} is obtained from online analyzing the last $n_{\Delta\text{nonlin}} = 300$ samples. With the proposed correction term, a satisfying plant performance was achieved and the constraints were violated in 10.2% of the cases, see Figure 5.

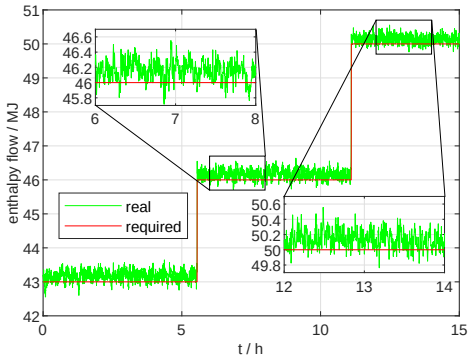

Figure 5: The enthalpy flow to the steam turbine complies with the permitted violation probability.

The disturbance covariance is estimated accurately, see Figure 6. The estimation quickly approaches the actual value and converges.

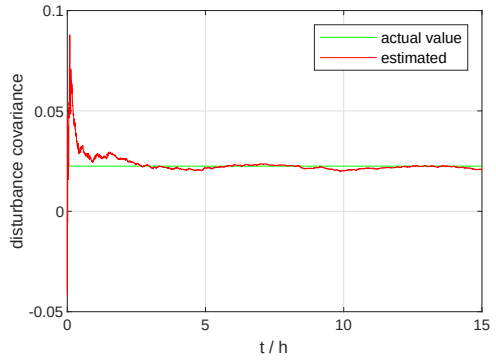

Figure 6: The observer estimates the disturbance covariance accurately.

7.3. Demonstration of the cooperation concept

The operation optimization framework is tested with three different control concepts in the lower operation optimization layer: (1) a standard MPC, (2) a stochastic MPC with a permitted violation probability of 3 %, and (3) a stochastic MPC in combination with the cooperation concept resulting in an optimal permitted violation probability. In the upper operation optimization layer, the EHO optimizes the economic plant operation statically under real industrial constraints for district heating demand, production schedules, the electricity market, and cost factors. The EHO provides setpoints to the MPC and the cost function sensitivities to the cooperation concept. The disturbances act on the input of the furnace u_{FN} (e.g., due to fluctuating fuel quality) and are only compensated for in the MPC. To account for the stochastic nature of the disturbances, each control concept is tested in ten simulation runs for the simulation study. The simulation study is analyzed in terms of three different cost factors: the additional plant operating costs, which can be split into the violation costs and the additional fuel costs.

The incurred additional plant operating costs are due to the non-optimal plant operation in case of disturbances. If there are no disturbances present, the steam demand could be exactly fulfilled and the additional costs would be zero. Figure 7 shows the total additional plant operating costs due to the occurrence of disturbances. The MPC with the novel cooperation concept is able to minimize the additional plant operating costs, while they are significantly higher in the case of the standard MPC. As a result, the additional plant operating costs were reduced by 54.5 % with the novel cooperation concept compared to the standard MPC.

The additional costs (seen in Figure 7) can be divided into those arising from the violation of the required setpoints and those arising from the additional fuel costs for overproduced steam. The violation costs are similar for the MPC with a permitted violation probability of 3 % and with optimal permitted violation probability, while they are significantly higher in the standard MPC case, see Figure 8. The fuel cost for overproduced steam is minimal if no measures are taken to stochastically compensate for violations, as in the standard MPC case. Fuel costs are significantly higher in the MPC with the 3 % permitted violation probability than with the optimal permitted violation probability, see Figure 9. Thus, in total, the additional plant operating costs are the lowest with the developed cooperation concept, optimally solving the conflict between additional fuel costs and violation costs.

In summary, the developed cooperation concept is able to achieve the cost-critical setpoints while limiting additional fuel consumption and thus emissions to the necessary level.

8. Conclusions

The developed operation optimization framework is able to operate an industrial plant at optimal expected costs in the presence of stochastic disturbances. The method is based on a hierarchical structure in which a higher layer (EHO) optimizes the economic costs and provides setpoints to a lower layer (MPC) that compensates for disturbances and considers dynamic performance. A cooperation concept between the optimization layers is proposed to operate the entire plant in an efficient way. In the cooperation concept, the EHO's cost function sensitivities and stochastic information about the disturbances are exploited to compute an optimal permitted violation probability of the setpoints. The MPC tracks the desired setpoints with the permitted violation probability, resulting in an optimal trade-off between fuel and violation costs. Observers are employed to estimate the true states of the plant and the disturbance covariance.

The operation optimization framework is tested using models calibrated with industrial measured data and in simulation scenarios under real industrial constraints for district heating demand, production schedules, the electricity market, and cost factors. It is seen that the proposed operation optimization framework is perfectly suited for controlling plant operation in the presence of stochastic disturbances. The expected operating costs of the plant are reduced by 54.5 % compared to a standard

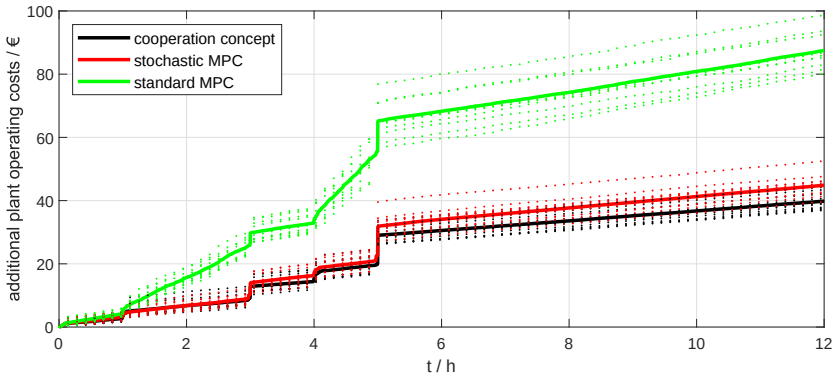

Figure 7: The presence of disturbances leads to additional plant operating costs, which can be minimized with the novel cooperation concept. The solid lines are the mean values of the ten simulation runs, whereas the dashed lines represent each individual run.

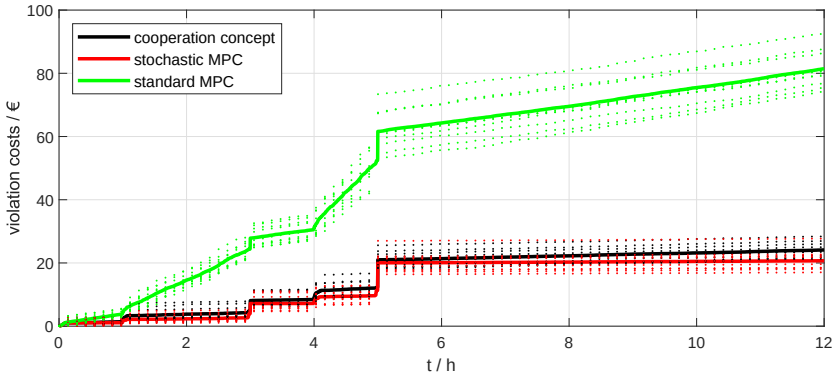

Figure 8: The violation costs in the presence of disturbances are similar between the stochastic MPC with 3 % permitted violation probability and with optimal permitted violation probability, while they are significantly worse in the standard MPC case. The cooperation concept provides the best trade-off between additional fuel and violation costs. The solid lines are the mean values of the ten simulation runs, whereas the dashed lines represent each individual run.

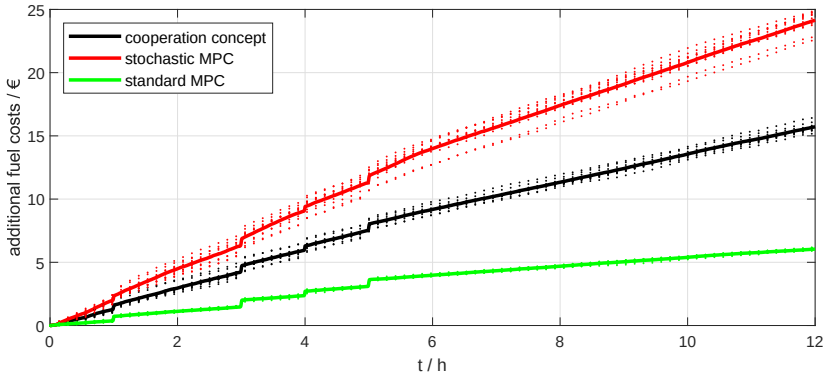

Figure 9: The fuel costs are significantly higher using the stochastic MPC with 3 % permitted violation probability than with optimal permitted violation probability. The cooperation concept provides the best trade-off between additional fuel and violation costs. The solid lines are the mean values of the ten simulation runs, whereas the dashed lines represent each individual run.

MPC case and no further expert knowledge is required to control the plant, e.g., to adjust control parameters. The observers accurately estimate the true system states and the disturbance covariance. The developed operation optimization framework is appropriate for a real process, since there are almost always such random disturbances present, caused, for example, by imperfections of fuel compositions or reactions.

Acknowledgements

The authors want to acknowledge the support provided by the doctoral school Smart Industrial Concept [SIC!] (https://sic.tuwien.ac.at). Our special thanks go to our industrial partner FunderMax GmbH along with Eduard Pleschutznig, who made the analysis of the chipboard production plant possible and provided the necessary data. The authors acknowledge TU Wien Bibliothek for financial support through its Open Access Funding Programme.

References

Abdi, H., 2021. Profit-based unit commitment problem: A review of models, methods, challenges, and future directions. Renewable and Sustainable Energy Reviews 138, 110504. doi:10.1016/j.rser.2020.110504.

Abdou, I., Tkiouat, M., 2018. Unit commitment problem in electrical power system: A literature review. International Journal of Electrical and Computer Engineering (IJECE) 8, 1357. doi:10.11591/ijece.v8i3.pp1357-1372.

Amrit, R., Rawlings, J., Biegler, L., 2013. Optimizing process economics online using model predictive control. Computers & Chemical Engineering 58, 334–343. doi:10.1016/j.compchemeng.2013.07.015.

Baltes, M., Schneider, R., Sturm, C., Reuss, M., 1994. Optimal experimental design for parameter estimation in unstructured growth models. Biotechnology Progress 10, 480–488. doi:10.1021/bp00029a005.

Biegler, L., 2009. Technology Advances for Dynamic Real-Time Optimization, in: de Brito Alves, R.M., do Nascimento, C.A.O., Biscaia, E.C. (Eds.), 10th International Symposium on Process Systems Engineering: Part A. Elsevier. volume 27 of *Computer Aided Chemical Engineering*, pp. 1–6. doi:10.1016/S1570-7946(09)70220-2.

Boman, K., Thomas, J., Funkquist, J., 2010. Model-Based Power Plant Master Control. Värmeforsk Service AB, Stockholm (Sweden). URL: https://www.osti.gov/etdeweb/biblio/1004335. retrieved 2nd September 2021.

Chang, G., Tsai, Y., Lai, C., Chung, J., 2004. A practical mixed integer linear programming based approach for unit commitment, in: IEEE Power Engineering Society General Meeting, 2004., pp. 221–225 Vol.1. doi:10.1109/PES.2004.1372789.

Cramér, H., 1999. Mathematical Methods of Statistics. volume 9. Princeton University Press, Princeton (NJ, USA).

Ellis, M., Durand, H., Christofides, P.D., 2014. A tutorial review of economic model predictive control methods. Journal of Process Control 24, 1156–1178. doi:10.1016/j.jprocont.2014.03.010.

Engell, S., 2007. Feedback control for optimal process operation. Journal of Process Control 17, 203–219. doi:10.1016/j.jprocont.2006.10.011.

Favre-Perrod, P., 2005. A vision of future energy networks, in: 2005 IEEE Power Engineering Society Inaugural Conference and Exposition in Africa, pp. 13–17. doi:10.1109/PESAFR.2005.1611778.

González, A.H., Odloak, D., 2009. A stable mpc with zone control. Journal of Process Control 19, 110–122. doi:10.1016/j.jprocont.2008.01.003.

Guillaume, J.H., Jakeman, J.D., Marsili-Libelli, S., Asher, M., Brunner, P., Croke, B., Hill, M.C., Jakeman, A.J., Keesman, K.J., Razavi, S., Stigter, J.D., 2019. Introductory overview of identifiability analysis: A guide to evaluating whether you have the right type of data for your modeling purpose. Environmental Modelling & Software 119, 418–432. doi:10.1016/j.envsoft.2019.07.007.

Gurobi, 2021. Gurobi Optimizer Reference Manual. URL: https://www.gurobi.com. retrieved 2nd September 2021.

Halmschlager, V., Hofmann, R., 2021. Assessing the potential of combined production and energy management in industrial energy hubs – analysis of a chipboard production plant. Energy 226, 120415. doi:10.1016/j.energy.2021.120415.

Heirung, T.A.N., Paulson, J.A., O'Leary, J., Mesbah, A., 2018. Stochastic model predictive control — how does it work? Computers & Chemical Engineering 114, 158–170. doi:10.1016/j.compchemeng.2017.10.026.

Hinojosa, A., Ferramosca, A., Gonzalez, A., Odloak, D., 2017. One-layer gradient-based MPC + RTO of a propylene/propane splitter. Computers & Chemical Engineering 106, 160–170. doi:10.1016/j.compchemeng.2017.06.006.

Hlava, J., Opálka, J., Johansen, T.A., 2013. Model predictive control of power plant superheater — comparison of multi model and nonlinear approaches, in: 2013 18th International Conference on Methods Models in Automation Robotics (MMAR), pp. 311–316. doi:10.1109/MMAR.2013.6669925.

Hofmann, R., Halmschlager, V., Knöttner, S., Leitner, B., Pernsteiner, D., Prendl, L., Sejkora, C., Steindl, G., Traupmann, A., 2020. Digitalization in Industry - an Austrian Perspective. URL: https://www.klimafonds.gv.at/publication/white-paper-digitalization-in-industry-an-austrian-perspective/. retrieved 2nd September 2021.

IEA, 2020. World energy outlook 2020. URL: https://www.iea.org/reports/world-energy-outlook-2020. retrieved 2nd September 2021.

Jamaludin, M.Z., Swartz, C.L., 2017. Approximation of closed-loop prediction for dynamic real-time optimization calculations. Computers & Chemical Engineering 103, 23–38. doi:10.1016/j.compchemeng.2017.02.037.

Kadam, J., Marquardt, W., 2007. Integration of Economical Optimization and Control for Intentionally Transient Process Operation. volume 358. pp. 419–434. doi:10.1007/978-3-540-72699-9_34.

Kadam, J., Schlegel, M., Marquardt, W., Tousain, R., van Hessem, D., van den Berg, J., Bosgra, O., 2002. A Two-Level Strategy of Integrated Dynamic Optimization and Control of Industrial Processes—a Case Study, in: Grievink, J., van Schijndel, J. (Eds.), European Symposium on Computer Aided Process Engineering-12. Elsevier. volume 10 of *Computer Aided Chemical Engineering*, pp. 511–516. doi:10.1016/S1570-7946(02)80113-4.

Kadam, J.V., Marquardt, W., 2004. Sensitivity-based solution updates in closed-loop dynamic optimization. IFAC Proceedings Volumes 37, 947–952. doi:10.1016/S1474-6670(17)31930-4.

Lawrynczuk, M., 2014. Model predictive control with on-line optimal linearisation, in: 2014 IEEE International Symposium on Intelligent Control (ISIC), pp. 2177–2182. doi:10.1109/ISIC.2014.6967645.

Ljung, L., 1999. System Identification: Theory for the User. PTR Prentice-Hall, Hoboken (NJ,USA).

Löfberg, J., 2004. Yalmip : A toolbox for modeling and optimization in matlab, in: In Proceedings of the CACSD Conference, Taipei, Taiwan.

Ma, H., Yan, L., Xia, Y., Fu, M., 2020. Kalman Filter with Recursive Process Noise Covariance Estimation. Springer Singapore, Singapore. pp. 21–49. doi:10.1007/978-981-15-0806-6_3.

Marchetti, A., Ferramosca, A., González, A., 2014. Steady-state target optimization designs for integrating real-time optimization and model predictive control. Journal of Process Control 24, 129–145. doi:10.1016/j.jprocont.2013.11.004.

MATLAB, 2018. version 9.5.0 (R2018b). The MathWorks Inc., Natick, Massachusetts.

Miao, H., Xia, X., Perelson, A.S., Wu, H., 2011. On Identifiability of Nonlinear ODE Models and Applications in Viral Dynamics. SIAM Review 53, 3–39. doi:10.1137/090757009.

Mohammadi, M., Noorollahi, Y., Mohammadi-ivatloo, B., Yousefi, H., 2017. Energy hub: From a model to a concept – a review. Renewable and Sustainable Energy Reviews 80, 1512–1527. doi:10.1016/j.rser.2017.07.030.

MOSEK, 2019. The MOSEK optimization toolbox for MATLAB manual. Version 9.0. URL: http://docs.mosek.com/9.0/toolbox/index.html.

Muske, K.R., 1997. Steady-state target optimization in linear model predictive control, in: Proceedings of the 1997 American Control Conference (Cat. No.97CH36041), pp. 3597–3601 vol.6. doi:10.1109/ACC.1997.609493.

Prasad, G., Irwin, G., Swidenbank, E., Hogg, B., 2000. Plant-wide predictive control for a thermal power plant based on a physical plant

model. Control Theory and Applications, IEE Proceedings 147, 523 – 537. doi:10.1049/ip-cta:20000634.

Prasad, G., Irwin, G., Swidenbank, E., Hogg, B., 2002. A hierarchical physical model-based approach to predictive control of a thermal power plant for efficient plant-wide disturbance rejection. Transactions of The Institute of Measurement and Control 24, 107–128. doi:10.1191/0142331202tm053oa.

Qin, S., Badgwell, T.A., 2003. A survey of industrial model predictive control technology. Control Engineering Practice 11, 733–764. doi:10.1016/S0967-0661(02)00186-7.

Rawlings, J., Mayne, D., 2009. Model Predictive Control: Theory and Design. Nob Hill Pub., Santa Barbara (CA, USA).

Rawlings, J.B., Angeli, D., Bates, C.N., 2012. Fundamentals of economic model predictive control, in: 2012 IEEE 51st IEEE Conference on Decision and Control (CDC), pp. 3851–3861. doi:10.1109/CDC.2012.6425822.

Ritzberger, D., Höflinger, J., Du, Z.P., Hametner, C., Jakubek, S., 2021. Data-driven parameterization of polymer electrolyte membrane fuel cell models via simultaneous local linear structured state space identification. International Journal of Hydrogen Energy 46, 11878–11893. doi:10.1016/j.ijhydene.2021.01.037.

Scattolini, R., 2009. Architectures for distributed and hierarchical model predictive control – a review. Journal of Process Control 19, 723–731. doi:10.1016/j.jprocont.2009.02.003.

Simon, D., 2006. Optimal state estimation: Kalman, H∞, and nonlinear approaches. John Wiley & Sons, Hoboken (NJ, USA). doi:10.1002/0470045345.

Åström, K., Bell, R., 2000. Drum-boiler dynamics. Automatica 36, 363–378. doi:10.1016/S0005-1098(99)00171-5.

Tatjewski, P., 2008. Advanced control and on-line process optimization in multilayer structures. Annual Reviews in Control 32, 71–85. doi:10.1016/j.arcontrol.2008.03.003.

Tosukhowong, T., Lee, J.M., Lee, J.H., Lu, J., 2004. An introduction to a dynamic plant-wide optimization strategy for an integrated plant. Computers & Chemical Engineering 29, 199–208. doi:10.1016/j.compchemeng.2004.07.028. pSE 2003.

UN, 2015. Paris Agreement. United Nations Treaty Collection URL: https://treaties.un.org/Pages/ViewDetails.aspx?src=IND&mtdsg_no=XXVII-7-d&chapter=27&clang=_en. retrieved 2nd September 2021.

van den Bergh, K., Bruninx, K., Delarue Erik, D'haeseleer William, 2014. A mixed-integer linear formulation of the unit commitment problem URL: https://www.mech.kuleuven.be/en/tme/research/energy_environment/pdf/wpen2014-07-1.pdf. retrieved 2nd September 2021.

Varella, H., Guérif, M., Buis, S., 2010. Global sensitivity analysis measures the quality of parameter estimation: The case of soil parameters and a crop model. Environmental Modelling & Software 25, 310–319. doi:10.1016/j.envsoft.2009.09.012.

Vega, P., Revollar, S., Francisco, M., Martín, J., 2014. Integration of set point optimization techniques into nonlinear mpc for improving the operation of wwtps. Computers & Chemical Engineering 68, 78–95. doi:10.1016/j.compchemeng.2014.03.027.

Willis, M., Tham, M., 1994. Advanced process control. URL: http://citeseerx.ist.psu.edu/viewdoc/download?doi=10.1.1.462.7646&rep=rep1&type=pdf#page=2. retrieved 2nd September 2021.

Würth, L., Hannemann, R., Marquardt, W., 2009a. Neighboring-extremal updates for nonlinear model-predictive control and dynamic real-time optimization. Journal of Process Control 19, 1277–1288. doi:10.1016/j.jprocont.2009.02.001. special Section on Hybrid Systems: Modeling, Simulation and Optimization.

Würth, L., Hannemann, R., Marquardt, W., 2011. A two-layer architecture for economically optimal process control and operation. Journal of Process Control 21, 311–321. doi:10.1016/j.jprocont.2010.12.008.

Würth, L., Rawlings, J.B., Marquardt, W., 2009b. Economic Dynamic Real-Time Optimization and Nonlinear Model-Predictive Control on Infinite Horizons. IFAC Proceedings Volumes 42, 219–224. doi:10.3182/20090712-4-TR-2008.00033.

Wu, X., Shen, J., Li, Y., Lee, K.Y., 2015. Steam power plant configuration, design, and control. WIREs Energy and Environment 4, 537–563. doi:10.1002/wene.161.

Zhakatayev, A., Rakhim, B., Adiyatov, O., Baimyshev, A., Varol, H.A., 2017. Successive linearization based model predictive control of variable stiffness actuated robots, in: 2017 IEEE International Conference on Advanced Intelligent Mechatronics (AIM), pp. 1774–1779. doi:10.1109/AIM.2017.8014275.

Zullo, L., 1991. Computer Aided Design of Experiments. Ph.D. Thesis, University of London, London (U.K.).

Curriculum Vitae

Personal Information

Name	Dipl.-Ing. Dominik Pernsteiner
Date of birth	19th of February, 1991
Birthplace	Salzburg
Citizenship	Austria
Gender	Male
Adress	Fred-Zinnenmann-Platz 4/6/15, 1030 Wien

Education

09/2018 -	TU Wien Doctoral studies in Mechanical Engineering
10/2010 - 06/2018	TU Wien Diploma studies in Mechanical Engineering Graduation with distinction Specialization in finite elements, thermal energy systems, fluid mechanics & CFD Final examination passed on June 21th, 2018
09/2001 - 06/2009	Akademische Gymnasium Salzburg (secondary school) Final secondary-school examinations passed on June 18th, 2009

Diploma Thesis

Title	Numerical simulation of heat transfer in fluidized beds
Supervisor	Univ.Prof. Dr.techn. René Hofmann

Professional Work Experience

09/2018 -	University assistant at TU Wien Institute of Mechanics and Mechatronics Division of Control and Process Automation
03/2017 – 06/2018	Tutor at TU Wien
03/2015 - 06/2016	Institute of Mechanics and Mechatronics Subject: Mechanics 1 and 2
07/2016	Internship at Robel Bahnbaumaschinen
07/2015-08/2015	Sales Department and Prototyping Department
07/2013	Internship at Marbach Werkzeugbau GmbH Tools manufacturing department

Experience abroad

09/2016 - 12/2016	Study semester abroad University of Waterloo, Canada
08/2014 – 09/2014	China Know-How Summer School Peking University und Fudan University (Shanghai)

IT Skills

Operation systems	Windows
Office	Microsoft Office, LaTeX
Programming	Matlab
Simulation	Ansys Fluent

Languages

German	Native language
English	Fluent in written and spoken

Leisure Interests

Traveling, sports

List of scientific publications

International Journal Publications

1. **Efficient sensitivity-based cooperation concept in multi-layer operation optimization architectures**.
   Dominik Pernsteiner, Verena Halmschlager, Alexander Schirrer, René Hofmann, and Stefan Jakubek.
   submitted to Computers & Chemical Engineering (2021).

2. **State estimation concept for a nonlinear melting/solidification problem of a latent heat thermal energy storage**.
   Dominik Pernsteiner, Alexander Schirrer, Lukas Kasper, René Hofmann, and Stefan Jakubek.
   Computers & Chemical Engineering 153 (2021) p. 107444.
   DOI: 10.1016/j.compchemeng.2021.107444

3. **Data-based model reduction for phase change problems with convective heat transfer**.
   Dominik Pernsteiner, Alexander Schirrer, Lukas Kasper, René Hofmann, and Stefan Jakubek.
   Applied Thermal Engineering 184 (2021) p. 116228.
   DOI: 10.1016/j.applthermaleng.2020.116228

4. **Numerical studies on the influence of natural convection under inclination on optimal aluminium proportions and fin spacings in a rectangular aluminium finned latent-heat thermal energy storage**.
   Lukas Kasper, Dominik Pernsteiner, Martin Koller, Alexander Schirrer, Stefan Jakubek, and René Hofmann.
   Applied Thermal Engineering 190 (2021) p. 116448.
   DOI: 10.1016/j.applthermaleng.2020.116448

5. **Co-simulation methodology of a hybrid latent-heat thermal energy storage unit**.
   Dominik Pernsteiner, Lukas Kasper, Alexander Schirrer, René Hofmann, and Stefan Jakubek.
   Applied Thermal Engineering 178 (2020) p. 115495.
   DOI: 10.1016/j.applthermaleng.2020.115495

6. **Experimental and Numerical Investigations on Heat Transfer of Bare Tubes in a Bubbling Fluidized Bed with Respect to Better Heat Integration in Temperature Swing Adsorption Systems**.
   Hannes Vogtenhuber, Dominik Pernsteiner, and René Hofmann.
   Energies 12 (2019) p. 2646.
   DOI: 10.3390/en12142646

Scientific report

1. **Digitalization in Industry - an Austrian Perspective**
   René Hofmann, Verena Halmschlager, Sophie Knöttner, Benedikt Leitner, Dominik Pernsteiner, Leopold Prendl, Christoph Sejkora, Gernot Steindl, and Anna Traupmann.
   Austrian Climate and Energy Funds (Klima- und Energiefonds) (2020).
   URL: https://www.klimafonds.gv.at/publication/white-paper-digitalization-in-industry-an-austrian-perspective/